To the Graduate Council:

I am submitting herewith a dissertation written by Wilhelmus M. J. Ruyten entitled "Aspects of Laser Induced Fluorescence Employing Pulsed and Modulated Excitation." I have examined the final copy of this dissertation for form and content and recommend that it be accepted in partial fulfillment of the requirements for the degree of Doctor of Philosophy, with a major in Physics.

J. W. L. Lewis, Major Professor

We have read this dissertation
and recommend its acceptance:

Accepted for the Council:

Vice Provost
and Dean of The Graduate School

ASPECTS OF LASER INDUCED FLUORESCENCE EMPLOYING PULSED AND MODULATED EXCITATION

A Dissertation

Presented for the

Doctor of Philosophy

Degree

The University of Tennessee, Knoxville

Wilhelmus M. J. Ruyten

August 1989

Copyright© Wilhelmus M. J. Ruyten
All rights reserved, 1989

To God be the glory

Aan mijn ouders
To my wife Belle

ACKNOWLEDGMENTS

There are many persons at the University of Tennessee Space Institute who have contributed to this work. Among these are my major professor, James W. L. Lewis, and the other committee members, Drs. Horace W. Crater, John B. Dicks, Dennis R. Keefer, and Arthur A. Mason.

In addition, many present and former members of the Applied Physics Research Group have offered innumerable advice, discussion, technical help, and administrative assistance. Of these I should like to mention in particular: Mary Helen Brittain, Donna Brewer, Jean Broadway, Linda Crosslin, Herbert Crowder, Lloyd Davis, Jim Few, Bruce Hill, Jim Hornkohl, Eric Howard, San-Mou Jeng, Christian Parigger, Connie Payne, Dragan Petrovic, Fred Schwartz, Monty Smith, Jim White, and Newton Wright.

Finally I gratefully acknowledge the funding from the Tennessee Higher Education Commission through the "Centers of Excellence Program," and the permission to reprint copyrighted material, as listed in the PREFACE, by the American Institute of Physics, the American Physical Society, and the Optical Society of America.

ABSTRACT

This work reports on various aspects of employing strong, pulsed or modulated excitation in laser induced fluorescence (LIF) experiments. Part I is motivated by two-photon LIF measurements in nitric oxide, used for the determination of temperatures and concentrations in cold flows. It is found that dynamical Stark effects modify the lineshapes of individual rotational transitions significantly, thereby invalidating conventional methods of data analysis. It is shown that, to maintain calibration, one must extract the true intensity dependence of the underlying nonlinear interactions from data that are spatially and temporally unresolved. This inversion problem is developed and solved for nonsaturated as well as saturated excitation, namely by the use of Abel inversion, moment expansion, and collocation in terms of kernel or spline basis functions. Further applications of these techniques to problems in laser diagnostics are discussed.

Part II is concerned with fundamental aspects of a proposed laser fluorescence velocimeter. In this instrument, flow velocities are derived from the depth-of-modulation or the phase-shift of the fluorescence signal with respect to the bichromatic (fully amplitude modulated) input field. By solving the pertinent Bloch equations it is found that, unlike for weak excitation, the inhomogeneously broadened response of such a system deviates considerably from that of a similar system driven by a broadband field. Thus, conventional results from phase-sensitive fluorometry are inapplicable. Instead, much insight can be gained from the concepts of multiple quantum resonances and Bloch-Siegert shifts, taken from magnetic resonance. However, this work moves beyond merely transferring these concepts to optical resonance, in particular by studying the behavior of harmonic interaction components. Also, it is discussed how similar insights can be applied to other optical interactions, for example those involving phase-modulation.

PREFACE

The subject matter of this dissertation reflects the results of both experimental and theoretical work conducted in the Center for Laser Applications at the University of Tennessee Space Institute during the period Spring 1985 through Summer 1989. The original focus of the project was the study of two-photon laser induced fluorescence (LIF) of nitric oxide for the measurement of temperatures and concentrations in cold flows. But as the research progressed, primarily as an experimental activity, it also digressed into a largely unrelated project, namely that of the study of a laser fluorescence velocimeter. In both projects fundamental questions concerning the underlying optical field-matter interactions arose. Thus the emphasis of the work turned to the formulation of adequate theoretical models to account for effects such as nonuniform excitation, saturation, and multiple quantum resonances. As a result of an unfortunate accident in the laboratory, much of the equipment needed to put into practice and verify the results of this theoretical work was damaged. Accordingly, the bulk of the material in this dissertation concerns various theoretical aspects of field-matter interactions.

Because of the disparate nature of the two projects the respective results are presented independently in parts I and II, each of which has its own introduction, sections, references and appendices. Apart from the theoretical work, the introduction to part I also contains some of the experimental results that were obtained at an early stage of the work on two-photon LIF of nitric oxide. A more extensive account of this experimental work may be found in an internal report (see Ref. 20 on page 91). Furthermore, most of the work presented in this dissertation has been published or submitted for publication elsewhere, or has been presented at conferences, as listed below:

[1] J. O. Hornkohl and W. M. Ruyten, "Corrections to two-photon Hönl-London factors," J. Mol. Spectr. **123**, 499-500 (1987).

*†[2] W. M. Ruyten, L. M. Davis, C. Parigger, and D. R. Keefer, "Atomic response to bichromatic crossed-beam field," in *Advances in Laser Science-III*, A. C. Tam, J. L. Gole, and W. C. Stwalley, eds. (American Institute of Physics, New York, 1988), pp. 155–157.

*†[3] W. M. Ruyten and J. W. L. Lewis, "Recovery of excitation intensity dependence in pulsed, focused beams: nonsaturated case," J. Opt. Soc. Am. B **5**, 2368–2373 (1988).

*[4] W. M. Ruyten, "Rabi structures in a Doppler broadened gas?" OSA Annual Meeting, 1988 Technical Digest Series, Vol. 11 (Optical Society of America, Washington, DC, 1988), paper MY6, p. 63.

*[5] W. M. Ruyten and J. W. L. Lewis, "Recovery of excitation intensity dependence in pulsed focused beams," OSA Annual Meeting, 1988 Technical Digest Series, Vol. 11 (Optical Society of America, Washington, DC, 1988), paper WZ5, p. 124.

[6] W. M. Ruyten, "Comment on absorption and fluorescence in strong frequency-modulated and amplitude-modulated fields," Phys. Rev. A **39**, 442–444 (1989).

*†[7] W. M. Ruyten "Multiphoton resonances in the modulated fluorescence from an inhomogeneously broadened medium," Opt. Lett. **14**, 506–508 (1989).

*†[8] W. M. Ruyten, "Harmonic behavior of the multiple quantum resonances of a two-level atom driven by a fully amplitude modulated field," Phys. Rev. A **40**, 1447–1455 (1989).

*†[9] W. M. Ruyten, "Subharmonic resonances in terms of multiphoton processes and generalized Bloch-Siegert shifts," J. Opt. Soc. Am. B, to appear October 1989.

[10] W. M. Ruyten, "Resonance behavior of a two-level atom driven by amplitude- or frequency-modulated fields," presented at the Sixth Rochester Conference on Coherence and Quantum Optics, Rochester, June 26–28 (1989); proceedings to be published by Plenum, L. Mandel, ed.

*[11] W. M. Ruyten, "Inversion of spatio-temporally averaged data using a regularized spline collocation scheme," J. Opt. Soc. Am. A, submitted for publication.

*[12] W. M. Ruyten, "Optical Haroche and Hanle resonances excited by a resonant phase-modulated field," Phys. Rev. Lett., submitted for publication.

In the above list, asterisks (*) indicate that the material from the respective references has been included in this dissertation in more or less unmodified form. Daggers (†) indicate that the respective sources have granted permission to reproduce copyrighted material here.

Wilhelmus M. J. Ruyten,
Tullahoma, July 1989.

TABLE OF CONTENTS

PART I: INVERSION OF SPATIALLY AND TEMPORALLY AVERAGED DATA IN LASER DIAGNOSTICS

I INTRODUCTION 2

II STATEMENT OF THE INVERSION PROBLEM 14
- II-1 Signal Versus Excitation Rate 14
  - II-1.1 Nonsaturated regime 17
  - II-1.2 Saturated regime: fast pulse limit 18
  - II-1.3 Saturated regime: slow pulse limit 19
- II-2 Transformation to Kernels 20
- II-3 Kernels Resulting from Exponential Profiles 25

III METHODS OF INVERSION 31
- III-1 Abel Inversion 32
- III-2 Moment Method 35
- III-3 Inversion by Collocation 36
- III-4 Direct Inversion 39

IV INVERSION BY REGULARIZED SPLINE COLLOCATION 44
- IV-1 Theory 45
  - IV-1.1 Spline equations 45
  - IV-1.2 Regularization 46
  - IV-1.3 Fidelity of inversion results 48
  - IV-1.4 Residue-of-fit 50
  - IV-1.5 Numerical computation 51
- IV-2 Overview of Sample Cases 52
  - IV-2.1 Kernels and cross-sections 52
  - IV-2.2 Experimental conditions 54
  - IV-2.3 Spline parameters 54
- IV-3 Numerical Results 55
- IV-4 Summary and Conclusions 65

V INVERSION OF NONSATURATED AND SATURATED LINESHAPES 67
- V-1 Nonsaturated Regime 68
- V-2 Saturated Regime 71

VI DISCUSSION 84

LIST OF REFERENCES 89

APPENDICES 94
Appendix A: Two-Photon Hönl-London Factors 95
Appendix B: Exponential Profiles 97
B-1 Kernels and moments 97
B-2 Abel inversion 99
B-3 Integer shape parameters 101
Appendix C: Simple Model of Stark Broadened Lineshapes 103
Appendix D: List of Symbols 105

PART II: RESPONSE OF A SIMPLE QUANTUM SYSTEM TO A FULLY AMPLITUDE MODULATED FIELD

I INTRODUCTION 111

II OVERVIEW OF OPTICAL AND MAGNETIC RESONANCE . . . 119
II-1 Experimental Aspects 119
II-2 Optical Bloch Equations 122
II-3 Magnetic Bloch Equations 128
II-4 Resonance Behavior 131
II-4.1 Multiple quantum resonances 132
II-4.2 Bloch-Siegert shifts 133

III RESONANCE BEHAVIOR OF A TWO-LEVEL ATOM IN A FULLY AMPLITUDE MODULATED FIELD 138
III-1 Motivation and Organization 138
III-2 General Solution 140
III-3 Vanishing Damping Solution 148
III-4 Generalized Bloch-Siegert Shifts 151
III-5 Prospects for Experimental Verification 158

IV EFFECTS OF INHOMOGENEOUS BROADENING 162
IV-1 Relevance to the Laser Fluorescence Velocimeter 163
IV-2 Weak Field Results 166
IV-2.1 Narrowband solution 166
IV-2.2 Broadband solution 171
IV-2.3 Inhomogeneously broadened solution 172
IV-3 Strong Field Results 174

V DISCUSSION 185

LIST OF REFERENCES 188

APPENDICES 195
Appendix A: Zero Detuning Solution 196
Appendix B: Calculation of Power Series Coefficients of the Generalized Bloch-Siegert Shifts 200
Appendix C: Weak Field Solutions 203
C-1 Details of narrowband solution 203
C-2 Details of broadband solution 204
C-3 Details of inhomogeneously broadened solution 206
Appendix D: Optical Haroche and Hanle Resonances Excited by a Resonant Phase-Modulated Field 207
Appendix E: List of Abbreviations and Symbols 217

VITA 221

LIST OF FIGURES

PART I

I–1: Schematic representation of a laser induced fluorescence experiment 4

I–2: Example of Stark broadened molecular transitions 7

I–3: Example of deviations from pure power law behavior 10

II–1: Rate equation model to describe pulsed, nonlinear excitation . . . 15

II–2: Kernels for exponential beam- and pulse-profiles 27

II–3: Illustration of spatial and/or temporal averaging 28

II–4: Further illustrations of spatial and/or temporal averaging 29

III–1: Eigenvalues of direct inversion matrix 41

III–2: Eigenvalues of direct inversion matrix versus the central intensities of the corresponding basis vectors 42

III–3: Example of direct inversion results 43

IV–1: Condition numbers of the spline inversion matrix 56

IV–2: Inversion results without and with noise 56

IV–3: Fidelities, residue-of-fit, and condition as a function of the regularization parameter 58

IV–4: Fidelity versus residue-of-fit 59

IV–5: Best fidelities for different numbers of data and different cross-sections 61

IV–6: Best fidelities for different noise amplitudes 61

IV–7: Best fidelities for different numbers of knots 62

IV–8: Regularized inversion results for linear splines 64

IV–9: Best fidelities for different kernels 64

V–1: Effect of averaging on Stark broadened lineshapes 69

V–2: Illustration of the effects of saturation on the lineshapes 74

V–3: Inversion procedure for nonsaturated lineshapes 76

V–4: Examples of linearly inverted saturated lineshapes 77

V–5: Inversion procedure for saturated lineshapes 80

V–6: Average deviations of the spectrally integrated lineshapes 82

PART II

I–1: Schematic diagram of the laser fluorescence velocimeter 112

II–1: Schematic representation of optical and magnetic resonance experiments 120

II–2: Schematic representations of various magnetic resonance configurations 130

II–3: Illustration of multiple quantum resonances in an optical two-level system 134

II–4: Bloch-Siegert resonance curves for a longitudinally pumped magnetic resonance experiment 137

III–1: DC fluorescence and in-phase component of the lowest fluorescence harmonic as a function of the Rabi frequency and the detuning 145

III–2: DC fluorescence and in-phase component of the lowest fluorescence harmonic as a function of the detuning for a fixed Rabi frequency 146

III–3: Detuning scans of the lowest fluorescence harmonic for various damping ratios 148

III–4: Generalized Bloch-Siegert resonance curves for various fluorescence and susceptibility components 154

III–5: Doubly branched resonances for nonzero damping 160

IV–1: Mapping from laboratory frame to atom's rest frame 164

IV–2: Fluorescence signal as a function of the detuning for several values of the damping 169

IV–3: Narrowband phase-shift versus detuning for the same conditions as in Figure IV-2 170

IV–4: Inhomogeneously broadened values of several fluorescence and susceptibility components 176

IV–5: Inhomogeneously broadened values of the depth-of-modulation and phase-shift for several fluorescence harmonics 178

IV–6: Inhomogeneously broadened values of the depth-of-modulation and phase-shift for several values of the damping ratio 180

IV–7: Influence of the Doppler width on the inhomogeneously broadened values of the depth-of-modulation 181

D–1: Magnetic resonance geometries, whose optical counterparts are as indicated 208

D–2: Generalized Bloch-Siegert resonance curves for both odd and even resonances, obtained in the limit of vanishing damping 212

D–3: Time-averaged upper state population as a function of the scaled electric field 214

D–4: As Figure D-3 for the magnitude of the upper state population modulated at twice the modulation frequency 216

PART I:

INVERSION OF SPATIALLY AND TEMPORALLY AVERAGED DATA IN LASER DIAGNOSTICS

I INTRODUCTION

It may be stated without reservation that the advent of the laser has brought forth a revolution in modern physics, indeed, in modern technology in general. From the computerized scanning of UPC-symbols in the local supermarket to the most accurate measurements of fundamental constants of nature to date, the laser has inevitably replaced older methods and techniques, or has — as is more frequently the case — created entirely new applications. The continuing development of laser sources even calls for a new vocabulary: power levels are now frequently expressed in terawatts, pulse durations in femtoseconds. Acronyms such as CARS (coherent anti-Stokes Raman scattering) and REMPI (resonantly enhanced multi-photon ionization) have become household words in the scientific laboratory. And yes, although the word "laser" has been around long enough to be freely used as a verb ("lasing") and be subject to the wear-and-tear of American spelling ("lazer"), let it not be forgotten that it is an acronym itself: "light amplification by stimulated emission of radiation."

Throughout its history, the development of the laser has been tightly interwoven with advances in atomic and molecular spectroscopy and their applications in the diagnostics of solids, liquids, gases and plasmas. It is not within the scope of this work to give a comprehensive overview of the field, so that we must refer the interested reader to recent review articles [1–3]* and textbooks on nonlinear optics [4–7]. Suffice it to say that the quantities that can be monitored by optical techniques are as varied as the techniques themselves. Among the former are composition, number density, temperature and velocity. One of the more

---

*Here and in the following, numbers within square brackets refer to the similarly numbered entries in the List of References on page 89.

prominent among the latter is laser induced fluorescence (LIF) by either single- or multi-photon excitation.

Figure I-1 depicts the basic elements of a LIF experiment: a laser beam is focused into an interaction region which contains the — usually gaseous — medium of interest. By tuning the wavelength of the laser into resonance with a particular species, this species undergoes a transition from its ground state to an excited state by absorption of one or more laser photons. Within a time that is characteristic of both the species and its ambient environment the excited state returns to the ground state. If this takes place through a radiative decay, one or more fluorescence photons are emitted, which may be detected at right angles to the laser beam. From the magnitude of the detected signal one obtains information on the number density of the species. By probing different ground states of the same species one can deduce the temperature of the medium, if thermodynamic equilibrium is assumed. Finally, because atoms or molecules in motion "see" a laser wavelength that is Doppler shifted in direct proportion to their velocity, one can, in principle, calculate this velocity from the amount of detuning that is necessary to obtain a maximum LIF signal. We add to this succinct description that the technique of LIF is very versatile, very sensitive, and very widely used. Still, although LIF techniques have been around as long as lasers themselves have, many of the underlying principles and potential applications remain open to investigation and exploration.

Both parts I and II of this dissertation address fundamental aspects of employing laser induced fluorescence as a diagnostic tool for the study of nonreacting and reacting flows, such as those found in wind-tunnel testing and flames. Because of the different emphases and methodologies, however, we present the respective analyses independently. Thus part I restricts itself to the problem of the extraction

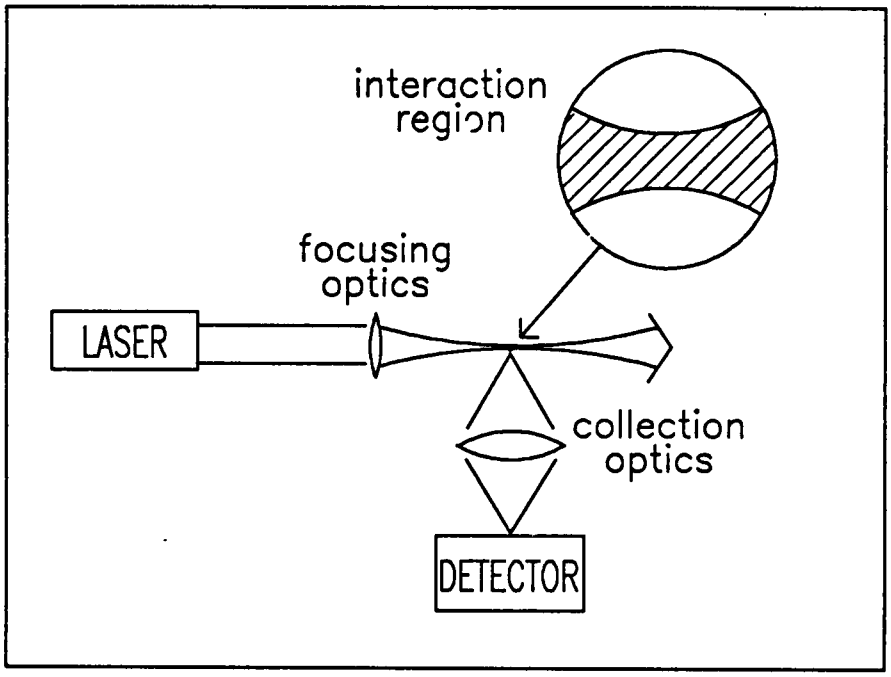


Figure I–1: *Schematic representation of a laser induced fluorescence experiment.*

of the true intensity-dependence of some nonlinear optical process from data, such as those obtained in pulsed LIF experiments, in which averaging takes place over the spatial extent of the focused beam and/or its pulse duration. Subsequently, in part II, the LIF response of a simple quantum system (such as an atomic species) to amplitude-modulated excitation is investigated.

The primary motivation for the work in part I was a series of publications by Gross and McKenzie who studied pulsed, two-photon LIF of nitric oxide as a diagnostic tool for measuring temperatures and concentrations in various gasdynamic processes [8–12]. Although the NO molecule is but one of many species that lends itself to the technique of two-photon LIF, it is of significant interest because of its natural occurrence as a combustion product and because of its potential as

a tracer in cold, nonreacting flows. The most important advantage of two-photon instead of single-photon LIF is that excitation takes place in the visible rather than the ultraviolet part of the spectrum. This allows for more efficient generation and easier manipulation of the exciting light, as well as greater rejection of the unwanted, scattered radiation from the actual, ultraviolet fluorescence signal. Another advantage stems from the selection rules for dipole-allowed transitions, which give rise to O- and S-branches in addition to the P-, Q-, and R-branches for single-photon excitation. This generally facilitates the excitation of isolated rotational lines in a cluttered vibrational band system which may consist of hundreds of lines. A third advantage stems from the quadratic dependence of the excitation rate on intensity, as a result of which significant absorption of the exciting light takes place only near the focus of the laser beam. Thus no attenuation takes place as the beam propagates toward the interaction region, and some amount of spatial resolution along the beam-axis is achieved without an additional effort. Finally, in Doppler-free spectroscopy with counter-propagating beams, inhomogeneous broadening may be eliminated [13-15].

The most serious disadvantage of two-photon LIF over its single-photon counterpart is that much higher power densities are required to obtain strong fluorescence signals. Indeed, in the absence of near-resonant intermediate states two-photon transitions are found only in second-order perturbation theory. Thus, following its initial prediction by Göppert-Mayer in 1933 [16], experimental verification of the existence of two-photon processes had to await the availability of intense, nearly monochromatic light (for some of the earliest reports of two-photon excitation of NO see Ref. [17]). To be sure, not only is strong two-photon excitation of species such as NO now possible, it is even feasible to saturate individual rotational transitions, that is, to cause a significant depletion of the ground state

of the transition during the laser pulse. But even at power levels below those required to achieve saturation, an additional complication arises, namely power broadening and shifting of the lines due to the dynamical Stark effect. From the viewpoint of laser diagnostics, Stark broadening is an undesirable effect, because it complicates the analysis of LIF data. This is particularly the case when measuring species concentrations, which requires an absolute calibration of the detection apparatus. However, Stark effects also compromise the accuracy of temperature measurements which are based on the relative intensities of two or more rotational lines [18,19].

Figure I-2 demonstrates the dynamical Stark effect for two adjacent lines in the two-photon excitation spectrum of nitric oxide, namely the $O_{12}(5\frac{1}{2})$ and $O_{12}(6\frac{1}{2})$ rotational transitions in the γ-band ($v' = 0 \leftarrow v'' = 0$) of the $A^2\Sigma^+ \leftarrow X^2\Pi_{3/2}$ system. Experimental details are given in the figure caption. For a more extensive account of the experimental work that was carried out in the initial phase of this research see Ref. [20]. For the lowest pulse energy in Figure I-2 (0.013 mJ) the spectral width of the two lines is essentially that of the exciting laser (0.023Å). As the pulse energy is increased by two orders of magnitude the two lines undergo substantial broadening. Note that this broadening is asymmetric and is quite different for the two lines. Although such behavior has been qualitatively confirmed by ab-initio calculations in which couplings to higher molecular states are taken into account [11], a precise characterization of the effect remains an experimental effort. However, the very experimental arrangement that is used directly influences the measured lineshapes. This is easily understood: the spectral lineshape is a function of the intensity of the field. This lineshape, which we refer to as the *true* lineshape, would be obtained if continuous, plane-wave light were used to perform the experiment (in which case it would be impossible to achieve the

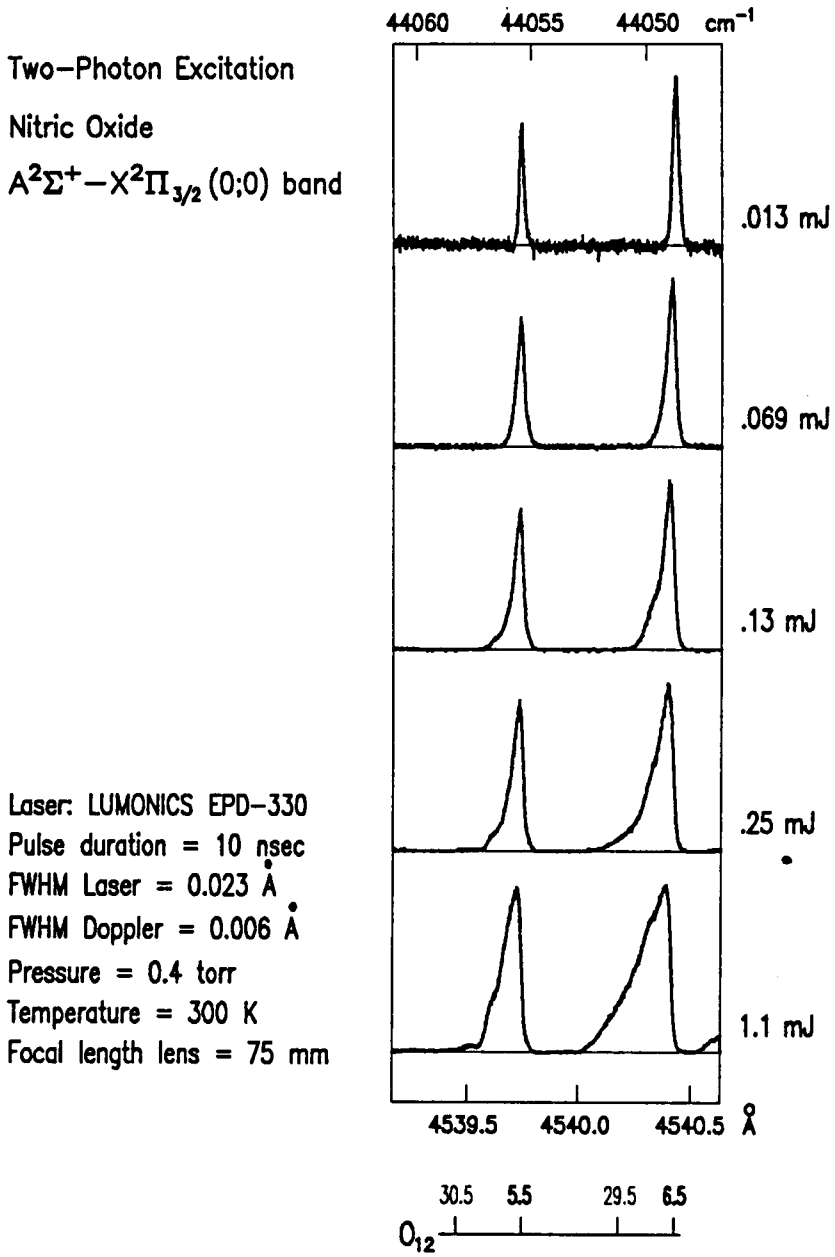


Figure I–2: *Example of Stark broadened molecular transitions.*

Experimental LIF signals (a.u.) of the $O_{12}(5\frac{1}{2})$ *and* $O_{12}(6\frac{1}{2})$ *lines in the* $\gamma(0;0)$ *band of nitric oxide are plotted versus laser wavelength (Å) and transition wavenumber* (cm^{-1}) *for five pulse energies (mJ). Experimental parameters are as indicated.*

same high power densities), or else, if a detection system were used with such high spatial and temporal resolution that no significant intensity variations within the "windowed" interaction region would exist. For the pulsed, strongly focused radiation that is typically employed to cause significant multi-photon excitation, such high resolution may not only be impossible to achieve, but also undesirable because it would decimate the detected signal to unacceptably low levels. Thus, in a typical experimental arrangement, fluorescence data are collected from an interaction region across which exists a significant spread of values of the local, instantaneous intensity of the exiting light, as shown in the expanded portion of Figure I-1. Thus the measured lineshapes constitute an average over a range of true intensity-dependent lineshapes. Because these averaged lineshapes depend on the spatial and temporal mode patterns of the laser beam, the pulse shape, the focusing optics, and the collection optics, they cannot be compared straightforwardly to those obtained by different researchers or even those from the same experiment in which, say, lenses with different focal lengths are used.

The dynamical Stark effect not only influences the true intensity-dependent lineshapes of a transition, but also the associated cross-sections. For example, at a fixed frequency within the spectral lineshape, the excitation rate depends on the intensity if the lineshape itself does. Thus, the n-photon excitation rate $R_n(I)$ can no longer be expressed simply in terms of the intensity I and a constant cross-section σ_n as*

$$R_n(I) = I^n \sigma_n, \tag{I-1}$$

but the cross-section itself becomes intensity-dependent:

$$R_n(I) = I^n \sigma_n(I). \tag{I-2}$$

---

*A comprehensive list of symbols for Part I may be found in Appendix D.

As a result, one can no longer simply scale the signals from one or more rotational transitions by the appropriate Hönl-London factors of the cross-sections to calculate temperatures or concentrations, as is done in the absence of Stark effects (we have listed Hönl-London factors for two-photon $\Sigma \leftarrow \Pi$ transitions pertinent to the NO molecule in Appendix A, which is compiled from Ref. [21] with corrections as noted in Ref. [22]).

Figure I-3 illustrates the intensity-dependence of the cross-sections associated with the two-photon LIF data from Figure I-2. Specifically, it displays the spectrally integrated signals (that is, the areas underneath the peaks in Figure I-2) of the $O_{12}(5\frac{1}{2})$ and $O_{12}(6\frac{1}{2})$ lines as a function of the pulse energy. Up to about 0.2 mJ a strict quadratic dependence of the signal on pulse energy is found, signifying a constant cross-section. By displaying the spectrally integrated signal rather than the signal at a fixed frequency within the lineshape, the quadratic dependence still holds slightly beyond the onset of Stark broadening. For larger intensities, however, the signals fall significantly below the extrapolated quadratic behavior. As it turns out, an analysis of the data from Figures I-2 and I-3 calls for the inclusion of saturation effects in addition to those of Stark effects, as is discussed in more detail in Sections V and VI. But in any event, in the region where a strict quadratic dependence is no longer valid, experimental values of the cross-sections derived from the data in Figure I-3 would be specific to the experimental arrangement in the same way as the experimental lineshapes themselves are: they would constitute an average over a range of the true intensity-dependent cross-sections.

Returning to the discussion on the complications that Stark effects and saturation effects cause in the analysis of LIF data we note that the easiest solution is to operate only in those regimes where these effects are negligible or at least

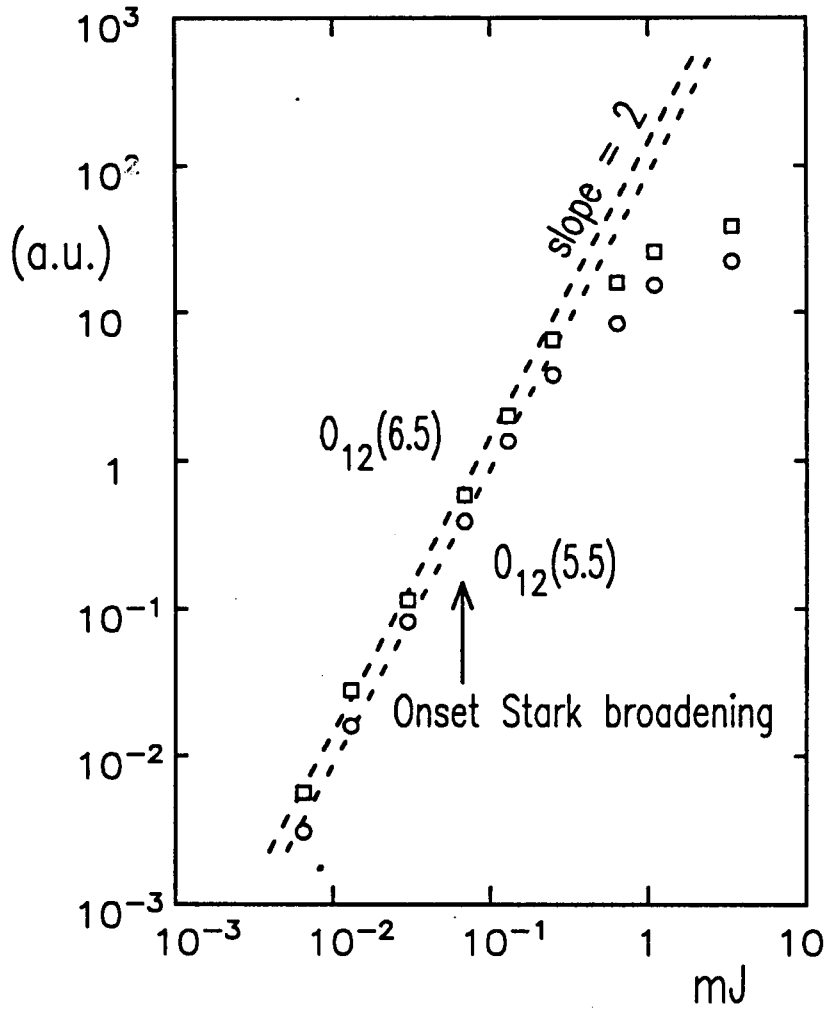


Figure I–3: *Example of deviations from pure power law behavior.*

Spectrally integrated LIF signals (a.u.) are obtained from the data in Figure I-2 and are plotted versus the pulse energy (mJ). Dashed lines represent pure quadratic behavior.

small. This, in fact, is suggested in the surveying work by Gross and McKenzie [8-11]. However, this approach precludes the larger signals and hence better signal-to-noise ratios that are feasible with available pulse energies. But to be able to properly scale experimental data for different rotational lines, pulse energies, and focusing geometries, one must know the true intensity-dependences of the lineshapes and cross-sections that underly these experimental data.

In this manner presents itself the problem of extracting the true intensity-dependence of some nonlinear optical process from spatially and/or temporally averaged data. Although this is a problem that numerous researchers must have encountered in applications involving LIF as well as other optical techniques — or, for that matter, techniques in fields other than optics — it appears that no general approach to this problem has been discussed in the literature. Most frequently, data such as cross-sections and excitation rates are presented simply as a function of the pulse energy or the average intensity in the pulse, and the appropriate experimental parameters are stated [1,11,23,24]. Sometimes, the effects of nonuniform excitation in some idealized geometry such as involving rectangular or Gaussian beam- and detector-profiles are simulated for assumed models of the intensity-dependence of the excitation process [24,25]. In still other cases, the parameters of specific model functions for the nonlinear process at hand are obtained by such techniques as least-squares fitting or other parameter estimation methods [26-28].

By contrast, in part I we show that the extraction of the true intensity-dependence of some nonlinear optical process from spatially and/or temporally averaged data can be formulated as an inversion problem, and we discuss explicit analytical and numerical techniques for its solution. Although we occasionally refer to the specific two-photon LIF data from Figures I-2 and I-3 we generalize

the problem statement to that of some arbitrary nonlinear process, both in terms of the excitation mechanism and signal generation. Thus the approach is not only applicable to LIF, but also to such processes as multi-photon ionization, harmonic generation and spontaneous and stimulated Raman scattering.

In Section II we introduce a simple rate equation model which forms the basis for subsequent calculations. In particular, we derive explicit integral expressions that relate the experimental signal to the true intensity-dependent cross-section. The simplest case is that of a nonsaturated excitation process, namely one in which the ground state of the atom or molecule is never appreciably depleted. In this case, a linear integral expression results, despite the nonlinear behavior of the optical process itself. Also, spatial and temporal coordinates are on the same mathematical footing. This is no longer true if the exciting light is intense enough and of sufficient duration to cause saturation effects, in which case more complex integral expressions result. However, we show that in either case, the true intensity-dependence can be extracted by single or successive inversions.

In Section III we present a general overview of inversion methods that can be used. For example, if the distribution of the exciting light in the interaction region can be written in terms of exponential profiles (not neccessarily Gaussian), inversions can be performed analytically using a variant of the Abel transform. In realistic applications, data are generally noisy and discrete. This poses a special difficulty due to the ill-posed nature of inversion problems. In this case, we contend that the best approach is that of collocation, that is, the true, unknown, intensity-dependent cross-section is expanded in terms of suitable basis functions, and the inversion consists of determining the expansion coefficients. Unlike most analytical methods of inversion, this approach accommodates various methods of regularization, thereby limiting the effect of data noise on the inversion results.

In Section IV we apply the theory from Section III to specific, simulated experimental data. In particular, we investigate the inversion of discrete, noisy, spatially and/or temporally averaged data by a collocation scheme that employs polynomial splines. In this case, regularization is achieved by constraining the discontinuities in the highest derivatives of the splines at the knots. We show that this scheme compares quite favorably with the proved method of Tikhonov regularization, and we establish general guidelines for choosing optimum spline- and regularization-parameters.

In Section V we extend the theory from Sections II, III, and IV to the study of intensity-dependent lineshapes. Specifically, we show how the influence of Stark effects can be iteratively isolated from the effects due to saturation by making the assumption that the spectrally integrated area of the true intensity-dependent lineshape is independent of the intensity. For illustration we present a number of calculations, based on a simple model of Stark broadened lineshapes.

Finally, in Section VI, we present a discussion of the theory and the results in part I of this dissertation. Specifically, we discuss the implementation of the methods of part I to actual experimental problems, and we identify areas of further research.

II STATEMENT OF THE INVERSION PROBLEM

In Section II we consider a general experiment in which some nonlinear optical process is driven by a pulsed, focused laser beam, thereby generating a signal such as fluorescence or ion-yield, which remains spatially and temporally unresolved. First, in Section II-1, we use a simple rate equation model to derive integral expressions that relate the spatially and temporally averaged signal to the true, unknown, intensity-dependent cross-section of the nonlinear process. Then, in Section II-2, we introduce kernels that allow these integral equations to be transformed into forms amenable to inversion. Finally, in Section II-3, we calculate these kernels explicitly for the case of exponential beam- and pulse-profiles.

II–1 Signal Versus Excitation Rate

Figure II-1 gives a schematic representation of the dynamics of the type of nonlinear optical process that we envisage: pulsed excitation of some atomic or molecular ground state, state $|1\rangle$, takes place by some n-photon process which is characterized by the true, intensity-dependent excitation rate $R_n(I)$. Deexcitation of the excited state, state $|2\rangle$, takes place through stimulated emission at a rate $g_{12}R_n(I)$, where g_{12} is the multiplicity ratio of states $|1\rangle$ and $|2\rangle$, and through a combination of random, radiative and nonradiative processes, at a combined rate A. A fraction β_{12} of these random deexcitation processes causes the system to return to its ground state, while the remaining fraction $1-\beta_{12}$ decays into a combination of "drain" states, which we collectively denote by state $|3\rangle$. Furthermore, we assume that thermalization of states $|1\rangle$ and $|3\rangle$ takes place on a timescale short compared with the excitation pulse and the random decay of the excited state $|2\rangle$. Thus we do not take into account the decay from state $|3\rangle$ back to state

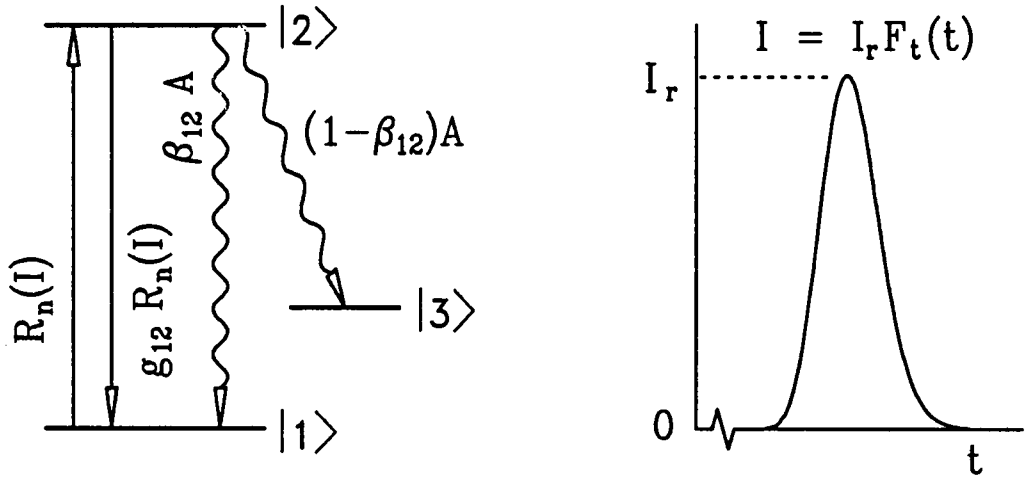


Figure II–1: *Rate equation model to describe pulsed, nonlinear excitation.*

$|1\rangle$.* From Figure II-1 we obtain the following rate equations:

$$\dot{n}_1 = -R_n n_1 + g_{12} R_n n_2 + \beta_{12} A n_2; \quad n_1(-\infty) = 1; \qquad \text{(II–1a)}$$

$$\dot{n}_2 = R_n n_1 - g_{12} R_n n_2 - A n_2; \qquad n_2(-\infty) = 0; \qquad \text{(II–1b)}$$

$$\dot{n}_3 = (1-\beta_{12}) A n_2; \qquad n_3(-\infty) = 0, \qquad \text{(II–1c)}$$

where n_1, n_2, and n_3 are the populations of the states $|1\rangle$, $|2\rangle$, and $|3\rangle$, and the dots denote differentiation with respect to time. As indicated, states $|2\rangle$ and $|3\rangle$ are assumed to be initially unpopulated, and the initial population of state

---

*This is a good assumption in the case of two-photon excitation of nitric oxide using nanosecond-type pulses, in which both states $|1\rangle$ and $|3\rangle$ are in the same electronic state of the molecule, whereas state $|2\rangle$ is an electronically excited state.

$|1\rangle$ is normalized to unity. Since, after the pulse, state $|2\rangle$ becomes completely depopulated again, the "number" of excited states $|2\rangle$ per laser pulse can be written as

$$N_{\rm pp} = A \int_{-\infty}^{\infty} n_2(t)\, dt, \tag{II-2a}$$

or, alternatively, as

$$N_{\rm pp} = n_3(\infty)/(1-\beta_{12}) = \big[1 - n_1(\infty)\big]/(1-\beta_{12}), \tag{II-2b}$$

which follows from Eq. (II-1c) and the conservation of states ($n_1 + n_2 + n_3 = 1$). In Sections II-1.1, II-1.2, and II-1.3 we derive explicit expressions for the number of excited states per pulse, $N_{\rm pp}$, which are of the general form

$$N_{\rm pp} = H(Z); \quad Z = \int_{-\infty}^{\infty} G\Big(R_n\big(I(t)\big)\Big)\, dt, \tag{II-3}$$

where G and H are analytical functions of a single variable. For now, suffice it to say that, among other things, $N_{\rm pp}$ depends on the peak intensity $I_{\mathbf{r}}$ of the pulse (see Figure II-1) which, in the case of a focused laser beam, depends on the spatial coordinates $\mathbf{r}$ in the beam. Thus, the signal that is measured in an experiment as shown in Figure I-1 on page 4 is given by

$$S(I_0) = S_0 \iiint_{-\infty}^{\infty} N_{\rm pp}(\mathbf{r})\, P(\mathbf{r})\, d^3\mathbf{r}, \tag{II-4}$$

where $P(\mathbf{r})$ is a function that describes the detection probability as determined by the detection optics, S_0 is a proportionality constant, and I_0 is the peak intensity in the pulsed, focused beam. In writing Eq.(II-4) it has been assumed that the signal is directly proportional to the number of excited states $|2\rangle$, such as is the case for fluorescence or ion-yield. Thus the constant S_0 contains such factors as the number density of the ground state $|1\rangle$ and, in the case of a LIF experiment, the ratio of radiative to nonradiative decay rates. In writing Eqs.(II-2)–(II-4) it

has also been implicitly assumed that the signal from the excited state is collected during the entire temporal duration of the laser pulse. Finally, Eq.(II-4) assumes that the medium in the probe volume may be considered optically thin, so that no significant attenuation of the signal occurs as fluorescence radiation or ions travel toward the detector.

Given some nonlinear expression for the true, unknown intensity-dependent excitation rate $R_n(I)$ it would be a straightforward matter to calculate the signal $S(I_0)$ by numerical integration of the rate equations for various experimental configurations. However, it is our goal to derive analytical expressions from which, given a set of spatially and temporally averaged data $S(I_0)$, the true, unknown rate $R_n(I)$ can be obtained, namely by inversion. Toward this goal we derive explicit analytical expressions that are symbolized by Eq.(II-3). We distinguish three special cases, namely those in which: (i) the exciting pulse does not cause a significant depletion of the ground state $|1\rangle$; (ii) during the pulse, significant depletion of the ground state occurs, but random decay of the excited state $|2\rangle$ can be neglected; (iii) random deexcitation of state $|2\rangle$ is much faster than the laser pulse.

II–1.1 Nonsaturated regime

The simplest situation is that in which the exciting pulse never causes an appreciable depletion of the ground state because it is too weak and/or of too short duration. In this case, the number of excited states per pulse is simply the integral of the excitation rate:

$$N_{\mathrm{pp}} = \int_{-\infty}^{\infty} R_n\big(I(t)\big)\, dt, \qquad \text{(II–5)}$$

as can be found from Eqs.(II-2a) and (II-1b) by sustituting $n_1 = 1$ and neglecting the term $g_{12}R_n n_2$ in the latter. Thus both the functions G and H from Eq.(II-3)

are merely identity operators:

$$G(R_n) = R_n; \tag{II-6a}$$

$$H(Z) = Z. \tag{II-6b}$$

Note that, if Eq.(II-5) is substituted into Eq.(II-4), space- and time-integrals are mathematically equivalent. Accordingly, the signal depends linearly on the excitation rate [29]:

$$S(I_0) = S_0 \iiint_{-\infty}^{\infty} P(\mathbf{r})\, d^3\mathbf{r} \int_{-\infty}^{\infty} dt\, R_n\big(I(t)\big). \tag{II-7}$$

II–1.2 Saturated regime: fast pulse limit

The next simplest case is that in which the laser pulse is strong enough and of sufficient duration to cause significant depletion of the ground state, yet much faster than the random deexcitation processes. In this case, deexcitation of the excited state during the laser pulse may be neglected and, for the duration of the pulse, states $|1\rangle$ and $|2\rangle$ in Figure II-1 may be regarded as a closed two-level system. Thus Eq.(II-1b) may be written as

$$\dot{n}_2 = R_n\,(1 - n_2) - g_{12} R_n n_2; \quad n_2(-\infty) = 0, \tag{II-8}$$

and the number of excited states per pulse becomes

$$N_{\mathrm{pp}} = n_2(\infty) = \frac{1}{1+g_{12}}\left[1 - \exp\left\{-(1+g_{12}) \int_{-\infty}^{\infty} R_n\big(I(t)\big)\, dt\right\}\right]. \tag{II-9}$$

Comparison of Eq.(II-9) with Eq.(II-3) shows that the corresponding functions G and H are given by

$$G(R_n) = R_n; \tag{II-10a}$$

$$H(Z) = \frac{1}{1+g_{12}}\left[1 - \exp\{-(1+g_{12})Z\}\right]. \tag{II-10b}$$

In the limit $R_n \to 0$ we find $H(Z) \to Z$, so that the results from Section II-1.1 for weak excitation are reproduced. Note that, if Eq.(II-9) is substituted into Eq.(II-4), the signal $S(I_0)$ no longer depends linearly on the excitation rate $R_n(I)$.

II–1.3 Saturated regime: slow pulse limit

A third special case is that in which the random deexcitation rate is much faster than the excitation rate. In this case, the excited state is in equilibrium with the ground state during the entire duration of the laser pulse. Thus, in Eq.(II-1b), the term $\dot{n}_2$ can be set equal to zero, yielding

$$n_2 = \frac{R_n}{A + g_{12}R_n} n_1. \tag{II–11}$$

Substituting Eq.(II-11) into Eq.(II-1a) and integrating then yields $n_1(\infty)$, and with Eq.(II-2b):

$$N_{\rm pp} = \frac{1}{1-\beta_{12}}\left[1 - \exp\left\{-(1-\beta_{12})\int_{-\infty}^{\infty} \frac{AR_n\big(I(t)\big)}{A + g_{12}R_n\big(I(t)\big)}\, dt\right\}\right]. \tag{II–12}$$

The corresponding functions G and H from Eq.(II-3) are given by

$$G(R_n) = \frac{AR_n}{A + g_{12}R_n} \simeq R_n; \tag{II–13a}$$

$$H(Z) = \frac{1}{1-\beta_{12}}\Big[1 - \exp\{-(1-\beta_{12})Z\}\Big]. \tag{II–13b}$$

By the assumption of a fast random deexcitation rate ($A \gg g_{12}R_n$) G may be approximated simply by $G(R_n) \simeq R_n$, as indicated in Eq.(II-13a). Thus the slow pulse results take exactly the same mathematical form as the fast pulse results from Section II–1.2, except that the multiplicity ratio g_{12} is replaced by the negative of the branching ratio β_{12}. Note also that, again, the weak field results are reproduced in the limit $R_n \to 0$.

If the exciting pulse is strong, but is neither much faster or slower than the random deexcitation processes, more complicated solutions to the rate equations

of Eqs.(II-1) must be obtained. We have pursued this approach and have found that, except for the relatively uninteresting case of a "somewhat" slow pulse, integral expressions like those in Eq.(II-3) result, in which the function G contains also derivatives of the excitation rate: $G = G(R_n, \dot{R}_n, \ddot{R}_n, \ldots)$. Because such expressions are not suited for the inversion techniques that we develop in subsequent sections, we do not elaborate any further on these "intermediate" pulse cases.

II–2 Transformation to Kernels

With Eqs.(II-3) and (II-4), the signal is expressed in terms of the excitation rate $R_n(I)$ as

$$S(I_0) = S_0 \iiint_{-\infty}^{\infty} H\big(Z(\mathbf{r})\big)\, P(\mathbf{r})\, d^3\mathbf{r}; \qquad \text{(II–14a)}$$

$$Z(\mathbf{r}) = \int_{-\infty}^{\infty} R_n\big(I(\mathbf{r},t)\big)\, dt, \qquad \text{(II–14b)}$$

where we have substituted $G(R_n) = R_n$, in accordance with Eqs.(II-6a), (II-10a), and the approximation in Eq.(II-13a). Also, we have explicitly indicated the spatial dependence of the intensity I and the integral denoted by Z. Because it is our goal to find the true, unknown, intensity-dependent rate $R_n(I)$ from a given set of data $S(I_0)$, we transform from the spatial and temporal coordinates $\mathbf{r}$ and t to the local, instantaneous intensity I. Thus we express the focused, pulsed laser intensity in the probe volume in terms of the peak intensity I_0 and spatial and temporal profiles $F_{\mathbf{r}}(\mathbf{r})$ and $F_t(t)$, respectively:

$$I(\mathbf{r},t) = I_0\, F_{\mathbf{r}}(\mathbf{r})\, F_t(t) = I_{\mathbf{r}}(\mathbf{r})\, F_t(t). \qquad \text{(II–15)}$$

Here $I_{\mathbf{r}}(\mathbf{r})$ is the local peak intensity at position $\mathbf{r}$, and I_0 is the largest of these local peak intensities in the interaction region.

Before proceeding we note that Eq.(II-15) assumes that the functional dependences of the spatial and temporal contributions to the intensity are separable and that, furthermore, the profiles $F_{\mathbf{r}}(\mathbf{r})$ and $F_t(t)$ are independent of the peak intensity I_0. If such is not the case, the theory as presented below can be modified accordingly. However, because it is doubtful that, given such complicated experimental conditions, one would attempt the inversion techniques that we develop in subsequent sections, we assume throughout the following that Eq.(II-15) holds.

Using the spatial and temporal profiles $F_{\mathbf{r}}(\mathbf{r})$ and $F_t(t)$ we define the spatial and temporal "volumes"

$$V_{\mathbf{r}}(I_0; I_{\mathbf{r}}) = \iiint_{I_0 F_{\mathbf{r}}(\mathbf{r}) > I_{\mathbf{r}}} P(\mathbf{r})\, d^3\mathbf{r}, \tag{II-16a}$$

and

$$V_t(I_{\mathbf{r}}; I) = \int_{I_{\mathbf{r}} F_t(t) > I} dt. \tag{II-16b}$$

Note that the spatial volume is weighted by the detection probablity function $P(\mathbf{r})$. With Eqs.(II-16), Eqs.(II-14) can be transformed to

$$S(I_0) = S_0 \int_0^{I_0} H\big(\tilde{Z}(I_{\mathbf{r}})\big) \left[-\frac{\partial V_{\mathbf{r}}(I_0; I_{\mathbf{r}})}{\partial I_{\mathbf{r}}}\right] dI_{\mathbf{r}}; \tag{II-17a}$$

$$\tilde{Z}(I_{\mathbf{r}}) = \int_0^{I_{\mathbf{r}}} R_n(I) \left[-\frac{\partial V_t(I_{\mathbf{r}}; I)}{\partial I}\right] dI, \tag{II-17b}$$

where, as indicated, the integral $\tilde{Z}$ is now a function of the local peak intensity $I_{\mathbf{r}}$. In principle, we can regard the quantities within square brackets in Eqs.(II-17) as the kernels of the respective integral expressions. However, we prefer to work with the cross-sections rather than the excitation rate $R_n(I)$ and the signal $S(I_0)$. Thus we recall from Eq.(I-2) on page 8 that the true, n-photon cross-section $\sigma_n(I)$ is related to the true, unknown excitation rate $R_n(I)$ by

$$R_n(I) = I^n \sigma_n(I). \tag{II-18}$$

By analogy we define the experimentally averaged excitation rate $\hat{R}_n(I_0)$ and a corresponding experimentally averaged cross-section $\hat{\sigma}_n(I_0)$ as follows:

$$\hat{R}_n(I_0) = {I_0}^n \, \hat{\sigma}_n(I_0) = S(I_0)/S_0 \kappa_r \kappa_t, \tag{II-19}$$

where the coefficients κ_r and κ_t are defined below. Here and in the following, we use a caret to denote an experimentally averaged quantity. Eqs. (II-18) and (II-19) now suggest the following definition of the spatial and temporal kernels:

$$K_r(I_0; I_r) = -\frac{1}{\kappa_r} \left(\frac{I_r}{I_0}\right)^n \frac{\partial}{\partial I_r} V_r(I_0; I_r), \tag{II-20a}$$

and

$$K_t(I_r; I) = -\frac{1}{\kappa_t} \left(\frac{I}{I_r}\right)^n \frac{\partial}{\partial I} V_t(I_r; I), \tag{II-20b}$$

where the coefficients κ_r and κ_t are chosen such that the kernels are normalized:

$$\int_0^{I_0} K_r(I_0; I_r)\, dI_r = \int_0^{I_r} K_t(I_r; I)\, dI = 1. \tag{II-21}$$

In Ref. [29] we have refered to these kernels as "excitation density functions," since they express how the nth power of the intensity is distributed in the effective probe volume of a given experiment. Throughout the present work we refer to the quantities in Eqs.(II-20) merely as kernels.

Substitution of Eqs.(II-18)–(II-20) into Eqs.(II-17) yields the desired integral expressions relating the true cross-section $\sigma_n(I)$ and the experimentally averaged cross-section $\hat{\sigma}_n(I_0)$. For convenience, we introduce two additional intensity-dependent cross-sections:

$$\hat{\sigma}_n(I_0) = \int_0^{I_0} K_r(I_0; I_r)\, \sigma_r(I_r)\, dI_r; \tag{II-22a}$$

$$\sigma_r(I_r) = \frac{1}{\kappa_t {I_r}^n} H\big(\kappa_t {I_r}^n \, \sigma_t(I_r)\big); \tag{II-22b}$$

$$\sigma_t(I_r) = \int_0^{I_r} K_t(I_r; I)\, \sigma_n(I)\, dI. \tag{II-22c}$$

Eqs.(II-22) state that $\hat{\sigma}_n(I_0)$ is related to $\sigma_n(I)$ by means of two Volterra integral equations of the first kind, namely Eqs.(II-22a) and (II-22c), and one simple algebraic equation, namely Eq.(II-22b). The function H is given by Eqs.(II-6b), (II-10b), or (II-13b), depending on the intensity and the duration of the laser pulse. Note that Eqs.(II-22a) and (II-22c) are linear whereas Eq.(II-22b) is nonlinear in general. From Eqs.(II-22) it follows that, if a set of temporally and spatially averaged data is obtained for a series of peak intensities I_0, the true, unknown, intensity-dependent cross-section $\sigma_n(I)$ can be obtained, in principle, by three successive inversions, the second of which is a simple algebraic operation.

If the exciting laser pulse does not cause significant saturation effects then, by Eq.(II-6b), the function H is simply the identity operator, so that $\sigma_r(I_r) = \sigma_t(I_r)$ in Eq.(II-22b). In this case, the experimentally averaged cross-section $\hat{\sigma}_n(I_0)$ and the true, unknown cross-section $\sigma_n(I)$ can be related by a single integral expression, namely:

$$\hat{\sigma}_n(I_0) = \int_0^{I_0} K(I_0; I)\, \sigma_n(I)\, dI, \tag{II-23}$$

where the composite kernel is given by:

$$K(I_0; I) = \int_I^{I_0} K_r(I_0; I_r)\, K_t(I_r; I)\, dI_r. \tag{II-24}$$

From Eq.(II-21) it follows that this kernel is also normalized:

$$\int_0^{I_0} K(I_0; I)\, dI = 1. \tag{II-25}$$

As in Eqs.(II-20), it can be expressed in terms of a "volume" function $V(I_0; I)$:

$$K(I_0; I) = -\frac{1}{\kappa}\left(\frac{I}{I_0}\right)^n \frac{\partial}{\partial I} V(I_0; I); \qquad \kappa = \kappa_r \kappa_t, \tag{II-26}$$

where

$$V(I_0; I) = -\int_I^{I_0} V_t(I_r; I) \frac{\partial}{\partial I_r} V_r(I_0; I_r)\, dI_r = \int_I^{I_0} V_r(I_0; I_r) \frac{\partial}{\partial I_r} V_t(I_r; I)\, dI_r$$

$$= \iiiint_{I_0 F_r(\mathbf{r}) F_t(t) > I} P(\mathbf{r})\, d^3\mathbf{r}\, dt. \tag{II-27}$$

The last result is most easily understood from Eqs.(II-7) and (II-15). In any case, from Eq.(II-23) it follows that, in the case of weak excitation, the true intensity-dependent cross-section $\sigma_n(I)$ may be obtained from the experimentally averaged cross-section $\hat{\sigma}_n(I_0)$ by a single inversion.

We conclude this section with two final remarks. Firstly, because of the normalization of the kernels in Eqs.(II-21) and (II-25) and because of the corresponding scaling of the signal $S(I_0)$ in Eq.(II-19), Eq.(II-23) implies that

$$\sigma_n(I) = \sigma_c \iff \hat{\sigma}_n(I_0) = \sigma_c, \tag{II-28}$$

and

$$\sigma_{n0} = \lim_{I \downarrow 0} \sigma_n(I) = \lim_{I_0 \downarrow 0} \hat{\sigma}_n(I_0) \tag{II-29}$$

[analogous expressions hold for the cross-sections from Eqs.(II-22a) and (II-22c)]. That is, if the true cross-section σ_n is independent of the intensity, then the non-saturated, experimental cross-section $\hat{\sigma}_n$ is equal to the same, constant value, and vice versa. Analogously, the true cross-section and the experimentally averaged cross-section have the same limiting behavior for small intensity.

Secondly and finally, although we have treated the peak intensity I_0 and the spatial and temporal profiles $F_r(\mathbf{r})$ and $F_t(t)$ as deterministic quantities, stochastic variations of either of these can be incorporated into the model. For example, if the peak intensity I_0 has a probability density function $P_I(\overline{I_0}; I_0)$, where $\overline{I_0}$ is some average peak intensity, the kernel $K(I_0; I)$ in Eq.(II-23) merely needs to be replaced by the average kernel

$$\overline{K}(\overline{I_0}; I) = \int_0^\infty P_I(\overline{I_0}; I_0)\, K(I_0; I)\, dI_0 \tag{II-30}$$

[again, similar expressions can be obtained for Eqs.(II-22)].

II–3 Kernels Resulting from Exponential Profiles

Ideally, in a given experiment, the kernels from Eqs.(II-20a), (II-20b), and (II-24) should be obtained by measuring the spatial and temporal profiles $F_{\mathbf{r}}(\mathbf{r})$ and $F_t(t)$ along with the detection probablity function $P(\mathbf{r})$, and the resulting kernels would be obtained by some numerical method. However, for the important class of exponential beam- and pulse-profiles and constant detection probability, the kernels can be calculated analytically: consider the composite profile

$$F_{\mathbf{x}}(\mathbf{x}) = \prod_{i=1}^{n_{\mathbf{x}}} \exp\left\{-\left|\frac{x_i}{a_i^{\pm}}\right|^{\mu_i}\right\}, \tag{II-31}$$

where the vector $\mathbf{x}$ signifies any number $n_{\mathbf{x}}$ of spatial and/or temporal coordinates, and where the widths a_i^+ (a_i^-) correspond to $x_i > 0$ ($x_i < 0$). Thus, for $a_i^+ \neq a_i^-$, the profile $F_{\mathbf{x}}(\mathbf{x})$ can be asymmetrical in any of the coordinates x_i. In Eq.(II-31) the exponents μ_i are arbitrary, although only positive values correspond to physically realizable profiles. Note that $\mu_i = 2$ and $\mu_i = \infty$ correspond to Gaussian and rectangular profiles in the ith coordinate, respectively. If, in addition to the exponential behavior of the profile $F_{\mathbf{x}}(\mathbf{x})$, the associated probability function $P(\mathbf{x})$ is constant [see Eq.(II-16a)]:

$$P(\mathbf{x}) = p, \tag{II-32}$$

then the corresponding volumes from Eqs.(II-16a), (II-16b), or (II-27) can be calculated in terms of gamma functions [30], as shown in Appendix B-1. Thus, for example, the combined spatial and temporal kernel from Eq.(II-24) becomes

$$K(I_0; I) = \frac{n^{\beta}}{\Gamma(\beta)} \frac{I^{n-1}}{{I_0}^n} \left\{\ln \frac{I_0}{I}\right\}^{\beta-1}. \tag{II-33}$$

In Eq.(II-33), β is a composite shape parameter which, in terms of the exponents μ_i from Eq.(II-31), is given by:

$$\beta = {\mu_x}^{-1} + {\mu_y}^{-1} + {\mu_z}^{-1} + {\mu_t}^{-1}, \tag{II-34}$$

where x, y, and z are the respective spatial coordinates of $\mathbf{r}$, and t is the temporal coordinate. Loosely speaking, β is half the number of Gaussian components in the composite profile $F_{\mathbf{x}}(\mathbf{x})$. Eqs.(II-33) and (II-34) are modified in an obvious manner if less coordinates are involved in the derivation of the kernel.

Figure II-2 displays a number of one-photon and two-photon kernels, calculated from Eq.(II-33) for various values of β. Note that the smaller the value of β and the larger the order n of the interaction, the more the kernel resembles a Dirac-delta function at the peak intensity, and the less averaging takes place (for $\beta = 0$, Eq.(II-23) becomes an identity: $\sigma_n(I) = \hat{\sigma}_n(I)$ for arbitrary values of I). In this regard, two-photon excitation suffers less spatial and/or temporal averaging effects than does single-photon excitation under otherwise identical conditions, and the associated inversion problem is less ill-posed, as is discussed in more detail in Sections III and IV.

Figures II-3 and II-4 illustrate the effects of spatial and/or temporal averaging for hypothetical intensity-dependent cross-sections $\sigma_n(I)$, assuming that the averaging kernels are given by Eq.(II-33). Figure II-3 shows an example in which the true cross-section $\sigma_n(I)$ is sampled at five equidistant peak intensities I_{01} through I_{05}, yielding five values of the experimental cross-section $\hat{\sigma}_n(I_0)$. These results were obtained by numerical integration of Eq.(II-23), assuming two-photon excitation ($n=2$) and a composite shape parameter $\beta=1.5$. Note that, in general, the functional dependence of $\hat{\sigma}_n(I_0)$ differs from that of $\sigma_n(I)$, except in the limit of zero intensity, in accordance with Eq.(II-29).

Figure II-4 shows similar results for the cross-section $\sigma_n(I)$ from Figure II-3 [Figure II-4(a)], as well as for a different cross-section $\sigma_n(I)$ [Figure II-4(b)]. The left (right) parts of Figure II-4 are for one-photon (two-photon) excitation, and the curves are for various values of the composite shape parameter β. As noted

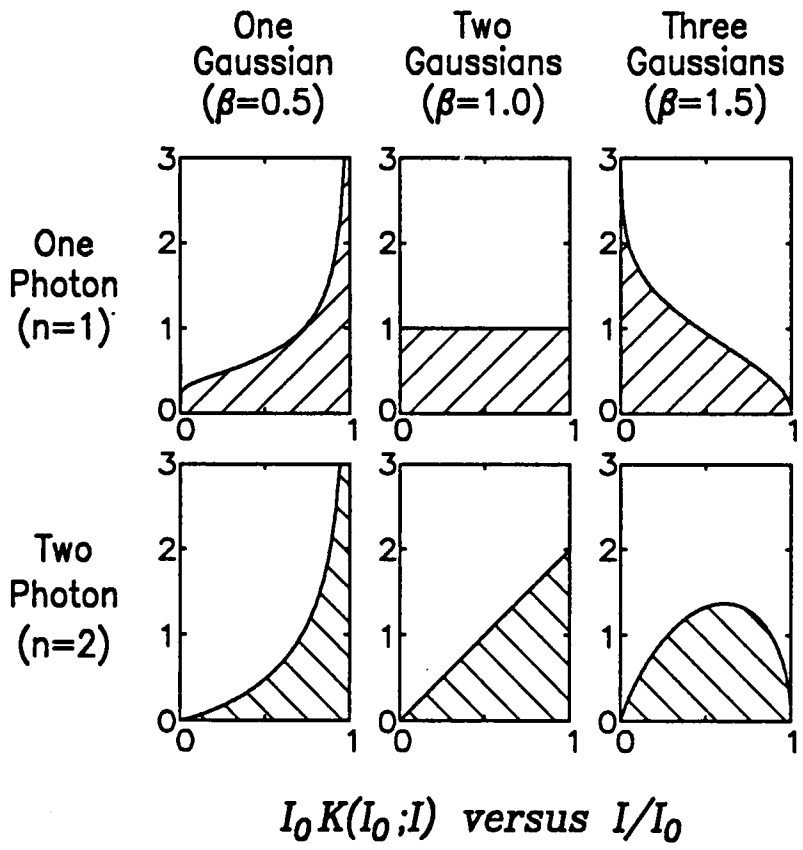


Figure II–2: *Kernels for exponential beam- and pulse-profiles.*

above, the true and experimental cross-sections are identical in the limit $\beta = 0$. The larger the value of β, the more the respective functional dependences differ although, in each case, the limiting behavior for zero intensity is the same. Note also that, indeed, averaging effects are more serious in the single-photon case than in the case of two-photon excitation.

Even if the kernels represented by Eq.(II-33) do not describe a given experimental configuration exactlty, they may be used for approximate results. In Sections III, IV, and V we use them extensively to demonstrate essential features

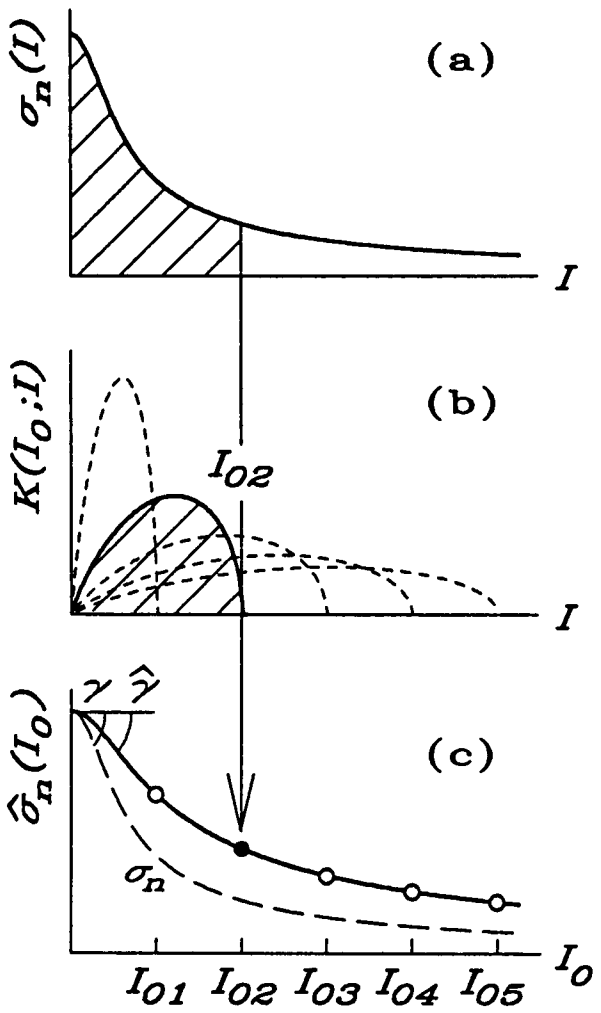


Figure II–3: *Illustration of spatial and/or temporal averaging.*

(a) *Fictitious true, intensity-dependent cross-section* $\sigma_n(I)$; (b) *Kernels from Eq.(II-33) with* $n = 2$ *and* $\beta = 1.5$, *for five equidistant peak intensities* I_{0i}; (c) *Resulting experimentally averaged cross-section* $\hat{\sigma}_n(I_0)$ *(solid curve), and true cross-section* $\sigma_n(I)$ *from (a) for comparison (dashed curve).*

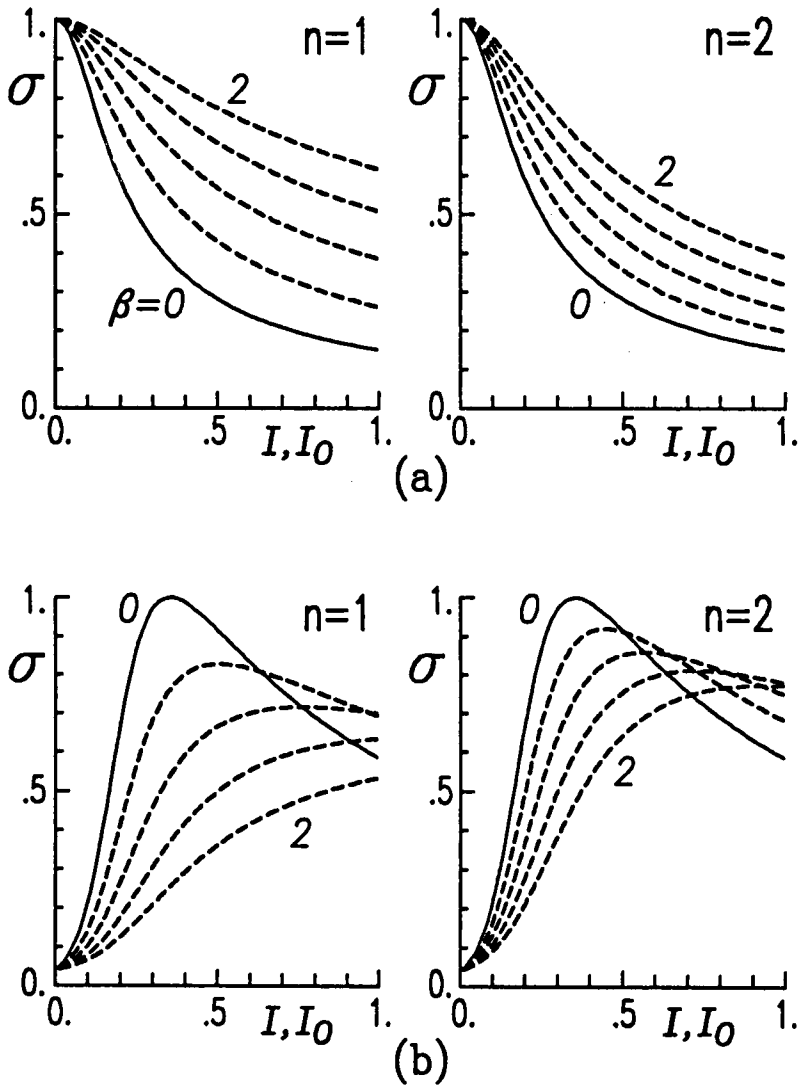


Figure II–4: *Further illustrations of spatial and/or temporal averaging.*

Solid and dashed curves represent the true cross-sections $\sigma_n(I)$ *and the experimentally averaged cross-sections* $\hat{\sigma}_n(I_0)$*, respectively, for* $n = 1$ *and* $n = 2$*, and composite shape parameters* β = 0.0, 0.5, 1.0, 1.5, *and* 2.0. *For* $\beta = 0$, σ_n *and* $\hat{\sigma}_n$ *are identical. The* $\sigma_n(I)$*'s in (a) are identical to those in Figure II-3.*

of the inversion process. Thus we close Section II by listing some of their special properties, which are derived in Appendix B-1. Firstly, the normalization constant κ from Eqs.(II-20) or (II-26) associated with the composite profile from Eq.(II-31) is given by

$$\kappa = p\, n^{-\beta} \prod_{i=1}^{n_x} \left\{ (a_i^+ + a_i^-)\, \Gamma(1 + 1/\mu_i) \right\}. \qquad \text{(II–35)}$$

Secondly, for use in subsequent sections, we list here the complete moments of the kernel from Eq.(II-33):

$$M_{k0} = \int_0^{I_0} K(I_0; I)\, (I/I_0)^k\, dI = \left(1 + k/n\right)^{-\beta}. \qquad \text{(II–36)}$$

For integral and half-integral values of β it is also possible to calculate the incomplete moments explicitly, namely, for $0 \le I_j \le I_0$:

$$M_k(I_0; I_j) = \int_{I_j}^{I_0} K(I_0; I)\, (I/I_0)^k\, dI = M_{k0} \times \mathcal{M}(\beta; p; q), \qquad \text{(II–37a)}$$

where

$$p = \left(I_j/I_0\right)^{n+k}; \qquad q = \left(-\ln p\right)^{1/2}, \qquad \text{(II–37b)}$$

and

$$\mathcal{M}(1; p; q) = 1 - p; \qquad \mathcal{M}(2; p; q) = 1 - p - pq^2; \qquad \text{(II–37c)}$$

$$\mathcal{M}(\tfrac{1}{2}; p; q) = \mathrm{erf}(q); \qquad \mathcal{M}(\tfrac{3}{2}; p; q) = \mathrm{erf}(q) - 2\pi^{-1/2} pq, \qquad \text{(II–37d)}$$

and $\mathrm{erf}(q)$ denotes the normalized error function of q.

III METHODS OF INVERSION

Section III addresses the problem of obtaining the intensity-dependent cross-section $\sigma_n(I)$ from a set of data $S(I_0)$, such as those of Figure I-3 on page 10. As expressed in Eq.(II-23), this requires inversion of a single Volterra integral equation of the first kind in the case of a nonsaturated excitation process, whereas, in the case of a saturated excitation, successive inversions of a Volterra equation, a nonlinear algebraic equation, and another Volterra equation are required, as expressed in Eqs.(II-22). Of course, inversion of the Volterra equations is possible only if the associated kernels can somehow be calculated. Inversion of the algebraic equation of Eq.(II-22b) is trivial in principle. However, because of its nonlinear nature, the scaling of the experimental signal $S(I_0)$ in Eq.(II-19) becomes crucial, except in the limit of no saturation. In many applications, an exact determination of the scaling parameters from Eq.(II-19) is difficult, if not impossible, because an absolute calibration of the detection apparatus is required [for example, by Eqs.(II-16a), (II-20a), and (II-21), $\kappa_{\mathbf{r}}$ depends on the detection probability function $P(\mathbf{r})$]. Thus, in the saturated regime, inversion of Eq.(II-22b) requires a precise knowledge of the scaling factors S_0, $\kappa_{\mathbf{r}}$, and κ_t from Eq.(II-19).

In Section V we show that in the case of spectral lineshapes the additional information of the frequency dependence of the nonlinear optical process may be used to obtain inversion results, even if the exact values of the normalization constants in Eq.(II-19) are not *a priori* known. Thus, in Sections III and IV, we concentrate on the inversion of the Volterra equations expressed by Eqs.(II-22a), (II-22c), and (II-23). For ease of reference, we repeat Eq.(II-23) here:

$$\hat{\sigma}_n(I_0) = \int_0^{I_0} K(I_0; I)\, \sigma_n(I)\, dI. \qquad \text{(III-1)}$$

Because Eq.(III-1) is linear, the exact scaling of the experimental signal merely

affects the magnitude of the inverted cross-sections, not their functional behavior.

Having cast the extraction of the true intensity-dependence of some nonlinear process from spatially and/or temporally averaged data into the form of an integral equation, the solution is, in principle, merely an exercise in applied mathematics. However, despite an extensive body of literature on inversion problems (see, for example, Refs. [31–33]), individual problems have unique features and difficulties, depending on the kernels involved. In Sections III-1 and III-2 we show that analytical solutions are actually possible, namely by Abel inversion for the case of exponential beam- and pulse-profiles, and by a moment method in general. In actual applications, data are generally discrete and noisy. In such cases, numerical techniques are prefered over analytical solutions. Thus we discuss the method of collocation in Section III-3, and we treat a specific application of collocation in Section III-4, namely that of "direct inversion." Then, in Section IV, we return to the method of collocation, namely for the specific case of spline basis functions.

III–1 Abel Inversion

For the class of kernels introduced in Section II-3, explicit, analytical inversions of the Volterra integral equation can be obtained if the experimental signal is regarded as a continuous function of the peak intensity I_0. In this case, it is convenient to work with the true, intensity-dependent excitation rate $R_n(I)$ and the experimentally averaged excitation rate $\hat{R}_n(I_0)$ from Eq.(II-19) rather than with the cross-sections $\sigma_n(I)$ and $\hat{\sigma}_n(I_0)$. Thus, with the substitutions

$$\omega = \ln I; \quad \omega_0 = \ln I_0; \quad \mathcal{R}_n(\omega) = R_n(I); \quad \hat{\mathcal{R}}_n(\omega_0) = \hat{R}_n(I_0), \tag{III–2}$$

Eq.(III-1) becomes a generalized Abel-equation [34]:

$$\hat{\mathcal{R}}_n(\omega_0) = \frac{n^\beta}{\Gamma(\beta)} \int_{-\infty}^{\omega_0} (\omega_0 - \omega)^{\beta-1} \mathcal{R}_n(\omega)\, d\omega. \tag{III–3}$$

For $0 \leq \beta \leq 1$, the inversion of Eq.(III-3) is given by [34]:

$$\mathcal{R}_n(\omega) = \frac{1}{n^\beta \Gamma(1-\beta)} \frac{d}{d\omega} \int_{-\infty}^{\omega} (\omega - \omega_0)^{-\beta} \, \hat{\mathcal{R}}_n(\omega_0) \, d\omega_0. \qquad \text{(III–4a)}$$

In Appendix B-2 we show that, for $\beta \geq 1$, Eq.(III-4a) can be generalized to

$$\mathcal{R}_n(\omega) = \frac{1}{n^\beta \Gamma(1-\beta')} \frac{d}{d\omega} \int_{-\infty}^{\omega} (\omega - \omega_0)^{-\beta'} \left(\frac{d}{d\omega_0}\right)^k \hat{\mathcal{R}}_n(\omega_0) \, d\omega_0, \qquad \text{(III–4b)}$$

where

$$\beta' = \beta - k; \quad \text{with } 0 \leq \beta' < 1, \quad \text{and } k = \text{integer}. \qquad \text{(III–4c)}$$

Returning to the original variables and bringing $(k-1)$ factors $I_0 \, (d/dI_0)$ outside the integral (replacing I_0 by I — see Appendix B-2), the inversion of Eq.(III-1), in terms of excitation rates, becomes:

$$R_n(I) = \frac{1}{n^\beta \Gamma(1-\beta')} \left(I \frac{d}{dI}\right)^k \int_0^I \left(\ln \frac{I}{I_0}\right)^{-\beta'} \frac{d\hat{R}_n(I_0)}{dI_0} \, dI_0. \qquad \text{(III–5)}$$

If the composite shape-parameter β is an integer the interesting result is obtained that $R_n(I)$ follows from $\hat{R}_n(I)$ simply by differentiation:

$$R_n(I) = \left(\frac{I}{n} \frac{d}{dI}\right)^\beta \hat{R}_n(I); \quad \beta = \text{integer}, \qquad \text{(III–6)}$$

a result that may also be obtained by direct differentiation of Eq.(III-1) as shown in Appendix B-3. For rectangular beam- and pulse-profiles ($\beta = 0$), the inversion yields $R_n(I) = \hat{R}_n(I)$, as required. Apart from this trivial case, the simplest situation is that in which $\beta = 1$, so that only a single differentiation is needed [35]. From the definition of β in Eq.(II-34) it follows that $\beta = 1$ in an experiment in which a continuous, collimated, Gaussian TEM_{00} beam is employed. Finally, we note that, for noninteger values of β, Eqs.(III-4) may be used as the definition of a fractional derivative, in analogy with Eq.(III-6) [36].

Sometimes, the intensity-dependence of a nonlinear optical process is assigned to the order of the interaction, rather than the cross-section [25]. Thus, the effective order $n(I)$ of an interaction follows from the slope of the excitation rate versus intensity in a doubly logarithmic plot, such as Figure I-3 on page 10. In this case, the following experimentally averaged orders $\hat{n}(I_0)$ are obtained:

$$\hat{n}(I_0) = \frac{d\big(\ln S(I_0)\big)}{d\big(\ln I_0\big)} = \frac{d\big(\ln \hat{R}_n(I_0)\big)}{d\big(\ln I_0\big)}, \tag{III-7}$$

whereas the true intensity-dependent order $n(I)$ is given by

$$n(I) = \frac{d\big(\ln R_n(I)\big)}{d\big(\ln I\big)}. \tag{III-8}$$

In Appendix B-3 we show that, by Eq.(III-6), the true intensity-dependent order $n(I)$ then follows from the experimental order $\hat{n}(I_0)$ as

$$n(I) = \hat{n}(I) + \frac{d\big(\ln A^{(\beta)}(I)\big)}{d\big(\ln I\big)}, \tag{III-9}$$

where

$$A^{(\beta)}(I) = \left\{\hat{n}(I) + I\frac{d}{dI}\right\}^{\beta} \times 1. \tag{III-10}$$

The correction term in Eq.(III-9) contains first- through βth order derivatives of $\hat{n}(I)$, and is thus zero only if $\beta = 0$, or if the order of the interaction is constant.

Finally we note that the transformation from Eq.(III-2) may be used to bring Eq.(III-1) into convolution form for arbitrary kernels, as long as the scaled kernel $I_0 K(I_0; I)$ can be written solely in terms of the relative intensity I/I_0, which is the case if the spatial and temporal profiles $F_{\mathrm{r}}(\mathrm{r})$ and $F_t(t)$ from Eq.(II-15) do not depend on the peak intensity [29]. In principle, the inversion of Eq.(III-1) can then be obtained, say, as the inverse Laplace transform of the quotient of the Laplace transforms of the kernel and the experimental cross-section, respectively.

Because, in general, these inverse transforms cannot be obtained explicitly, we do not elaborate further.

III–2 Moment Method

Inversion of Eq.(III-1) is particularly simple if the experimental cross-section $\hat{\sigma}_n(I_0)$ is expanded in a power series:

$$\hat{\sigma}_n(I_0) = \sigma_{n0}\,(1 + \hat{\gamma}_1 I_0 + \hat{\gamma}_2 {I_0}^2 + \ldots). \qquad \text{(III–11)}$$

Substitution of Eq.(III-11) into Eq.(III-1) then yields a similar power series for the true intensity-dependent cross-section:

$$\sigma_n(I) = \sigma_{n0}\,(1 + \gamma_1 I + \gamma_2 I^2 + \ldots), \qquad \text{(III–12)}$$

where the coefficients γ and $\hat{\gamma}$ are related by the complete moments of the kernel:

$$\gamma_k = \hat{\gamma}_k \,/\, M_{k0}\,; \quad k = 1, 2, 3, \ldots; \qquad \text{(III–13a)}$$

$$M_{k0} = \int_0^{I_0} K(I_0; I)\,(I/I_0)^k\, dI. \qquad \text{(III–13b)}$$

In Eqs.(III-11) and (III-12) we have also used Eq.(II-29), which is a result of the normalization of the kernels ($M_{00} = 1$). The less uniform the intensity distribution, the more rapidly the moments M_{k0} decrease with increasing order k, and the larger is the relative contribution of the corresponding terms to $\sigma_n(I)$ than to $\hat{\sigma}_n(I_0)$. Thus, measurement error in $\hat{\sigma}_n(I_0)$ leads to the largest errors in $\sigma_n(I)$ for the largest intensities in a given set of data. As a case in point, consider the special kernels from Section II-3, which, with Eqs.(II-36) and (III-13) yield:

$$\gamma_k = \hat{\gamma}_k\,(1 + k/n)^{\beta}. \qquad \text{(III–14)}$$

This result, which holds for arbitrary β, is easily checked for integer values using Eq.(III-6). Note that the ratio $\gamma_k/\hat{\gamma}_k$ increases not only with the power k, but

also with the shape parameter β. Thus, inaccurate determination of β for a given experimental geometry also causes an ill-posed behavior of the inversion at the highest intensities, although the resulting error is systematic rather than stochastic in origin. In Figure II-3 on page 28, the coefficients γ and $\hat{\gamma}$ have been indicated schematically. Attribution of, say, $\hat{\gamma}_1$ to the true cross-section $\sigma_n(I)$ would yield the incorrect value $\hat{\gamma}_1 \simeq \gamma_1/1.84$.

Even though the effects of nonuniform excitation have been discussed in terms of moments of the involved kernels [1], the results do not seem to have been used to obtain inversion results. The moment method is especially useful if only a few terms of the power series in Eqs.(III-11) and (III-12) are needed for an accurate fit to the data. However, for strongly nonlinear behavior of the cross-sections, more robust inversion methods are required, particularly if the data are noisy.

III–3 Inversion by Collocation

If the averaged cross-section $\hat{\sigma}_n(I_0)$ is obtained as discrete, noisy data, the above analytical inversion techniques are of limited use. For example, due to the ill-posed nature of inversion problems in general, and of Volterra problems in particular, one normally needs to apply some type of regularization to prevent serious amplification of noise components in the inversion. Indeed, we quote from Brunner and van der Houwen's recent text: "Satisfactory methods for solving [*integral equations like Eq.(III-1)*] where the data is noisy can in general not be derived by appealing solely to theoretical numerical analysis..." [37]. One of the most powerful techniques in such cases is that of collocation, in which the true, unknown cross-section $\sigma_n(I)$ is expanded in terms of some suitable set of basis

functions $\phi_j(I)$:

$$f(I) = \sum_{j=1}^{M} a_j \, \phi_j(I), \tag{III-15}$$

where we have used the notation $f(I)$ rather than $\sigma_n(I)$ on the left hand side to distinguish the solution $f(I)$ of the inversion problem from the actual, true, cross-section $\sigma_n(I)$. The number of basis functions, M, may be either finite or infinite, and the basis functions themselves may or may not be orthogonal. If the experimental cross-section $\hat{\sigma}_n(I_0)$ is sampled at N values of the peak intensity I_0 (that is, at the values I_{0i}, with $i = 1, \ldots, N$) then substitution of Eq.(III-15) into Eq.(III-1) yields a system of N linear equations from which the M expansion coefficients a_j must be determined:

$$\sum_{j=1}^{M} A_{ij} \, a_j = s_i; \quad i = 1, \ldots, N. \tag{III-16}$$

In Eq.(III-16), s_i denotes the measured, possibly noisy value of the experimental cross-section $\hat{\sigma}_n(I_0)$ at the peak intensity I_{0i}, and the elements of $\mathbf{A}$ are given by the projections of the kernels onto the basis functions:

$$A_{ij} = \int_0^{I_{0i}} K(I_{0i}; I) \, \phi_j(I) \, dI. \tag{III-17}$$

Alternatively, the elements of $\mathbf{A}$ may be obtained directly from the spatial and/or temporal profiles $F_{\mathbf{r}}(\mathbf{r})$ and $F_t(t)$. For example, for the nonsaturated case, it follows from Eqs.(II-26), (II-27), and (III-17) that

$$A_{ij} = \frac{1}{\kappa} \iiint_{-\infty}^{\infty} P(\mathbf{r}) \, d^3\mathbf{r} \int_{-\infty}^{\infty} dt \, \left(F_{\mathbf{r}}(\mathbf{r}) F_t(t)\right)^n \phi_j\left(I_{0i} F_{\mathbf{r}}(\mathbf{r}) F_t(t)\right). \tag{III-18}$$

Eq.(III-18) is particularly useful if the profiles $F_{\mathbf{r}}(\mathbf{r})$ and $F_t(t)$ have been measured experimentally.

In the general case of an overdetermined system ($N > M$), the solution of Eq.(III-16) is found by least-squares fitting, that is, by minimizing the residue-of-fit

$$Q_{\rm fit}(\mathbf{a}) = \sum_{i=1}^{N} w_i \left[\sum_{j=1}^{M} A_{ij}\, a_j - s_i \right]^2, \qquad \text{(III–19)}$$

where the w_i's are weights, assigned to the data s_i. The least-squares solution satisfies the normal equations

$$\tilde{\mathbf{A}}^T \tilde{\mathbf{A}}\, \mathbf{a} = \tilde{\mathbf{A}}^T \tilde{\mathbf{s}}, \qquad \text{(III–20)}$$

where $\tilde{\mathbf{A}}$ and $\tilde{s}$ are the scaled elements of the design matrix and the experimental data, respectively:

$$\tilde{A}_{ij} = {w_i}^{1/2}\, A_{ij}; \quad \tilde{s}_i = {w_i}^{1/2}\, s_i; \quad i = 1, \ldots, N. \qquad \text{(III–21)}$$

Although direct solution of Eq.(III-20) is straightforward, it suffers the drawback that squaring of the condition of the inversion matrix takes place, perhaps leading to unnecessary machine roundoff errors. Rather, the prefered approach to solving Eq.(III-16) is to use such powerful techniques as Householder transformation and/or singular value decomposition (SVD) [38]. For example, let the SVD of $\tilde{\mathbf{A}}$ be given by

$$\tilde{\mathbf{A}} = \mathbf{U}\, \mathbf{W}\, \mathbf{V}^T, \qquad \text{(III–22)}$$

where $\mathbf{U}$ is an orthogonal $N \times M$ matrix ($\mathbf{U}^T\mathbf{U} = \mathbf{I}$), $\mathbf{W}$ is the diagonal matrix whose elements are the singular values of $\tilde{\mathbf{A}}$ ($W_{ij} = \delta_{ij}\, w_j$), and $\mathbf{V}$ is an orthonormal $M \times M$ matrix ($\mathbf{V}^T\mathbf{V} = \mathbf{V}\mathbf{V}^T = \mathbf{I}$; $\mathbf{V}^{-1} = \mathbf{V}^T$). Thus, the least-squares solution to Eqs.(III-16) is given by [38]:

$$\mathbf{a} = \mathbf{V}\, \mathbf{W}^{-1}\, \mathbf{U}^T\, \tilde{\mathbf{s}}, \qquad \text{(III–23)}$$

where the inverse $\mathbf{W}^{-1}$ is a diagonal matrix whose elements are just the reciprocals of the elements of $\mathbf{W}$, that is, $(\mathbf{W}^{-1})_{ij} = \delta_{ij} w_j^{-1}$. From Eq.(III-23) it is apparent that small singular values w_j will cause serious amplification of noise components of the data s_i, hence the ill-posed nature of the inversion problem.

In connection with SVD a common approach to limiting the amplification of noise components is that of Tikhonov regularization [39,40], which consists of replacing the inverse of the diagonal matrix $\mathbf{W}$ in Eq.(III-23) by the regularized diagonal matrix $\mathbf{W}_T$, with elements

$$(\mathbf{W}_T)_{ij} = \delta_{ij} \frac{w_j}{w_j^2 + \epsilon}, \qquad \text{(III–24)}$$

where ϵ is the (Tikhonov) regularization parameter. It is easily checked that, whereas the elements of $\mathbf{W}^{-1}$ can be arbitrarily large, those of $\mathbf{W}_T$ can be no larger than $1/(2\epsilon^{1/2})$, thereby limiting the amplification of noise components of the data $\mathbf{s}$. It may also be checked that the solution vector $\mathbf{a}_T$, obtained by substituting into Eq.(III-23) $\mathbf{W}_T$ instead of $\mathbf{W}^{-1}$, satisfies the regularized normal equations

$$(\tilde{\mathbf{A}}^T \tilde{\mathbf{A}} + \epsilon \mathbf{I})\, \mathbf{a}_T = \tilde{\mathbf{A}}^T \tilde{\mathbf{s}}, \qquad \text{(III–25)}$$

where $\mathbf{I}$ is the $M \times M$ identity matrix. Eq.(III-25) implies that Tikhonov regularization of the least-squares solution of the inversion problem may actually be achieved without performing the time-consuming singular value decomposition. This time, the possible consequences of squaring the condition of $\tilde{\mathbf{A}}$ are less serious, because the regularization conditions are built into the normal equations.

III–4 Direct Inversion

A special case of singular value decomposition is that of "direct inversion," in which the basis functions $\phi_j(I)$ in Eq.(III-15) are constructed as orthonormal, lin-

ear combinations of the kernels [41,42]. Toward this goal, let the kernel covariance matrix **C** be defined as

$$\mathbf{C} = \int_0^{I_{0,\max}} \mathbf{k}(I)\,\mathbf{k}^T(I)\,dI, \tag{III–26}$$

where $k_j(I) = K(I_{0j}; I)$, and $I_{0,\max}$ is the largest of the peak intensities I_{0i}. Because **C** is symmetric, its SVD can be written as

$$\mathbf{C} = \mathbf{U}\,\mathbf{\Lambda}\mathbf{U}^T, \tag{III–27}$$

in analogy with Eq.(III-22). Thus **U** is an orthonormal matrix, and **Λ** is a diagonal matrix. In this context we refer to the diagonal elements λ_j as eigenvalues, rather than singular values. It is easily shown that, in terms of **U** and **Λ**, the orthonormal basis functions $\phi_j(I)$ are now given by

$$\phi_j(I) = \left[\mathbf{\Lambda}^{-1/2}\,\mathbf{U}^T\,\mathbf{k}(I)\right]_j, \tag{III–28}$$

and that the solution of the inversion problem is given by

$$f(I) = \underline{\phi}^T(I)\,\mathbf{\Lambda}^{-1/2}\,\mathbf{U}^T\,\mathbf{s}. \tag{III–29}$$

As in the general case of SVD, the ill-posed nature of the inversion problem can be attributed to the existence of small eigenvalues (or singular values) of the inversion matrix.

As an illustration we have computed the eigenvalues λ_j for the special kernels described by Eq.(II-33). Maximum and minimum values of the eigenvalues are displayed in Figure III-1 as a function of the shape parameter β for one-photon and two-photon excitation, and for either $N = 10$ or $N = 25$ equidistant peak intensities I_{0i}. A dramatic decrease in the eigenvalues is observed as β becomes larger than 0.5. To show that the smallest eigenvalues lead to ill-posed behavior of

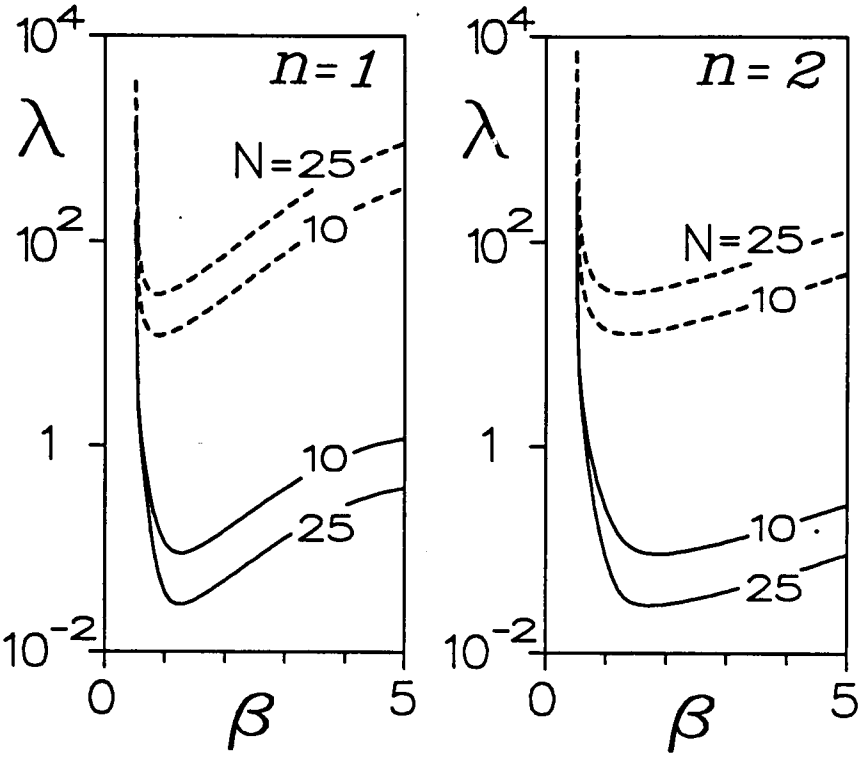


Figure III–1: *Eigenvalues of direct inversion matrix.*

Minimum and maximum values are displayed as a function of the composite shape parameter β, for either one-photon or two-photon excitation, and data sets of $N = 10$ or $N = 25$ points.

the inversion for the highest intensities in particular, we correlate the eigenvalues λ_j with the central intensities of the corresponding basis functions, defined as

$$\langle I \rangle_j = \int_0^{I_{0,\max}} I \, \phi_j^2(I) \, dI. \qquad \text{(III–30)}$$

Figure III-2 displays the results for a two-photon kernel with $\beta = 1.5$, and either $N = 10$ or $N = 25$ data points. Indeed, the smaller the eigenvalue, the larger is the corresponding central intensity, and the more will the inversion for the largest intensities be affected by noise on the data.

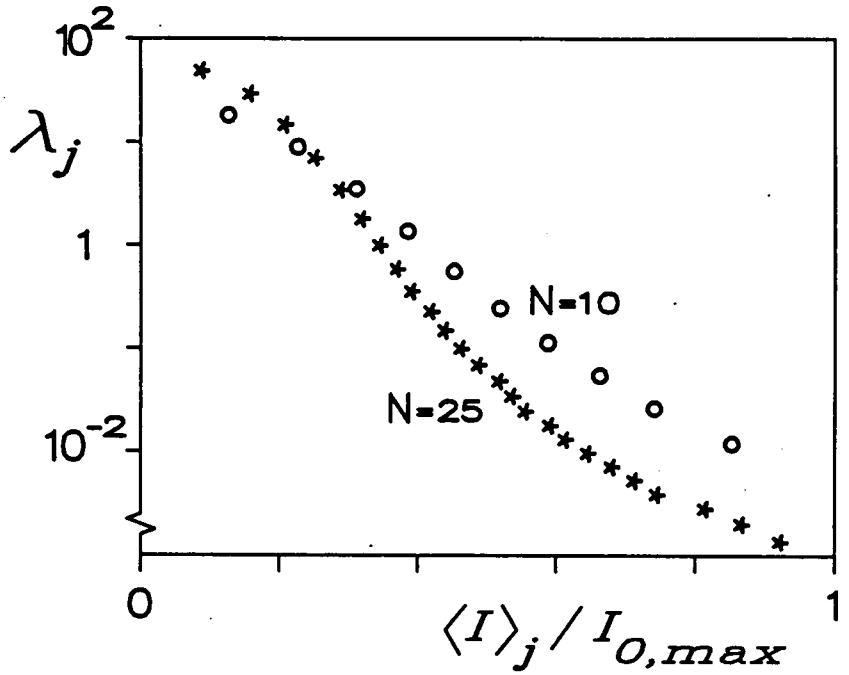


Figure III–2: *Eigenvalues of direct inversion matrix versus the central intensities of the corresponding basis vectors.*

Results are for a two-photon kernel with $\beta = 1.5$, *and either* $N = 10$ *or* $N = 25$ *data.*

Finally, Figure III-3 shows an actual example of a direct inversion, in which the data from Figure II-3 on page 28 have been used, except that the number of equidistant data has been increased from 5 to 10. Also, the experimental data were corrupted with a 0.5 percent rms noise amplitude in 20 consecutive runs. Because no regularization was applied, the noise amplitude is amplified by up to a factor of 160 for the highest intensities. Thus this example of a direct inversion illustrates the need for regularization, and shows explicitly that the inversion problem is especially ill-posed for the highest intensities in a given set of data. However, Figure III-3 also illustrates an undesirable feature of the direct inversion method, namely the discontinuous derivatives at the peak intensities. Thus, smoother basis

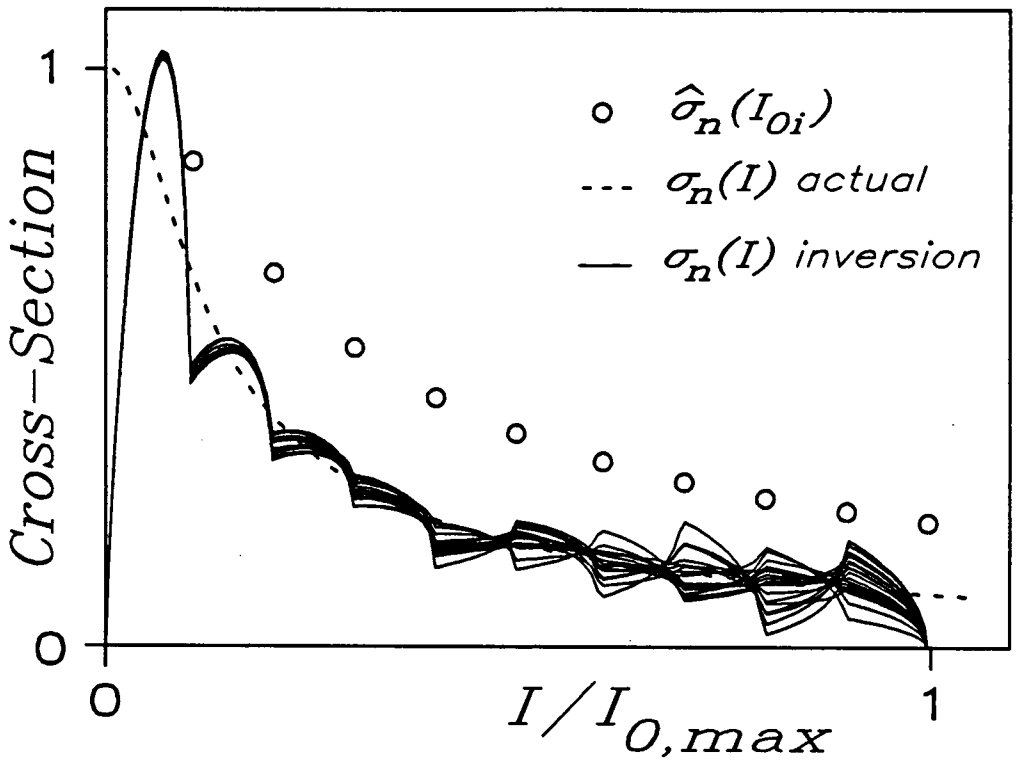


Figure III–3: *Example of direct inversion results.*

functions would be prefered. In Section IV we discuss the use of a particular type of such basis functions, namely polynomial splines.

IV INVERSION BY REGULARIZED SPLINE COLLOCATION

Section IV addresses once again the problem of inversion of the Volterra integral equation

$$\hat{\sigma}_n(I_0) = \int_0^{I_0} K(I_0; I)\, \sigma_n(I)\, dI, \qquad \text{(IV–1)}$$

for the situation in which $\hat{\sigma}_n(I_0)$ is obtained as discrete, noisy data. Specifically, we investigate a collocation scheme in which polynomial splines are employed as basis functions. Polynomial splines have been used in a variety of applications because of their versatility and ease of use [43–46]. Here we adapt a regularization scheme that has been employed successfully for the deconvolution of integrals of the Fredholm type [46]. One of the surprising results is that linear splines are found to give the best inversion results, a result we believe to be valid for problems of the Fredholm type as well.

The material in Section IV is taken from Ref. [47], and is self-contained in the sense that it is not essential for an understanding of the material in the remaining part of this dissertation. However, it does draw from Section II-3 ("Kernels Resulting from Exponential Profiles") to illustrate essential aspects of the inversion scheme, and from Section III-3, which discusses the general principles of inversion by collocation. Thus Section IV is arranged as follows. Section IV-1 presents the theory, namely the spline collocation equations (§IV-1.1), the regularization scheme (§IV-1.2), measures for the fidelity of inversion results (§IV-1.3) and for the residue-of-fit (§IV-1.4), and aspects of the numerical algorithm (§IV-1.5). Section IV-2 discusses briefly the sample cases that we have used for illustration, and Section IV-3 presents numerical results obtained for these sample cases. Finally, Section IV-4 concludes with a summary.

IV–1 Theory

IV–1.1 Spline equations

In our collocation scheme we now use polynomial splines as basis functions. However, we do not use the state-of-the-art formalism in which splines are defined in terms of normalized divided differences (B splines). Although this formalism has advantages, such as good numerical stability, it is less transparent than the straightforward spline definition that we use here. The two methods should give identical results, as long as machine roundoff errors are negligible, which we find to be the case when using double precision (64-bit) arithmetic. For an authoritative treatment, we refer the reader to the literature [48].

Using the straightforward notation we write the spline approximation $f(I)$ to $\sigma_n(I)$ as:

$$f(I) = \sum_{j=1}^{K} a_j \left(I - I_j\right)_+^D + \sum_{j=0}^{D} a_{K+j+1}\, I^j, \qquad \text{(IV–2a)}$$

where $\left(I - I_j\right)_+ = \max\{0; I - I_j\}$. In Eq.(IV-2a), D is the degree of the spline, for example $D=3$ for a cubic spline, the I_j's are the knots, and K is the number of knots. Note that, for $D>0$, $f(I)$ and its first $D-1$ derivatives are continuous for all values I, but that its Dth derivative is discontinuous at the knots, unless the corresponding coefficients a_j vanish. For notational convenience we introduce the additional knots $I_j = 0$ for $j > K$ so that Eq.(IV-2a) can be written as [cf. Eq.(III-15)]:

$$f(I) = \sum_{j=1}^{M} a_j \left(I - I_j\right)_+^{n_j}, \qquad \text{(IV–2b)}$$

where M is the number of coefficients, i.e., $M = K + D + 1$, and

$$n_j = \begin{cases} D; & j \le K, \\ j - K - 1\ ; & j > K. \end{cases} \qquad \text{(IV–2c)}$$

We assume that the experimental cross-section $\hat{\sigma}_n(I_0)$ from Eq.(IV-1) has been sampled at N values I_{0i} of the peak-intensity I_0, yielding the values s_i. Substitution of Eq.(IV-2b) into Eq.(IV-1) then yields the linear system of equations [cf. Eq.(III-16)]:

$$\sum_{j=1}^{M} A_{ij}\, a_j = s_i; \qquad i = 1, \ldots, N, \tag{IV–3}$$

where the A_{ij}'s are the projections of the spline components onto the kernels [cf. Eq.(III-17)]:

$$A_{ij} = \int_0^{I_{0i}} K(I_{0i}; I)\, (I - I_j)_+^{n_j}\, dI$$

$$= \sum_{k=0}^{n_j} \binom{n_j}{k} (-I_j)^{n_j - k}\, (I_{0i})^k\, M_k(I_{0i}; I_j), \tag{IV–4a}$$

and the M_k's are the incomplete moments of the kernel:

$$M_k(I_{0i}; I_j) = \int_{\min(I_j; I_{0i})}^{I_{0i}} K(I_{0i}; I)\, (I/I_{0i})^k\, dI. \tag{IV–4b}$$

Assuming that values for D, K, and the I_j's have been chosen, the inversion consists of determining the coefficients a_j from Eq.(IV-3). For an overdetermined system ($N > M$) this is accomplished by least-squares fitting, that is, by minimizing the residue-of-fit [cf. Eq.(III-19)]:

$$Q_{\text{fit}}(\mathbf{a}) = \sum_{i=1}^{N} w_i \left[\sum_{j=1}^{M} A_{ij} a_j - s_i\right]^2, \tag{IV–5}$$

where the w_i's are weights, assigned to the data s_i. Once the a_j's have been found, the spline $f(I)$ is determined.

IV–1.2 Regularization

Because of the ill-posed nature of the inversion problem, small noise components of the s_i's generally cause large deviations in the solution $f(I)$. To suppress

oscillatory behavior of $f(I)$ we supplement the residue $Q_{\rm fit}$ from Eq.(IV-5) with the functional

$$Q_{\rm knot}(\mathbf{a}) = w_{\rm knot}\left[\sum_{j=1}^{K} a_j^2\right], \tag{IV–6}$$

which is a measure of the discontinuities in the Dth derivative of the spline at the knots, each with weight $w_{\rm knot}$. From Eq.(IV-2a) it follows that minimization of $Q_{\rm knot}(\mathbf{a})$ forces the spline toward a single polynomial of degree D (the supporting polynomial) which, for small D, is nonoscillatory indeed. This type of regularization, which we refer to as "knot regularization," has been used successfully for inverse problems of the Fredholm-type [46].

The coefficient vector a that minimizes the sum $Q_{\rm fit} + Q_{\rm knot}$ is given by the least-squares solution of the weighted, regularized linear system

$$\sum_{j=1}^{M} \tilde{A}_{ij}\, a_j = \tilde{s}_i; \qquad i = 1, \ldots, \tilde{N}, \tag{IV–7a}$$

where $\tilde{N} = N + K + 1$, and the elements of the design matrix and the data vector are given respectively by [cf. Eq.(III-21)]:

$$\tilde{A}_{ij} = \begin{cases} w_i^{1/2} A_{ij}; & 1 \le i \le N, \\ w_{\rm knot}^{1/2} \delta_{i-N,j}; & N+1 \le i \le \tilde{N}, \end{cases} \tag{IV–7b}$$

and

$$\tilde{s}_i = \begin{cases} w_i^{1/2} s_i; & 1 \le i \le N, \\ 0; & N+1 \le i \le \tilde{N}. \end{cases} \tag{IV–7c}$$

This least-squares solution satisfies the normal equations [cf. Eq.(III-20)]:

$$\left(\tilde{\mathbf{A}}^T \tilde{\mathbf{A}}\right) \mathbf{a} = \tilde{\mathbf{A}}^T \tilde{\mathbf{s}}. \tag{IV–8}$$

If the nonregularized portions of $\tilde{\mathbf{A}}$ and $\tilde{\mathbf{s}}$ (i.e., the first M rows) are designated by $\tilde{\mathbf{A}}_{\rm nr}$ and $\tilde{\mathbf{s}}_{\rm nr}$, respectively, Eq.(IV-8) can be written alternatively as

$$\left(\tilde{\mathbf{A}}_{\rm nr}^T \tilde{\mathbf{A}}_{\rm nr} + w_{\rm knot} \mathbf{\Lambda}^{(K)}\right) \mathbf{a} = \tilde{\mathbf{A}}_{\rm nr}^T \tilde{\mathbf{s}}_{\rm nr}, \tag{IV–9a}$$

where $\Lambda^{(K)}$ is a diagonal matrix with elements

$$\Lambda_{kk}^{(K)} = \begin{cases} 1; & 1 \leq k \leq K, \\ 0; & K < k \leq M. \end{cases} \qquad \text{(IV–9b)}$$

Thus, especially for low degree splines ($K \simeq M$), knot regularization strongly resembles Tikhonov regularization [39,40], which would be obtained by replacing $\Lambda^{(K)}$ in Eqs.(IV-9) by the $M \times M$ identity matrix, as expressed in Eq.(III-25) on page 39. Note that, in this case, the origin of the extra term in the normal equations is the result of supplying additional constraints, rather than modifying the singular values of the design matrix. In Section IV-3 we briefly compare numerical results obtained with Tikhonov regularization to those obtained with knot regularization. In Section IV-3 we also discuss the tactics for choosing optimum values for the regularization parameter w_{knot}.

IV–1.3 Fidelity of inversion results

Ultimately, the success of any inversion scheme is measured by how well $f(I)$ approximates the true $\sigma_n(I)$. Thus we define the noise amplification function

$$\Delta(I) = \left\langle \left(f(I) - \sigma_n(I)\right)^2 \right\rangle^{1/2} \Big/ ds_{\text{rms}}, \qquad \text{(IV–10)}$$

where ds_{rms} is the average amplitude of the noise ds_i on the data s_i:

$$ds_{\text{rms}} = \left\{ \frac{1}{N} \sum_{i=1}^{N} \langle ds_i^2 \rangle \right\}^{1/2}, \qquad \text{(IV–11)}$$

and the brackets indicate expectation values, taken over an infinite ensemble of possible realizations of the data **s**. Intuitively, values of $\Delta(I)$ on the order of unity would appear to be excellent, considering the ill-posed nature of the inversion problem. Assuming that the noise and the function $\sigma_n(I)$ are uncorrelated, $\Delta(I)$ separates into two parts, due to systematic error and noise, respectively:

$$\Delta^2(I) = \Delta_S^2(I) + \Delta_N^2(I). \qquad \text{(IV–12)}$$

The systematic contribution is given by

$$\Delta_S(I) = \left| f_0(I) - \sigma_n(I) \right| / ds_{\rm rms}, \qquad \text{(IV–13)}$$

where $f_0(I)$ is the spline solution in the absence of noise. If we denote the weighted, noise-free data by $\tilde{\mathbf{s}}_0$, and the ith column of the matrix $\left(\tilde{\mathbf{A}}^T\tilde{\mathbf{A}}\right)^{-1}\tilde{\mathbf{A}}^T$ by $\mathbf{b}^{(i)}$, i.e.,

$$\mathbf{b}^{(i)} = \left(\tilde{\mathbf{A}}^T\tilde{\mathbf{A}}\right)^{-1}\tilde{\mathbf{A}}^T\,\hat{\mathbf{e}}^{(i)}; \qquad i = 1,\ldots,N, \qquad \text{(IV–14)}$$

where $\hat{\mathbf{e}}^{(i)}$ is a unit vector with elements $\hat{e}_j^{(i)} = \delta_{ij}$, then $f_0(I)$ is given by

$$f_0(I) = \sum_{j=1}^{M}\Big(\sum_{i=1}^{N} b_j^{(i)}\tilde{s}_{0i}\Big)\,(I - I_j)_+^{n_j}. \qquad \text{(IV–15)}$$

The second contribution in Eq.(IV-12) is due to noise only. If this noise is uncorrelated, i.e., $\langle ds_i ds_j \rangle = 0$ for $i \neq j$, and the weights w_i in Eq.(IV-5) are chosen such that

$$w_i = \langle ds_i^2 \rangle^{-1}; \qquad i = 1,\ldots,N, \qquad \text{(IV–16)}$$

then, from Eqs.(IV-2b) and (IV-8), $\Delta_N(I)$ is obtained as

$$\Delta_N(I) = \Big\{ \sum_{i=1}^{N} g_i^2(I) \Big\}^{1/2} \Big/ ds_{\rm rms}, \qquad \text{(IV–17)}$$

where the $g_i(I)$'s are splines, given by

$$g_i(I) = \sum_{j=1}^{M} \Big\{ b_j^{(i)}\,(I - I_j)_+^{n_j} \Big\}. \qquad \text{(IV–18)}$$

The sum in Eq.(IV-17) contains N rather than $\tilde{N}$ terms because, in Eq.(IV-7c), no noise is associated with the data $\tilde{s}_i$ for $N+1 \leq i \leq \tilde{N}$. From Eqs.(IV-17) and (IV-18), it follows that $\Delta_N(I)$ is a piecewise polynomial of degree $2D$, with discontinuous Dth and higher derivatives at the knots. Note that, with Eqs.(IV-12)–(IV-18), ensemble averaged values for the fidelities of inversion results can be obtained without actually performing Monte-Carlo-type calculations.

To specify the fidelity of the inversion by a single quantity we define the average noise amplification factors

$$\mathcal{D}_{(S,N)} = \left\{ \int_0^{I_{0,\max}} \left[\Delta_{(S,N)}(I)\right]^2 dI / I_{0,\max} \right\}^{1/2}, \qquad \text{(IV–19)}$$

where $I_{0,\max}$ is the largest of the peak-intensities I_{0i} and the subscripts refer to either of the three quantities $\Delta(I)$, $\Delta_S(I)$, or $\Delta_N(I)$. We propose that, for a given problem, the best inversion scheme is that which yields the smallest value of $\mathcal{D}$ which, below, we refer to simply as "the fidelity" of the inversion result. In the present formulation this implies an optimization problem with $K+3$ parameters (D, K, the K knots I_j, and w_{knot}). Of course, in a typical application, the function $\sigma_n(I)$ is not known, so that the systematic errors $\Delta_S(I)$ and $\mathcal{D}_S$, and therefore the total errors $\Delta(I)$ and $\mathcal{D}$, cannot be computed. However, we show in Section IV-3 how general guidelines can be developed by performing the regularization scheme with known functions $\sigma_n(I)$ and their corresponding noise-free data $\tilde{\mathbf{s}}_0$.

IV–1.4 Residue-of-fit

The most direct measure of the success of inversion results is the residue Q_{fit} from Eq.(IV-5). The ensemble averaged value of Q_{fit}, which we denote by χ^2, can be calculated in a similar manner as the noise amplification function $\Delta(I)$ from Section IV-1.3. Specifically, if the noise $\mathbf{ds}$ and the noise-free data $\tilde{\mathbf{s}}_0$ are uncorrelated, χ^2 separates into two parts [cf. Eq.(IV-12)]:

$$\chi^2 \equiv \langle Q_{\text{fit}} \rangle = \chi_S^2 + \chi_N^2. \qquad \text{(IV–20)}$$

If we define the matrix $\mathbf{E}$ as

$$\mathbf{E} = \tilde{\mathbf{A}}\left(\tilde{\mathbf{A}}^T\tilde{\mathbf{A}}\right)^{-1}\tilde{\mathbf{A}}^T - \mathbf{I}, \qquad \text{(IV–21)}$$

where $\mathbf{I}$ is the $N \times N$ identity matrix, then the systematic and noise contributions to χ^2 respectively are given by

$$\chi^2_S = \sum_{h=1}^{N} \Big\{ \sum_{i=1}^{N} E_{hi}\, \tilde{s}_{0i} \Big\}^2, \tag{IV-22}$$

and

$$\chi^2_N = \sum_{h=1}^{N} \sum_{i=1}^{N} E^2_{hi}. \tag{IV-23}$$

It can be shown that

$$N - M \leq \chi^2_N \leq N - D - 1, \tag{IV-24}$$

where the lower and upper limits correspond to no regularization ($w_{\text{knot}} = 0$) and maximum regularization ($w_{\text{knot}} \to \infty$), respectively. Thus χ^2_N equals the number of data minus the effective number of fit coefficients, the latter of which depends on the regularization parameter w_{knot}.

IV–1.5 Numerical computation

Although the most powerful techniques for finding the least-squares solution of Eqs.(IV-7) are based on such methods as Householder transformation and singular value decomposition [38], we use here the orthodox approach of solving the normal equations (IV-8) directly. We employ the LINPACK subroutines DSICO and DSIFA [49] which are based on symmetric indefinite factorization of $\tilde{\mathbf{A}}^T\tilde{\mathbf{A}}$. Because the regularization conditions are built into the matrix $\tilde{\mathbf{A}}$, the squaring of the condition number of $\tilde{\mathbf{A}}$ is generally acceptable. As a practical measure of the condition of the inversion problem we monitor the quantity

$$C = \Big\{ \text{RCOND}(\tilde{\mathbf{A}}^T\tilde{\mathbf{A}}) \Big\}^{-1}, \tag{IV-25}$$

where RCOND is an estimate of the reciprocal condition of $\tilde{\mathbf{A}}^T\tilde{\mathbf{A}}$, as determined at little added computational effort during factorization of $\tilde{\mathbf{A}}^T\tilde{\mathbf{A}}$ by the LINPACK

subroutine DSICO. Small values of C generally lead to good inversion results [50,51]. For our calculations in 64-bit arithmetic we find roundoff errors to be negligible as long as $C \lesssim 10^{16}$, i.e., $C \ll 2^{64}$. For the small systems that we have investigated ($M \leq 30$) this condition is satisfied, except for poor choices of spline and regularization parameters.

To compute the ensemble averaged fidelities and residues from Sections IV-1.3 and IV-1.4 we obtain the vectors $\mathbf{b}^{(i)}$ from Eq.(IV-14) by solving

$$(\tilde{\mathbf{A}}^T\tilde{\mathbf{A}})\,\mathbf{b}^{(i)} = \tilde{\mathbf{A}}^T\,\hat{\mathbf{e}}^{(i)}; \qquad i = 1,\ldots,N, \tag{IV–26}$$

using the factorization of the matrix $\tilde{\mathbf{A}}^T\tilde{\mathbf{A}}$. The elements of $\mathbf{E}$ from Eq.(IV-21) are then calculated as

$$E_{hi} = E_{ih} = \sum_{j=1}^{M}\{\tilde{A}_{hj}\,b_j^{(i)}\} - \delta_{hi}. \tag{IV–27}$$

The integrations in Eq.(IV-19) are obtained as a discrete sum (with about 80 points) over the interval $0 \leq I \leq I_{0,\max}$.

IV–2 Overview of Sample Cases

In this section we discuss the kernels, cross-sections, experimental conditions, and spline parameters that we use in the numerical experiments of Section IV-3. Neither of these choices are a prerequisite for the general theory of Section IV-1 and serve for the purpose of illustration only. Table IV-1 gives a summary.

IV-2.1 Kernels and cross-sections

For illustration, we use the kernels and cross-sections that are introduced in Section II-3. Thus we use the kernels that result from exponential beam- and pulse-profiles, as given by Eq.(II-33). Note that, for selected values of β,

Table IV–1: *Summary of sample cases, used in Section IV-3.*

Quantity	Choice
Kernel $K(I_0; I)$	Exponential intensity-profile: Eq.(II-33) on page 25 with $n=2$ and $\beta=1.5$.
Cross-sections $\sigma_n(I)$, $\hat{\sigma}_n(I_0)$	Figures II-4(a) and II-4(b) on page 29.
Sampling $I_{0i};\ i=1,\ldots,N$	Uniform: Eq.(IV-28) with $N=10$ or $N=25$ data.
Noise $\langle ds_i^2 \rangle^{1/2}$	Uniform: Eq.(IV-29) with $ds_{\rm rms}=0.005$, $ds_{\rm rms}=0.0025$, or $ds_{\rm rms}=0.010$.
Spline degree D	$0 \leq D \leq 4$.
Number of knots K	Adjustable.
Spline knots $I_j;\ j=1,\ldots,K$	Single parameter stretch: Eq.(IV-30), with $\alpha=1.3$.
Regularization-parameter $w_{\rm knot}$	See Section IV-3.

the incomplete moments M_k from Eqs.(IV-4) can be calculated analytically, as expressed in Eqs.(II-36) and (II-37). Unless stated otherwise, we assume a two-photon excitation process ($n=2$) and a composite shape parameter $\beta=1.5$, respresenting, for example, one rectangular and three Gaussian profiles among the beam- and pulse-profiles $F_{\mathbf{r}}(\mathbf{r})$ and $F_t(t)$.

Furthermore, we use the two intensity-dependent cross-sections $\sigma_n(I)$ from Figure II-4 on page 29. Neither was generated as a spline, so the $f(I)$'s from

Eqs.(IV-2) are at best good approximations to $\sigma_n(I)$. Figure II-4 displays also the corresponding experimental cross-sections $\hat{\sigma}_n(I_0)$. Note that the effects of spatial and temporal averaging are more serious in Figure II-4(b) than in Figure II-4(a), because the corresponding $\sigma_n(I)$ has an extremum for $I > 0$. We treat both the intensities and cross-sections as dimensionless quantities, with values between zero and unity.

IV-2.2 Experimental conditions

We assume that $\hat{\sigma}_n(I_0)$ is sampled equidistantly on the interval $0 \leq I_0 \leq I_{0,\max}$:

$$I_{0i} = \big((i-1)/(N-1)\big) I_{0,\max}; \qquad i = 1, \ldots, N \tag{IV–28}$$

(actually we use a small but nonvanishing value for I_{01}, namely $I_{01} = 10^{-3} I_{0,\max}$). We take $I_{0,\max} = 1$, and assume $N = 10$ or $N = 25$ data. We take the noise to be uniform [cf. Eq.(IV-11)]:

$$\langle ds_i^2 \rangle = ds_{\rm rms}^2; \qquad i = 1, \ldots, N, \tag{IV–29}$$

and we choose the weights w_i from Eq.(IV-5) as in Eq.(IV-16). In most calculations we use $ds_{\rm rms} = 0.005$, which corresponds roughly to a relative error of one percent.

IV-2.3 Spline parameters

We consider only low degree splines, namely $0 \leq D \leq 4$. The number of knots is chosen such that the number of spline coefficients M in Eqs.(IV-2) is no larger than the sum of the number of data and the number of regularization constraints. Thus $K \leq N - D - 1$ if no regularization is applied. Otherwise the

number of knots is arbitrary, as long as $D \leq N$. However, we show in Section IV-3 that the best results are generally obtained for $K \simeq N - D - 1$.

Although the placement of K knots is a K-parameter problem, we study in particular the case

$$I_j = \big(j/(K+1)\big)^{\alpha} I_{0,\max}; \qquad j = 1, \ldots, K. \tag{IV-30}$$

Thus the positions of the knots are governed by the stretch parameter α. Equidistant knots ($\alpha = 1$) do not necessarily give the best inversion results. This is illustrated in Figure IV-1, in which the condition number C from Eq.(IV-25) is plotted as a function of α for parameters as given in the figure caption, and various values of w_{knot}. If no regularization is applied a strong dependence of C on α results. For $C \gtrsim 10^{16}$ numerical roundoff errors become apparent. However, for realistic values of w_{knot} (namely those that minimize the fidelity D) the choice of α is much less critical. Thus, for the two-photon kernel with $\beta = 1.5$, we use the value $\alpha = 1.3$ throughout Section IV-3. Having fixed the positions of the knots the inversion problem is reduced to one with only three parameters, namely the spline degree D, the number of knots K, and the regularization parameter w_{knot}.

IV–3 Numerical Results

To illustrate the essential features of the inversion scheme we now apply the theory of Section IV-1 to the specific sample cases from Section IV-2. In particular we seek to establish guidelines for choosing optimum values for the parameters D, K, and w_{knot}.

First, in Figure IV-2, we demonstrate the need for regularization. To this effect we assume that the cross-section $\sigma_n(I)$ from Figure II-4(b) on page 29 (dashed curves in Figure IV-2) is sampled at $N = 10$ points (circles in Figure

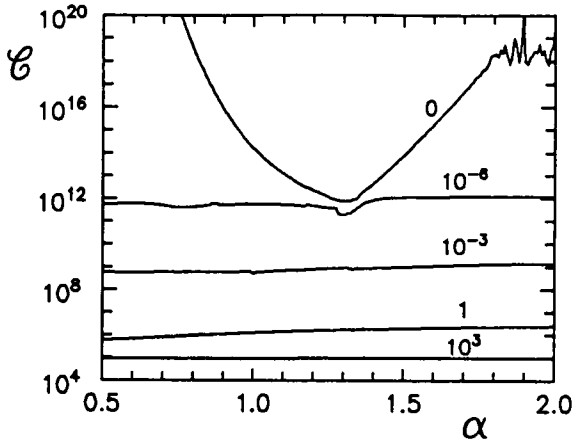


Figure IV–1: *Condition numbers of the spline inversion matrix.*

Values of C from Eq.(IV-25) as a function of the knot stretch parameter α from Eq.(IV-30) for a two-photon kernel with $\beta = 1.5$, noise amplitude $ds_{\rm rms} = 0.005$, $N = 10$ data, spline degree $D = 3$, and $K = 6$ knots. Curves are labeled with the value of $w_{\rm knot}$.

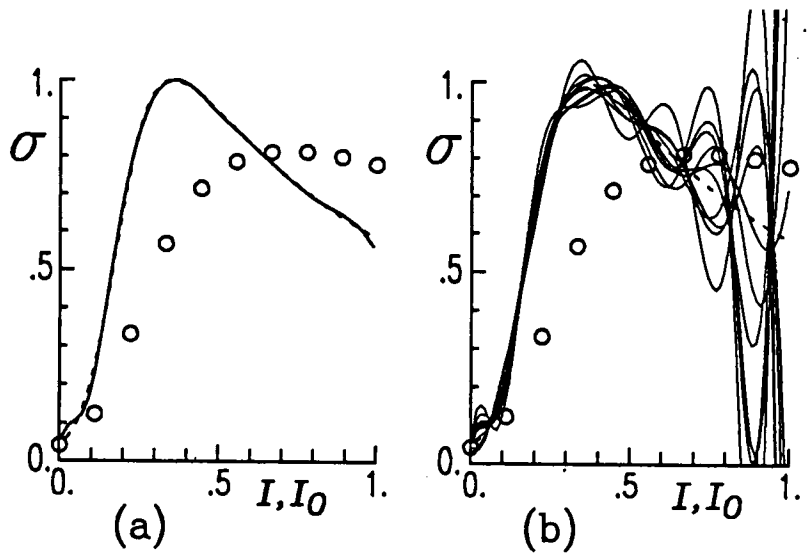


Figure IV–2: *Inversion results without and with noise.*

Results are for the cross-section $\sigma_n(I)$ from Figure II-4(b) on page 29 (dashed curves in Figure IV-2), sampled at $N = 10$ points (circles) by a two-photon kernel with $\beta = 1.5$. Solid curves are inversion results for a cubic spline with $K = 6$ knots and $\alpha = 1.3$. (a) *Inversion for noise-free data;* (b) *Ensemble of ten solutions for $ds_{\rm rms} = 0.005$.*

IV-2) by a two-photon kernel with $\beta = 1.5$. If the sampled data are noise-free [Figure IV-2(a)], excellent reconstructions of the true cross-section can be obtained with an unconstrained inversion. For example, the solid curve in Figure IV-2(a) represents the inversion result for a cubic spline with $K = 6$ knots and a knot stretch parameter $\alpha = 1.3$. However, if noise is added to the data, inversion results obtained without regularization become highly oscillatory, particularly for the largest intensities. This is shown in Figure IV-2(b), in which the solid curves represent the cubic spline solutions for an ensemble of ten sets of noisy data ($ds_{\rm rms} = 0.005$). The particularly ill-posed nature of the inversion problem for the largest intensities is typical for Volterra problems: whereas all data contain information on $\sigma_n(I)$ for $I \simeq 0$, only a few data contain information for $I \simeq I_{0,\rm max}$.

The effects of applying regularization are illustrated in Figure IV-3 which displays, as a function of $w_{\rm knot}$, the ensemble averaged values of the fidelity $\mathcal{D}$ and residue-of-fit χ^2 from Sections IV-1.3 and IV-1.4, respectively, and the condition number $\mathcal{C}$ from Section IV-1.5, for conditions as given in the figure caption. Figure IV-3(a) clearly shows that the choice of $w_{\rm knot}$ establishes a trade-off between small systematic error (for small $w_{\rm knot}$) and small noise amplification (for large $w_{\rm knot}$). On the other hand, both systematic and noise contributions to the residue χ^2 are monotonically increasing functions of $w_{\rm knot}$ (note that Eq.(IV-24) is satisfied: $0 \leq \chi^2_N \leq 6$). As $w_{\rm knot}$ increases the condition of the inversion problem improves, as can be seen in Figure IV-3(c). Although the functional behavior of $\mathcal{D}$ versus $w_{\rm knot}$ is fairly complicated and case-dependent, an important feature is that a global minimum occurs for a value of $w_{\rm knot}$ for which $\chi^2 \simeq N$. This can be seen more clearly in Figure IV-4, which gives the fidelity $\mathcal{D}$ as a function of the residue-of-fit χ^2, not only for the data from Figure IV-3, but also for different

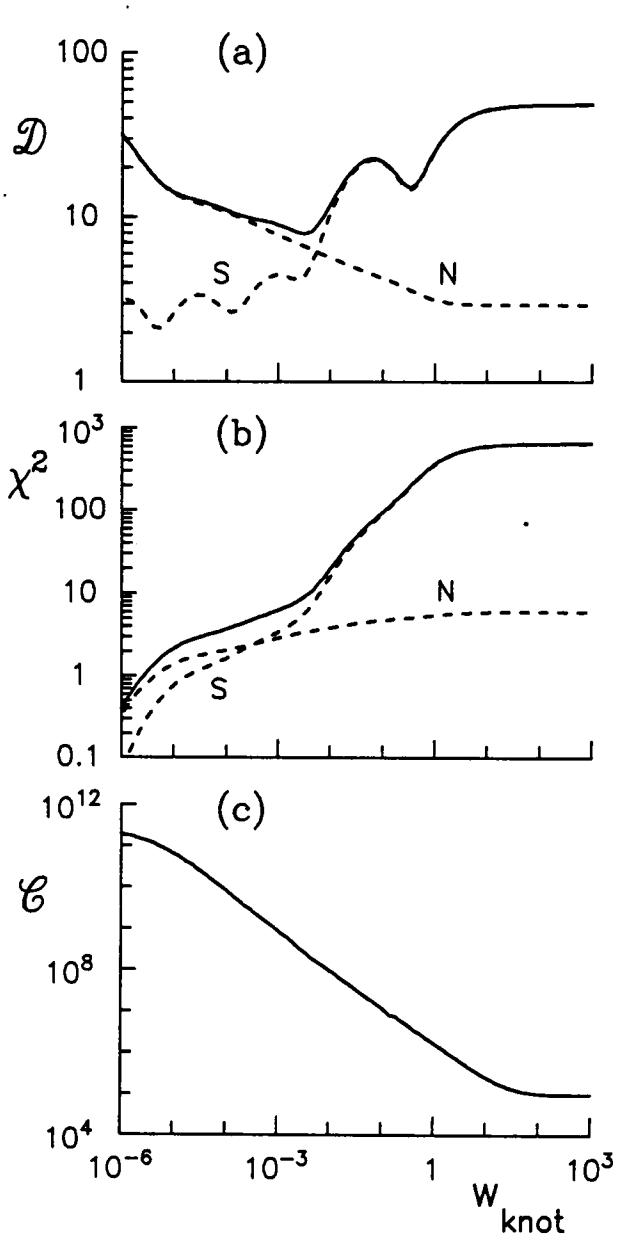


Figure IV–3: *Fidelities, residue-of-fit, and condition as a function of the regularization parameter.*

Fidelity $\mathcal{D}$ from Eq.(IV-19), residue-of-fit χ^2 from Eq.(IV-20), and condition number $\mathcal{C}$ from Eq.(IV-25) as a function of w_{knot} for conditions as in Figure IV-2(b). In (a) and (b) systematic (S) and noise (N) contributions are indicated by dashed curves.

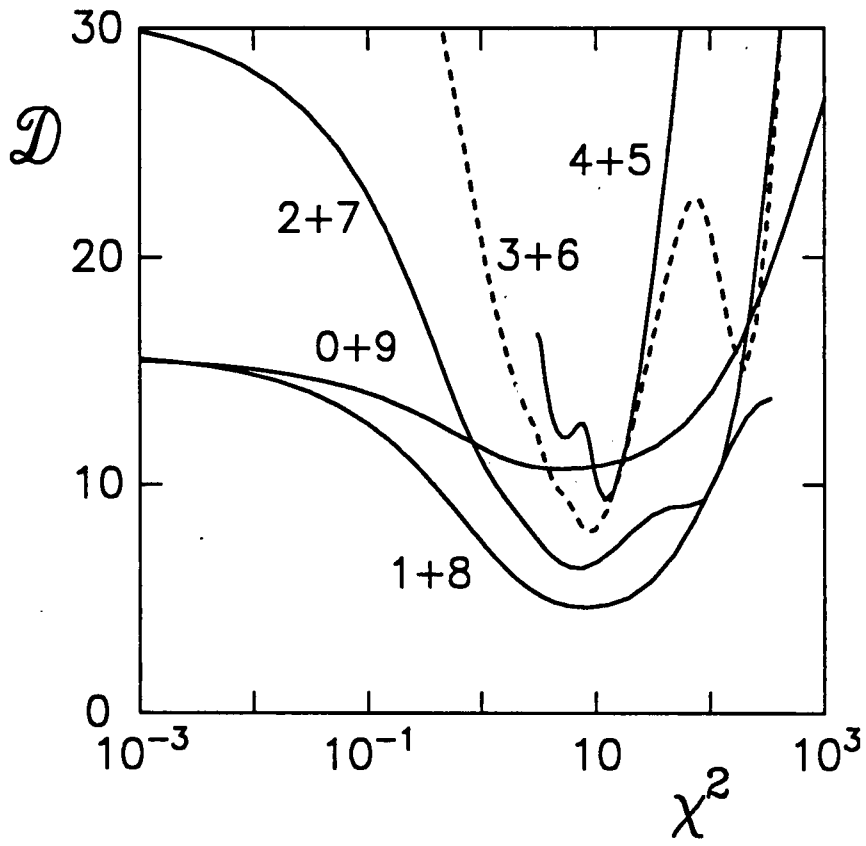


Figure IV–4: *Fidelity versus residue-of-fit.*

Displayed are the fidelities $\mathcal{D}$ as a function of the residue-of-fit χ^2 with w_{knot} as (unspecified) parameter along the curves. The dashed curve ($D + K = 3 + 6$) is obtained from the data in Figure IV-3. The other curves are calculated for the same conditions as in Figure IV-3 but different values of $D + K$, as indicated. Note that all curves have minima for $\chi^2 \simeq N = 10$.

choices for the degree D and the number of knots K (while keeping the number of fit parameters the same). Indeed, although the details are different, all curves have global minima for $\chi^2 \simeq N$. This result can be generalized in the usual manner: in an application where $\mathcal{D}$ and χ^2 cannot be computed (because the true cross-section is not known), optimum inversion results should be obtained if w_{knot} is

chosen such that the residue $Q_{\rm fit}$ from Eq.(IV-25) is in the range $N \pm \sqrt{2N}$ [46].* Note that the lower the degree of the spline, the broader is the minimum of the curves in Figure IV-4. Thus, the lower the degree of the spline, the more likely one is to achieve a fidelity close to the optimum value if, for a specific realization of noisy data, one chooses $w_{\rm knot}$ so that $Q_{\rm fit} \simeq N$.

Somewhat surprisingly, the best fidelities in Figure IV-4 are obtained for linear splines ($D = 1$). We have found this result to hold for all the cases that we have investigated. The most important of these are illustrated in Figures IV-5, IV-6, and IV-7. Figure IV-5(a) gives the minimum values of $\mathcal{D}$ from Figure IV-4. Figure IV-5(b) shows the same trend in the dependence of the fidelity on the degree of the spline for the other cross-sections, namely those from Figure II-4(a) on page 29. These yield better overall values of the fidelity due to the less complicated behavior of $\sigma_n(I)$. Figure IV-5(c) shows that better fidelities are also obtained if the noise amplitude is kept constant, but more data are supplied. However, except for zero degree splines, the reduction in $\mathcal{D}$ is less than the square-root of the ratio of the numbers of data (i.e., less than a factor $(25/10)^{1/2}$). Similarly, despite the scaling of the difference of the calculated and true functions $f(I)$ and $\sigma_n(I)$ by the average noise amplitude $ds_{\rm rms}$ in Eq.(IV-10), the fidelity $\mathcal{D}$ depends generally on $ds_{\rm rms}$ as is shown in Figure IV-6. This is because, unlike the noise amplification function $\Delta_N(I)$ from Eq.(IV-17), the systematic error $\Delta_S(I)$ depends on $ds_{\rm rms}$ (the true $\sigma_n(I)$ does not scale with $ds_{\rm rms}$). Still, smaller values of $ds_{\rm rms}$ *do* yield

---

*Obviously, ideal inversion is achieved if the fit-function $f(I)$ is identical to the true function $\sigma_n(I)$, yielding $\mathcal{D} = 0$ and $\chi^2_S = 0$. In this case $f(I)$ is a zero-parameter function and, by Eq.(IV-24), the ensemble averaged residue is given by $\chi^2 = \chi^2_N = N$. For normally distributed noise the standard deviation is then $\sqrt{2N}$. The statement that, for more realistic model functions, the best fidelity $\mathcal{D}$ is achieved if χ^2 is in the range $N \pm \sqrt{2N}$ follows strictly only by abstraction from this ideal inversion case.

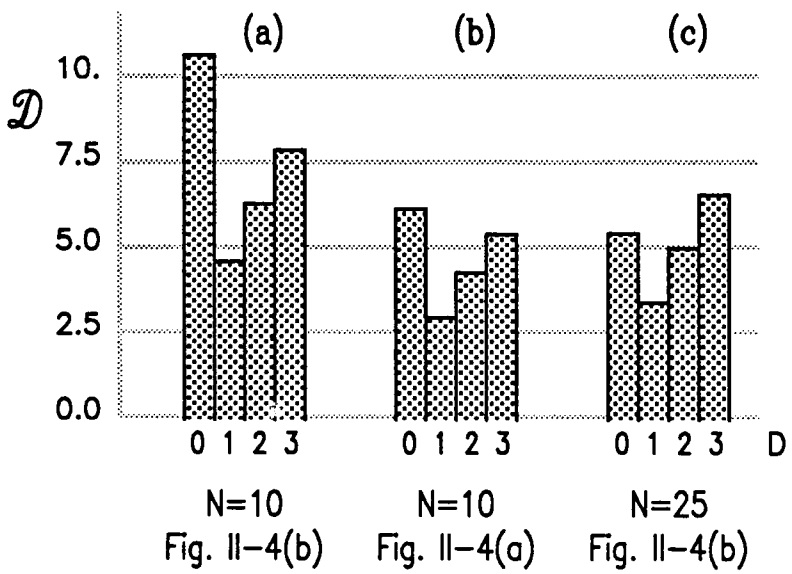


Figure IV–5: *Best fidelities for different numbers of data and different cross-sections.*

(a) *Best values of $\mathcal{D}$ from Figure IV-4 [$N = 10$ data and cross-sections from Figure II-4(b) on page 29] for various degrees D;* (b) *Same for the cross-sections from Figure II-4(a);* (c) *Same for the cross-sections from Figure II-4(b) with $N = 25$ data and $K = N - D - 1$.*

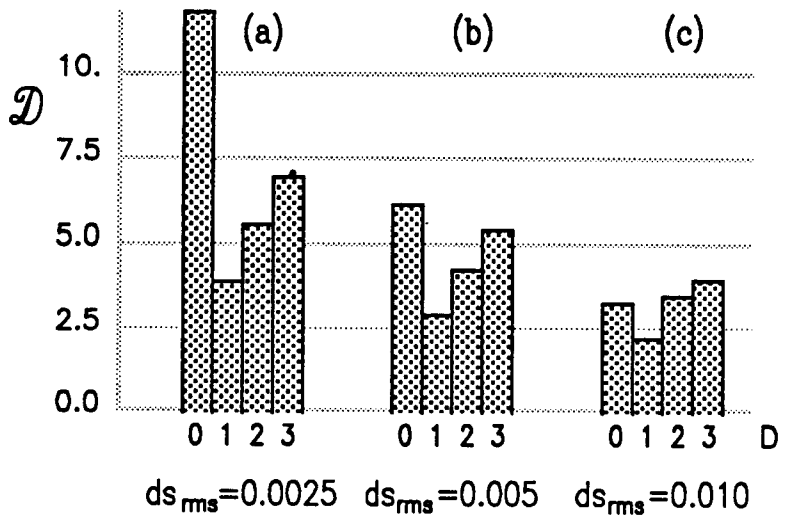


Figure IV–6: *Best fidelities for different noise amplitudes.*

As Figure IV-5(b) with $ds_{\rm rms} = 0.005$ [Figure IV-6(b)], as well as noise amplitudes that are half as small (a) or twice as large (c).

better values of the absolute fidelity, given by the product $\mathcal{D}ds_{\rm rms}$, as is easily checked from Figure IV-6.

Figure IV-7 displays the optimum values of $\mathcal{D}$ as a function of the number of knots K for a given degree of the spline, and either $N = 10$ or $N = 25$ data. It is seen that the curves flatten out into a broad minimum for values of K such that the number of spline coefficients M is roughly equal to the number of data N, i.e., $K \simeq N - D - 1$. Especially for small values of N, smaller values of K unnecessarily limit the number of degrees of freedom of the fit function. Much larger values, however, lead to ill-conditioning of the problem as well as an unnecessary increase in the number of inversion equations. Note that, again, the best fidelities are obtained for linear splines.

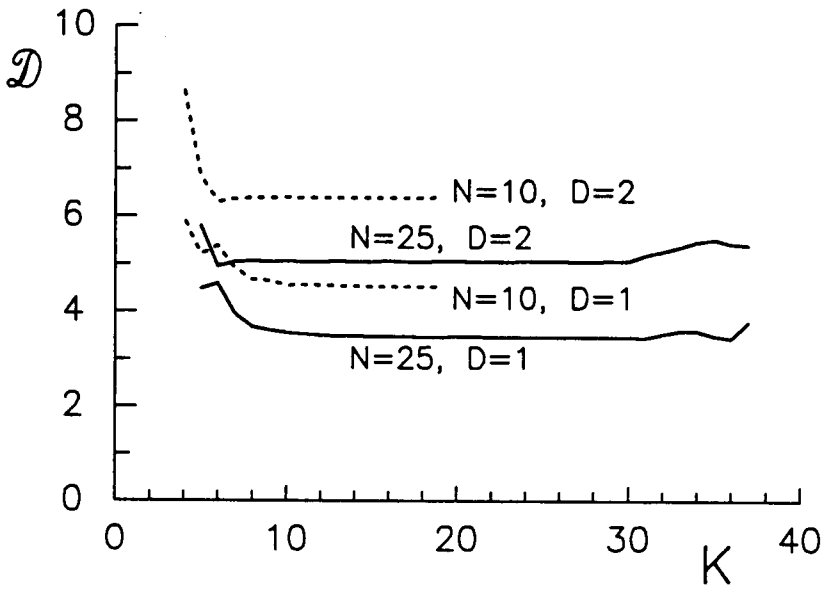


Figure IV–7: *Best fidelities for different numbers of knots.*

Best values of $\mathcal{D}$ as a function of K for conditions as in Figures IV-5(a) and IV-5(c) with $N = 10$ and $N = 25$ data, respectively, and spline degrees $D = 1$ or $D = 2$.

Figure IV-8(a) shows typical inversion results obtained with constrained linear splines, namely for the same conditions as in Figure IV-2(b). Note the dramatic improvement that is obtained by applying regularization. Still, the qualitative behavior of the fidelity as a function of the intensity is retained. This is illustrated in Figure IV-8(b), which displays the ensemble averaged noise amplification functions $\Delta_N(I)$ (dashed) and $\Delta(I)$ from Section IV-1.3 for the same data. For $I \simeq 1$, the main contribution to the fit-error is that of the noise function $\Delta_N(I)$. For $I \simeq 0$ the noise amplification function is about unity. Thus, even when applying regularization, the more accurate inversion results are obtained for $I \simeq 0$, and the expected error is no smaller than that of the data themselves.

Thus far, our calculations have been for two-photon kernels with a composite shape parameter $\beta = 1.5$ in Eq.(II-33). For other kernels we obtain the same qualitative results. However, different values are obtained for the optimum fidelities, as Figure IV-9 shows for conditions as given in the figure caption. In agreement with the discussion in Section II-3 the fidelity gets worse as β increases, that is, as more averaging takes place. Also, two-photon kernels give better results than those for single-photon processes.

Finally, we compare our knot regularization scheme with that of Tikhonov regularization, as discussed in Section III-3 in connection with singular value decomposition. As mentioned in Section IV-1.1, Tikhonov regularization rather than knot regularization is obtained by replacing the diagonal matrix $\mathbf{\Lambda}^{(K)}$ in Eqs.(IV-9) by the identity matrix. Thus not only the first K coefficients in Eq.(IV-2a) are constrained, but also the remaining D+1 coefficients of the supporting polynomial. For the cases that we have invesigated ($0 \leq D \leq 4$) we find differences of at most a few percent between the optimum fidelities obtained with the two methods. For linear and quadratic splines the differences are only about 0.1 and 0.2 percent,

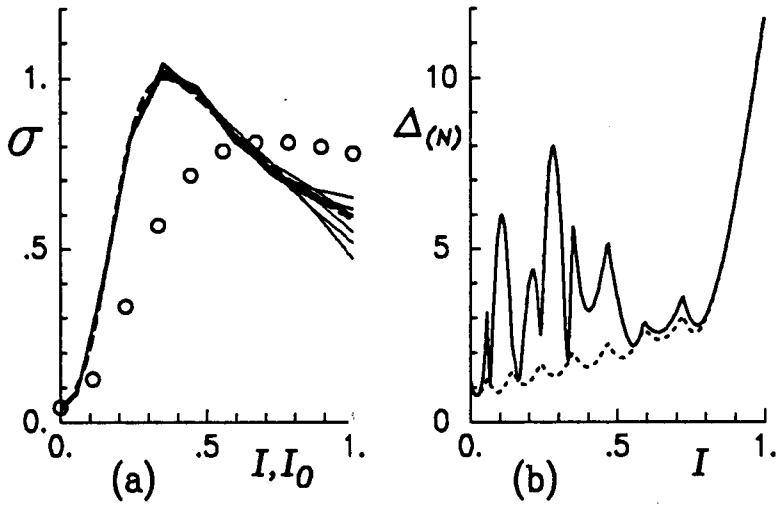


Figure IV–8: *Regularized inversion results for linear splines.*

As Figure IV-2: (a) *Inversion results for the cross-section* $\sigma_n(I)$ *from Figure II-4(b) on page 29 [dashed curve in Figure IV-8(a)], sampled at* $N = 10$ *points (circles) with* $ds_{\rm rms} = 0.005$. *The solid curves represent an ensemble of ten inversions, obtained with* $D = 1$, $K = 8$, *and* $w_{\rm knot} = 0.66$ *(the value that gives the best fidelity* $\mathcal{D}$*).* (b) *Corresponding ensemble averages of the noise amplification functions* $\Delta_N(I)$ *from Eq.(IV-17) (dashed) and* $\Delta(I)$ *from Eq.(IV-10) (solid).*

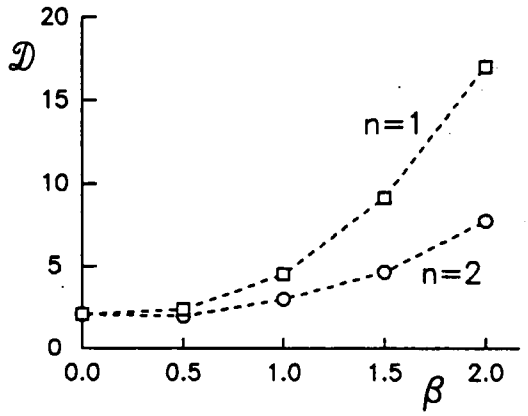


Figure IV–9: *Best fidelities for different kernels.*

Optimum fidelities $\mathcal{D}$ *for several values of the order of the interaction* n *and the shape parameter* β *of the kernels from Eq.(II-33) on page 25. Calculations are for the cross-section from Figure II-4(b) on page 29 with* $N = 10$, $ds_{\rm rms} = 0.005$, *and spline parameters* $D = 1$, $K = 8$, $\alpha = 1.3$, *and* $w_{\rm knot}$ *such that* $\mathcal{D}$ *is a minimum.*

respectively. Thus our regularization scheme compares quite favorably with the proved method of Tikhonov regularization.

IV–4 Summary and Conclusions

In Section IV, we have discussed the inversion of spatially and/or temporally averaged data by a collocation scheme involving polynomial splines. Regularization of this Volterra problem is achieved by constraining the discontinuities in the highest derivatives of the spline at the knots. In our formulation (unlike that in which B splines are employed [46]) this type of regularization strongly resembles that of Tikhonov regularization. Explicit analytical expressions for the ensemble averaged values of the fidelity of inversion results and the residue-of-fit are given. Using these expressions we have performed numerical experiments for specific model functions for the actual intensity-dependent cross-section and the averaging kernel. From these experiments we draw the following general conclusions:

(1) Inversion results with the best fidelities are obtained for values of the regularization parameter that yield a residue-of-fit approximately equal to the number of data (i.e., $\chi^2 \simeq N$).

(2) For such values of the regularization parameter the fidelity of the inversion is quite insensitive to the placement of the knots of the spline.

(3) For a given number of data and degree of the spline, the optimum number of knots is such that the number of fit coefficients is approximately equal to the number of data.

(4) Somewhat surprisingly, the best inversion results are obtained for linear splines, which yield 20 to 30 percent better fidelities than quadratic splines. These, in turn, yield 15 to 20 percent better fidelities than cubic splines. Results obtained

with piecewise constant (zero degree) splines are usually inferior to those of either linear, quadratic, or cubic splines. Linear splines have the added advantage that in the neighborhood of the best achievable fidelity, the fidelity depends less critically on the regularization parameter.

We believe that the above conclusions will hold for inversion problems of the Fredholm type as well, in particular the apparent superiority of linear splines, as measured by the integrated fidelities from Eq.(IV-19). It should also be interesting to compare the fidelities obtained with linear splines to those obtained with other basis functions, such as the kernel basis functions employed in direct inversion, and Legendre or other orthonormal polynomials. The outcome of such numerical experiments should be a noteworthy, and far as we know, novel contribution to the extensive literature on inversion problems.

V INVERSION OF NONSATURATED AND SATURATED LINESHAPES

Sections II, III, and IV have dealt with the inversion of spatially and/or temporally averaged data such as cross-sections and excitation rates, without explicitly taking into account any spectral frequency dependence of the nonlinear process. By contrast, Section V focuses on processes such as multi-photon excitation from some well defined ground state to a well defined excited state (rather than an ionization continuum), using a narrowband laser. Thus, the nonlinear process has a spectral lineshape associated with it which, in the case of dynamical Stark effects, is intensity-dependent. If temporal and/or spatial averaging effects take place in the measurement of, say, the fluorescence signal, then the measured lineshape is different from the true, intrinsic, intensity-dependent lineshape. Basically, this problem can be dealt with in exactly the same manner as the foregoing treatment of the inversion of cross-sections and excitation rates, merely by performing an inversion for each frequency within the spectral lineshape. However, we show that, in addition, the information of the frequency dependence of the process can be used to invert saturated data, even if no exact calibration of the measurement apparatus is available. But first, in Section V-1, we illustrate the effects of spatial and/or temporal averaging on a typical Stark broadened transition, assuming that no saturation of the transition occurs. Then, in Section V-2, we treat the case of a saturated excitation, namely one in which the ground state of the transition undergoes significant depletion during the laser pulse, at least for some frequencies within the spectral lineshape. Specifically we consider the case in which the duration of the laser pulse is short compared with the random deexcitation processes of the excited state ("fast pulse limit").

V–1 Nonsaturated Regime

As before, we assume that the nonlinear process of interest can be described by intensity-dependent cross-sections. Because of the spectral dependence, however, we refer to these cross-sections as lineshapes. Thus, the true and experimentally averaged lineshapes are represented by the functions $\sigma_n(I;\nu)$ and $\hat{\sigma}_n(I_0;\nu)$, where I and I_0 are the local, instantaneous intensity and the peak intensity in the focused laser pulse, respectively. For simplicity, we assume that the peak intensities I_0 are independent of the frequency ν. This assumption is usually a good one, since the typical spectral range of, say, a tunable dye laser exceeds a typical Stark broadened linewidth by many orders of magnitude.

To illustrate the effects of experimental averaging on the lineshapes we use a simple model of a Stark broadened transition as shown in Figure V-1(a). Thus, in the limit of zero intensity, the true lineshape $\sigma_n(I;\nu)$ is Gaussian, with line center at $\nu = \nu_0$. As the intensity I increases, the line broadens and shifts toward lower frequencies, much like the experimental data in Figure I-2 on page 7. The true lineshapes $\sigma_n(I;\nu)$ for $I > 0$ in Figure V-1(a) are obtained by convolving a constant width Gaussian with a constant area right triangle, the apex of which is fixed at $\nu = \nu_0$, and the base of which increases linearly with intensity, as expressed in detail in Appendix C. The origin of such behavior lies in the — usually unresolved — magnetic substructure of the excitation process, that is, the lineshape is composed of a number of fine structure and hyperfine structure components, each of which undergo intensity-dependent shifts [11]. The constant Gaussian then represents the effect of inhomogeneous broadening. The resulting lineshape can be described by the continuous function $\sigma_n(I;\nu)$ with intensity-dependent line center $\nu_c(I)$, where line center is defined as the frequency at which

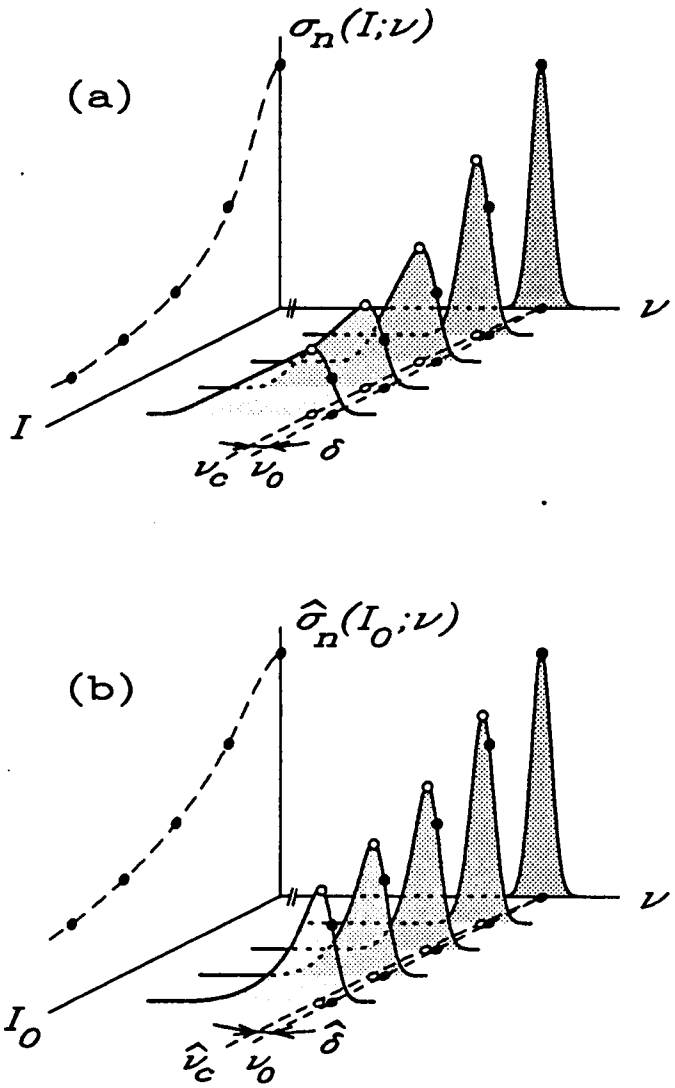


Figure V–1: *Effect of averaging on Stark broadened lineshapes.*

(a) *True intensity-dependent lineshapes calculated from Appendix C;* (b) *Experimentally averaged lineshapes, assuming nonsaturated, two-photon excitation and a composite shape parameter* $\beta = 1.5$. *Open and closed circles correspond to the intensity-dependent line centers* $\nu_c(I)$ *and* $\hat{\nu}_c(I_0)$, *and the zero-intensity line centers* ν_0, *respectively.*

the associated lineshape has a maximum. In the limit $I \to 0$ we have $\nu_c(0) = \nu_0$.

Figure V-1(b) displays the corresponding experimentally averaged lineshapes $\hat{\sigma}_n(I_0;\nu)$, obtained for a two-photon kernel with composite shape parameter $\beta = 1.5$, that is, the kernel from Eq.(II-33) on page 25 that results for the case of exponential beam- and pulse-profiles. Comparing Figures V-1(a) and V-1(b) we note that, whereas for small intensities I and I_0 the two lineshapes are identical (namely Gaussian), the functional forms become increasingly different as the intensities increase. Also, the positions of the experimental line center, which we denote by $\hat{\nu}_c(I_0)$, deviates increasingly from the true line center $\nu_c(I)$. Thus, if one desires to extract the true intensity-dependent lineshapes from experimental data such as those of Figure V-1(b), an inversion procedure is, once again, required.

As we have already indicated, inversion of the spectral lineshape can be performed by applying the inversion techniques from Sections III and IV to each frequency ν within the lineshape separately. For example, Figure V-1 shows the projections of the lineshapes $\sigma_n(I;\nu)$ and $\hat{\sigma}_n(I_0;\nu)$ at zero-intensity line center ($\nu = \nu_0$) as the solid dots in the left part of the figure. Incidentally, the cross-sections $\sigma_n(I)$ and $\hat{\sigma}_n(I_0)$ of Figure II-3 on page 28 are just these projections from Figure V-1. Thus, inversion of the lineshape is accomplished by separately inverting the projections for each frequency within the lineshape, that is, for some sufficiently large, finite number of values ν.

To accomplish this inversion, any of the methods from Sections III and IV may be used. Note that, unless the kernels depend on ν — a situation that is as unlikely as that of a significant dependence of the peak intensity I_0 on ν — the most time-consuming step in a collocation scheme has to be performed only once, namely the decomposition of the (regularized) inversion matrix. Here we address once again the moment method from Section III-2, because it provides

a convenient method for finding the true intensity-dependent line center $\nu_c(I)$, given the experimental values $\hat{\nu}_c(I_0)$. Indeed, let the latter be expanded as a power series as follows [cf. Eq.(III-11)]:

$$\hat{\nu}_c(I_0) = \nu_0 \left(1 + \hat{\delta}_1 I_0 + \hat{\delta}_2 {I_0}^2 + \ldots\right). \tag{V-1}$$

By describing the true intensity-dependent lineshapes near line center as a polynomial with intensity-dependent coefficients, it can be shown that the true intensity-dependent line center is then given by [cf. Eq.(III-12)]:

$$\nu_c(I) = \nu_0 \left(1 + \delta_1 I + \delta_2 I^2 + \ldots\right), \tag{V-2}$$

where the lowest nonvanishing coefficient δ_k follows from the corresponding experimental coefficient $\hat{\delta}_k$ by [cf. Eq.(III-13a)]:

$$\delta_k = \hat{\delta}_k \,/\, M_{k0}; \quad \text{lowest nonvanishing } k, \tag{V-3}$$

and M_{k0} is the complete kth moment of the kernel defined in Eq.(III-13b). From Eq.(V-3) small corrections to lineshift measurements can be made without actually carrying out the inversion for the entire lineshape. In Figure V-1, the factors δ and $\hat{\delta}$ are indicated schematically. As in Figure II-3(c) on page 28, there is a factor 1.84 difference between δ_1 and $\hat{\delta}_1$.

V–2 Saturated Regime

If the exciting pulse is strong enough and of sufficient duration to cause a significant depletion of the ground state, the signal no longer depends linearly on the excitation rate, as has been discussed in detail in Sections II-1.2, II-1.3, and II-2. Here we consider in particular the fast pulse limit, in which the duration of the laser pulse is short compared with the random deexcitation processes of the

excited state. From Eqs.(II-22) and (II-10b), the relation between the true lineshapes $\sigma_n(I;\nu)$ and the experimental lineshapes $\hat{\sigma}_n(I_0;\nu)$ may then be expressed as follows:

$$\hat{\sigma}_n^*(I_0;\nu) = \int_0^{I_0} K_r(I_0;I_r)\,\sigma_r^*(I_r;\nu)\,dI_r; \tag{V-4a}$$

$$\sigma_r^*(I_r;\nu) = \frac{1}{\alpha(I_r^*)^n}\Big[1-\exp\{-\alpha(I_r^*)^n\sigma_t^*(I_r;\nu)\}\Big]; \tag{V-4b}$$

$$\sigma_t^*(I_r;\nu) = \int_0^{I_r} K_t(I_r;I)\,\sigma_n^*(I;\nu)\,dI, \tag{V-4c}$$

where the frequency dependences have been indicated explicitly. In Eqs.(V-4), asterisks indicate scaling to dimensionless quantities. Thus, if we denote the maximum value of the true, intensity-dependent lineshape $\sigma_n(I;\nu)$ by $\sigma_{n\nu}^{(0)}$, and the maximum peak intensity I_0 by $I_{0,\max}$, then the scaled intensities and cross-sections are given by

$$\hat{\sigma}_n^*(I_0;\nu) = \hat{\sigma}_n(I_0;\nu)/\sigma_{n\nu}^{(0)} \le 1, \tag{V-5a}$$

$$\sigma_r^*(I_r;\nu) = \sigma_r(I_r;\nu)/\sigma_{n\nu}^{(0)} \le 1, \tag{V-5b}$$

$$\sigma_t^*(I_r;\nu) = \sigma_t(I_r;\nu)/\sigma_{n\nu}^{(0)} \dot{\le} 1, \tag{V-5c}$$

$$\sigma_n^*(I;\nu) = \sigma_n(I;\nu)/\sigma_{n\nu}^{(0)} \le 1, \tag{V-5d}$$

and

$$I_r^* = I_r/I_{0,\max} \le 1, \tag{V-5e}$$

respectively. Finally, the dimensionless parameter α in Eq.(V-4b) is defined as:

$$\alpha = (1+g_{12})\,\kappa_t\,(I_{0,\max})^n\,\sigma_{n\nu}^{(0)}. \tag{V-6}$$

Note that for the slow pulse limit from Sections II-1.3, Eqs.(V-4) – (V-6) would remain unchanged, except for a replacement of the quantity $(1+g_{12})$ in Eq.(V-6)

by the quantity $(1-\beta_{12})$, as follows from Eq.(II-13b). Note also that the constant κ_t in Eq.(V-6) is basically a measure of the duration of the laser pulse. For example, if the temporal profile of the laser pulse is Gaussian:

$$F_t(t) = \exp\left\{-\left(\frac{t-t_0}{\Delta t}\right)^2\right\}, \qquad \text{(V-7a)}$$

then, by Eqs.(II-31), (II-34), and (II-35), κ_t is given by

$$\kappa_t = (\pi/n)^{1/2}\,\Delta t, \qquad \text{(V-7b)}$$

where, as before, n is the order of the nonlinear optical process. From Eqs. (V-4b) and (V-5) it follows that for $\alpha \ll 1$ saturation effects are negligible, whereas, for $\alpha(I_r^*)^n\sigma_t^* \gtrsim 1$, strong linearities result. Thus we refer to α as the "saturation parameter."*

Figure V-2 illustrates the possible effects of saturation on experimentally averaged lineshapes. Lineshapes (a) represent the actual (true) lineshapes $\sigma_n(I;\nu)$ from Figure V-1(a) for zero and maximum intensity. Lineshapes (b) are obtained by numerically integrating lineshapes (a) using Eq.(V-4c), assuming a shape parameter $\beta = 0.5$, as would be the case for the Gaussian laser pulse from Eq.(V-7a). We refer to the resulting lineshapes (b) as the temporally averaged lineshapes.

Now we distinguish between two cases, namely one without and one with saturation. In the first case, Eq.(V-4b) yields $\sigma_r^* = \sigma_t^*$, which holds for values of the saturation parameter much less than unity. As an example of the second case, we have calculated the saturated, temporally averaged lineshapes σ_r^* from Eq.(V-4b) for a saturation parameter $\alpha = 5$. (Actually, the numerical values of α in Figures V-2 through V-6 are the values from Eq.(V-6) divided by $(\pi/2)^{1/2}$:

---

*This saturation parameter α is completely unrelated to the knot stretch parameter α from Section IV-2.

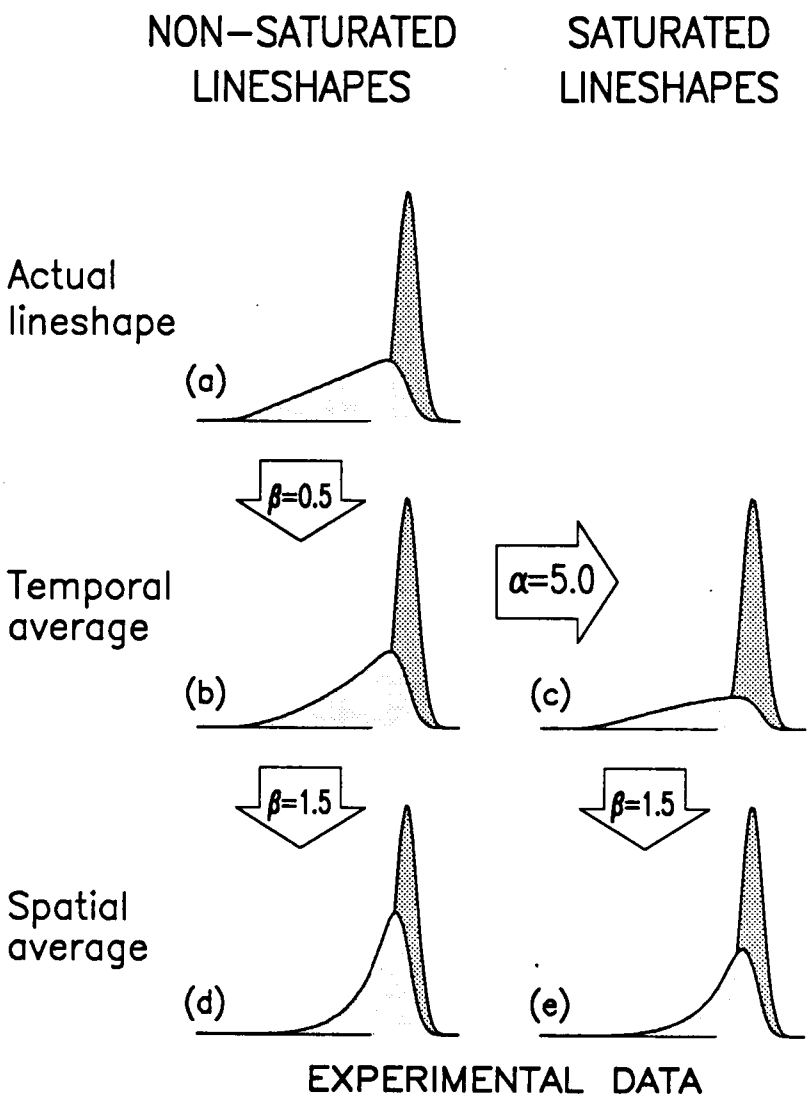


Figure V–2: *Illustration of the effects of saturation on the lineshapes.*

For each of the lineshapes (a) through (e) only the lineshapes for zero (dark) and maximum intensity (light) are shown.

at the time of generation of these figures the numerical factor from Eq.(V-7b) was not included in the definition of α.) The results are displayed as lineshapes (c) in Figure V-2. Again, only the lineshapes for zero and maximum intensity are displayed. The effects of saturation are most notable in the center of the lineshape, which yields the largest values of the product $\alpha(I_r^*)^n\sigma_t^*$. Of course, the zero-intensity lineshape does not show any saturation effects, because $I_r^* \simeq 0$.

Finally, the lower part of Figure V-2 displays the experimental lineshapes $\hat{\sigma}_n(I_o;\nu)$, which are obtained from the lineshapes (b) and (c) by spatial averaging as expressed in Eq.(V-4a), assuming a kernel as expressed in Eq.(II-33) with a shape parameter $\beta = 1.5$. Once again, only the lineshapes at zero and maximum intensity are shown. Because of the spatial averaging, the difference between the zero- and maximum-intensity lineshapes are not as profound as for the temporally averaged lineshapes (b) and (c). Also, the effects of saturation are "smoothed out," as may be noted by comparing lineshapes (b) and (c) on the one hand, and lineshapes (d) and (e) on the other.

Before addressing the inversion of the saturated lineshapes, we first look at the inversion of the nonsaturated lineshapes, or, alternatively, at what happens if one — incorrectly — *assumes* that the measured lineshapes are nonsaturated. Thus, as illustrated in Figure V-3, the actual (true) lineshape may be obtained from the experimental lineshapes by two successive inversions (namely with shape parameters $\beta = 1.5$ and $\beta = 0.5$, respectively), or by a single, combined inversion (namely one with a composite shape parameter $\beta = 1.5 + 0.5 = 2.0$). However, if the experimental lineshapes are actually saturated, this procedure necessarily results in incorrect reconstructions of the true lineshape $\sigma_n(I;\nu)$. This is illustrated in Figure V-4(a), which displays the reconstructed lineshapes (for the highest intensities only) for various values of the saturation parameter α. These recon-

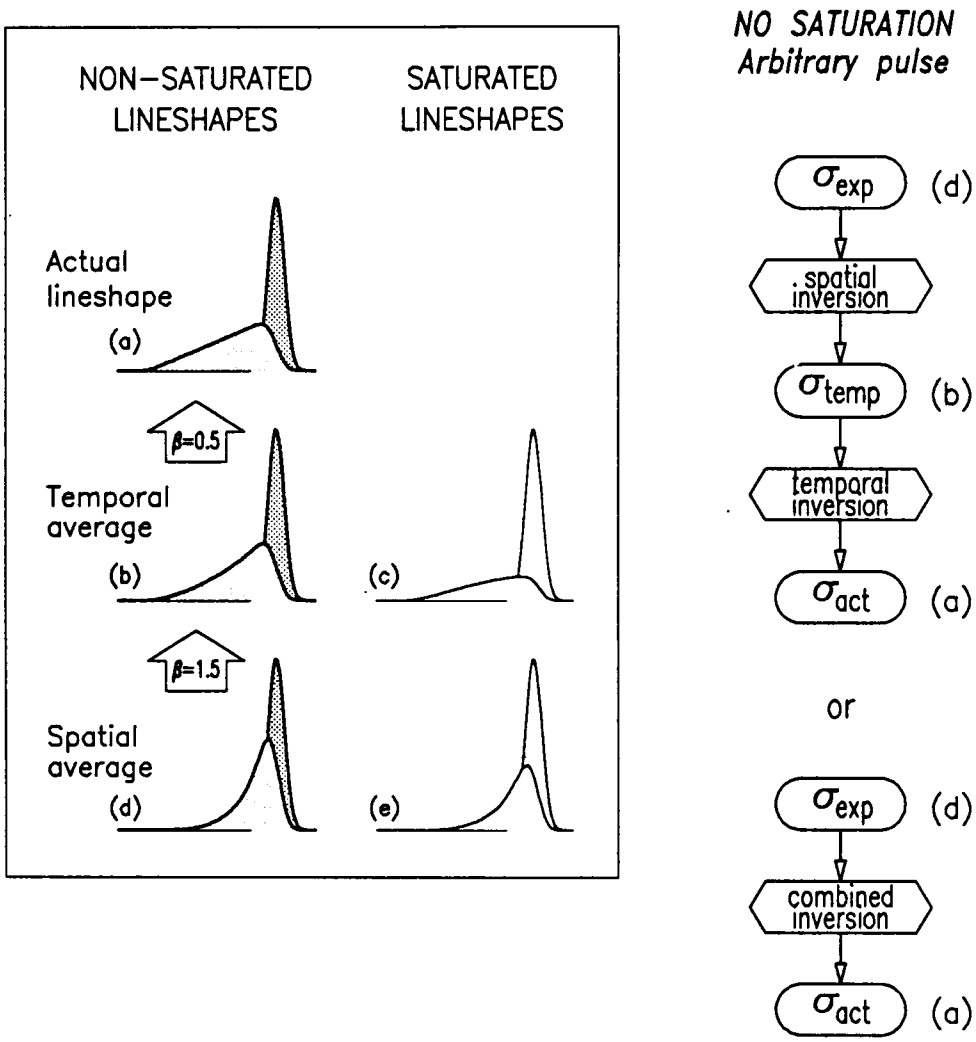


Figure V–3: *Inversion procedure for nonsaturated lineshapes.*

Lineshapes shown are the same of those from Figure V-2. The actual (true) lineshapes can be obtained from the experimentally averaged lineshapes either in two steps (top), or in a single step (bottom), as indicated in the flow diagrams.

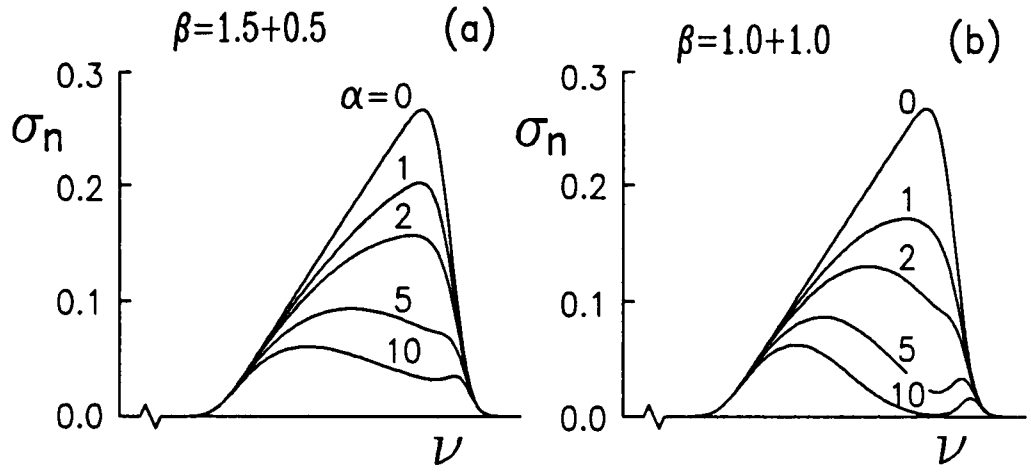


Figure V–4: *Examples of linearly inverted saturated lineshapes.*

Shown are the reconstructions of the true intensity-dependent lineshapes at maximum intensity for various values of the saturation parameter α and for two experimental conditions with the same composite shape parameter β but different spatial and temporal contributions.

structions were obtained from the saturated lineshapes by a single inversion with composite shape parameter $\beta = 2.0$. The inversion was performed using Eq.(III-6), in which the required derivatives were calculated as a finite difference of three lineshapes, namely at intensity values $I_{0,\max}$ and $(1 \pm 0.005) I_{0,\max}$. Figure V-4(a) shows that only in the case $\alpha = 0$ is the correct reconstruction obtained (compare the result for $\alpha = 0$ in Figure V-4(a) with the lineshapes (a) for the highest intensities in Figures V-2 and V-3). For nonzero values of α the reconstructed lineshapes are too small, especially in the center of the lineshapes, and the more so for large values of α.

Figure V-4(b) displays results for a situation similar to that of Figures V-

2 and V-3, except that the shape parameters associated with the spatial and temporal averages are both assumed to be unity, rather than $\beta = 1.5$ and $\beta = 0.5$, respectively. Comparison of Figure V-4(b) with Figure V-4(a) shows that, although the composite shape parameter is the same (namely $\beta = 2.0$), the effects of incorrectly assuming that the excitation process is nonsaturated lead to poorer reconstructions of the true lineshapes. This is because the process of spatial averaging is less effective in "smoothing out" the saturation effects, because of the smaller value of the spatial shape parameter β.

Having demonstrated the obvious, namely that inverting saturated lineshapes by assuming that no saturation occurs yields incorrect reconstructions of the actual (true) lineshapes, we now turn to the less obvious, namely how to invert saturated lineshapes correctly. In principle, the solution is simple. All that is required is to carry out the inversion of Eq.(V-4b) in addition to the inversions of the two Volterra integral equations from Eqs.(V-4a) and (V-4c). This is simply an algebraic operation:

$$\sigma_t^*(I_r;\nu) = \frac{1}{\alpha(I_r^*)^n} \ln\Big[\frac{1}{1-\alpha(I_r^*)^n\,\sigma_r^*(I_r;\nu)}\Big]. \qquad \text{(V–8)}$$

However, in order to apply Eq.(V-8) one must know the value of the saturation parameter α. That is, by Eq.(V-6), one must know the values of the degeneracy ratio g_{12}, the constant κ_t, the maximum peak intensity $I_{0,\max}$, and the absolute value of the n-photon cross-section $\sigma_{n\nu}^{(0)}$. Although determination of the first three of these is relatively straightforward (in order to determine κ_t one must measure the temporal profile $F_t(t)$ of the pulse), an exact determination of $\sigma_{n\nu}^{(0)}$ poses a major difficulty. Because we have used $\sigma_{n\nu}^{(0)}$ merely as a scaling parameter to bring Eqs.(V-4) into dimensionless form, other absolute measures for the cross-section would serve equally well, for example the spectrally integrated value at

vanishingly small intensity. However, few exact values of multi-photon cross-sections are available. Even if they are, they are usually known only within a factor of two (at best) [9,52]. Furthermore, in order to obtain an absolute value of α, one must also have an absolute calibration of the measurement apparatus available, as we discuss in a little more detail below [following Eq.(V-12)].

Thus, since one is generally unable to obtain a piori values for the saturation parameter α, additional information is needed. We propose that such additional information is indeed available, namely the constancy of the spectral area under the true, intensity-dependent lineshape:

$$\int \sigma_n(I;\nu)\, d\nu = \overline{\sigma_n}, \tag{V–9}$$

where the integrated value $\overline{\sigma_n}$ is independent of the intensity I, and where the limits of integration are such that the Stark broadened lineshape of interest is included, whereas any neighboring lines are excluded (this requirement may pose a complication in the case of a dense spectrum). As we have already alluded to in Section V-1, Eq.(V-9) is expected to hold if the Stark broadening of the lineshape $\sigma_n(I;\nu)$ is the result of intensity-dependent shifts of fine structure and hyperfine structure components within the lineshape which, however, do not change the respective line strengths [11]. Because of the linearity of Eq.(V-4c) and the normalization of the kernel $K_t(I_r;I)$ [see Eq.(II-21)], the spectrally integrated values of the temporally averaged lineshape are constant as well:

$$\int \sigma_t^*(I_r;\nu)\, d\nu = \overline{\sigma_n}^* = \overline{\sigma_n}/\sigma_{n\nu}^{(0)}. \tag{V–10}$$

However, because of the nonlinearity introduced by saturation effects, the same is not true for the lineshapes $\sigma_r^*(I_r;\nu)$ and $\sigma_n^*(I;\nu)$. Thus suggests itself the iterative procedure illustrated in Figure V-5: First, one performs the spatial inversion of the

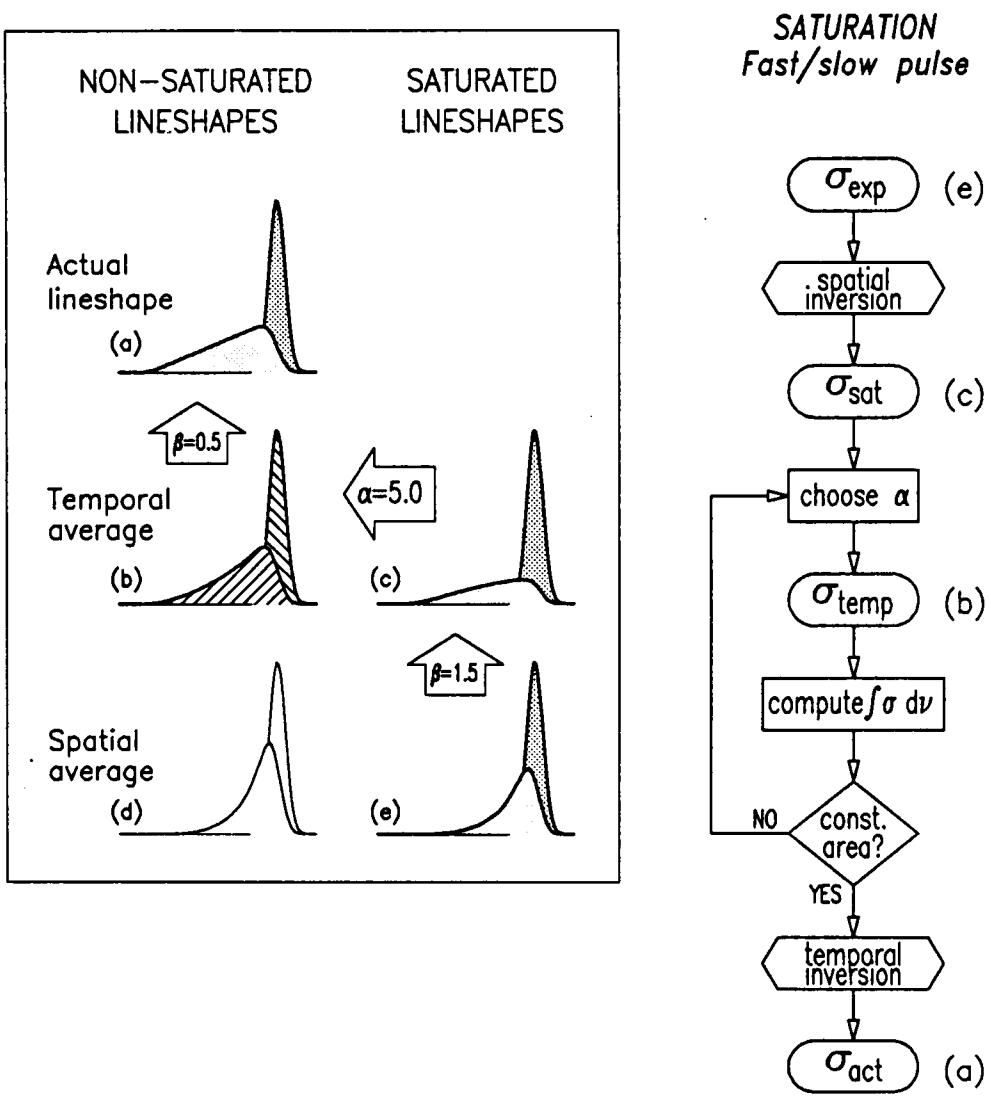


Figure V–5: *Inversion procedure for saturated lineshapes.*

Lineshapes shown are the same of those from Figures V-2 and V-3. The actual (true) lineshapes can be obtained from the experimentally averaged lineshapes by a linear integral inversion [(e)→(c)], a nonlinear algebraic inversion, [(c)→(b)], and another linear integral inversion, [(b)→(a)], as indicated in the flow diagram. However, the second step must be iterated to give constant areas for the lineshapes in (b).

experimental lineshapes (e) to yield the lineshapes (c). Then one *guesses* a value for α, and performs the algebraic inversion as expressed by Eq.(V-8), to arrive at lineshapes (b). For these, one checks if Eq.(V-10) holds. That is, one computes the spectrally integrated cross-sections for each of the intensities $I_r = 0$ through $I_r = I_{r,max} = I_0$, and decides whether or not these spectrally integrated values are independent of I_r. If they are not, one guesses new values of α and so on, until constant-area lineshapes (b) are obtained. Then, finally, one performs the temporal inversion to arrive at a reconstruction of the true intensity-dependent lineshapes, namely lineshapes (a) in Figure V-5.

Because of the simple algebraic nature of Eq.(V-8), the iterative procedure is fast and straightforward. Also, if indeed Eqs.(V-9) and (V-10) hold, the procedure should yield a unique value of α. This is illustrated in Figure V-6, which displays the average rms deviation for the lineshapes (b) from Figure V-5 as a function of the guess parameter α_{guess}, both for the saturation parameter from Figure V-5 ($\alpha = 5$, true value) and a value $\alpha = 1$. This relative deviation is defined as:

$$\overline{\sigma}^*_{rms} = \left\{ \frac{1}{I_0} \int_0^{I_0} \left[\overline{\sigma_n}^*(I_r) - \langle \overline{\sigma_n}^* \rangle \right]^2 dI_r \right\}^{1/2} \Big/ \langle \overline{\sigma_n}^* \rangle, \qquad \text{(V-11a)}$$

where

$$\langle \overline{\sigma_n}^* \rangle = \frac{1}{I_0} \int_0^{I_0} \overline{\sigma_n}^*(I_r)\, dIr, \qquad \text{(V-11b)}$$

and $\overline{\sigma_n}^*(I_r)$ is the spectrally integrated value of the cross-sections from Eq.(V-10) — which, for incorrect guesses of α, is intensity-dependent. Figure V-6 shows that the value of $\overline{\sigma}^*_{rms}$ has a single, global minimum (namely zero), for $\alpha_{guess} = \alpha$, and that the larger the saturation parameter α, the more pronounced is this minimum. For too large a guess α_{guess}, the argument within the logarithm in Eq.(V-8) becomes negative for at least some frequencies ν. Thus, the curve for $\alpha = 5$ in Figure V-6 terminates at a value $\alpha_{guess} \simeq 1.13\alpha$.

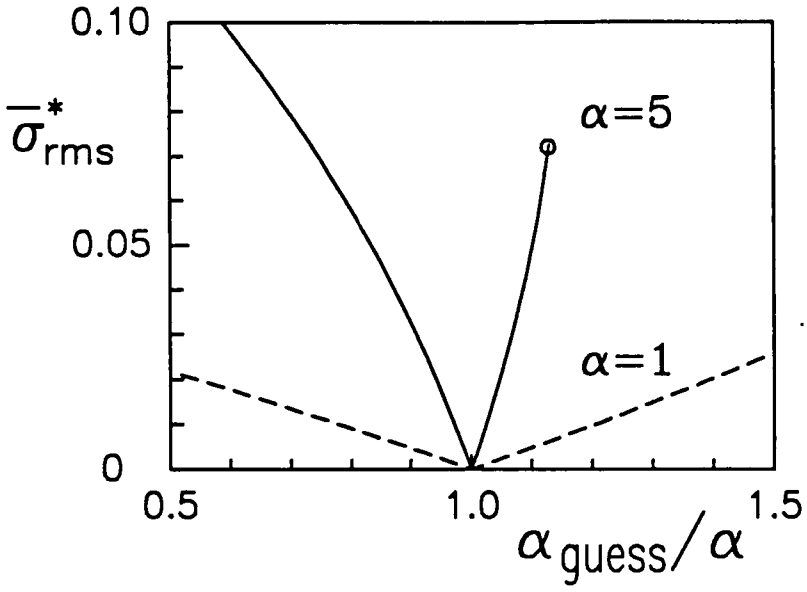


Figure V–6: *Average deviations of the spectrally integrated lineshapes.*

The relative deviations $\overline{\sigma}^*_{rms}$ are calculated from Eqs.(V-11) for several values of the saturation parameter α, and are displayed as a function of the ratio of guessed versus actual saturation parameters.

As we have argued above, the constant spectral area of the true intensity-dependent lineshape $\sigma_n(I;\nu)$ as expressed in Eq.(V-9) may be used to obtain inversion results in the case of saturated lineshapes. Note that, by this procedure, an explicit value for the saturation parameter α is found. By inspecting the definition of α in Eq.(V-6) once again, one is tempted to think that, in this manner, an absolute value of the cross-section $\sigma^{(0)}_{n\nu}$ may be obtained. However, a word of caution is in order: Eqs.(II-19) and (II-29) show that, in order to define an experimental cross-section (or lineshape) $\hat{\sigma}_n$ such that it has the same value as the true σ_n in the limit of zero intensity, one must know the calibration constants S_0 and κ_r, which require a knowledge of such quantities as the number density

of the ground states of the excitation process and the exact detection efficiency of the measuring apparatus (see Eqs.(II-16a), (II-20a), and (II-21) for a definition of κ_r). If, say, the constants S_0 and κ_r are not known exactly, a careful analysis shows that the experimental, absolute value of the saturation parameter α is not given by Eq.(V-6), but rather by

$$\alpha = (1 + g_{12})\, \kappa_t\, (I_{0,\max})^n\, \sigma_{n\nu}^{(0)}\, \frac{(S_0\kappa_r)_{\text{guess}}}{S_0\kappa_r}, \qquad \text{(V-12)}$$

where $S_0\kappa_r$ and $(S_0\kappa_r)_{\text{guess}}$ are the actual and guessed values of the calibration constants. Thus, measurement of α allows an absolute calculation of $\sigma_{n\nu}^{(0)}$ only if an absolute calibration of the apparatus is available. But in this case, absolute values of the cross-sections may also be calculated from data in the linear, nonsaturated regime. However, in the absence of absolute calibrations, the iterative inversion procedure described here appears to be the most straightforward, indeed, the only possible procedure for the inversion of spatially and temporally averaged lineshapes to date.

VI DISCUSSION

In Sections I through V we have formulated the extraction of the true intensity-dependence of some nonlinear optical process from spatially and/or temporally averaged data as an inversion problem, and we have presented a number of analytical and numerical methods by which the inversion can be accomplished. A discussion of the numerical techniques is given at the end of Section IV and will not be repeated here. For the case of saturated lineshapes, we have shown how the requirement of constant spectral area of the true intensity-dependent lineshape can be used to obtain inversion results even if the value of the saturation parameter is not *a priori* known.

We suggest that a possible experiment to apply and verify the theory from the previous sections would be to perform accurate measurements of the Stark broadened lineshapes associated with two-photon excitation of rotational lines in the $\gamma(0,0)$-band of nitric oxide, as shown in Figure I-2 on page 7. It should be recalled that the data from Figure I-2 were obtained during a preliminary investigation of two-photon LIF as a diagnostic tool, that is, before the formulation of the theory in Sections II through V. As a result, the spatial and temporal profiles of the exciting laser pulses were not measured, so that the kernels required for inversion can not be calculated. Furthermore, in attempting to invert the data from Figure I-2 by *assuming* exponential beam- and pulse-profiles with various shape parameters, we experienced several more complications. Firstly, in the region of significant Stark broadening, not enough peak intensities (pulse energies) were represented in the data set. Secondly, no stringent frequency calibration was performed. Thus, large errors resulted in taking the projections of the lineshapes at individual frequencies (note that, in Figure V-1 on page 69, large error bars on

the projections in the left part of the figure would result if the spectral positions of the lineshapes were uncertain). Finally, the lineshapes in Figure I-2 on page 7 are extremely saturated. This is most evident from Figure I-3 on page 10, which displays the spectrally integrated signals from Figure I-2. In this regard we recall the discussion immediately prior to Eq.(V-10) on page 79 stating, in essence, that if the averaging process is linear, the spectral areas of the lineshapes are not affected by the averaging process. Consequently, because the spectral areas in Figure I-3 on page 10 become intensity-dependent for large intensities, the averaging process must not have been linear, that is, saturated. Indeed, extreme saturation must have occurred because, despite the "smoothing" effect of the spatial averaging process, the spectral areas for the highest pulse energy in Figure I-3 (3.4 mJ) are only about two percent of the values expected from the extrapolation from small pulse energies. By contrast, even for a saturation parameter $\alpha = 5$, the spectral area of the lineshape at maximum intensity in Figure V-2 on page 74 [lineshapes (e)] is still 75 percent of that of the zero intensity lineshape.

Apart from the intensity-dependence of the spectral areas in Figure I-3 on page 10, the qualitative behavior of the lineshapes in Figure I-2 on page 7 also hints directly at the occurrence of saturation effects, namely by the relative positions of the "shoulders" on the low wavelength sides of the lineshapes of both the $O_{12}(5\frac{1}{2})$ and $O_{12}(6\frac{1}{2})$ lines: With increasing pulse energies, the shoulders move closer and closer toward the peaks of the lineshapes. Irrespective of the origin of the shoulders, this behavior is indeed expected in the case of saturation, because the largest values of the projections of the cross-sections, that is, the values near the peaks of the lineshapes, yield the largest values of the product $\alpha\left(I_r^*\right)^n\sigma_r^*$ [see Eq.(V-4b)], so that they experience the strongest saturation effects.

In a dedicated effort, none of the above complications should be insurmount-

able: beam- and pulse-profiles can be measured, a sufficiently large number of data can be taken, and a precise frequency calibration can be performed. Moreover, one would not necessarily have to probe quite so deep into the saturation regime — nor would one have to refrain from doing so, if sufficiently accurate data were taken [the larger the saturation parameter, the larger will be the amplification of random error when taking the logarithm in Eq.(V-8)]. In this type of effort, the goal would not be to show that, using inversion techniques, the same lineshapes and cross-sections can be obtained as those measured in experiments with little or no averaging, because such data (true, nonsaturated lineshapes at high intensities) are simply not available. Rather, the goal would be to show that the theory of inversion from Sections II through V is internally consistent. This might be shown in several ways.

Firstly, having performed measurements with some experimental configuration, and having calculated the corresponding inversion results, one might change the focusing optics or change, if possible, the pulse duration, and repeat the measurements and corresponding inversions. Even though, as a result of different experimental geometries, different intensity-dependent lineshapes would be obtained, the reconstructed lineshapes should be identical.

A second consistency check would be to perform a series of measurements of intensity-dependent lineshapes for several molecular lines within the same vibrational band system. If lines are chosen with cross-sections that differ by a factor two or more, one line might show substantial saturation effects whereas, for the same experimental conditions, another would not. In this case, the true intensity-dependent lineshapes are not expected to be the same for each line. However, it is expected that the true, spectrally integrated cross-sections will vary exactly as the respective Hönl-London factors of the lines (see Appendix A).

A third, most interesting, but not so simple check would be to perform measurements in both the fast and slow pulse limits of the saturation regime. In this case, the goal would be to show that the saturation parameters, obtained from the experimentally averaged lineshapes, differ, essentially, by a factor determined by the degeneracy ratio and branching ratio, namely by $(1 + g_{12})/(1 - \beta_{12})$, as follows from Sections II-1.2, II-1.3, and V-2 (essentially, that is, if all other factors contributing to the saturation parameter are equal). One way to probe both the fast and slow pulse limits would be to use, say, both nanosecond and picosecond pulses. Alternatively, one might use nanosecond pulses only and, in order to move from the fast pulse limit to the slow pulse limit, mix the low pressure gas of interest with a high pressure buffer gas, thereby decreasing the excited state lifetime of the gas of interest by several orders of magnitude (thus rendering the laser pulse slow compared to the random deexcitation processes of the excited state). In both approaches, the difficulty would arise that frequency resolution would be strongly limited, either because of the wide spectral bandwidth of a picosecond pulse, or because of the large homogeneous linewidth associated with a strongly collisionally quenched transition. Thus, in order to realize a quantitative comparison between fast pulse and slow pulse results, one might have to work with an atomic rather than a molecular system, so as to keep the density of lines small. However, a successful quantitative comparison of these two limits, which correspond to quite different physical conditions, would constitute an impressive confirmation of the theory.

After the succesful demonstration of the consistency and validity of the various methods for the inversion of temporally and spatially averaged data, one should be able to apply the techniques in various diagnostic applications, for example in two-photon LIF. Particularly, in experiments such as described in

Refs.[8–11], and in Section I of this dissertation, one should be able to maintain a precise calibration of the measuring apparatus even when working with such high intensities that nonlinear effects become manifest, such as Stark broadening and saturation effects of molecular transitions.

Perhaps the greatest tribute to this work would be if, some day, researchers in nonlinear optics would seek to use these and similar methods to present their data in experiment-independent form. That is, if they would seek to present data describing the true intensity-dependence of nonlinear optical processes, rather than data that are particular to the individual experimental configurations. Whether such will be the case, only the future can tell.

LIST OF REFERENCES

[1] J. H. Eberly and J. Krasinski, "Atomic multi-photon processes," in *Advances in multi-photon processes and spectroscopy*, S. H. Lin ed. (Academic, Orlando, 1984), pp. 1–49.

[2] R. R. Birge, "One-photon and two-photon excitation spectroscopy,"in *Quantum Electronics — Principles and Applications*, D. S. Kliger, ed. (Academic, New York, 1983), pp. 109–173.

[3] A. C. Eckbreth, "Recent advances in laser diagnostics for temperature and species concentration in combustion," Eighteenth Symposium on Combustion, Waterloo, Canada, Aug 1980, pp. 1471–1488.

[4] N. Bloembergen, *Nonlinear Optics* (Benjamin, New York, 1965).

[5] V. S. Letokhov and V. P. Chebotayev, *Nonlinear Laser Spectroscopy* (Springer, Berlin, 1977).

[6] Y. R. Shen, *The Principles of Nonlinear Optics* (Wiley, New York, 1984).

[7] M. D. Levenson and S. S. Kano, *Introduction to Nonlinear Laser Spectroscopy*, revised ed. (Academic, Boston, 1988).

[8] R. L. McKenzie and K. P. Gross, "Two-photon excitation of nitric oxide fluorescence as a temperature indicator in unsteady gasdynamic processes," Appl. Opt. **20**, 2153–2165 (1981).

[9] K. P. Gross and R. L. McKenzie, "The two-photon absorptivity of rotational transitions in the $A^2\Sigma^+(v'=0)-X^2\Pi(v''=0)$ gamma band of nitric oxide," J. Chem. Phys. **76**, 5260–5266 (1982).

[10] K. P. Gross and R. L. McKenzie, "Single pulse gas thermometry at low temperatures using two-photon laser-induced fluorescence in $NO-N_2$ mixtures," Opt. Lett. **8**, 368–370 (1983).

[11] W. M. Huo, K. P. Gross, and R. L. McKenzie, "Optical Stark effect in the two-photon spectrum of NO," Phys. Rev. Lett. **54**, 1012–1015 (1985).

[12] L. Branst, "News: laser diagnostics to aid space shuttle flight," in *Lasers & Applications*, August 1985, pp. 20–22.

[13] J. A. Gelbwachs, P. F. Jones, and J. E. Wessel, "Doppler-free two-photon electronic absorption of nitric oxide and benzene," Appl. Phys. Lett. **27**, 551–552 (1975).

[14] R. Wallenstein and H. Zacharias, "Λ-type doubling and spin-rotation splitting of NO, measured in simultaneous one- and two-photon laser spectroscopy," Opt. Comm. **25**, 363–367 (1978).

[15] A. Timmerman and R. Wallenstein, "Doppler-free two-photon excitation of nitric oxide with frequency stabilized cw dye laser radiation," Opt. Comm. **39**, 239–242 (1981).

[16] M. Göppert-Mayer, Ann. Phys. **9**, 273–285 (1933).

[17] R. G. Bray and R. M. Hochstrasser, "Two-photon absorption by rotating diatomic molecules," Mol. Phys. **31**, 1199–1211 (1976).

[18] T. Ozaki, Y. Matsui, and T. Oshawa, "Rotational temperature measurement of NO gas using two-photon excitation spectrum," J. Appl. Phys. **52**, 2593–2595 (1981).

[19] T. Ozaki, H. Yuize, and T. Oshawa, "Observation of higher lines of NO $\gamma(0,0)$ band O_{12} branch using two-photon excitation," J. Opt. Soc. Am. **73**, 345–348 (1983).

[20] W. M. Ruyten, "An experimental study of two-photon laser induced fluorescence in nitric oxide," Internal report, Center for Laser Applications, University of Tennessee Space Institute, Tullahoma, Tennessee, May 1987.

[21] J. B. Halpern, H. Zacharias and R. Wallenstein, "Rotational line strengths in two- and three-photon transitions in diatomic molecules," J. Mol. Spectr. **79**, 1–30 (1980).

[22] J. O. Hornkohl and W. M. Ruyten, "Notes: corrections to two-photon Hönl-London factors," J. Mol. Spectr. **123**, 499–500 (1987).

[23] G. Mainfray and C. Manus, in *Multi-Photon Ionization of Atoms*, S. L. Lin and P. Lambropoulos eds. (Academic, New York, 1984), pp. 7–34; Y. Gontier and M. Trahin, *ibid.*, pp. 35–64.

[24] P. Lambropoulos and X. Tang, "Multiple excitation and ionization of atoms by strong lasers," J. Opt. Soc. Am. B **4**, 821–832 (1987).

[25] Y. Gontier and M. Trahin, "Spatio-temporal effects in resonant multiphoton ionisation of the caesium atom," J. Phys. B **13**, 259–272 (1980).

[26] C. D'Ambrosio, W. Fuss, K. L. Kompa, and W. E. Schmid, "Multiphoton dissociation in a focused Gaussian beam," J. Opt. Soc. Am. B **5**, 1540–1544 (1988).

[27] M. R. Sogard, "Nonresonant multiphoton-ionization yields from Gaussian laser beams," J. Opt. Soc. Am. A **5**, 1890–1899 (1988).

[28] E. Suzuki, S. Kato, and K. Takeuchi, "Accurate extraction of reaction probabilities in IR multiphoton dissociation by a focused Gaussian beam: an

improved analytical method," Appl. Opt. **27** 4445–4449 (1988).

[29] W. M. Ruyten and J. W. L. Lewis, "Recovery of excitation intensity dependence in pulsed, focused beams: nonsaturated case," J. Opt. Soc. Am. B **5**, 2368–2373 (1988). Some errors appear on page 2371: "collection approach" (bottom left) should be "collocation approach," $F^h(I_{0i};\mathbf{x})$ in Eq.(4.14) should be $F^n(I_{0i};\mathbf{x})$, and Eq.(4.15) should be as Eq.(III-29) on page 40 of this dissertation.

[30] For partial result, see: P. M. Morse and H. Feshbach, *Methods of Theoretical Physics I* (McGraw-Hill, New York, 1953), p. 475, problem 4.28.

[31] L. M. Delves and J. Walsh, eds., *Numerical Solution of Integral Equations* (Clarendon, Oxford, 1974).

[32] C. T. H. Baker, *The Numerical Treatment of Integral Equations* (Clarendon, Oxford, 1977).

[33] G. Hämmerlin and K.-H. Hoffmann, eds., *Constructive Methods for the Practical Treatment of Integral Equations*, Vol. 73 of International Series of Numerical Mathematics (Birkhäuser, Basel, 1985).

[34] G. R. Arfken, *Mathematical Methods for Physicists* 2nd ed. (Academic, New York, 1970), Secs. 16.1 and 16.2.

[35] P. Kolodner, H. S. Kwok, J. G. Black, and E. Yablonovitch, "Exact decomposition of a Gaussian-averaged nonlinear function," Opt. Lett. **4**, 38–39 (1979).

[36] R. R. Nigmatullin and M. Kh. Salakhov, "Regularized algorithm for solving the generalized Abel's equation using fractional derivatives," Opt. Spectr. **63**, 536–538 (1987) [Opt. Spektr. **63**, 907–910 (1987)].

[37] H. Brunner and P. J. van der Houwen, *The Numerical Solution of Volterra Equations* (North-Holland, Amsterdam, 1986), p. 401.

[38] W. H. Press, B. P. Flannery, S. A. Teukolsky, and W. T. Vetterling, *Numerical Recipes: The Art of Scientific Computing* (Cambridge, Cambridge, 1986), Chs. 10 and 14.

[39] A. N. Tikhonov and V. Y. Arsenin, *Solution of Ill-Posed Problems* (Winston, Washington, D.C., 1977).

[40] M. C. Jones and C. H. Travis, "Bidiagonalization for linear inverse problems," J. Opt. Soc. Am. A **5**, 660–665 (1988).

[41] S. Twomey, *Developments in Geomathematics 3—Introduction to the Mathematics of Inversion in Remote Sensing and Indirect Measurements*, (Elsevier, Amsterdam, 1977), p. 169.

[42] R. L. Henning, C. D. Capps, and G. M. Hess, *Inversion Technique Evaluation*, U.S. Army Chem. Sc. Lab. Rep. ARCSL-CR-82047, (Defense Technical Information Center, Alexandria, Va., 1982).

[43] J. J. Monaghan, "Extrapolating B splines for interpolation," J. Comp. Phys. **60**, 253–262 (1985).

[44] N. Morishima, "Spectral estimation through cubic-spline approximation of a discrete time series," J. Comp. Phys. **56**, 93–110 (1984).

[45] U. Ascher, "Solving boundary-value problems with a spline-collocation code," J. Comp. Phys. **34**, 401–413 (1980).

[46] P. Dierckx, "An algorithm for experimental data deconvolution using spline functions," J. Comp. Phys. **52**, 163–186 (1983).

[47] W. M. Ruyten, "Inversion of spatio-temporally averaged data using a regularized spline collocation scheme," J. Opt. Soc. Am. A., submitted for publication.

[48] C. de Boor, *A Practical Guide to Splines* (Springer, New York, 1978).

[49] J. J. Dongarra, J. R. Bunch, C. B. Moler, and G. W. Stewart, *LINPACK Users' Guide* (SIAM, Philadelphia, 1979), Ch. 5.

[50] R. C. Allen, W. R. Boland, and G. M. Wing, "Numerical experiments involving Galerkin and collocation methods for linear integral equations of the first kind," J. Comp. Phys. **49**, 465–477 (1983).

[51] G. M. Wing, "Condition numbers of matrices arising from the numerical solution of linear integral equations of the first kind," J. Integr. Eqs. **9** (Suppl.), 191–204 (1985).

[52] C. H. Chen, M. P. McCann, and M. G. Payne, "Absolute rate measurements of two-photon process of gases, liquids, and solids," in *Advances in Laser Science-III*, A. C. Tam, J. L. Gole, and W. C. Stwalley, eds. (American Institute of Physics, New York, 1988), pp. 130–132.

[53] E. U. Condon and G. H. Shortley, *The Theory of Atomic Spectra* (University Press, Cambridge, 1963), Table 4^3.

[54] G. Herzberg, *Molecular Spectra and Molecular Structure I, Spectra of Diatomic Molecules* (Van Nostrand, New York, 1950).

APPENDICES

Appendix A: Two-Photon Hönl-London Factors

For the case of diatomic molecules, Halpern *et al.* have derived two- and three-photon Hönl-London factors for transitions between electronic states [21]. While working on two-photon excitation of nitric oxide, some inconsistencies in expressions in Ref.[21] were found, such as violations of sum rules. These inconsistencies were traced back to incorrect expressions in Tables IV and VI from Ref.[21]. Corrected expressions, obtained with Clebsch-Gordon coefficients from Ref.[53], have since been published [22]. Because the expressions from Refs.[21] and [22] are rather cumbersome, we give here simplified expressions that hold for $\Sigma \leftarrow \Pi$ transitions ($\Lambda'' = 1$; $\Delta\Lambda = -1$) in diatomic molecules with coupling intermediate between Hund's cases "a" and "b," such as NO and OH. Thus, let the rotational constants of the ground state be denoted by B'' and D'', the spin-angular momentum coupling constant by A, and the spin-rotation coupling constant by γ'' (for a general background see Ref.[54]). Then, from Refs.[21] and [22], the two-photon Hönl-London factors can be expressed as [20]:

$$S^{(2)}_{J''J'} = \frac{f_1}{240} \times \begin{cases} (F^+ f_2 + F_- f_3)^2; & 11 \text{ branch;} \\ (F^- f_2 - F_+ f_3)^2; & 12 \text{ branch;} \\ (F^+ f_2 - F_- f_3)^2; & 21 \text{ branch;} \\ (F^- f_2 + F_+ f_3)^2; & 22 \text{ branch,} \end{cases} \tag{A-1}$$

where, in terms of the rotational ground state quantum number J'':

$$F_\pm = \left(1 \pm UZ\right)^{1/2}, \tag{A-2}$$

$$UZ = \left[1 + X\left\{\frac{2B'' - 4D''X - \gamma''}{2B'' - 4D''X - A}\right\}^2\right]^{-1/2}, \tag{A-3}$$

$$X = \left(J'' + \frac{1}{2}\right)^2 - 1, \tag{A-4}$$

and the factors f_1, f_2, and f_3 are given in Table A-1, for O-, P-, Q-, R-, and S-branches separately. For the nomenclature determining the subscripts 11, 12, 21, and 22 see Ref.[54].

Table A-1: Factors from Eq.(A-1).

Branch	f_1	f_2	f_3
O	$\frac{J''-3/2}{J''(J''-1)}$	$\sqrt{J''-\frac{1}{2}}$	$\sqrt{J''+\frac{3}{2}}$
P	$\frac{1}{J''(J''-1)(J''+1)}$	$J''\sqrt{J''-\frac{1}{2}}$	$(J''-2)\sqrt{J''+\frac{3}{2}}$
Q	$\frac{6}{J''(J''+1)}$	0	1
R	$\frac{1}{J''(J''+1)(J''+2)}$	$(J''+1)\sqrt{J''+\frac{3}{2}}$	$(J''+3)\sqrt{J''-\frac{1}{2}}$
S	$\frac{J''+5/2}{(J''+1)(J''+2)}$	$\sqrt{J''+\frac{3}{2}}$	$\sqrt{J''-\frac{1}{2}}$

Appendix B: Exponential Profiles

Appendix B deals with some of the mathematics associated with the exponential beam- and pulse-profiles introduced in Section II-3. In Section B-1 we derive the kernels and its moments, and in Sections B-2 and B-3 we derive some of the inversion results particular to these kernels, especially that of Abel inversion.

B-1 Kernels and moments

Given the general composite profile $F_{\mathbf{x}}(\mathbf{x})$ from Eq.(II-31), the first step toward calculating the associated kernel is to calculate the "volume" $V(I_0;I)$ from Eq.(II-27). With $P(\mathbf{x}) = p$, this "volume" is p times the conventional volume enclosed by the surface

$$\left|\frac{x_1}{a_1^{\pm}}\right|^{\mu_1} + \ \ldots\ + \left|\frac{x_{n_{\mathbf{x}}}}{a_{n_{\mathbf{x}}}^{\pm}}\right|^{\mu_{n_{\mathbf{x}}}} = \ln\frac{I_0}{I}, \tag{B-1a}$$

or

$$\left|\frac{x_1}{\left(\ln\frac{I_0}{I}\right)^{1/\mu_1} a_1^{\pm}}\right|^{\mu_1} + \ \ldots\ + \left|\frac{x_{n_{\mathbf{x}}}}{\left(\ln\frac{I_0}{I}\right)^{1/\mu_{n_{\mathbf{x}}}} a_{n_{\mathbf{x}}}^{\pm}}\right|^{\mu_{n_{\mathbf{x}}}} = 1. \tag{B-1b}$$

Comparison of Eq.(B-1b) with Problem 4.28 in Ref. [30] and substitution of β from Eq.(II-34) then yields for each "octant" the "volume":

$$V_{\text{oct}}(I_0;I) = \frac{p}{\Gamma(1+\beta)} \cdot \left\{\ln\frac{I_0}{I}\right\}^{\beta} \cdot \prod_{i=1}^{n_{\mathbf{x}}} \left\{\frac{\Gamma(1/\mu_i)}{\mu_i}\, a_i^{\pm}\right\}. \tag{B-2}$$

Using $\frac{1}{\mu_i}\Gamma\left(\frac{1}{\mu_i}\right) = \Gamma\left(1+\frac{1}{\mu_i}\right)$, summing over all "octants," and substituting the definition of κ from Eq.(II-35) then yields for the total "volume":

$$V(I_0;I) = \frac{\kappa}{\beta}\,\frac{n^{\beta}}{\Gamma(\beta)} \left\{\ln\frac{I_0}{I}\right\}^{\beta}, \tag{B-3}$$

where we have also used $\Gamma(1+\beta) = \beta\,\Gamma(\beta)$. Application of Eq.(II-26) now leads immediately to the desired expression for the kernel from Eq.(II-33). It remains

to be shown that the normalization condition expressed in Eq.(II-25) is satisfied, that is, that the definition of κ in Eq.(II-35) is indeed the correct one. To show this we compute the kth moments of the kernels from Eq.(II-33). Using the definition in Eq.(II-36) we find

$$M_{k0} = \frac{n^\beta}{\Gamma(\beta)} \int_0^{I_0} \left(\frac{I}{I_0}\right)^{n+k-1} \left\{\ln\frac{I_0}{I}\right\}^{\beta-1} d\left(\frac{I}{I_0}\right)$$

$$= \left(\frac{n}{n+k}\right)^\beta \frac{1}{\Gamma(\beta)} \int_0^\infty x^{\beta-1} \mathrm{e}^{-x}\, dx = \left(\frac{n}{n+k}\right)^\beta. \qquad \text{(B–4)}$$

The last two steps follow with the substitution $x = (n+k)\ln(I_0/I)$, and with the definition of the gamma function, respectively. Thus, we have proved both the normalization of the kernel ($M_{00} = 1$) and the expression for its complete moments, namely Eq.(II-36). The expressions for the incomplete moments from Eqs.(II-37) are found with the same substitution. For example, for $\beta = 3/2$, Eqs.(II-33), (II-36), and (II-37a) yield $[1/\Gamma(3/2) = 2/\pi^{1/2}]$:

$$M_k(I_0; I_j) = M_{k0}\,(2/\pi^{1/2}) \int_0^{q^2} x^{1/2}\, \mathrm{e}^{-x}\, dx, \qquad \text{(B–5)}$$

with q as defined in Eq.(II-37b). Upon substitution of $y = x^{1/2}$, the expression for $M(\frac{3}{2}; p; q)$ in Eq.(II-37d) is then easily obtained.

An alternative way to derive the kernel from Eq.(II-33) is to note that, for a single coordinate x, the profile

$$\frac{I}{I_0} = F(x) = \exp\left[-\left(\frac{x}{a}\right)^\mu\right] \qquad \text{(B–6a)}$$

leads, with Eq.(II-26), to

$$K(I_0; I) = -\frac{1}{\kappa}\left(\frac{I}{I_0}\right)^n \frac{d}{d(I/I_0)} F^{-1}\left(\frac{I}{I_0}\right) \frac{1}{I_0}$$

$$= \frac{a}{\mu\kappa} \frac{I^{n-1}}{I_0^n} \left\{\ln\frac{I_0}{I}\right\}^{\frac{1}{\mu}-1}. \qquad \text{(B–6b)}$$

Upon normalization, the kernel from Eq.(II-33) is obtained, with shape parameter $\beta = 1/\mu$. To show that, for an arbitrary number of coordinates, the kernel is still given by Eq.(II-33) with, however, a composite shape parameter β as defined in Eq.(II-34), we use the expression for the convolution of two kernels from Eq.(II-24). Thus, let the two kernels be given by

$$K_i(I_0;I) = \frac{n^{\beta_i}}{\Gamma(\beta_i)} \frac{I^{n-1}}{{I_0}^n} \left\{\ln \frac{I_0}{I}\right\}^{\beta_i - 1}; \quad i = \mathbf{r}, t. \tag{B-7}$$

With Eq.(II-24) this gives for the composite kernel:

$$K(I_0;I) = \frac{n^{\beta_\mathbf{r}+\beta_i}}{\Gamma(\beta_\mathbf{r})\Gamma(\beta_i)} \frac{I^{n-1}}{{I_0}^n} \int_I^{I_0} \left\{\ln \frac{I_0}{I_\mathbf{r}}\right\}^{\beta_\mathbf{r}-1} \left\{\ln \frac{I_\mathbf{r}}{I}\right\}^{\beta_t - 1} \frac{dI_\mathbf{r}}{I_\mathbf{r}}. \tag{B-8a}$$

With the substitution $x = \ln(I_\mathbf{r}/I)/\ln(I_0/I)$, the integral in Eq.(B-8a) becomes:

$$\int_I^{I_0} \ldots \frac{dI_\mathbf{r}}{I_\mathbf{r}} = \left\{\frac{I_0}{I}\right\}^{\beta_\mathbf{r}+\beta_t-1} \int_0^1 (1-x)^{\beta_\mathbf{r}} x^{\beta_t}\, dx. \tag{B-8b}$$

Finally, the last integral in Eq.(B-8b) is just the definition of the beta function, which, in turn, can be expressed in terms of gamma functions:

$$\int_0^1 (1-x)^{\beta_\mathbf{r}} x^{\beta_t}\, dx = B(\beta_\mathbf{r};\beta_t) = \frac{\Gamma(\beta_\mathbf{r})\Gamma(\beta_t)}{\Gamma(\beta_\mathbf{r}+\beta_t)}. \tag{B-8c}$$

Combining Eqs.(B-8a), (B-8b), and (B-8c) we find that the composite kernel is again given by Eq.(B-7) [or Eq.(II-33)] with a shape parameter $\beta = \beta_\mathbf{r} + \beta_t$, which is what we set out to prove. Thus, by iteration, Eq.(B-6b) can be shown to hold for arbitrary numbers of coordinates with exponential profiles.

B-2 Abel inversion

Eq.(III-3) in Section III-1 is basically the standard Abel equation, except for the numerical factor $n^\beta/\Gamma(\beta)$ and the lower integral bound $-\infty$ rather than zero

[34]. To generalize the standard inversion result to values $\beta > 1$, we differentiate Eq.(III-3) k times, with k (and β') as defined in Eq.(III-4c). This yields:

$$\left(d/d\omega_0\right)^k \hat{\mathcal{R}}_n(\omega_0) = \frac{n^\beta}{\Gamma(\beta')} \int_{-\infty}^{\omega_0} (\omega_0 - \omega)^{\beta'-1}\, \mathcal{R}_n(\omega)\, d\omega, \tag{B-9}$$

where we have used

$$\begin{aligned} \Gamma(\beta) &= \Gamma(1+\beta-1) = (\beta-1)\Gamma(\beta-1) = \ \ldots \\ &= (\beta-1)(\beta-2)\cdots(\beta-k)\Gamma(\beta'). \end{aligned} \tag{B-10}$$

Thus, for $\beta > 1$, the standard inversion result from Eq.(III-4a) is changed to Eq.(III-4b) by replacing $\Gamma(\beta)$ by $\Gamma(\beta')$, and replacing $\hat{\mathcal{R}}_n(\omega_0)$ by its kth derivative. Note also that the numerical factor in the Abel equation may be written in different ways, by using the identity [34]:

$$\frac{\sin\pi\beta'}{\pi} = \frac{1}{\Gamma(\beta')\Gamma(1-\beta')}. \tag{B-11}$$

Transforming Eq.(III-4b) back with the aid of Eq.(III-2) yields the inversion result

$$R_n(I) = \frac{1}{n^\beta \Gamma(1-\beta')} \left(I\frac{d}{dI}\right) \int_0^I \left\{\ln\frac{I}{I_0}\right\}^{-\beta'} \left(I_0\frac{d}{dI_0}\right)^k \hat{R}_n(I_0)\, \frac{dI_0}{I_0}. \tag{B-12}$$

To show that $(k-1)$ factors $I_0(d/dI_0)$ can be brought outside the integral, replacing I_0 by I, we substitute $f = I_0/I$ in the integrand:

$$\int_0^I \ \ldots\ \frac{dI_0}{I_0} = \int_0^1 \left\{\ln\frac{1}{f}\right\}^{-\beta'} \left(f\frac{d}{df}\right)^k \hat{R}_n(fI)\, \frac{df}{f}, \tag{B-13}$$

and note that

$$\left(f\frac{d}{df}\right)^k \hat{R}_n(fI) = \left(I\frac{d}{dI}\right)^{k-1} \left(f\frac{d}{df}\right) \hat{R}_n(fI). \tag{B-14}$$

Bringing the $(k-1)$ factors $I(d/dI)$ outside the integral, and returning to I_0 as the variable of integration then leads to Eq.(III-5).

B-3 Integer shape parameters

If β is an integer, Eq.(III-6) may be proved directly from the definition of the kernel in Eq.(II-33), rather than via the Abel inversion from Eq.(III-5). Indeed, substituting Eq.(II-33) into Eq.(III-1) and replacing the cross-sections by excitation rates yields:

$$\hat{R}_n(I_0) = \frac{n^\beta}{(\beta-1)!} \int_0^{I_0} \left\{ \ln \frac{I_0}{I} \right\}^{\beta-1} R_n(I) \, \frac{dI}{I}, \tag{B-15}$$

where we have used $\Gamma(\beta) = (\beta-1)!$, by virtue of the fact that β is integer. Differentiating Eq.(B-15) once gives

$$\left(\frac{I_0}{n} \frac{d}{dI_0} \right) \hat{R}_n(I_0) = \frac{n^{\beta-1}}{(\beta-2)!} \int_0^{I_0} \left\{ \ln \frac{I_0}{I} \right\}^{\beta-2} R_n(I) \, \frac{dI}{I}. \tag{B-16}$$

Thus, $(\beta-1)$-fold differentiation (and multiplication) of Eq.(B-15) gives

$$\left(\frac{I_0}{n} \frac{d}{dI_0} \right)^{\beta-1} \hat{R}_n(I_0) = n \int_0^{I_0} R_n(I) \, \frac{dI}{I}, \tag{B-17}$$

so that one more differentiation yields Eq.(III-6) indeed.

To prove Eq.(III-9) from Eq.(III-6) we first show that, by Eqs.(III-8) and (III-10):

$$\begin{aligned} \left(I \frac{d}{dI} \right) \left\{ \hat{R}_n \, A^{(m)} \right\} &= \hat{R}_n \left\{ \frac{I}{\hat{R}_n} \frac{d\hat{R}_n}{dI} + I \frac{d}{dI} \right\} A^{(m)} \\ &= \hat{R}_n \left\{ \hat{n}(I) + I \frac{d}{dI} \right\} A^{(m)} = \hat{R}_n \, A^{(m+1)}, \end{aligned} \tag{B-18}$$

where $\hat{R}_n = \hat{R}_n(I)$ and $A^{(m)} = A^{(m)}(I)$. Starting with $A^{(0)} = 1$ [see Eq.(III-10)] and iterating Eq.(B-18) m times then gives

$$\left(I \frac{d}{dI} \right)^m \hat{R}_n = \left(I \frac{d}{dI} \right)^m \left\{ \hat{R}_n \, A^{(0)} \right\} = \hat{R}_n \, A^{(m)}. \tag{B-19}$$

By Eqs.(III-6) and (III-8) we have $[R_n = R_n(I)]$:

$$n(I) = \frac{I}{R_n} \frac{dR_n}{dI} = \frac{\left(I \frac{d}{dI} \right)^{\beta+1} \hat{R}_n}{\left(I \frac{d}{dI} \right)^{\beta} \hat{R}_n} = \frac{A^{(\beta+1)}}{A^{(\beta)}}, \tag{B-20}$$

where the last step follows by substitution of Eq.(B-19). With the definition of $A^{(\beta)}(I)$ in Eq.(III-10) we then get

$$n(I) = \frac{1}{A^{(\beta)}} \left[\hat{n}(I) + I\frac{d}{dI}\right] A^{(\beta)} = \hat{n}(I) + \frac{1}{A^{(\beta)}} \frac{d}{dI} A^{(\beta)}, \qquad \text{(B-21)}$$

which leads immediately to Eq.(III-9).

Appendix C: Simple Model of Stark Broadened Lineshapes

In order to demonstrate the essential features of the averaging and inversion of spectral lineshapes in Section V, it was desirable to have a simple analytical model of Stark broadened lineshapes. Thus, to reproduce — rather than to describe exactly — the main features of the experimental data in Figure I-2 on page 7, we have used a true, intensity-dependent lineshape $\sigma_n(I;\nu)$ that is a convolution of a Gaussian profile with constant width $\Delta\nu$:

$$g(\nu) = \frac{1}{\sqrt{2\pi}\Delta\nu} \exp\left\{-\frac{\nu^2}{2\Delta\nu^2}\right\}, \tag{C-1}$$

and a right triangle with apex at $\nu = 0$ and intensity-dependent base and height $\nu_I(I)$ and $\sigma_I(I)$, respectively:

$$f(I;\nu) = \begin{cases} \sigma_I(I)\left[1 + \nu/\nu_I(I)\right]; & -\nu_I \le \nu \le 0, \\ 0; & \text{otherwise.} \end{cases} \tag{C-2}$$

Thus,

$$\sigma_n(I;\nu) = \int_{-\infty}^{\infty} f(I;\nu - x)\, g(x)\, dx. \tag{C-3}$$

Because the Gaussian profile has unit spectral area, the spectral area of $\sigma_n(I;\nu)$ is just that of the triangular profile:

$$S_\nu(I) = \int_{-\infty}^{\infty} \sigma_n(I;\nu)\, d\nu = \int_{-\infty}^{\infty} f(I;\nu)\, d\nu = (1/2)\,\nu_I(I)\sigma_I(I). \tag{C-4}$$

In the limit $\nu_I \to 0$ ($I \to 0$) the maximum value of $\sigma_n(I;\nu)$ is just this area multiplied by the forefactor of the Gaussian profile in Eq.(C-1):

$$\sigma_{n\nu}^{(0)} = \lim_{\nu_I \to 0} \sigma_n(I;\nu) = \frac{S_\nu(I)}{\sqrt{2\pi}\Delta\nu}. \tag{C-5}$$

In this work we have required that $\sigma_{n\nu}^{(0)} = 1$, and that the spectral area S_ν be independent of $\nu_I(I)$. Thus, it may be shown that the true, intensity-dependent

lineshape from Eq.(C-3) is given by:

$$\sigma_n(u;du) = \frac{1}{du^2}\left\{\sqrt{\pi}(u+du)\left[\mathrm{erf}(u+du)-\mathrm{erf}(u)\right]+\exp\left(-(u+du)^2\right)-\exp\left(-u^2\right)\right\}, \tag{C-6a}$$

where the dimensionless frequencies u and du are given by

$$u = \frac{\nu}{\sqrt{2}\Delta\nu}; \qquad du = du(I) = \frac{\nu_I(I)}{\sqrt{2}\Delta\nu}, \tag{C-6b}$$

and where "erf" denotes the normalized error function. It may be shown that the maximum value of $\sigma_n(u;du)$ occurs at a value u_c which satisfies

$$\left(2du/\sqrt{\pi}\right)\exp\left(-u_c^2\right) = \mathrm{erf}(u_c+du) - \mathrm{erf}(u_c), \tag{C-7}$$

from which, for small du:

$$u_c = -\frac{1}{3}du + \frac{1}{135}du^3 \ldots. \tag{C-8}$$

So far, we have not specified how the base $\sigma_I(I)$ or its normalized value $du(I)$ depend on intensity. In this work, we have assumed a linear dependence:

$$du(I) = \lambda_\nu I. \tag{C-9}$$

The true, intensity-dependent lineshapes $\sigma_n(I;\nu)$ in Figure V-1(a) on page 69 were obtained with a value $\lambda_\nu = 8\sqrt{2}\Delta\nu/I_{\max}$, where $I_{\max}$ is the maximum intensity in the figure, and the spectral range in the figure was such that $-20\Delta\nu \le \nu \le 5\Delta\nu$.

Appendix D: List of Symbols

Below follows a list of symbols found in Sections I through VI. Symbols that occur only in the Appendices are not included. In case of slight variations in notation only the primary definition is mentioned, for example, $M_k(I_0; I_j)$ is listed, but $M_k(I_{0i}; I_j)$ is not. The alphabetical order of the list is: small Roman, capital Roman, small Greek, capital Greek.

$a_i^{\pm}$, a	Width of exponential profile.
$\mathbf{a}$, a_j	Collocation coefficient vector and component thereof.
$\mathbf{a}_T$	As a for the case of Tikhonov regularization.
$\mathbf{b}^{(i)}$	Column vector defined in Eq.(IV-14).
$\mathbf{ds}$, ds_i	Experimental data noise vector and component thereof.
ds_{rms}	Average noise amplitude defined in Eq.(IV-11).
$\hat{\mathbf{e}}^{(i)}$, $\hat{e}_j^{(i)}$	Unit vector and component thereof.
$f(I)$	Collocation approximation to $\sigma_n(I)$.
$f_0(I)$	Noise free solution of $f(I)$.
g_{12}	Degeneracy ratio in rate equation model.
$g_i(I)$	Splines defined in Eq.(IV-18) (noise contribution).
h, i, j	Summation indices.
k	Order in power series expansion.
k	Number of differentiations in Abel inversion [Eq.(III-5)].
$\mathbf{k}(I)$, $k_j(I)$	Short notation for kernels such as $K(I_0; I)$.
n	Order of nonlinear interaction.
n_1, n_2, n_3	Number densities in rate equation model.
$n_{\mathbf{x}}$	Number of coordinates in composite profile $F_{\mathbf{x}}(\mathbf{x})$.

$n(I)$	True, intensity-dependent order of interaction.
$\hat{n}(I_0)$	Experimentally averaged value of $n(I)$.
n_j	Power of spline basis function.
p	Constant value of detection probability $P(\mathbf{r})$.
p, q	Parameters defined in Eq.(II-37b).
$\mathbf{r}$	Spatial coordinate vector.
$\mathbf{s}$, s_i	Experimental data vector and component thereof.
$\tilde{\mathbf{s}}$, $\tilde{s}_i$	Weighted values of $\mathbf{s}$, s_i.
$\tilde{\mathbf{s}}_0$, $\tilde{s}_{0i}$	Noise free values of $\tilde{\mathbf{s}}$, $\tilde{s}_i$.
$\tilde{\mathbf{s}}_{\mathrm{nr}}$	Nonregularized part of $\tilde{\mathbf{s}}$.
t, t_0	Time coordinates.
w_i	Weight factor for ith experimental data point.
w_j	Singular value of singular value decomposition.
w_{knot}	Weight factor for knot regularization constraints.
$\mathbf{x}$, x_i, x	Spatial coordinates.
A	Total random deexcitation rate of excited state.
$A^{(\beta)}(I)$	Quantity defined in Eq.(III-10).
$\mathbf{A}$, A_{ij}	Inversion matrix and component thereof.
$\tilde{\mathbf{A}}$, $\tilde{A}_{ij}$	Weighted values of $\mathbf{A}$, A_{ij}.
$\tilde{\mathbf{A}}_{\mathrm{nr}}$	Nonregularized part of $\tilde{\mathbf{A}}$.
C	Condition number defined in Eq.(IV-25).
$\mathbf{C}$	Kernel covariance matrix defined in Eq.(III-27).
D	Degree of polynomial spline.
$\mathcal{D}$, $\mathcal{D}_S$, $\mathcal{D}_N$	Total, systematic, and noise contributions to the integrated fidelities defined in Eq.(IV-19).
$\mathbf{E}$, E_{hi}	Residu matrix and element thereof [Eqs.(IV-21), (IV-27)].

$F_{\mathbf{r}}(\mathbf{r})$, $F_t(t)$	Spatial and temporal intensity profiles.
$F_{\mathbf{x}}(\mathbf{x})$	Composite intensity profile.
$G(R_n)$, $H(Z)$	Generic notation of analytical functions resulting from the analytical integration of the rate equation model.
$\mathbf{I}$	Identity matrix.
I, $I(\mathbf{r})$, $I(\mathbf{r},t)$	Local, instantaneous values of the intensity.
$\langle I \rangle_j$	Central intensity of jth basis vector, defined in Eq.(III-30).
I_j	Knot position of polynomial spline.
$I_{\mathbf{r}}$, $I_{\mathbf{r}}(\mathbf{r})$, $I_{\mathbf{r}}^*$	Local peak intensity (* dimensionless).
I_0	Peak intensity in focused laser pulse.
$\overline{I_0}$	Averaged value of I_0.
$I_{0,\max}$	Maximum value in a series of values of I_0.
K	Number of knots of polynomial spline.
$K_{\mathbf{r}}(I_0;I_{\mathbf{r}})$,$K_t(I_{\mathbf{r}};I)$	Spatial and temporal kernels.
$K(I_0;I)$	Composite or generic kernel.
$\overline{K}(\overline{I}_0^*;I)$	Averaged kernel $K(I_0;I)$.
M	Number of collocation basis functions.
M_{k0}	Complete kth moment of kernel.
$M_k(I_0;I_j)$	Incomplete kth moment of kernel.
$\mathcal{M}(\beta;p;q)$	Ratio of incomplete to complete moments of kernel.
N, $\tilde{N}$	Number of inversion equations without, with regularization.
N_{pp}, $N_{\mathrm{pp}}(\mathbf{r})$	Number of excited states per laser pulse per molecule.
$P(\mathbf{r})$, $P(\mathbf{x})$	Detection probability functions.
$P_I(\overline{I}_0;I_0)$	Probability density function of peak intensity distribution.
Q_{fit}, $\langle Q_{\mathrm{fit}} \rangle$	Residu of fit and expectation value thereof.
Q_{knot}	Functional of knot constraints.

RCOND	Condition as determined by LINPACK subroutine DSICO.
$R_n(I)$	True, intensity-dependent excitation rate.
$\hat{R}_n(I_0)$	Experimentally averaged value of $R_n(I)$.
$\mathcal{R}_n(\omega)$, $\hat{\mathcal{R}}_n(\omega_0)$	Transformed functions $R_n(I)$ and $\hat{R}_n(I_0)$.
S_0	Calibration constant for experimental signal.
$S(I_0)$	Experimentally averaged signal.
$(S_0\kappa_t)_{\text{guess}}$	Guessed value of the product $S_0\kappa_t$.
$\mathbf{U}$	Orthogonal matrix from singular value decomposition, or orthonormal matrix from direct inversion.
$\mathbf{V}$	Orthonormal matrix from singular value decomposition.
$V_{\mathrm{r}}(I_0;I_{\mathrm{r}})$, $V_t(I_{\mathrm{r}};I)$	Spatial and temporal "volumes" defined in Eqs.(II-16).
$V(I_0;I)$	Composite or generic volume defined in Eq.(II-27).
$\mathbf{W}$, W_{ij}	Singular value matrix and element thereof.
$\mathbf{W}_T$	Tikhonov regularized inverse of $\mathbf{W}$ from Eq.(III-24).
Z, $Z(\mathrm{r})$, $\tilde{Z}(I_{\mathrm{r}})$	Generic notations for integral of excitation rate.
α	Knot stretch parameter defined in Eq.(IV-30).
α	Saturation parameter defined in Eq.(V-6).
β, β'	Shape parameters associated with exponential profiles.
β_{12}	Branching ratio of random decay processes of excited state.
γ_k, $\hat{\gamma}_k$	Power series coefficients of cross-section in Section III-2.
δ_k, $\hat{\delta}_k$	Power series coefficients of line centers in Section V-1.
δ_{ij}	Kronecker delta.
ϵ	Tikhonov regularization parameter.
κ, κ_{r}, κ_t	Kernel normalization constants.
λ_j	Eigenvalue of direct inversion matrix.
μ, μ_x, μ_y, μ_z, μ_t	Orders of exponential profiles (2 = Gaussian).

ν, ν_0	Spectral frequency and zero intensity line center.
$\nu_c(I)$, $\hat{\nu}_c(I_0)$	True and experimental intensity-dependent line centers.
$\sigma_n(I)$, $\hat{\sigma}_n(I_0)$	True and experimental intensity-dependent cross-sections.
$\sigma_r(I_r)$, $\sigma_t(I_r)$	Nonsaturated and saturated temporal averages of $\sigma_n(I)$.
σ_c, σ_{n0}	Limiting behaviors of cross-sections from Eqs.(II-28), (II-29).
$\sigma_n(I;\nu)$, $\sigma_n^*(I;\nu)$	True intensity-dependent lineshapes (* dimensionless).
$\hat{\sigma}_n(I_0;\nu)$, $\hat{\sigma}_n^*(I_0;\nu)$	Experimental lineshapes (* dimensionless).
$\sigma_r^*(I_r;\nu)$, $\sigma_t^*(I_r;\nu)$	Dimensionless lineshapes corresponding to $\sigma_r(I_r)$, $\sigma_t(I_r)$.
$\sigma_{n\nu}^{(0)}$	Maximum value of intensity-dependent lineshape $\sigma_n(I;\nu)$.
$\overline{\sigma_n}$, $\overline{\sigma_n}^*$,	Spectral areas of lineshapes (* dimensionless).
$\langle\overline{\sigma_n}^*\rangle$	Average value of $\overline{\sigma_n}^*$ from Eq.(V-11b).
$\overline{\sigma}_{\rm rms}^*$	Average relative deviation of $\overline{\sigma_n}$ from Eq.(V-11a).
$\underline{\phi}(I)$, $\phi_j(I)$	Basis vector of direct inversion and component thereof.
χ^2, χ_S^2, χ_N^2	Total, systematic, and noise contributions to the residu.
ω, ω_0	Logarithms of the intensities as defined in Eq.(III-2).
Δt	Measure of pulse duration.
$\Delta(I)$,$\Delta_S(I)$,$\Delta_N(I)$	Total, systematic, and noise contributions to the noise amplification function defined in Eq.(IV-10).
$\mathbf{\Lambda}$	Eigenvalue matrix of direct inversion.
$\mathbf{\Lambda}^{(K)}$, $\Lambda_{kk}^{(K)}$	Diagonal matrix from Eq.(IV-9b) and element thereof.

PART II:

RESPONSE OF A SIMPLE QUANTUM SYSTEM TO A FULLY AMPLITUDE MODULATED FIELD

I INTRODUCTION

In part II we present theoretical work that, like the work in part I, pertains to specific aspects of employing laser induced fluorescence (LIF) in the diagnostics of gasdynamic or fluiddynamic processes. This time, the objective of the envisaged LIF experiment is to measure local velocities in a flowfield, rather than temperature or concentrations of its constituents. The concept of this technique, which has been termed a "laser fluorescence velocimeter" (LFV) is described in Ref. [1],* and is shown schematically in Figure I-1. The beam from a frequency stabilized dye laser is split and recombined at a small angle so as to produce a pattern of interference fringes parallel to the optical axis. The frequency of one of the beams is shifted, say, by passage through a Bragg cell. Thus the interference fringes move transverse to the optical axis. This arrangement is much like that of a conventional laser Doppler velocimeter (LDV) [2], in which the beams are generally of the same frequency, yielding a stationary fringe pattern. Note that in the case of two distinct frequencies of equal intensity the superposition field may be regarded either as a bichromatic field, or a field that is fully amplitude modulated.

The concept of the conventional LDV relies on the scattering of the laser light off individual, macroscopic particles in the probe volume. That is, as a macroscopic particle traverses the fringe pattern, it scatters a modulated signal into a detector, which is located away from (generally perpendicular to) the optical axis. The modulation period is simply the ratio of the fringe spacing and the transverse velocity of the scatterer, that is, its velocity component transverse

---

*Here and in the following, numbers within square brackets refer to the similarly numbered entries in the List of References on page 188.

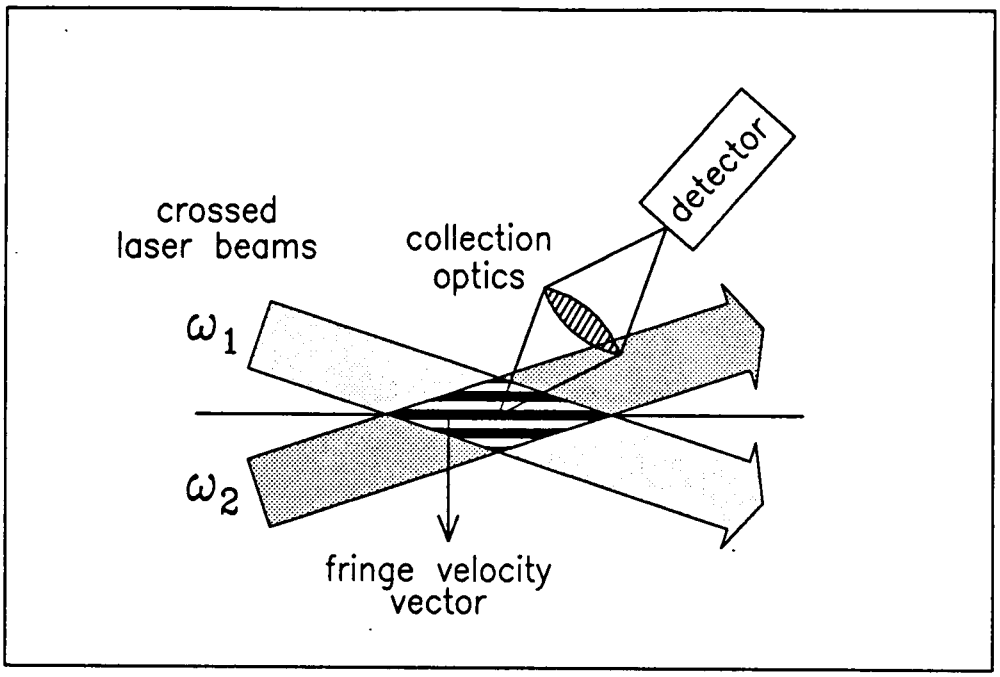


Figure I–1: *Schematic diagram of the laser fluorescence velocimeter.*

The angle between the two beams is shown larger than the actual angle, which is on the order of 20 mrad; ω_1 and ω_2 denote the frequencies of the two beams..

to the fringes. Because the fringe spacing is known, the transverse velocity is easily found from the modulation period of the detected signal (if moving fringes are employed in an LDV, one merely needs to subtract their velocity from that calculated from the modulated signal to obtain the transverse velocity of the scatterer). By using three orthogonal fringe patterns it is possible to obtain all three velocity components of the scatterer. Note that in either case, the effective viewing region of the detector(s) should span at least several fringes.

By contrast, the concept of the proposed LFV relies on the laser induced fluorescence signal from atoms or molecules in the probe volume that are nearly resonant with the laser light. Even if the concentrations of these species in the

host medium are dilute, the fluorescing species may be considered as a continuous medium for all practical purposes. Again, the scattered signal, that is, the fluorescence signal is detected, say, perpendicular to the optical axis, as illustrated in Figure I-1. Unlike for the LDV, the effective viewing region of the detector should be on the order of, or less than the width of a single fringe. Thus, again, a modulated signal is detected. This time, however, the modulation period is just the inverse of the frequency difference between the two beams. That is, the signal is modulated at the frequency of the device that is used to shift the frequency of one of the two beams, say, that of the Bragg cell driver. This then allows for the use of lock-in techniques to achieve phase sensitive detection of the fluorescence signal. The transverse velocity of the fluorescing medium is now determined from the depth-of-modulation (or visibility) of the fluorescence signal, and/or its phase-shift relative to the fringe pattern in the probe volume, as discussed in more detail in Section IV.

The primary advantage of the proposed LFV over its conventional LDV predecessor is that scattering takes place by an essentially continuous medium, rather than by discrete, macroscopic particles in the flowfield. Because atomic or molecular species are expected to better track the flow in which they are embedded than macroscopic particles, the measured velocity should better approximate that of the host medium. This is particularly true for strongly accelerating flows, such as found in shock waves and supersonic expansions. Also, the continuous rather than discrete nature of the scattering medium should give rise to continuous signals rather than individual bursts, with the potential for using refined signal processing techniques.

The serious disadvantage of the LFV concept is that there are many mechanisms that can reduce the visibility of the modulated fluorescence signal. Among

these are quenching of the excited state of the fluorescing species, detection of fluorescence that originates outside of the targeted sub-fringe-size probe volume, background scatter from the laser light itself, and vibration of optical components. In fact, efforts toward an experimental demonstration of the LFV concept on a cold nitrogen flow seeded with sodium atoms have been unsuccessful [3], causes being attributed to the factors mentioned above. But rather than to discuss the many problems that originate with the geometrical arrangement of the experiment and the atomic or molecular dynamics in the host medium [4], the work in part II of this dissertation investigates the fundamental interaction of the narrowband laser light with the fluorescing medium, which, from now on, we assume to be an atomic species.

In this regard we note that the response of an atomic system to modulated excitation has been investigated by a number of workers. In particular, Duschinsky is credited with the derivation of the corresponding depth-of-modulation and phase-shift of the fluorescence signal [5]. His work, published in 1933, precedes the development of intense, narrowband dye lasers by over three decades. Indeed, his derivation holds strictly only for weak, broadband excitation, that is, excitation that does not significantly deplete the atomic ground state and has a spectral width that is much larger than the homogeneous linewidth of the absorber. In this regime, the response of the atom can be calculated from a rate equation model, or, alternatively, by assuming that the fluorescence signal is the convolution of the modulated, incident light and the exponential decay of the fluorescing species. Measurement of the phase-shift of the fluorescence, a method generally refered to as "phase sensitive fluorometry," has since been widely used to determine fluorescence lifetimes of species as varied as low pressure gases, organic liquids, or even solids [6].

In its conception [1], expressions for the depth-of-modulation and phase-shifts in a LFV were exactly those of conventional phase sensitive fluorometry [5]. However, it has been recognized that when using narrowband rather than broadband excitation these expressions are no longer valid [7–10]. For example, due to the coherent interaction between field and absorber, the phase-shift for resonant excitation may be twice that for the corresponding broadband result [10,11]. Moreover, with available power levels, it is easy to achieve strong saturation of the atomic medium, leading to even more complicated expressions for the depth-of-modulation and phase-shift of the fluorescence signal [9,10]. In particular, these coherently driven saturation effects have been shown to give rise to the creation of higher harmonic components in the modulated fluorescence signal, an effect related to that of Rabi oscillations. A group at the University of Rochester has recently pursued experimental demonstrations of these coherent effects in the bichromatic operation of a homogeneously broadened laser [12,13] as well as in an atomic beam setup resembling the LFV geometry shown in Figure I-1 [14,15]. Also, Thomann has performed related work with an atomic beam excited by a narrowband, *not* fully amplitude modulated field, that is, a field with three rather than two frequency components [16–18].

The goal of the work in part II has been to calculate explicitly the response of the simplest imaginable atomic system, namely a strict two-level atom, to a narrowband, nearly resonant field that consists of two unequal frequencies of the same amplitude, or, in an alternative view, a narrowband field that is fully amplitude modulated. Although — even for the general case of (possibly) strong excitation — the solution has been known for some time in the form of continued fractions for the various fluorescence components [13–15], important aspects of this solution have not been investigated previously. In particular, because only the

time-averaged behavior has been measured in the experimental work mentioned above [12–18], not much analysis has been devoted to the study of modulated fluorescence components. Yet it would be precisely these components that would be measured in the proposed LFV.

In pursuing the analysis of the response of a two-level atom driven by a fully amplitude modulated optical field we have drawn extensively from the literature on equivalent experiments in the field of magnetic resonance, namely those in which a two-level atom is subjected to a combination of static and oscillating magnetic fields. Much of this magnetic resonance work was carried out in the period 1955 – 1975. Quite importantly, the basic equations that describe the repective magnetic and optical interactions — the Bloch equations — are identical for the two regimes. Thus many results from the magnetic resonance literature can be applied straightforwardly to the case of an optical interaction. Specifically, these results include the derivation of multi-photon (multiple quantum) resonances [19] and the calculation of the power-shifts of these resonances, which have become known as Bloch-Siegert shifts [20].

In Section II we start with a concise overview of the theory of magnetic and optical interactions. Thus we derive the Bloch equations and identify equivalent optical and magnetic resonance geometries. Also we explain the physical origin of multiple quantum resonances, and we review the known expressions for the Bloch-Siegert shifts of these multiple quantum resonances. A discussion of how specific results from magnetic resonance apply to the experimental work performed at Rochester will not be repeated here [21]. However, in Section III we present an extensive analysis of the response of a two-level atom to a fully amplitude modulated field, paying particular attention to the behavior of modulated interaction components. As it turns out, this discussion is new even to the field of magnetic

resonance where, as in the optical regime, most analyses have been for the resonance behavior of time-averaged signals, since these were the quantities measured in the majority of the experiments.

The emphasis in Section III is not primarily on the relevance of the theory to the concept of the LFV, but rather on fundamental aspects of the atom-field interaction. Particularly, we extend the concept of Bloch-Siegert shifts of multiple quantum resonances to harmonic components of the interaction. Then in Section IV, we return to a specific aspect related to the interpretation of LFV data, namely the effects of inhomogeneous broadening. Unlike the experimental work performed at Rochester [14], which was carried out in an atomic beam setup to eliminate inhomogeneous broadening, a typical application involving an LFV would deal with a medium in which, in addition to a bulk motion, a substantial distribution of random, thermal velocities would exist. Because of the small angle between the crossed beams, there is a large asymmetry between the influences of the Doppler shifts due to transverse and parallel (that is, parallel to the fringes) velocity components of the fluorescing medium. Thus, in the rest frames of individual atoms, the frequency difference between the two Doppler shifted beams is generally well defined. However, in these rest frames, a large distribution of detunings exist, even at temperatures well below room temperature. Without pre-empting the detailed discussion of Section IV we note that this implies that in applications other than those designed to deliberately suppress inhomogeneous broadening one should average the results of Sections III and IV over the inhomogeneous profile of the two-level medium. Interestingly, this averaging yields the same expressions for modulation and phase-shift of the fluorescence signal in the case of weak, narrowband excitation as for the familiar case of weak, broadband excitation [11]. However, if the narrowband excitation (or, for that matter, the

broadband excitation) is sufficiently strong to cause saturation effects, the resulting expressions for modulation and phase-shift are significantly different. These results should be taken into account when extracting transverse velocities from, say, the phase-shift of the modulated fluorescence signal if the exciting light cannot be considered to be weak. From the point of view of the fundamental aspects of the interaction of a modulated field with a simple quantum system, the inhomogeneously broadened results for the modulated fluorescence component are interesting and surprising in that they, unlike the corresponding results for the usually measured time-averaged signals, retain the characteristic multiple quantum resonance structure that is found in the absence of inhomogeneous broadening [22]. This finding might alleviate the need for meticulously designed atomic beam setups such as those employed in the Rochester experiments.

Finally, in Section V we recapitulate the main results from Sections III and IV, and we give some discussion on further experimental activities that might be pursued to confirm the theoretical predictions of Sections III and IV, even if the successful operation of the proposed LFV proves to be beyond practicability under the stringent conditions that are encountered in a typical laboratory setting.

II OVERVIEW OF OPTICAL AND MAGNETIC RESONANCE

Section II presents a brief overview of the fields of optical and magnetic resonance on two-level atoms using modulated excitation. Section II-1 starts with a discussion of the experimental aspects of both types of experiment. Next, Sections II-2 and II-3 present the vehicle of choice for the analysis of optical and magnetic interactions, respectively, namely the Bloch equations. Also, Section II-3 points out the strong similarities of both types of experiment. Section II-4 deals specifically with an optical interaction driven by a fully amplitude modulated field, or, alternatively, a magnetic interaction under conditions of longitudinal pumping. In particular, Section II-4 gives some discussion on the occurrence of multiple quantum resonances and the (Bloch-Siegert) shifts of these resonances with increasing field strengths.

II–1 Experimental Aspects

Because the theories of optical and magnetic resonance are most easily developed for quantum systems that are composed strictly of two levels, experimenters have generally strived to approximate such ideal two-level systems as closely as possible. Thus, the relevant interactions can be schematically represented as in Figure II-1.

In an optical resonance experiment, an atomic ground state, state $|1\rangle$, is excited to the upper level of the two-level system, state $|2\rangle$, by a narrowband laser, whose frequency ω_l is generally close to the atomic transition frequency ω_{12}, with a detuning given by

$$\Delta = \Delta_{\text{opt}} = \omega_{12} - \omega_l. \qquad \text{(II–1)}$$

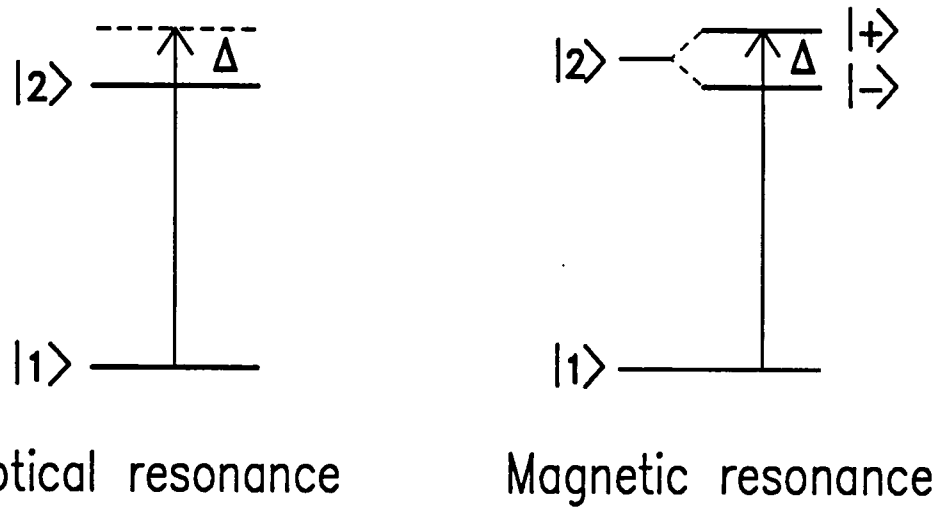


Figure II–1: *Schematic representation of optical and magnetic resonance experiments.*

Subsequently, either the absorption of the pump beam, or the fluorescence signal from state $|2\rangle$ is measured to obtain information on the field-atom interaction. In case of measurement of the fluorescence signal, either the total fluorescence intensity is measured, or, in a more sophisticated experiment, the spectral distribution of the fluorescence (for one of the earliest accounts see Ref.[23]). In the following, we are only concerned with measurements of the fluorescence intensity. The simplest experiment would be one in which the exciting light is a monochromatic plane wave of constant amplitude and phase. However, we are more interested in the types of experiment where the exciting light is either frequency modulated [24–26], amplitude modulated [7–18,26–28], or is perhaps a bichromatic field with unequal intensities in the two modes [15,29]. Because typical modulation frequencies are on the order of the homogeneous linewidth of an atomic transition ($\simeq$ 10 MHz), which, if the experiment is performed in a gas at room temperature,

is typically several orders of magnitude less than the linewidth due to inhomogeneous broadening ($\simeq$ 1 GHz), optical resonance experiments are generally carried out in atomic beam setups to eliminate the complications due to inhomogeneous broadening. Finally, to prepare the atomic system (usually one of the D-lines in the 3s–3p manifold of sodium) as a two-level system, the atomic beam is generally optically pumped with circularly polarized light, to allign the magnetic sublevels of state $|1\rangle$ [13,17].

Magnetic resonance experiments on two-level systems have been of a similar nature in that, again, some atomic ground state, state $|1\rangle$, is optically pumped to some excited state, state $|2\rangle$. Specific atomic systems that have been used include the D_1-line of the 6s–6p transition in cesium [30–39], the 3261Å line in ^{113}Cd [40,41], the 2537Å line in ^{199}Hg [42], and the D_1-line of ^{87}Rb [43–46]. In marked contrast to the optical resonance experiments, however, the two-level system of interest is *not* the system composed of states $|1\rangle$ and $|2\rangle$, but rather the two states $|+\rangle$ and $|-\rangle$ (see Figure II-1), into which the spin-1/2 state $|2\rangle$ splits under the influence of an applied magnetic field. This splitting is given by:

$$\Delta = \Delta_{\mathbf{mag}} = g_0 \beta H_0, \qquad \text{(II–2)}$$

where g_0 is the g-factor of state $|2\rangle$, β is the Bohr magneton, and H_0 is the Zeeman field that is used to split the two levels. Just as in the case of an optical interaction, the simplest situation is that in which the (static) Zeeman field is the only magnetic field present. In the more interesting experiments, however, additional static and radiofrequency (rf) fields are applied, either longitudinal, transverse, or at an arbitrary angle to the Zeeman field [30–46]. The modulation frequencies of the additional fields are typically on the order of 10–100 kHz, that is, several orders of magnitude smaller than those in optical resonance experiments. Moreover, because the transition frequency of the magnetic two-level

system ($\simeq$ 10–100 kHz) is some *eight* orders of magnitude less than for a typical optical two-level atom ($\simeq 5 \times 10^{14}$ Hz), inhomogeneous broadening is completely negligible, so that experiments have been performed simply in gas cells. Note that inhomogeneous broadening of the optical transition $|1\rangle \rightarrow |2\rangle$ does not affect the dynamics of the $|+\rangle \leftrightarrow |-\rangle$ system, because, as a result of the selection rules for dipole transitions, only one of the two sublevels $|+\rangle$ or $|-\rangle$ is optically pumped from the atomic ground state $|1\rangle$. For the same reason, it does not matter whether the sublevels of state $|2\rangle$ are excited by narrowband or broadband light. Indeed, because most of the magnetic resonance experiments were performed before the availability of strong, narrowband lasers, most experiments were performed with electrodeless discharge lamps, containing the same gas as the gas in the resonance cell. Light from the discharge lamp was then collimated and passed through a circular polarizer. Information on the dynamics of the interaction was then obtained by measuring the absorption signal, by placing a photo cell on the opposite side of the resonance cell, and measuring the transmitted intensity of the circularly polarized pump beam.

II–2 Optical Bloch Equations

Let the dynamics of the optical resonance experiment from Figure II-1 be described by the density matrix elements ρ_{ij} $(i,j = 1,2)$ of the two-level system. From the Liouville equation, the dynamical evolution of the two-level system may then be shown to obey the system of equations (see, for example, Ref.[47]):

$$i\hbar\left(\frac{\partial \rho_{22}}{\partial t} + \rho_{22}/T_1\right) = H_{\text{int}}\left[e^{i\omega_{12}t}\rho_{12} - e^{-i\omega_{12}t}\rho_{21}\right]; \qquad \text{(II–3a)}$$

$$i\hbar\left(\frac{\partial \rho_{12}}{\partial t} + \rho_{12}/T_2\right) = H_{\text{int}}\, e^{-i\omega_{12}t}(\rho_{22} - \rho_{11}); \qquad \text{(II–3b)}$$

$$\rho_{11} = 1 - \rho_{22}; \tag{II-3c}$$

$$\rho_{21} = \rho_{12}^{*}. \tag{II-3d}$$

Here $\hbar$ is Planck's constant divided by 2π, T_1^{-1} and T_2^{-1} are phenomenological decay rates, and the interaction Hamiltonian is given by

$$H_{\text{int}} = -p_{12}\, E(t), \tag{II-4}$$

where p_{12} is the electric dipole moment of the two-level transition, and $E(t)$ is the magnitude of the electric field component of the exciting light. Rather than work with the density matrix elements ρ_{ij}, we follow Allen and Eberly's notation (Ref.[48], Chapter 2), and transform to the variables U, V, and W, given by

$$U = \tilde{\rho}_{21} + \tilde{\rho}_{12} = 2\,\text{Re}\{\tilde{\rho}_{12}\}; \tag{II-5a}$$

$$V = i(\tilde{\rho}_{21} - \tilde{\rho}_{12}) = 2\,\text{Im}\{\tilde{\rho}_{12}\}; \tag{II-5b}$$

$$W = \rho_{22} - \rho_{11}, \tag{II-5c}$$

where $\tilde{\rho}_{12}$ is the off-diagonal density matrix element in a rotating frame:

$$\tilde{\rho}_{12} = \rho_{12}\, e^{i\Delta t} = \rho_{12}\, e^{i(\omega_{12} - \omega_l)t} = \tilde{\rho}_{21}^{*}. \tag{II-6}$$

In Eqs.(II-5), U and V are the real and imaginary parts of the susceptibility (or polarization) of the two-level system, respectively, and W is the population inversion. Also, we introduce the dipole coupling constant

$$\kappa = 2\,p_{12}/\hbar, \tag{II-7}$$

and write, in case of a monochromatic field of frequency ω_l and amplitude $\mathcal{E}$, the electric field as:

$$E(t) = 2\mathcal{E}\,\cos\,\omega_l t. \tag{II-8}$$

With Eqs.(II-4)–(II-8), Eqs.(II-3) may now be written as

$$\dot{U} = -U/T_2 - \Delta V + \kappa\mathcal{E}\,\sin(2\omega_l t)\,W; \qquad \text{(II–9a)}$$

$$\dot{V} = -V/T_2 + \Delta U + \kappa\mathcal{E}\,\left[1+\cos(2\omega_l t)\right]W; \qquad \text{(II–9b)}$$

$$\dot{W} = -(1+W)/T_1 - \kappa\mathcal{E}\,\sin(2\omega_l t)\,U - \kappa\mathcal{E}\,\left[1+\cos(2\omega_l t)\right]V, \qquad \text{(II–9c)}$$

where the dots denote differentiation with respect to time. Note that, by Eqs.(II-3) and (II-9), the excited state $|2\rangle$ is unpopulated in the absence of any driving fields, yielding the equilibrium values

$$\rho_{11}^{(0)} = 1; \qquad \rho_{22}^{(0)} = 0; \qquad W_{\rm eq} = -1. \qquad \text{(II–10)}$$

We assume that these equilibrium values hold throughout Section II, III, and IV. However, even if, by some pumping mechanism other than that of the electric field $E(t)$, a significant non-zero equilibrium population exists (as is the case in a laser medium, for example), Eqs.(II-3) and (II-9) remain essentially unmodified. Indeed, one merely needs to replace the terms ρ_{22}/T_1 and $(1+W)/T_1$ in Eqs.(II-3a) and (II-9c) by $\left(\rho_{22}-\rho_{22}^{(0)}\right)/T_1$ and $(W-W_{\rm eq})/T_1$, respectively, where $\rho_{22}^{(0)}$ and $W_{\rm eq}$ are the new equilibrium values. Thus, in Eqs.(II-9), the solution for the variables U, V, and W is simply multiplied by a factor $(-W_{\rm eq})$.

Eqs.(II-9) are the well known optical Bloch equations. Because, at optical frequencies, the terms $\cos(2\omega_l t)$ and $\sin(2\omega_l t)$ have a time-dependence that is far beyond the resolution of conventional spectroscopic techniques (see, however, Ref.[49]), these terms are generally omitted from the equations. This approximation constitutes the rotating wave approximation (RWA), and generally leads to excellent results. Certainly, it greatly facilitates the solution of the Bloch equations.

To allow an easy comparison of the optical Bloch equations with the corresponding magnetic Bloch equations in Section II-3, we note that, if the components

U, V, and W are written as a vector:

$$\mathbf{\Phi} = (U, V, W)^T. \tag{II-11}$$

Eqs.(II-9) can be written such that the interaction terms form a vector product:

$$\dot{\mathbf{\Phi}} = -\mathbf{\Lambda}\,\mathbf{\Phi} + \mathbf{R} \times \mathbf{\Phi} + \mathbf{C}, \tag{II-12}$$

where $\mathbf{\Lambda}$ is a diagonal damping matrix with elements T_2^{-1}, T_2^{-1}, and T_1^{-1}, and $\mathbf{C}$ is the inhomogeneous term given by

$$\mathbf{C} = (0, 0, -1/T_1)^T \sim (0, 0, 1)^T, \tag{II-13a}$$

or

$$\mathbf{C} = (0, 0, W_{\mathrm{eq}}/T_1)^T \sim (0, 0, 1)^T. \tag{II-13b}$$

The vector $\mathbf{R}$, which acts as a torque on the Bloch vector $\mathbf{\Phi}$, is given by

$$\mathbf{R} = \begin{pmatrix} -\kappa\mathcal{E}\left[1 + \cos(2\omega_l t)\right] \\ \kappa\mathcal{E}\,\sin(2\omega_l t) \\ \Delta \end{pmatrix}. \tag{II-14}$$

Note that for the constant, monochromatic field $E(t)$ from Eq.(II-8), $\mathbf{R}$ becomes time-independent in the rotating wave approximation. The resulting solution of the Bloch equations is well known, particularly the occurrence of Rabi oscillations [47,48]. Rabi oscillations are, however, a transient effect, which is damped out after a few cycles following excitation by a field that is switched on abruptly. Here, we are only concerned with steady-state solutions of the Bloch equations. However, we are interested in fields more general than the constant field of Eq.(II-8), namely (possibly) polychromatic fields with variable amplitude and phase. Thus we replace the field from Eq.(II-8) by the more general field

$$E(t) = \sum_i 2\mathcal{E}_i(t)\,\cos\bigl(\omega_i t + \varphi_i(t)\bigr), \tag{II-15}$$

where the summation is over an arbitrary number of field modes, and $\mathcal{E}_i(t)$ and $\varphi_i(t)$ denote amplitude and phase factors that are slowly varying with respect to the optical frequencies ω_i. The Bloch equations for such a field can be derived as before. This time, the transformation to a rotating frame from Eq.(II-6) is generalized to

$$\tilde{\rho}_{12} = \rho_{12}\, e^{i(\Delta t - \varphi_l(t))} = \rho_{12}\, e^{i(\omega_{12} t - \omega_l t - \varphi_l(t))} = \tilde{\rho}_{21}^{*}, \qquad \text{(II–16)}$$

where, as yet, the frequency ω_l and phase $\varphi_l(t)$ are undetermined [they may or may not be chosen equal to one of the factors ω_i and $\varphi_i(t)$ in Eq.(II-15)]. With Eqs.(II-15) and (II-16), the Bloch equations again take the form of Eq.(II-12). However, the optical torque $\mathbf{R}$ is now given by

$$\mathbf{R} = \begin{pmatrix} -\sum_i \kappa \mathcal{E}_i(t) \left[\cos \Omega_i^{(-)}(t) + \cos \Omega_i^{(+)}(t)\right] \\ \sum_i \kappa \mathcal{E}_i(t) \left[\sin \Omega_i^{(-)}(t) + \sin \Omega_i^{(+)}(t)\right] \\ \Delta - \dot{\varphi}_l(t) \end{pmatrix}, \qquad \text{(II–17a)}$$

where

$$\Omega_i^{(\pm)}(t) = \left(\omega_l t + \varphi_l(t)\right) \pm \left(\omega_i t + \varphi_i(t)\right). \qquad \text{(II–17b)}$$

Apart from the obvious addition of cosine and sine terms in the first two components of $\mathbf{R}$, the third component is also changed, namely by the time derivative of the phase factor $\varphi_l(t)$ from Eq.(II-16).

With Eqs.(II-15)–(II-17) it is a straightforward matter to derive the Bloch equations for special fields, such as fields that are frequency modulated [24–26], amplitude modulated [7–18,26–28], or bichromatic [15,29]. For example, it can be shown that amplitude modulated and frequency modulated fields can be described by the same Bloch equations, upon interchange of the first and third components of the Bloch vector Φ from Eq.(II-11). However, the nonvanishing component of

the inhomogeneous term C is then interchanged between the two cases, with important consequences for the resonance behavior of the two-level system [26]. In Part II of this dissertation, we are concerned primarily with fully amplitude modulated (FAM) driving fields. Denoting the carrier frequency and the modulation frequency by ω_l and Ω, respectively, such a field can be written as [cf. Eq.(II-15)]:

$$E^{(\mathrm{FAM})}(t) = 2\mathcal{E}\,\cos\Omega t\,\cos\omega_l t. \tag{II–18}$$

Comparison with Eq.(II-15) then yields with Eq.(II-17a) (take $\varphi_l(t) = 0$):

$$\mathbf{R}^{(\mathrm{FAM})}_{\mathrm{RWA}} = (-\kappa\mathcal{E}\cos\Omega t,\, 0,\, \Delta)^T, \tag{II–19}$$

where the subscript indicates that the rotating wave approximation has been made. Incidentally, Eq.(II-19) can be shown to be mathematically equivalent to the result that is obtained for a constant, monochromatic field, such as expressed in Eq.(II-8), and the rotating wave approximation is *not* made. However, to bring out the mathematical similarity, the conventional transformation from Eq.(II-6) must be replaced by the transformation

$$\tilde{\rho}_{12} = \rho_{12}\,e^{i\omega_{12}t} = \tilde{\rho}^*_{21}. \tag{II–20}$$

The resulting expression for the torque $\mathbf{R}$ can be obtained from Eq.(II-17), by setting $\omega_i = \omega_l$, and $\varphi_l(t) = \varphi_i(t) = -\omega_l t$, in which case the (no longer slowly varying) amplitude of the field is given by $\mathcal{E}\cos\omega_l t$ [note that, with these substitutions, the field in Eq.(II-15) is identical to the field in Eq.(II-8)]. Both the terms $\Omega_i^{(+)}$ and $\Omega_i^{(-)}$ in Eqs.(II-17) are now zero, so that Eq.(II-17a) becomes, instead of Eq.(II-14):

$$\mathbf{R}^{(\mathrm{c})} = (-2\kappa\mathcal{E}\cos\omega_l t,\, 0,\, \omega_{12})^T, \tag{II–21}$$

where the superscript (c) denotes a constant, monochromatic field. Eqs.(II-19) and (II-21) are mathematically equivalent indeed, although typical values of the

optical frequencies ω_l and ω_{12} may be eight orders of magnitude larger than the corresponding values of the modulation frequency Ω and the detuning Δ.

II–3 Magnetic Bloch Equations

For a magnetic resonance experiment, such as depicted in Figure II-1 on page 120, the Bloch equations can be expressed in terms of the magnetization $\mathbf{M}$ and the total applied magnetic field $\mathbf{H}$ as [30,31,33,37,45]:

$$\dot{\mathbf{M}} = -\mathbf{\Lambda}\,\mathbf{M} + g_0\beta\,\mathbf{M} \times \mathbf{H} + \mathbf{M}_0/T_P, \tag{II–22}$$

where, in terms of Cartesian coordinates

$$\mathbf{M} = (M_x, M_y, M_z)^T; \qquad \mathbf{H} = (H_x, H_y, H_z)^T. \tag{II–23}$$

In Eq.(II-22), g_0 and β have the same meaning as in Eq.(II-2), $\mathbf{\Lambda}$ denotes a diagonal damping matrix, and the term $\mathbf{M}_0/T_P$ is the pumping rate, in terms of a characteristic pumping time, T_P, and the equilibrium magnetization, $\mathbf{M}_0$, which would be achieved by the optical pumping process in the absence of any magnetic fields. Comparison of Eq.(II-22) with Eq.(II-12) shows a remarkable similarity between the magnetic and optical Bloch equations (with or without the rotating wave approximation). The following correspondences hold:

$$\mathbf{\Phi} \leftrightarrow \mathbf{M}; \tag{II–24a}$$

$$\mathbf{R} \leftrightarrow -g_0\beta\,\mathbf{H}; \tag{II–24b}$$

$$\mathbf{C} \leftrightarrow \mathbf{M}_0/T_P. \tag{II–24c}$$

The correspondence is born out in full if the x, y, z coordinate system in the magnetic resonance experiment is chosen such that the direction of the circularly

polarized pump beam is along the z-axis. Thus

$$\mathbf{M}_0/T_p \sim (0,0,1)^T, \tag{II–25}$$

which has the same nonvanishing component as the inhomogeneous term $\mathbf{C}$ in Eqs.(II-13) for the optical case. With the general expression for the optical torque $\mathbf{R}$ from Eqs.(II-17), it is now easy to establish equivalent magnetic and optical resonance geometries. In particular, the magnetic counterpart of the optical resonance experiment involving a fully amplitude modulated field is that of a so called longitudinally pumped geometry [Figure II-2(a)]. In this geometry, a static Zeeman field $\mathbf{H}_0$ is applied along the z-axis, and an oscillating radiofrequency field is applied orthogonal to the pump beam, say, along the x-axis. Thus, if we denote the modulation frequency and the rf amplitude by Ω and $H_{\rm rf}$, respectively, the total magnetic field can be written as

$$\mathbf{H} = (H_{\rm rf} \cos \Omega t,\, 0,\, H_0)^T, \tag{II–26}$$

which, with Eq.(II-24b), is fully equivalent to Eq.(II-19) [and Eq.(II-21)] indeed. Similarly, the geometries shown in Figures II-2(b) through II-2(f) can be shown to be equivalent to optical resonance experiments involving, respectively, a general amplitude modulated field, a frequency modulated field on resonance, a detuned frequency modulated field, a single constant field, and a bichromatic field with unequal field amplitudes. In Table II-1, the corresponding expressions for the magnetic and optical fields are given, as well as literature references for both the magnetic and optical interactions. These correspondences are quite important to work in the optical regime, because most of the equivalent magnetic resonance geometries have been studied in detail. However, in the much more recent work on

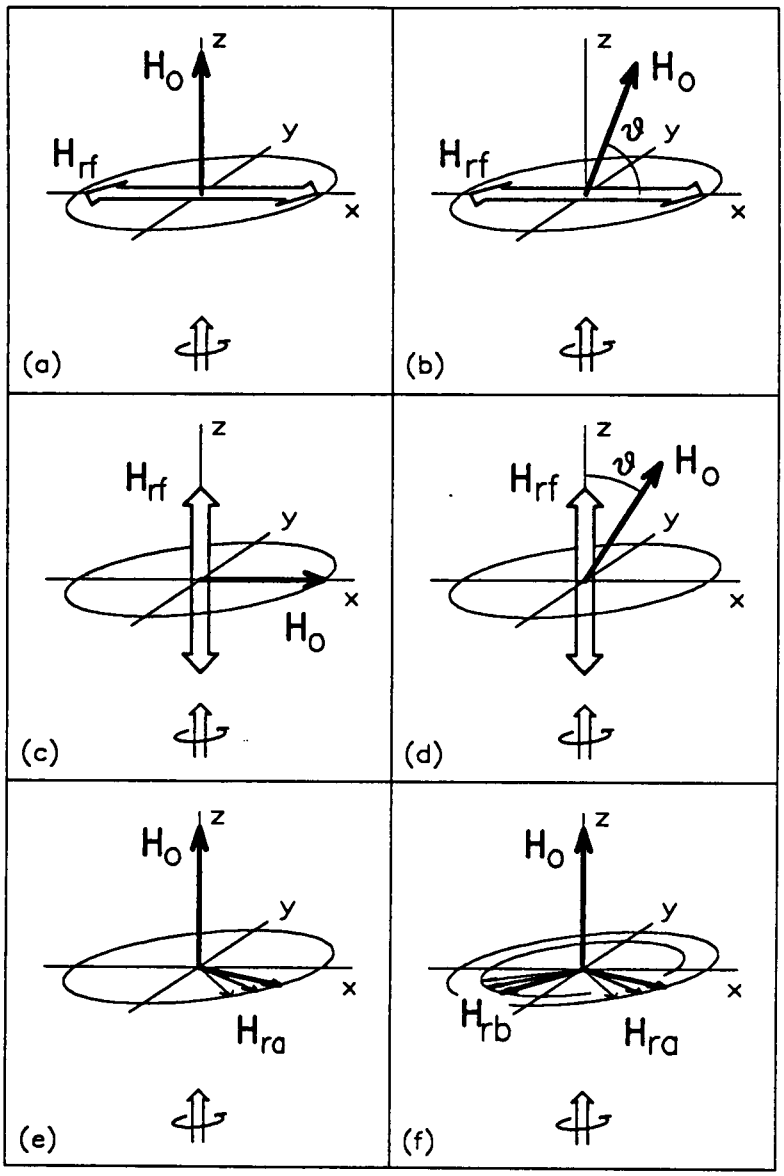


Figure II–2: *Schematic representations of various magnetic resonance configurations.*

In all cases, the circularly polarized pump beam is along the z-axis; $\mathbf{H}_0$, $\mathbf{H}_{rf}$, *and* $\mathbf{H}_{ri}$ $(i \doteq a, b)$) *represent a static field, an oscillating radiofrequency field, and a rotating field, respectively. See also Table II-1.*

Table II–1: *Equivalent magnetic and optical fields.*

Fig. II-2 entry	Equivalent fields and references
(a)	$\begin{cases} \mathbf{H}(t) = (H_{\rm rf}\cos\Omega t, 0, H_0); & [19,42\text{–}44,52,54\text{–}56,58\text{–}63] \\ E(t) = 2\mathcal{E}\cos\Omega t\cos\omega_l t; & [1,5,7,11\text{–}14,21\text{–}23,65\text{–}69] \end{cases}$
(b)	$\begin{cases} \mathbf{H}(t) = (\cos\vartheta H_0 + H_{\rm rf}\cos\Omega t, 0, H_0\sin\vartheta); & [36,38,64] \\ E(t) = 2\mathcal{E}(1 + M\cos\Omega t)\cos\omega_l t; & [8\text{–}10,16\text{–}18,26\text{–}28] \end{cases}$
(c)	$\begin{cases} \mathbf{H}(t) = (H_0, 0, H_{\rm rf}\cos\Omega t); & [33,34,45,46,53,57,63] \\ E(t) = 2\mathcal{E}\cos(\omega_l t + M\sin\Omega t); \quad \Delta = 0; & [\text{none}] \end{cases}$
(d)	$\begin{cases} \mathbf{H}(t) = (H_0\sin\vartheta, 0, H_0\cos\vartheta + H_{\rm rf}\cos\Omega t); & [30,(31),32,37] \\ E(t) = 2\mathcal{E}\cos(\omega_l t + M\sin\Omega t); \quad \Delta \neq 0; & [24\text{–}26] \end{cases}$
(e)	$\begin{cases} \mathbf{H}(t) = (H_{ra}\cos\omega_a t, H_{ra}\sin\omega_a t, H_0); & [(50),51] \\ E(t) = 2\mathcal{E}\cos\omega_a t; & [23] \end{cases}$
(f)	$\begin{cases} \mathbf{H}(t) = (\sum\limits_{i=a,b} H_{ri}\cos\omega_i t, \sum\limits_{i=a,b} H_{ri}\sin\omega_i t, H_0); & [20,39,(40,41)] \\ E(t) = 2\mathcal{E}_a\cos\omega_a t + 2\mathcal{E}_b\cos\omega_b t; & [15,29,70] \end{cases}$

optical resonance, these correspondences have not always been exploited, leading to the proverbial reinvention of the wheel [21,26].

II–4 Resonance Behavior

In Section III, we present a detailed discussion of the resonance behavior of a two-level system under the influence of either a fully amplitude modulated optical

field, or a combination of static and oscillating magnetic fields such as depicted in Figure II-2(a). Although such discussion has been presented previously, it has focused mostly on the time-averaged resonance behavior of the system (that is, the resonance behavior of the time-averaged absorption or fluorescence signal, as opposed to modulated components of these quantities). This is particularly true for those cases where the fields are sufficiently strong to cause saturation effects. Thus, the study of modulated interaction components has not received much attention. Before addressing this problem in detail in Section III, we review here the known features of the time-averaged resonance behavior, particularly the occurrence of multiple quantum resonances, and the shifts of these resonances as a function of the field strength.

II–4.1 Multiple quantum resonances

Consider once again the fully amplitude modulated field from Eq.(II-18). This field may be written alternatively as

$$E^{(\mathrm{FAM})}(t) = \mathcal{E}\,\cos\omega_+ t + \mathcal{E}\,\cos\omega_- t, \tag{II–27a}$$

where

$$\omega_\pm = \omega_l \pm \Omega. \tag{II–27b}$$

Thus the FAM field can be considered as a bichromatic field with equal intensities in the two modes. From Eq.(II-27) it is evident that, at least in the weak field limit, resonance occurs when either of the two frequencies ω_+ or ω_- is equal to the atomic transition frequency ω_{12}, that is, if the detuning Δ from Eq.(II-1) is equal to the modulation frequency:

$$\Delta = \pm\Omega. \tag{II–28}$$

For strong fields, however, additional resonances occur, namely by absorption of $n_a > 1$ photons, and stimulated emission of $(n_a - 1)$ photons. Some of these multi-photon or multiple quantum resonances are shown in Figure II-3. For these processes, the generalized (weak field) resonance condition becomes

$$n_a \omega_{\pm} - (n_a - 1)\omega_{\mp} = \omega_{12}, \qquad \text{(II–29)}$$

or, with Eqs.(II-1) and (II-27b):

$$\Delta = \pm(2n_a - 1)\Omega = \pm N\,\Omega, \qquad \text{(II–30)}$$

where $N = 2n_a - 1$ is the total number of photons, and is refered to as the quantum number of the resonances. Although our discussion has been for an optical interaction, the same principle applies to a magnetic resonance experiment, and the same multiple quantum resonance condition exists, except that the quantities Δ in Eqs.(II-28) and (II-30) are to be interpreted as the Zeeman splitting of the two-level atom, defined in Eq.(II-2), and Ω is now the frequency of the magnetic rf field. In both the magnetic and optical regimes, the quantum number of the resonances is, by definition, an odd integer (by contrast, the transversely pumped magnetic resonance geometry from Figure II-2(c) or its optical equivalent are characterized by virtual transitions involving even numbers of photons, and the corresponding resonances are refered to as Haroche resonances [53]).

II–4.2 Bloch-Siegert shifts

As early as 1940, it was realized that the resonance condition from Eq.(II-28) is modified in the presence of strong driving fields [20]. After their discoverers, the corresponding resonance shift is known as the Bloch-Siegert shift. The original calculation of this shift involved only the lowest order correction to the resonance

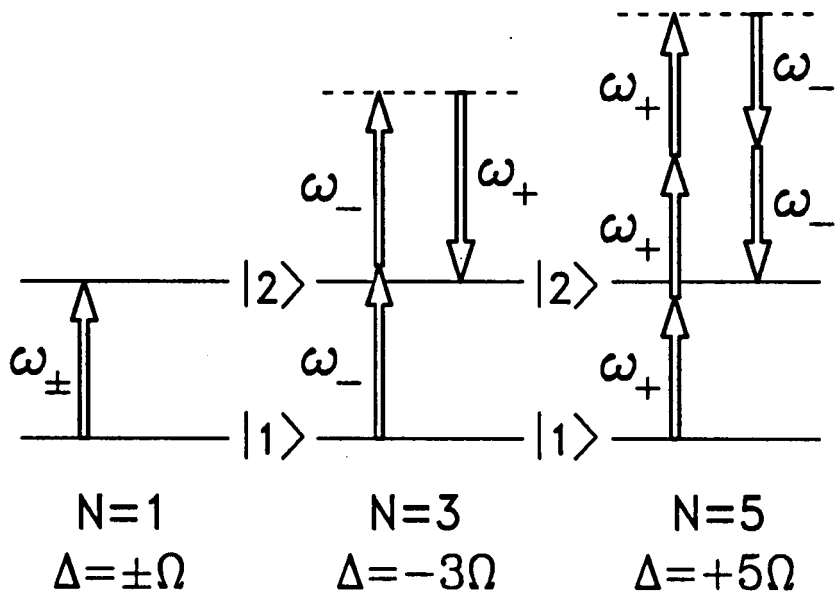


Figure II–3: *Illustration of multiple quantum resonances in an optical two-level system.*

condition of the main resonance ($N = 1$) from Eq.(II-28). For the longitudinally pumped magnetic resonance geometry from Eq.(II-26) it is given by:

$$\Delta = g_0 \beta H_0 = \pm\Omega\left[1 - \left(\frac{g_0 \beta H_{\rm rf}}{4\Omega}\right)^2\right] \qquad \text{(II–31a)}$$

Subsequently, the designation "Bloch-Siegert shift" has been used to denote the shift in the resonance condition for an optical resonance experiment due to the counter-rotating term in the optical Bloch equations from Eqs.(II-9), which, in the rotating wave approximation, is neglected. Indeed, by comparing Eq.(II-26) to Eq.(II-21), it is clear that the equivalent of Eq.(II-31a) for an optical resonance experiment involving a constant, monochromatic field is given by [48]:

$$\Delta = \omega_{12} - \omega_l = -\frac{(\kappa \mathcal{E})^2}{\omega_l}, \qquad \text{(II–31b)}$$

where $\mathcal{E}$ and ω_l are defined in Eq.(II-8). Typical values for this optical Bloch-Siegert shift can be obtained by setting $\kappa = ea_0/\hbar$, where e is the electron charge

and a_0 is the Bohr radius. With $\omega_l = 3 \times 10^{15}$ s^{-1} and an electric field amplitude that corresponds to a narrowband, 100 mW beam focused to a spot size with a diameter of 10 μm (about the strongest narrowband field achievable with state-of-the-art dye lasers), Eq.(II-31b) yields a Bloch-Siegert shift of only 0.5 MHz, which is an order of magnitude smaller than a typical homogeneous linewidth ($\simeq$ 10 MHz), and about equal to the best obtainable laser linewidths. Thus, it will be extremely difficult to measure this shift experimentally. Indeed, no such experiments have been reported to our knowledge.

The situation is quite different, however, for an optical resonance experiment involving a fully amplitude modulated field. Comparison of Eq.(II-26) with Eq.(II-19) shows that, in this case, the shift corresponding to Eq.(II-31a) is given by

$$\Delta = \pm\Omega\left[1 - \left(\frac{\kappa\mathcal{E}}{4\Omega}\right)^2\right], \qquad \text{(II–31c)}$$

where $\mathcal{E}$ and Ω are defined in Eq.(II-18). If we again set $\kappa = ea_0/\hbar$ it is easily calculated that, in order for the term $\kappa\mathcal{E}/4\Omega$ to be unity, only a 0.25 mW beam with a spot size of 1 mm is needed if the modulation frequency is 10 MHz. Of course, if $\kappa\mathcal{E}/4\Omega$ is unity, higher order correction terms to the resonance shift must be included. But the point is that in a FAM optical interaction, the Bloch-Siegert shift should be easily detectable. Recently, a group at the University of Rochester indeed reported such measurements, although — perhaps unfamiliar with the equivalent magnetic resonance experiments — the term Bloch-Siegert shift was not used in their work, nor was the concept of multiple quantum resonances, although these were clearly observed [14]. For a discussion see Ref.[21].

Around 1973, there was a flurry of activity to calculate higher and higher terms of the (magnetic) Bloch-Siegert shifts, using both semi-classical [60] and fully quantum mechanical calculations [59,71]. Also, expressions for the shifts

of multiple quantum resonances for quantum numbers $N > 1$ were calculated by several authors [58,61–63], and some calculations were performed for systems more complicated than a simple two-level system [72,73]. Here we suffice by giving the expressions for the shifts of the $N = 1$, $N = 3$, and $N = 5$ resonances. Conforming to the conventional notation from the magnetic resonance literature, we write [cf. Eq.(II-31a)]:

$$\frac{\omega_0}{\omega} = \frac{g_0 \beta H_0}{\Omega}; \qquad \frac{b}{\omega} = \frac{g_0 \beta H_{rf}}{\Omega}. \tag{II–32}$$

Thus, the resonance conditions for the $N = 1$, $N = 3$, and $N = 5$ multiple quantum resonances are given, respectively, by [61–63]:

$$\left(\frac{\omega_0}{\omega}\right)^2 = 1 - 2\left(\frac{b}{\omega}\right)^2 - \frac{3}{2}\left(\frac{b}{\omega}\right)^4 - \frac{21}{16}\left(\frac{b}{\omega}\right)^6 - \frac{63}{64}\left(\frac{b}{\omega}\right)^8 - \frac{193}{384}\left(\frac{b}{\omega}\right)^{10} \ldots, \tag{II–33a}$$

$$\left(\frac{\omega_0}{\omega}\right)^2 = 3^2\left[1 - \left(\frac{b}{\omega}\right)^2 + \frac{1}{16}\left(\frac{b}{\omega}\right)^4 + \frac{173}{1152}\left(\frac{b}{\omega}\right)^6 + \frac{4037}{36864}\left(\frac{b}{\omega}\right)^8 \ldots\right], \tag{II–33b}$$

and

$$\left(\frac{\omega_0}{\omega}\right)^2 = 5^2\left[1 - \frac{1}{3}\left(\frac{b}{\omega}\right)^2 + \frac{5}{432}\left(\frac{b}{\omega}\right)^4 - 0.00138\left(\frac{b}{\omega}\right)^6 \ldots\right]. \tag{II–33c}$$

Note that Eq.(II-33a) agrees with Eqs.(II-31) upon taking the square root. Quite generally, Bloch-Siegert shifts for arbitrary values of the rf amplitude are obtained by numerically solving for the zeros of a continued fraction [24,25,28,63], as is explained in detail in Section III. The results of such a calculation are displayed in Figure II-4 by plotting the calculated positions of some of the odd, multiple quantum resonances as a function of the quantities ω_0/ω and $4b/\omega$ from Eq.(II-32). For $(b/\omega) << 1$, the limiting behavior of the curves in Figure II-4 is given by the equivalent of Eq.(II-30), namely by $\omega_0/\omega = \pm N$ (only the positive branches are displayed in Figure II-4). For sufficiently strong rf fields, the resonances actually disappear, namely at values of $4b/\omega$ equal to the zeros of the zeroth order Bessel function. This well known result is also discussed in more detail in Section III.

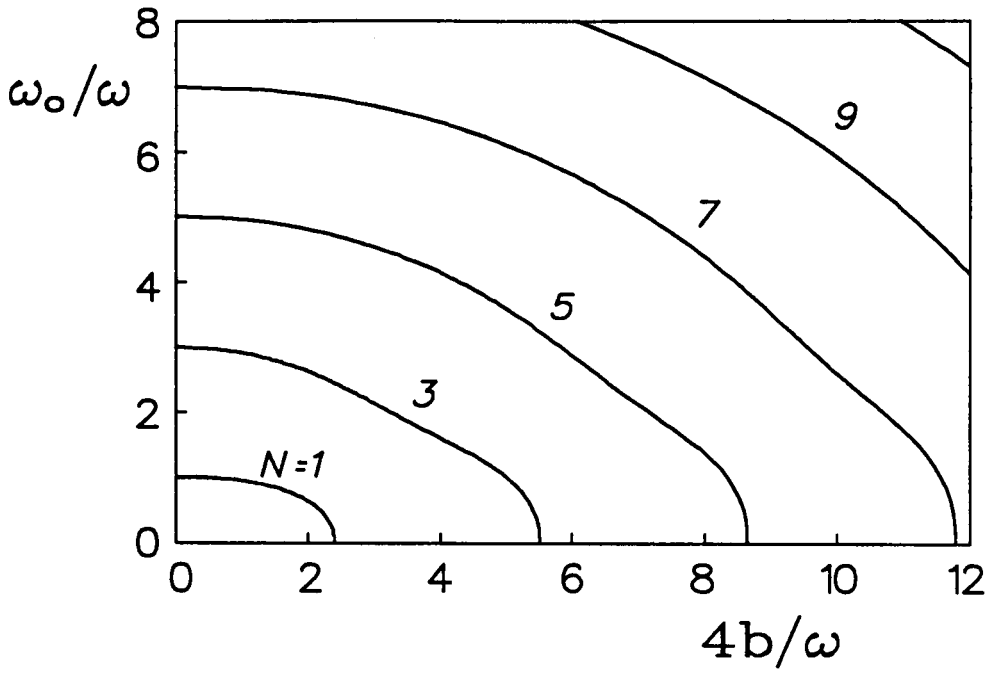


Figure II–4: *Bloch-Siegert resonance curves for a longitudinally pumped magnetic resonance experiment.*

Somewhat surprisingly, an aspect that has *not* received much attention in the literature is the resonance behavior of modulated interaction components. Herein lies the novelty of the work presented in Section III. For example, it is shown that, for modulated components, the Bloch-Siegert resonance curves become split. However, part of the mission of this work has also been to point out that the concepts of multiple quantum resonances and Bloch-Siegert shifts are directly applicable to optical resonance experiments involving modulated fields.

III RESONANCE BEHAVIOR OF A TWO-LEVEL ATOM IN A FULLY AMPLITUDE MODULATED FIELD

Section III addresses in detail the steady-state resonance behavior of a two-level atom driven by a narrowband, fully amplitude modulated, optical field. The material in Section III is taken from Ref. [28], which is reproduced here in essentially unmodified form. Only a few changes have been made, mostly in Section III-1, to provide continuity with Section II.

III–1 Motivation and Organization

In Section II, we have shown that the problem of an optical two-level atom interacting with a fully amplitude modulated field is formally identical to that of a longitudinally pumped magnetic resonance experiment. Also, we have reviewed the occurrence of multiple quantum resonances and the Bloch-Siegert shifts of these resonances with increasing field strengths. In 1972 Stenholm showed that, for this longitudinally pumped magnetic resonance experiment, the solution of the Bloch equations can be obtained in terms of scalar continued fractions for arbitrary rf amplitudes [54,55]. Unlike Shirley's earlier characteristic exponent method, which is based on diagonalization of the Floquet Hamiltonian, and does not include relaxation effects [52], Stenholm's theory not only gives the solution for the time-averaged (DC) behavior, but for modulated interaction components as well. However, expressions for the Bloch-Siegert shifts of the multiple quantum resonances as given in Section II-4.2, derived from Stenholm's theory or otherwise have been calculated for the DC fluorescence and absorption components only [58–63]. This is surprising because, concurrent with the development of the theory,

experimental work was performed in which modulated signals rather than DC signals were measured [42]. In their brief theoretical treatment, Arimondo and Moruzzi conclude that "... the same Bloch-Siegert shift is displayed by both the stationary term and the time dependent term [at twice the modulation frequency] at low intensities of the rf field ...," but that "... on the contrary, a different behavior is observed at higher fields ..." [42]. Thus, although it was recognized that the resonance behavior of modulated interaction components deviates from that of the DC behavior in general, no detailed analysis was performed.

By now, activities in the field of magnetic resonance have largely ceased. However, the mathematically identical problem that has emerged in the field of optical resonance, namely the interaction of a fully amplitude modulated (FAM), narrowband laser with an optical two-level atom is of considerable current interest. In 1976 Feneuille *et al.* solved the problem for strong, resonant excitation [7]. At about the same time, Thomann performed both theoretical and experimental work for a not fully amplitude modulated laser [16,17]. Then in 1984 Hillman *et al.* showed that the theory of a FAM interaction successfully describes the bichromatic operation of a homogeneously broadened laser [12,13]. But particularly, just recently Chakmakjian *et al.* reported experimental results for a FAM interaction in which multiple quantum resonances were directly observed (although they were not interpreted as such), namely as subharmonic resonances in the DC fluorescence signal from a beam of sodium atoms [14].

Conceivably, an experiment like that of Chakmakjian *et al.* could be performed, in which not the DC fluorescence but modulated components of the fluorescence would be detected. In fact, measurement of the fluorescence at the beat frequency of a modulated driving field forms the basis for many fluorometric techniques, and accounts for our interest in the subject [1,11,65]. Thus we inves-

tigate the influence of multiple quantum resonances on the harmonic behavior of a two-level system, driven by a FAM field. In the following we assume an optical resonance experiment — the treatment for a longitudinally pumped magnetic experiment would be identical.

In Section III-2 we review Stenholm's continued fraction solution and the Bessel function solution for zero detuning. To illustrate the resonance behavior of harmonic components we compute results for the DC fluorescence and the lowest fluorescence harmonic, and show that the corresponding multiple quantum resonances are singly and doubly branched, respectively. In Section III-3 we take the vanishing damping limit of the continued fraction solution and generalize the Bessel function result from Section III-2. In passing we show that, in the vanishing damping limit, a DC population inversion of the two-level system by optical pumping alone is impossible. Using the solution from Section III-3 we derive in Section III-4 the doubly branched structure of the multiple quantum resonances explicitly, and calculate expressions for the generalized Bloch-Siegert shifts of *all* harmonics. Finally, in Section III-5, we conclude with a discussion on practical implications and possible experimental verification of the theory.

III–2 General Solution

Following the notation of Allen and Eberly [48] we write the optical Bloch equations for a two-level atom interacting with an electric field of amplitude $\mathcal{E}(t)$ as in Eqs.(II-9), and make the rotating wave approximation:

$$\dot{U} = -U/T_2 - \Delta V, \tag{III–1a}$$

$$\dot{V} = -V/T_2 + \Delta U + \kappa \mathcal{E}(t) W, \tag{III–1b}$$

$$\dot{W} = -(W - W_{\mathrm{eq}})/T_1 - \kappa \mathcal{E}(t) V, \tag{III–1c}$$

where Δ is the detuning, κ is the dipole coupling constant, $W_{\rm eq}$ is the equilibrium inversion, and T_1 and T_2 are the longitudinal and transverse relaxation times. Assuming that the field is fully amplitude modulated at frequency Ω, we write the time-dependent Rabi frequency as [cf. Eq.(II-18)]

$$\kappa\mathcal{E}(t) = 2g\cos\Omega t. \tag{III-2}$$

Below we refer to the constant g simply as "the Rabi frequency." To allow for unequal damping rates for the susceptibility components U and V (as is generally the case in the equivalent magnetic resonance geometry) we replace the damping rates $1/T_2$, $1/T_2$, and $1/T_1$ in Eqs.(III-1) by Γ_u, Γ_v, and Γ_w, respectively. Also we choose alternative definitions for the components of the Bloch vector, for ease of notation below:*

$$u = -U; \qquad v = -iV; \qquad w = -W. \tag{III-3}$$

Thus v corresponds to the difference between (rather than the imaginary part of) the rotating-frame off-diagonal density matrix elements [cf. Eqs.(II-5)], and an inverted system is characterized by values $w < 0$. Finally, because the solution of Eqs.(III-1) scales linearly with $W_{\rm eq}$ we assume — without loss of generality — that $W_{\rm eq} = -1$. The Bloch equations from Eqs.(III-1) now become:

$$\dot{u} + \Gamma_u u = i\Delta v, \tag{III-4a}$$

$$\dot{v} + \Gamma_v v = i\Delta u + 2igw\cos\Omega t, \tag{III-4b}$$

$$\dot{w} + \Gamma_w w = 2igv\cos\Omega t + \Gamma_w. \tag{III-4c}$$

By the Floquet theorem the steady-state solution of Eqs.(III-4) can be written as

$$z(t) = \sum_{k=-\infty}^{\infty} z_k \exp(ik\Omega t); \qquad z = u, v, w. \tag{III-5}$$

---

*With these choices the vanishing damping expressions for the combined Floquet coefficients ψ_k from Eq.(III-7) do not have to differentiate between odd and even indices.

Substitution of Eq.(III-5) into Eqs.(III-4) yields a set of recurrence relations between the Floquet coefficients. As was first shown by Stenholm these recurrence relations can be solved in terms of scalar continued fractions [54,74]. Specifically, because even terms v_k and odd terms w_k vanish, and because the u_k's follow simply from the v_k's by

$$u_k = i\Delta v_k/(\Gamma_u + ik\Omega), \tag{III-6}$$

it suffices to solve for the combined coefficients

$$\psi_k = \begin{cases} v_k; & k = \text{odd}, \\ w_k; & k = \text{even}. \end{cases} \tag{III-7}$$

Thus Eqs.(III-4) can be reduced to a single, three term recurrence relation:

$$a_k\,\psi_k - ig\left(\psi_{k-1} + \psi_{k+1}\right) = \Gamma_w \delta_{k,0},$$

where

$$a_k = \begin{cases} \Gamma_v + ik\Omega + \dfrac{\Delta^2}{\Gamma_u + ik\Omega}; & k = \text{odd}, \\ \Gamma_w + ik\Omega; & k = \text{even}. \end{cases} \tag{III-8}$$

From this recurrence relation the quantities x_k, defined as $x_k = \psi_k/\psi_{k-1}$, can be obtained as continued fractions by backward iteration of

$$x_k = \left[a_k/ig - x_{k+1}\right]^{-1}; \qquad k \geq 1. \tag{III-9}$$

For accurate results the backward iteration should be started at a value of k no smaller than $(\Delta^2 + 4g^2)^{1/2}$. For $k \leq 0$ it can be shown that $x_k^{-1} = -x_{1-k}^*$. Thus the solution for the DC component becomes

$$\psi_0 = \left[1 + 2g\,\mathrm{Im}\{x_1\}/\Gamma_w\right]^{-1}. \tag{III-10}$$

Once the x_k's and ψ_0 have been determined, the harmonic components are obtained by forward recursion:

$$\psi_k = x_k \psi_{k-1}; \qquad k \geq 1. \tag{III-11}$$

For negative indices one finds

$$\psi_k = (-1)^k \psi^*_{-k}; \qquad k \leq 0, \tag{III-12}$$

which follows also from the fact that $v(t)$ and $w(t)$ are imaginary and real, respectively. With Eqs.(III-5)–(III-12) the steady-state solution of Eqs.(III-4) is completely determined.

For the special case $\Delta = 0$ and equal damping rates, i.e., $\Gamma_v = \Gamma_w$, Eqs.(III-4) can be solved analytically in terms of integer order Bessel functions [7,10,16,54–57,63]. If the results for $v(t)$ and $w(t)$ are expanded as a Floquet series as in Eq.(III-5), and the coefficients from Eq.(III-7) are denoted by ϕ_k, i.e.,

$$\phi_k \equiv \psi_k(\Delta = 0; \Gamma_v = \Gamma_w), \tag{III-13a}$$

one obtains (see Appendix A):

$$\phi_k = \sum_{l=-\infty}^{\infty} \frac{J_l(2g/\Omega) J_{k+l}(2g/\Omega)}{1 - il\Omega/\Gamma_w}. \tag{III-13b}$$

In the limit of vanishing damping only one term out of the infinite sum from Eq.(III-13b) contributes, yielding the simple result

$$\phi^0_k \equiv \lim_{\Gamma_w \to 0} \phi_k = J_0(2g/\Omega) J_k(2g/\Omega). \tag{III-14}$$

Eq.(III-14) provides an important clue about the resonance behavior of harmonic components of the interaction. That is, for $k \neq 0$, ϕ^0_k shares one set of zeros with the DC term ϕ^0_0, namely those of $J_0(2g/\Omega)$, but also contains an extra set of zeros, namely those of $J_k(2g/\Omega)$.

To illustrate the resonance behavior of the system we have computed several fluorescence components. The fluorescence signal is proportional to the upper

state population $\rho_{22}(t)$, which, by Eqs.(II-5c), (III-3), (III-5), (III-7), and (III-12), can be written as a Floquet series:

$$\rho_{22}(t) = \frac{1 - w(t)}{2} = \frac{1 - \psi_0}{2} - \frac{1}{2}\sum_{k=1}^{\infty}\left\{\psi_{2k}e^{2ik\Omega t} + \text{c.c.}\right\}. \qquad \text{(III–15)}$$

Thus, Figure III-1 displays the DC fluorescence component, $(1 - \psi_0)/2$, and the in-phase component $\text{Re}\{-\psi_2\}$ of the lowest fluorescence harmonic. The respective values were obtained from the continued fraction solution of Eqs.(III-8)–(III-11), and are displayed in Figure III-1 as a function of the scaled Rabi frequency and the scaled detuning, for small values of the damping ($\Gamma_u = \Gamma_v = \Gamma_w/2 = \Omega/10$). It is obvious that, in general, this resonance behavior is quite complicated. Figure III-2 shows similar results for a cross-section through Figure III-1 at a particular value of the interaction strength, namely $2g/\Omega = 4$. In Figure III-2, different curves correspond to different values of the damping, where it has been assumed that $\Gamma_u = \Gamma_v = \Gamma_w$. The solid curves are for a vanishingly small damping, namely $\Gamma_w/\Omega = 10^{-8}$. Their limiting values for $\Delta = 0$ are correctly given by Eq.(III-14), namely by $(1 - J_0^2(4))/2 \simeq 0.421$ and $|J_0(4)J_2(4)| \simeq 0.145$ for the DC and modulated fluorescence components, respectively.

In Figure III-2, the solid curve for the DC fluorescence component is identical to Figure 4 in Shirley's seminal paper [52], and displays clearly the $N = 3$ and $N = 5$ multiple quantum resonances. For arbitrary values of $2g/\Omega$ the positions of these resonances, whose deviations from the weak-field values are known as the Bloch-Siegert shifts, may be obtained by any of the methods of Refs. [58–63], or from the theory in Section III-4. The results are displayed as the projections (solid curves) in Figure III-1 (see Figure II-4 on page 137 also), which, in accordance with Eq.(III-14), intersect the $2g/\Omega$-axis at zeros of the zeroth order Bessel function. The limiting behavior for small interaction strengths, namely Δ/Ω equals an odd

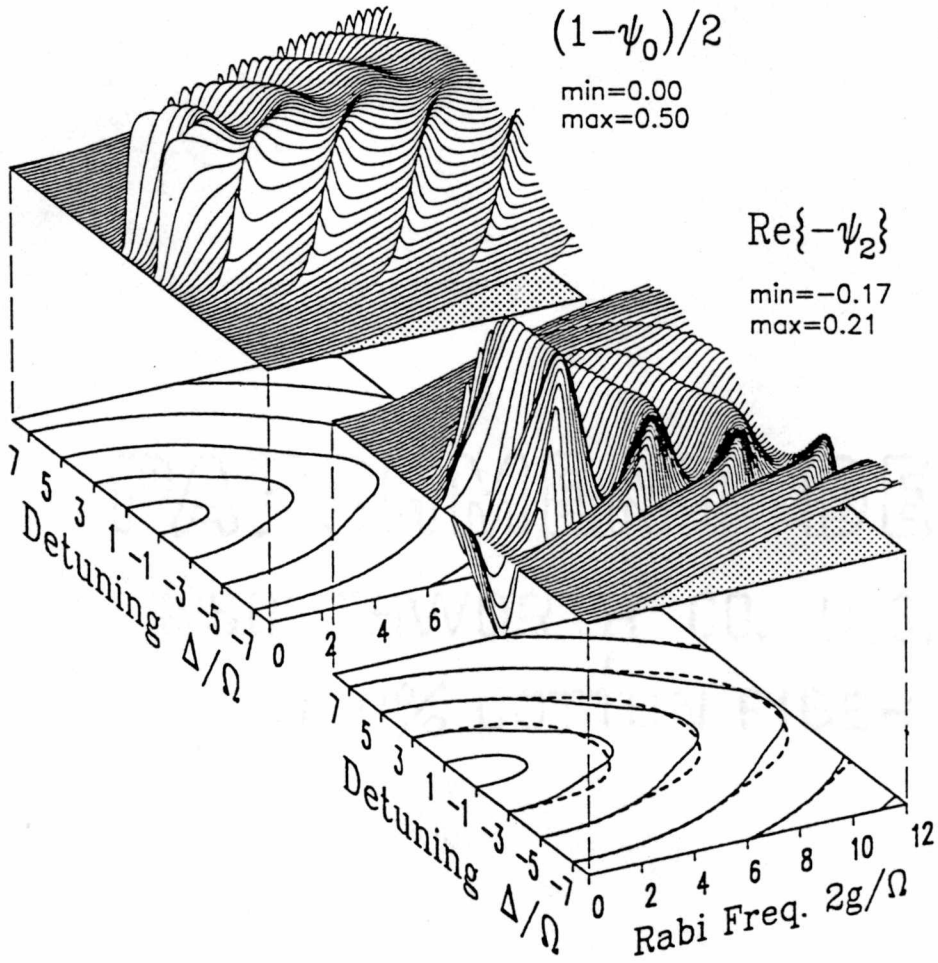


Figure III–1: *DC fluorescence and in-phase component of the lowest fluorescence harmonic as a function of the Rabi frequency and the detuning.*

Values of $(1-\psi_0)/2$ *(upper left) and* $\mathrm{Re}\{-\psi_2\}$ *(lower right) are displayed for* $\Gamma_u = \Gamma_v = \Gamma_w/2 = \Omega/10$. *Minimum [maximum] values are 0.00 [0.50] and -0.17 [0.21], for the DC and modulated components, respectively. Projections of the maxima of* $(1-\psi_0)/2$ *and the zeros of* $\mathrm{Re}\{-\psi_2\}$ *(intersections with the shaded plane) are shown in the limit* $\Gamma_u, \Gamma_v, \Gamma_w \to 0$.

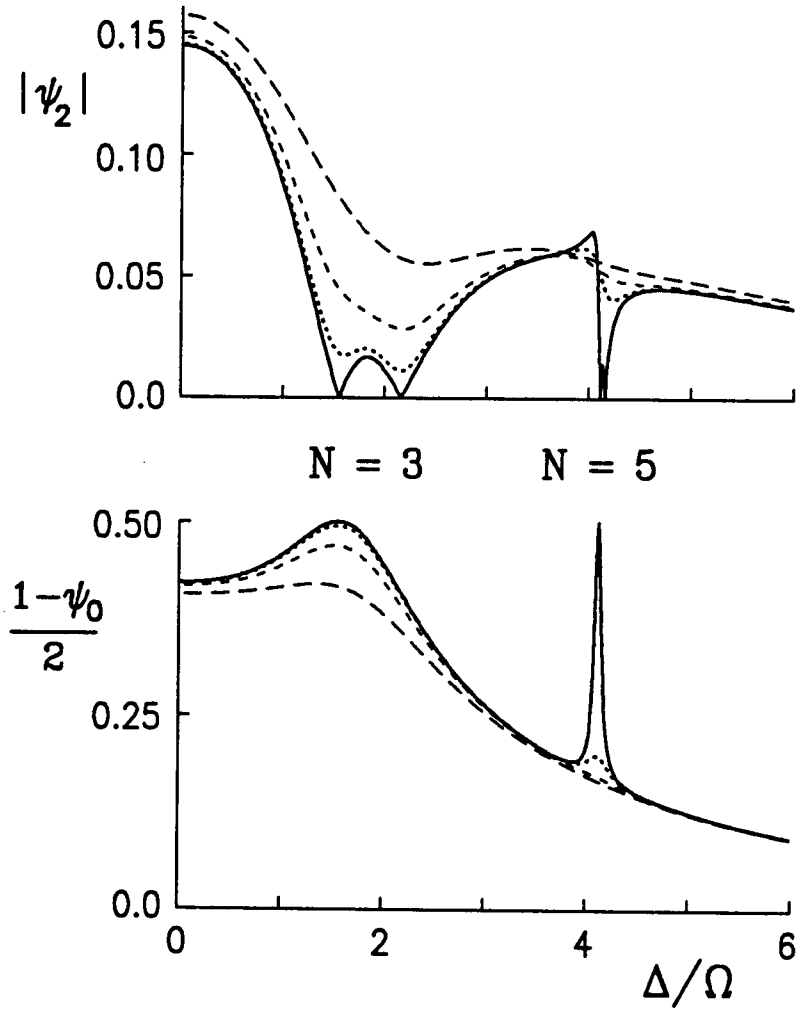


Figure III–2: *DC fluorescence and in-phase component of the lowest fluorescence harmonic as a function of the detuning for a fixed Rabi frequency.*

As Figure III-1, for a fixed Rabi frequency ($2g/\Omega = 4$). *Solid and dashed curves are for damping rates* $\Gamma_u/\Omega = \Gamma_v/\Omega = \Gamma_w/\Omega = 10^{-8}$, 0.1, 0.25, *and* 0.50, *respectively. Note the singly- and doubly-branched structures of the* $N = 3$ *and* $N = 5$ *multiple quantum resonances for the DC and modulated components, respectively.*

integer N for the N-quantum resonance, is either explained mathematically by the vanishing of the odd terms a_k from Eq.(III-8) in the zero damping limit, or is explained physically in terms of N-photon resonances, as explained in Section II-4.1.

Further inspection of Figure III-2 suggests that the statement following Eq.(III-14) can be generalized to the case $\Delta \neq 0$. That is, in the limit of vanishing damping, $|\psi_2|$ vanishes if ψ_0 does, so that the DC multiple quantum resonances are present in the modulated component as well. However, $|\psi_2|$ also has additional zeros which, so it appears, can be labeled with the same quantum numbers. Indeed, numerical calculation shows that all multiple quantum resonances of the ψ_2 component are doubly branched, except the $N = 1$ resonance. In Figure III-1 the locations of the additional branches of the fluorescence component at 2Ω are indicated by projections given by the dashed curves, which intersect the $2g/\Omega$-axis at zeros of the second-order Bessel function. For small interaction strengths the branches have the same limiting behavior (namely $\Delta/\Omega =$ odd N) so that the two parts of any branch are associated with the same quantum number indeed.

Before deriving the doubly branched structure of the Bloch-Siegert shifts explictly we note that, even in the limit of vanishing damping, the values of the Floquet coefficients depend generally on the ratios of the damping terms. This is illustrated for the fluorescence harmonic at 2Ω in Figure III-3, in which the solid curve with $\Gamma_u = \Gamma_v = \Gamma_w = 10^{-8}\Omega$ is identical to the upper solid curve from Figure III-2. The other two curves in Figure III-3 are for $\Gamma_u = \Gamma_v = 10^{-8}\Omega$, and $\Gamma_v/\Gamma_w = 0.5$ and $\Gamma_v/\Gamma_w = 2$, respectively. Indeed, the values of $|\psi_2|$ *do* depend on the damping ratio Γ_v/Γ_w. However, the zeros of $|\psi_2|$ seem to be independent of this ratio, a result which we show to be generally valid in Sections III-3 and III-4.

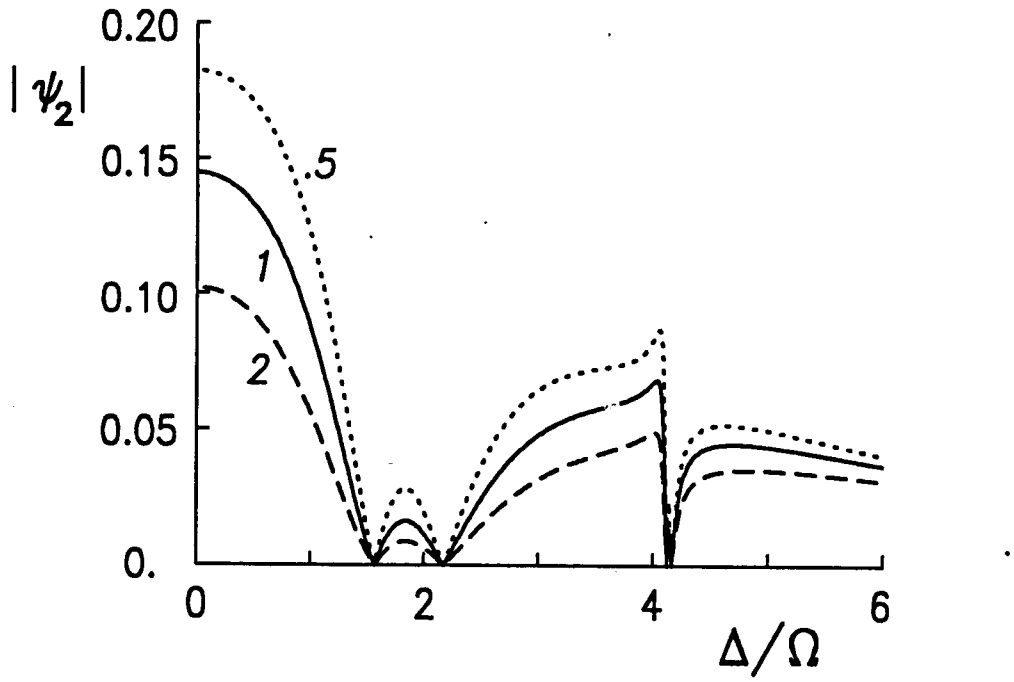


Figure III–3: *Detuning scans of the lowest fluorescence harmonic for various damping ratios.*

As the top of Figure III-2. Curves are for $\Gamma_u/\Omega = \Gamma_v/\Omega = 10^{-8}$, *but different values of the damping ratios* Γ_v/Γ_w, *as indicated. Note that the values of* $|\psi_2|$, *but not the positions of its zeros, depend on the ratio* Γ_v/Γ_w.

III–3 Vanishing Damping Solution

The theory from Section III-2 is well known, although it has been applied only sparingly to the study of modulated interaction components. Neither has it been applied to the study of an ideal atom, namely one that is undamped and interacts only with (is dressed by) the electomagnetic field. Thus, in Section III-3, we evaluate the Floquet coefficients u_k, v_k, and w_k from Eq.(III-5) in the limit of vanishing damping. That is, we calculate the coefficients

$$z_k^{\mathrm{VDCF}} \equiv \lim_{\Gamma_w \to 0} z_k \Big|_{\gamma_u, \gamma_v}; \qquad z = u, v, w. \tag{III–16}$$

As indicated, the limit is taken for fixed values of the damping ratios $\gamma_u \equiv \Gamma_u/\Gamma_w$ and $\gamma_v \equiv \Gamma_v/\Gamma_w$. Because we obtain this limit from the continued fraction solution of Eqs.(III-8)–(III-11), we refer to it as the vanishing damping continued fraction (VDCF) limit. As has been noted by Stenholm one cannot simply set the damping rates in Eq.(III-8) equal to zero, because the continued fractions x_k from Eq.(III-9) would become purely real and the ratio $\mathrm{Im}\{x_1\}/\Gamma_w$ in Eq.(III-10) would be undetermined. Thus we develop the x_k's to lowest order in the damping Γ_w:

$$x_k = x_k^{[0]} + (i\,\Gamma_w/g)\,x_k^{[1]} + O(\Gamma_w^2). \tag{III–17}$$

The factor i/g has been included for notational convenience below. By substituting Eqs.(III-8) and (III-17) into Eq.(III-9) and sorting out terms that are of the same order in the damping, recurrence relations for the $x_k^{[0]}$'s and $x_k^{[1]}$'s are obtained. Of course the $x_k^{[0]}$'s are just the x_k's for zero damping. That is,

$$x_k^{[0]} = \left[f_k - x_{k+1}^{[0]}\right]^{-1}; \qquad k \geq 1, \tag{III–18}$$

with

$$f_k = a_k(\Gamma_u = \Gamma_v = \Gamma_w = 0)/ig = (k\Omega/g) \times \begin{cases} 1-(\Delta/k\Omega)^2; & k = \text{odd}, \\ 1; & k = \text{even}. \end{cases} \tag{III–19}$$

Having obtained the $x_k^{[0]}$'s, the $x_k^{[1]}$'s follow by recursion of

$$x_k^{[1]} = \left(x_k^{[0]}\right)^2 \left[g_k + x_{k+1}^{[1]}\right]; \qquad k \geq 1, \tag{III–20}$$

where

$$g_k = \begin{cases} \gamma_v + \gamma_u(\Delta/k\Omega)^2; & k = \text{odd}, \\ 1; & k = \text{even}, \end{cases} \tag{III–21}$$

with γ_u and γ_v as defined following Eq.(III-16). All quantities in Eqs.(III-18)–(III-21) are real. Thus, with Eqs.(III-10) and (III-17), the VDCF result for the DC component becomes:

$$\psi_0^{\mathrm{VDCF}} = \left[1 + 2x_1^{[1]}\right]^{-1}. \tag{III–22}$$

By iteration of Eq.(III-20) $x_1^{[1]}$ can be expressed solely in terms of the $x_k^{[0]}$'s:

$$x_1^{[1]} = \sum_{k=1}^{\infty} g_k \, p_k^2, \tag{III-23}$$

where

$$p_k \equiv \prod_{l=1}^{k} x_l^{[0]}. \tag{III-24}$$

Because the g_k's from Eq.(III-21) are nonnegative it follows from Eqs.(III-22)–(III-23) that

$$\psi_0^{\mathrm{VDCF}} \geq 0.$$

With Eq.(III-7) ψ_0 is identified as the time-averaged population difference. Thus, in the VDCF limit, a DC population inversion of the two-level system is impossible for all values of the interaction strength, detuning, and damping ratios.

With Eqs.(III-11) and (III-24) the VDCF solution for the harmonic components becomes:

$$\psi_k^{\mathrm{VDCF}} = p_k \, \psi_0^{\mathrm{VDCF}}; \qquad k \geq 1. \tag{III-25}$$

Thus, with Eq.(III-7), all nonvanishing coefficients v_k and w_k are determined. The corresponding nonvanishing coefficients u_k are simply found from Eq.(III-6):

$$u_k^{\mathrm{VDCF}} = (\Delta/k\Omega) \, \psi_k^{\mathrm{VDCF}}; \qquad k = \text{odd}. \tag{III-26}$$

Eqs.(III-18)–(III-26) constitute the complete VDCF solution. Because all involved quantities are real, an algorithm based on Eqs.(III-18)–(III-21) requires fewer multiplications to compute the Floquet coefficients than the corresponding algorithm from Section III-2, which would involve complex quantities.

For the special case $\Delta = 0$ all coefficients f_k from Eq.(III-19) are given by $k\Omega/g$, so that the continued fractions $x_k^{[0]}$ from Eq.(III-18) can be summed analytically [75]:

$$x_k^{[0]}(\Delta = 0) = J_k(2g/\Omega)/J_{k-1}(2g/\Omega).$$

Thus, with Eqs.(III-21)–(III-25) and the Bessel function summation formula [75]:

$$\sum_{k=-\infty}^{\infty} (\pm 1)^k J_k^2(x) = J_0(x \mp x),$$

the VDCF solution for $\Delta = 0$ becomes:

$$\psi_k^{\mathrm{VDCF}}(\Delta = 0) = H^{-1}\, J_0(2g/\Omega) J_k(2g/\Omega), \qquad \text{(III–27)}$$

valid for all k. The factor H is given by

$$2H = (1 + \gamma_v) + (1 - \gamma_v) J_0(4g/\Omega). \qquad \text{(III–28)}$$

Eqs.(III-27) and (III-28) are the generalization of Eq.(III-14) for unequal damping rates Γ_v and Γ_w (for $\Gamma_v = \Gamma_w$, i.e., $\gamma_v = 1$, $H = 1$, as required). As shown in Appendix A, the correction term H may also be obtained by a perturbation calculation in terms of $\Gamma_v - \Gamma_w$, using the same analytical technique that originally led to Eqs.(III-13b) and (III-14). Because $J_0(4g/\Omega) \leq 1$ the factor H is positive for arbitrary values of $4g/\Omega$ and the ratio γ_v. Thus the zeros of $\psi_k^{\mathrm{VDCF}}(\Delta = 0)$ depend on the argument $2g/\Omega$ of the Bessel functions from Eq.(III-27) only and are independent of the damping ratio γ_v, as was established empirically for the zeros of $|\psi_2|$ at the end of Section III-2. For $\Delta = 0$ and $2g/\Omega = 4$ we calculate $H \simeq 0.793$ for $\gamma_v = 0.5$ and $H \simeq 1.414$ for $\gamma_v = 2$, thereby correctly predicting the values 0.182 and 0.102 at $\Delta = 0$ for the dashed curves in Figure III-3, respectively.

III–4 Generalized Bloch-Siegert Shifts

Practically speaking, values of the Floquet coefficients calculated from Section III-3 are hardly distinguishable from those obtained by substituting extremely small values of the damping rates in the general solution from Section III-2 (say,

$\Gamma_z \simeq 10^{-8}\Omega$, $z = u, v, w$). However, using the VDCF solution from Section III-3, the resonance behavior of both the DC and the harmonic components is easily analyzed. From Eqs.(III-21)–(III-23) it follows that $\psi_0^{\rm VDCF} = 0$ only if $p_l = \pm\infty$ for at least some $l \geq 1$. For $k \geq 1$ it follows from Eq.(III-25) that $\psi_k^{\rm VDCF} = 0$ if either $\psi_0^{\rm VDCF} = 0$ or $p_k = 0$. To establish the vanishing or singularity of the p_k's we note from Eq.(III-18) that if $f_{k+1} = x_{k+2}^{[0]}$ for some k, then $x_{k+1}^{[0]} = \pm\infty$, as a result of which $x_k^{[0]} = 0$, but $x_k^{[0]} x_{k+1}^{[0]} = -1$. From this and from Eq.(III-24) it follows that for $k \geq 1$, $p_k = 0$ if and only if $x_{k+1}^{[0]} = \pm\infty$, and that $p_k = \pm\infty$ if and only if $x_1^{[0]} = \pm\infty$. Combining all the above we conclude that for all $k \geq 0$:

$$\psi_k^{\rm VDCF} = 0 \iff \begin{cases} x_1^{[0]} = \pm\infty, \text{ or} \\ x_{k+1}^{[0]} = \pm\infty. \end{cases} \qquad \text{(III–29)}$$

To cast this result into a form most amenable to computing the positions of multiple quantum resonances we define the quantities $F_k \equiv (g/\Omega) f_k$ and $Y_k \equiv F_{k+1} - (g/\Omega) x_{k+2}^{[0]}$. Thus, with Eq.(III-19),

$$F_k = \begin{cases} k - (\Delta/\Omega)^2/k; & k = \text{odd}, \\ k; & k = \text{even}, \end{cases} \qquad \text{(III–30)}$$

and

$$Y_k = F_{k+1} - \frac{(g/\Omega)^2}{F_{k+2} -} \frac{(g/\Omega)^2}{F_{k+3} -} \cdots, \qquad \text{(III–31)}$$

where Y_k has been written as a continued fraction by iteration of Eq.(III-18). The resonance condition from Eq.(III-29) can now be expressed as

$$\psi_k^{\rm VDCF} = 0 \iff \Big\{ Y_0 = 0, \text{ or } Y_k = 0 \Big\}. \qquad \text{(III–32)}$$

This last result is a generalization of work by Swain in which, in essence, the resonance condition $Y_0 = 0$ is stated for the DC component of a longitudinally pumped magnetic resonance experiment [63]. With Eqs.(III-30)–(III-32) all information about the positions of multiple quantum resonances can be obtained.

Firstly, because the F_k's from Eq.(III-30) do not depend on the damping ratios γ_u and γ_v, neither do the positions of the resonances, as has already been alluded to in Sections III-2 and III-3.

Secondly, Eq.(III-32) implies that the DC component contains only a single set of resonances, namely those associated with zeros of Y_0. Moreover, these resonances also appear in each of the harmonic components. In turn, each harmonic component ψ_k has an additional set of resonances that are specific to that harmonic, namely those associated with zeros of Y_k. Thus the doubly branched resonance structure of harmonic components is established.

Thirdly, because, in the weak-field limit, (odd) N-quantum resonances are associated with the vanishing of the corresponding terms F_N from Eq.(III-30) (yielding the resonance conditions $\Delta/\Omega =$ odd N) it follows that the term Y_k — and therefore the additional branches of the kth harmonic — contain only those N-quantum resonances for which $N \geq k+1$.

From Eqs.(III-30)–(III-32) the positions of the multiple quantum resonances are easily found by numerical computation. A number of these generalized Bloch-Siegert resonance curves, thusly obtained, are displayed in Figure III-4 (see also the projections in Figure III-1 on page 145). Branches of the DC component are represented by solid curves, which are identical to those in Figure II-4 on page 137. Additional branches of even and odd harmonics, which are associated with the atomic population difference and the atomic susceptibility, are shown in Figures III-4(a) and III-4(b), respectively. In all calculations the continued fractions from Eq.(III-31) were truncated at no more than 20 terms. As mentioned under the third property above, additional branches of the kth harmonic are missing for those N-quantum resonances with $N < k+1$. Intersections with the $2g/\Omega$-axis are easily checked to be given by the zeros of the appropriate Bessel functions from

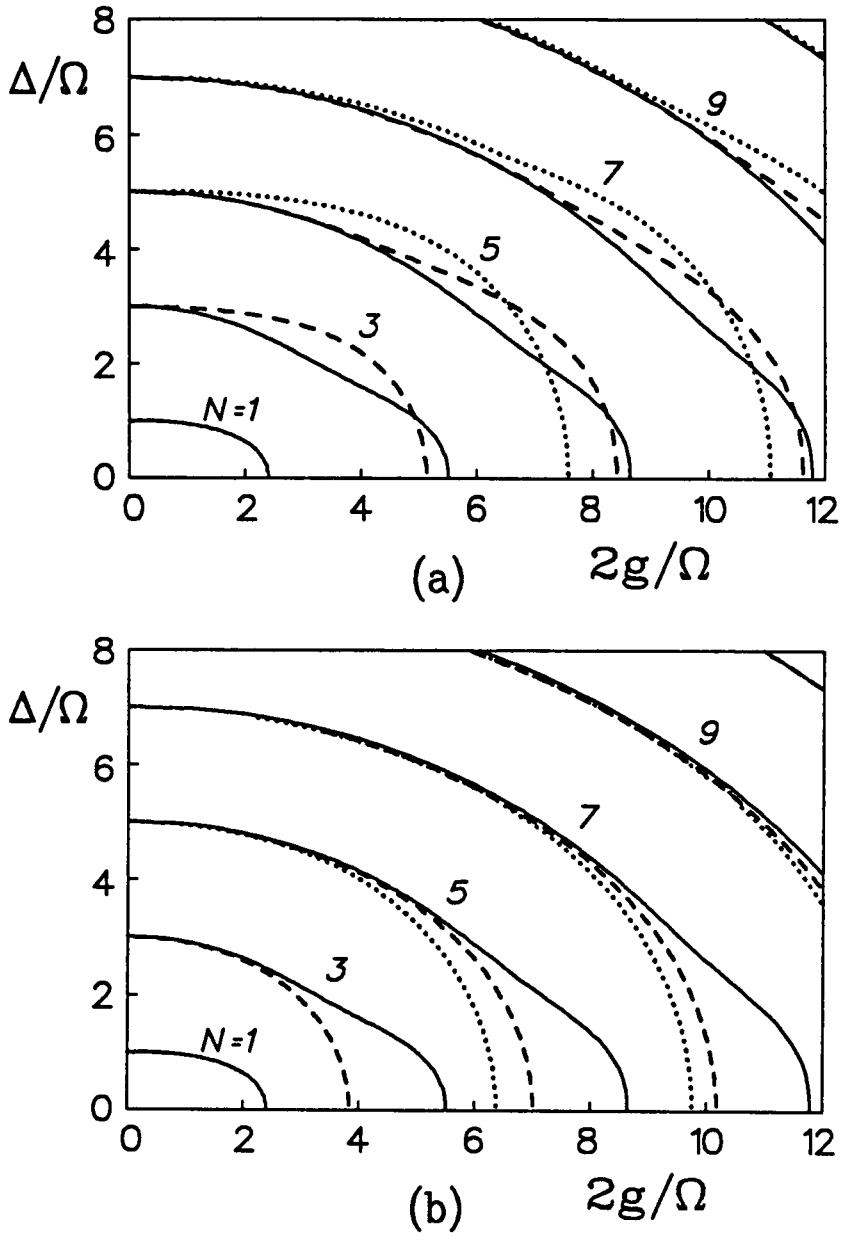


Figure III–4: *Generalized Bloch-Siegert resonance curves for various fluorescence and susceptibility components.*

The DC resonances (solid curves) appear also in each of the harmonics. In (a) the dashed and dotted curves represent the additional resonances of the components at 2Ω and 4Ω; in (b) the dashed and dotted curves represent the components at Ω and 3Ω. All intersections with the $2g/\Omega$-axis are given by Bessel zeros, according to Eq.(III-33).

Eqs.(III-14) or (III-27). That is, the intersection of the N-quantum resonance of the kth harmonic with the $2g/\Omega$-axis is given by

$$2g/\Omega = \tilde{x}_{kN} = \begin{cases} x_{k,(N-k)/2}; & k = \text{odd}, \\ x_{k,(N-k+1)/2}; & k = \text{even}, \end{cases} \qquad \text{(III–33)}$$

where x_{kl} denotes the lth zero of the kth order Bessel function (not counting the trivial zeros for zero argument). From the asymptotic approximation

$$x_{kl} = \left(k/2 + l - 1/4\right)\pi,$$

another property of the Bloch-Siegert resonance curves follows, namely:

Fourthly, for an even harmonic the two branches belonging to a certain quantum number converge for large $2g/\Omega$, whereas for an odd harmonic the branches become maximally split. Thus, for odd harmonics, the additional resonances are located midway between the DC-like resonances. Although this property is proved rigorously only from the Bessel function solution for $\Delta = 0$ we conclude from Figure III-4 that it is qualitatively correct away from the $2g/\Omega$-axis as well.

From Figure III-4 we draw another tentative conclusion about the Bloch-Siegert resonance curves:

Fifthly, for even harmonics branches belonging to the same quantum number N are mutually intersecting whereas the corresponding branches of odd harmonics are nonintersecting, apart from their common origins at $2g/\Omega = 0$.

In principle, explicit analytical expressions for the generalized Bloch-Siegert shifts may be obtained from Eqs.(III-30)–(III-32). Specifically, several authors have derived power series expansions for the DC resonance shifts of a longitudinally pumped magnetic resonance experiment. Thus we expand the position $\Delta_{kN}^{(n)}$ of the (odd) N-quantum resonance of the kth harmonic as

$$\left(\frac{\Delta_{kN}^{(n)}}{\Omega}\right)^2 = N^2\left\{1 + \sum_{m=1}^{n} a_{kN}^{(m)}\left(\frac{g}{2\Omega}\right)^{2m}\right\}. \qquad \text{(III–34)}$$

For an exact result an infinite number of terms n must be included. In practice, as many terms are chosen as the number of expansion coefficients one is willing to evaluate. Rather than the argument $2g/\Omega$, which is used elsewhere in Section III, we have chosen the argument $g/2\Omega$ in Eq.(III-34) because this quantity is equivalent to the scaled Rabi frequency associated with the radiofrequency field in magnetic resonance experiments, usually denoted as "b/ω" [cf. Eq.(II-32)]. Thus the expansion coefficients $a_{kN}^{(m)}$ may be compared directly with results from the magnetic resonance literature [58–63]. In Appendix B we present an outline for calculating the $a_{kN}^{(m)}$'s. If we introduce the notation

$$\Theta_k^N = \begin{cases} 1; & N \geq k, \\ 0; & \text{otherwise}, \end{cases} \tag{III–35}$$

the lowest coefficients can be written as

$$a_{kN}^{(1)} = -\frac{4}{N}\left\{\frac{1}{N+1}\Theta_{k+1}^N + \frac{1}{N-1}\Theta_{k+2}^N\right\}, \tag{III–36}$$

and

$$a_{kN}^{(2)} = -\frac{4}{N}\left\{\frac{N+2}{(N+1)^3}\Theta_{k+1}^N - \frac{N-2}{(N-1)^3}\Theta_{k+3}^N\right\}. \tag{III–37}$$

The relative simplicity of these last two results is misleading. Indeed, a laborious calculation shows that the next coefficient is given by

$$a_{kN}^{(3)} = -\frac{4}{N}\left\{\frac{(N+2)(N^2+5N+8)}{(N+1)^5(N+3)}\Theta_{k+1}^N - \frac{N(N+2)}{(N+1)^4(N-1)}\Theta_{k+2}^N \right.$$
$$\left. -\frac{(N-2)(N^2+N+2)}{(N-1)^5(N+1)}\Theta_{k+3}^N + \frac{(N-2)^2}{(N-1)^4(N-3)}\Theta_{k+4}^N\right\}, \tag{III–38}$$

and expressions for higher order terms will be increasingly complex.

Eqs.(III-36) and (III-37) agree with expressions for the DC component given by Ahmad and Bullough [61,62], who have also given the numerical values $-21/16$,

173/1152, and −0.00138 for the third order coefficients $a_{01}^{(3)}$, $a_{03}^{(3)}$, and $a_{05}^{(3)}$, respectively. These values are easily checked with Eq.(III-38), which identifies the decimally rounded value as −43/31104. In addition, Ahmad and Bullough have calculated the next higher terms for the DC main resonance, yielding $a_{01}^{(4)} = -63/64$ and $a_{01}^{(5)} = -193/384$ [61,62], and Swain has calculated the next higher term of the $N = 3$, DC resonance, yielding $9a_{03}^{(4)} = 4037/4096$ [63] [all these numerical values are also given in the expansions for the resonance shifts in Eqs.(II-33)].

To obtain the positions of the resonances accurately across the entire range (i.e., $0 \leq 2g/\Omega \leq \tilde{x}_{kN}$) the above power series expansions are of limited use, due to their slow convergence for $g/2\Omega > 1$. Indeed, it is generally more convenient to numerically solve for the zeros of the continued fractions Y_k from Eq.(III-31). However, from the structure of Eqs.(III-26)–(III-28), we conclude that, for $k \neq 0$:

$$a_{kN}^{(m)} = a_{0N}^{(m)} \iff 1 \leq m \leq N - k - 1. \qquad \text{(III–39)}$$

Thus $a_{kN}^{(1)} \neq a_{0N}^{(1)}$ only for $N = k + 1$. That is, the same Bloch-Siegert shift is displayed by both the DC component and the harmonic components for weak fields, except for the multiple quantum resonances with $N = k+1$. Note that this latter exception was not made by Arimondo and Moruzzi in their discussion of the harmonic signal at twice the modulation frequency in a longitudinally pumped magnetic resonance experiment [42] (see the quotation at the end of the first paragraph in Section III-1 of this dissertation). It is easily checked in Figures III-1 and III-4(a) that the additional $N = 3$ and $N = 5$ resonances of the fluorescence harmonics at 2Ω and 4Ω indeed deviate from the DC-like resonances for even small values of $2g/\Omega$. More generally it follows from Eq.(III-39) that the larger the diference $N - k$, the less the additional resonances deviate from the corresponding DC-like resonances. For example, the $N = 3$, $N = 5$, and $N = 7$ additional

resonances of the fluorescence harmonic at 2Ω deviate from the DC-like resonance by less than 0.01 (i.e., $|\Delta_{2N} - \Delta_{0N}|/\Omega < 0.01$) for $2g/\Omega \leq 0.40$, 3.13, and 6.13, respectively.

Analytical expressions for the (DC) Bloch-Siegert shifts in magnetic resonance experiments other than power series expansions have been derived, namely expressions in terms of rational fractions [63] and Bessel functions solutions for small but nonzero detuning (or rather, small but nonzero Zeeman fields) [58-63]. Although similar expressions might be derived for the additional resonances of harmonic components we contend that numerically solving Eqs.(III-30)–(III-32) is sufficiently easy and efficient for all practical purposes.

III–5 Prospects for Experimental Verification

We have shown that, for sufficiently small damping, the modulated interaction components of a two-level atom driven by a FAM field display not only the resonances that are found in the time-averaged fluorescence signal, but also additional resonances that are specific to the harmonic component. However, as shown in Figure III-2, this doubly branched resonance structure is easily obscured by relaxation effects. Thus, to verify this effect experimentally, one must employ a modulation frequency that is sufficiently large to overcome the loss of coherence due to spontaneous emission or other mechanisms.

To establish a quantitative criterion for the observability of the doubly branched resonances, we have computed the zeros of the real parts of the Floquet coefficients ψ_1 and ψ_2, which correspond to the quadrature component of the imaginary part of the susceptibility at Ω and the in-phase fluorescence component at 2Ω, respectively. The positions of the zeros of the $N = 1$ and $N = 3$ resonances,

which were calculated using the general theory of Section III-2, are displayed in Figure III-5. Radiative damping has been assumed (i.e., $\Gamma_u = \Gamma_v = \Gamma_w/2 \equiv 1/T_2$), and the curves are labeled with the value of $(\Omega T_2)^{-1}$. As can be seen from the solid curves, the lower and upper lobes of the $N = 3$ resonance of the fluorescence component at 2Ω disappear for $(\Omega T_2)^{-1} \simeq 0.075$ and $(\Omega T_2)^{-1} \simeq 0.175$, respectively. By contrast, the structure of the susceptibility component at Ω (dashed curves) is preserved for relatively large damping rates although, for $(\Omega T_2)^{-1} \simeq 0.45$, the $N = 1$ and $N = 3$ branches merge. This means that in an experiment like that of Chakmakjian *et al.* a modulation frequency of some 100 MHz should be employed to resolve the doubly branched structure of the $N = 3$ resonance in the modulated fluorescence signal from the sodium D_2 line [14].

The only relevant experimental work, known to us, in which a modulated interaction component is measured rather than a DC signal is that of Arimondo and Moruzzi. These authors have measured the population difference at twice the modulation frequency in a longitudinally pumped magnetic resonance experiment involving an optically pumped ^{199}Hg vapor [42]. Although different resonance behaviors for the modulated and DC signals are found, evidence for a doubly branched resonance structure is precluded due to too small a modulation frequency (i.e., too large a value of $(\Omega T_2)^{-1}$). Technically speaking, employing a larger modulation frequency would perhaps have been easier in these magnetic resonance experiments than it will be in the ongoing work on optical resonance. However, it seems not to have been realized at the time just how the resonance behavior of modulated interaction components differs from that of the DC component, so that no exhaustive investigation was conducted.

As we have argued recently [22], the doubly branched resonance structure of harmonic components significantly pronounces their resonance behavior over that

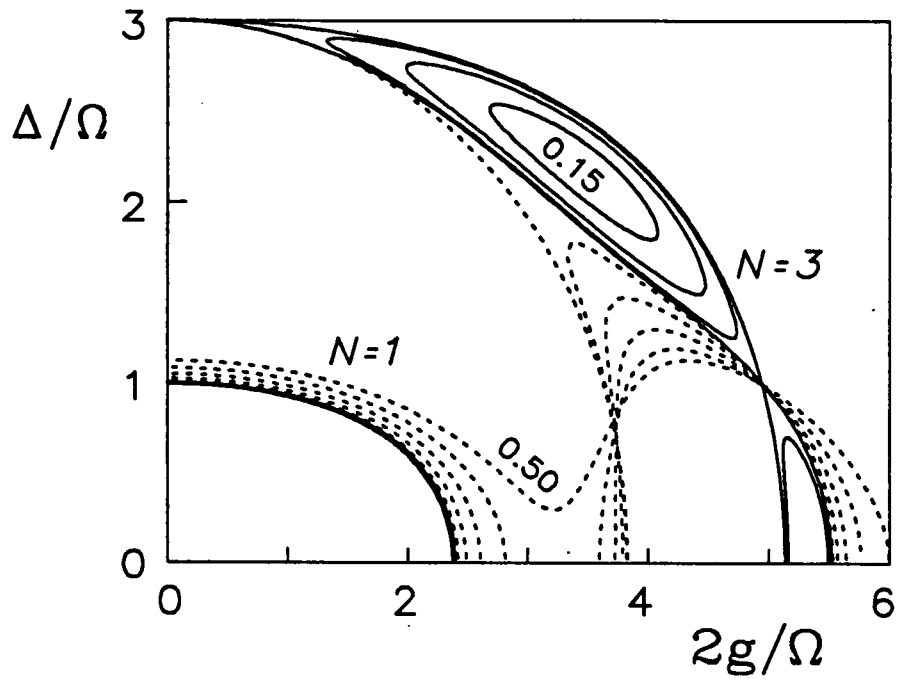


Figure III–5: *Doubly branched resonances for nonzero damping.*

Zeros of $\mathrm{Re}\{\psi_1\}$ *(dashed curves) and of* $\mathrm{Re}\{\psi_2\}$ *(solid curves) are displayed for* $T_1/T_2 = 0.5$ *and various values of the product* $(\Omega T_2)^{-1}$ *[see Eqs.(III-1)]. Solid curves correspond to the in-phase component of the fluorescence at* 2Ω *for* $(\Omega T_2)^{-1} = 0.00, 0.05, 0.10,$ *and* 0.15. *Dashed curves correspond to the quadrature component of the imaginary part of the susceptibility at* Ω *for* $(\Omega T_2)^{-1} = 0.0, 0.1, 0.2, 0.3, 0.4,$ *and* 0.5.

of the DC component, even if the doubly branched structure itself is obscured in the presence of damping. As a result, the modulated components, unlike the DC component, should retain significant resonance structure even in the case of a strongly inhomogeneously broadened medium. Thus experimental observation of this inhomogeneously broadened resonance behavior of harmonic components would constitute indirect support for the theory in Section III. These effects of inhomogeneous broadening are addressed in detail in Section IV.

Finally we remark that a similar treatment can be given for the excitation of

a two-level system by a not fully amplitude modulated field [8–10,16–18,26–28], a frequency modulated field [24-26], or a bichromatic field with unequal intensities in the two modes [15,29,70], each of which also have analogues in magnetic resonance, as discussed in Section II-3. However, we do not elaborate on these cases here (see Ref.[76]).

IV EFFECTS OF INHOMOGENEOUS BROADENING

Section IV addresses once again the interaction of a fully amplitude modulated source with a two-level atom, but considers in particular the effects of inhomogeneous broadening, that is, the effects of averaging over the Doppler profile of the two-level medium. Such averaging can be neglected only if the inhomogeneous linewidth is much smaller than the sum of the homogeneous linewidth of the medium and the bandwidth of the exciting light. In the case of excitation by a narrowband laser, this condition is generally satisfied only in beam experiments in which the transverse temperature is on the order of a few degrees Kelvin or less. More frequently, the Doppler width exceeds the natural linewidth of the medium by several orders of magnitude, so that inhomogeneous broadening must be taken into account.

Section IV-1 considers specifically the geometry of the laser fluorescence velocimeter (LFV) (see Figure I-1 on page 112) and shows that, because of the typically small angle between the two beams, the LFV can be considered essentially as a single-beam experiment, at least as far as the effects of inhomogeneous broadening are concerned.

Section IV-2 deals with the limiting case of weak excitation and shows that, upon inhomogeneous broadening, the familiar expressions for depth-of-modulation and phase-shift are obtained. Incidentally, it is shown that these results are the same as those obtained for a broadband source, so that, in the weak field limit, a broad source is equivalent to a broad absorber.

Section IV-3 considers the effects of inhomogeneous broadening for the general case of strong, fully amplitude modulated excitation and shows that, in this regime, values of the depth-of-modulation and phase-shift may deviate signifi-

cantly from the corresponding weak field results. On the one hand, this poses complications for the interpretation of LFV data. On the other hand, these results are interesting in that many of the characteristic features of the single atom resonance behavior calculated in Section III are retained in the inhomogeneously broadened quantities. This surprising result has been the subject of several brief publications [11,22,69] and is discussed in more detail in Section IV-3.

IV–1 Relevance to the Laser Fluorescence Velocimeter

Consider an atom, moving in the laboratory frame with some velocity $\mathbf{v}$, being exposed to an electromagnetic wave of frequency ω and wave vector $\mathbf{k}$. If the motion of the atom is nonrelativistic, the Doppler shifted frequency ω' in the atom's rest frame is then given by

$$\omega' = \omega - \mathbf{k} \cdot \mathbf{v}. \tag{IV–1}$$

Now consider an atom being exposed to a fully amplitude modulated field, as obtained in the LFV geometry shown in Figure I-1 on page 112. Let the frequencies ω_1 and ω_2 of the two beams be given by

$$\omega_1 = \omega_+ = \omega_l + \Omega; \tag{IV–1a}$$

$$\omega_2 = \omega_- = \omega_l - \Omega, \tag{IV–1b}$$

where ω_l and Ω denote the carrier frequency and modulation frequency of the fully amplitude modulated field, respectively [cf. Eq.(II-27b)]. Furthermore, as illustrated in Figure IV-1, let the two beams be placed symmetrically with respect to the optical axis, namely at angles $\vartheta/2$ and $-\vartheta/2$, respectively, and let the atomic velocity components, in the plane defined by the two wave vectors, parallel and

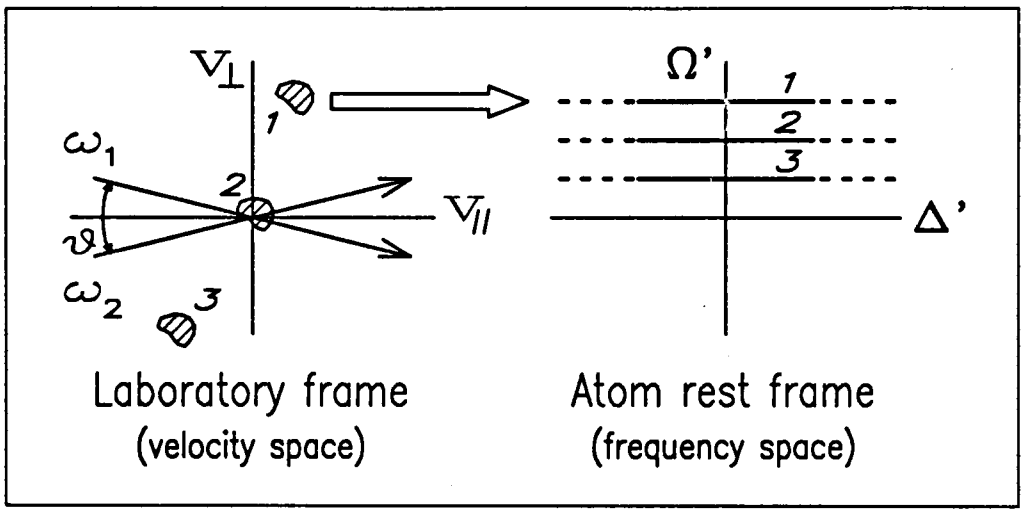


Figure IV–1: *Mapping from laboratory frame to atom's rest frame.*

perpendicular to the optical axis be given by $v_{\parallel}$ and $v_{\perp}$, respectively. Application of Eq.(IV-1) then yields for the carrier frequency and the modulation frequency in the atom's rest frame:

$$\omega_l' = \omega_l - kv_{\parallel} \cos\vartheta/2, \tag{IV–2}$$

and

$$\Omega' = \Omega + kv_{\perp} \sin\vartheta/2, \tag{IV–3}$$

where we have taken $|\mathbf{k}_1| = |\mathbf{k}_2| = k$, which is an excellent approximation since $\Omega \ll \omega_l$. With Eqs.(II-1) and (IV-2), the detuning in the atom's rest frame becomes:

$$\Delta' = \omega_0 - \omega_l' = \Delta + kv_{\parallel} \cos\vartheta/2. \tag{IV–4}$$

From Eqs.(IV-3) and (IV-4) it follows that, in general, neither the detuning nor the modulation frequency are equal in the laboratory frame and the atom's rest

frame. However, because the angle ϑ between the two beams is on the order of a few tens of milliradians in a typical LFV application [1,11,65], there is a large asymmetry between the effects of inhomogeneous broadening on the quantities Δ' and Ω'. This is illustrated in Figure IV-1, which shows the mapping of "velocity space" (left) to "frequency space" (right), as dictated by Eqs.(IV-3) and (IV-4), assuming a small angle ϑ. Thus, an ensemble in velocity space maps onto extremely elongated lines in frequency space. For a typical distribution of velocity components (that is, one with roughly equal spreads in $v_{\|}$ and $v_{\perp}$), the modulation frequencies Ω' in the atom's rest frames are then narrowly distributed around a value determined by the bulk transverse velocity of the medium, whereas, in the atom's rest frames, a wide distribution of detunings exists. Thus, for the purpose of accounting for the effects of inhomogeneous broadening, the LFV geometry may be approximated as a single-beam experiment. Specifically, if $\rho_{22}(t;\Delta')$ denotes the fluorescence response for a single detuning Δ', the ensemble averaged value for the fluorescence becomes:

$$\overline{\rho_{22}}(t) = \int_{-\infty}^{\infty} \rho_{22}(t;\Delta')\, G_{\|}(\Delta')\, d\Delta', \qquad \text{(IV–5)}$$

where $G_{\|}(\Delta')$ is the inhomogeneous profile, associated with the parallel velocity distribution [cf. Eq.(IV-4)]. If the angle between the two beams is sufficiently large and/or the transverse velocity distribution is sufficiently wide, some averaging must also be performed over the modulation frequencies Ω' in the atom's rest frames. However, the concept of the LFV assumes that this averaging over Ω' can be neglected, so that measurement of the phase-shift or depth-of-modulation of the fluorescence signal allows one to calculate Ω' (using Eqs.(IV-23) or (IV-24) from Section IV-2.3, respectively), and with Eq.(IV-3), the transverse velocity $v_{\perp}$.

In Sections IV-2 and IV-3 we carry out the integration from Eq.(IV-5) for a number of typical conditions. Most importantly, we consider the case in which

$G_{\|}(\Delta')$ is so wide with respect to the region in which $\rho_{22}(t;\Delta')$ is significantly different from zero that it may be approximated by a constant value, say, $G_{\|}(\Delta') = 1$. For weak fields, the resulting integration may be performed analytically, as is shown in Section IV-2. For the general case of strong fields, however, recourse must be made to numerical integration even for a constant profile $G_{\|}(\Delta')$, as discussed in Section IV-3.

IV–2 Weak Field Results

In Section III-2 we have given the general solution for a two-level atom exposed to a fully amplitude modulated, narrowband optical field. In the limit of weak excitation, the continued fraction solution may be truncated after a few terms, so that the fluorescence signal contains only a DC component and a component that is modulated at the beat frequency of the driving field, namely at 2Ω. In Section IV-2.1 we review this weak field, narrowband solution. For comparison, we treat the corresponding broadband solution in Section IV-2.2. Then, in Section IV-2.3, we derive the inhomogeneously broadened solution for the case of narrowband excitation, and show that, in the inhomogeneously broadened limit, the same results are obtained for both a narrowband and a broadband source.

IV–2.1 Narrowband solution

For weak fields, the response of a two-level atom to a fully amplitude modulated field may be calculated in several ways. Here we take the limit of the continued fraction solution from Section III-2. Retaining the notation from Section III-2, we recall that Ω and Δ are the modulation frequency and detuning (we drop the primes and let it be understood that Ω and Δ are actually the values in

the atom's rest frames). Furthermore, by Eq.(III-2), g denotes the Rabi frequency, which is linearly related to the electric field, and finally, T_1^{-1} and T_2^{-1} denote the longitudinal and transverse damping rates, respectively. Also, we introduce the (complex) quantity

$$M_{12} = \frac{1 + i\Omega T_2}{1 + 2i\Omega T_1} \equiv |M_{12}|\, e^{i\Phi_{12}}, \tag{IV–6}$$

the Lorentzian profiles

$$\mathcal{L}_{\pm}(\Delta) = \frac{T_2^{-1}}{(\Delta \pm \Omega)^2 + T_2^{-2}}, \tag{IV–7}$$

and the phase factors

$$\Phi_{\pm}(\Delta) = \tan^{-1}\Big(\frac{\Delta \pm \Omega}{T_2^{-1}}\Big). \tag{IV–8}$$

Thus, as shown in Appendix C-1, the solution for the upper state population $\rho_{22}(t;\Delta)$ in the weak field limit becomes

$$\begin{aligned}\rho_{22}(t;\Delta) = (g^2 T_1/2)\Big\{ &\mathcal{L}_+(\Delta) + \mathcal{L}_-(\Delta) \\ &+ 2|M_{12}|\, \mathcal{L}_+^{1/2}(\Delta)\mathcal{L}_-^{1/2}(\Delta)\, \cos\big(2\Omega t - \Phi_{\rm nb}(\Delta)\big)\Big\},\end{aligned} \tag{IV–9}$$

where the narrowband ("nb") phase-shift $\Phi_{\rm nb}$ is given by

$$\begin{aligned}\Phi_{\rm nb}(\Delta) &= \Phi_+(\Delta) - \Phi_-(\Delta) - \Phi_{12} \\ &= \tan^{-1}\Big(\frac{\Delta + \Omega}{T_2^{-1}}\Big) - \tan^{-1}\Big(\frac{\Delta - \Omega}{T_2^{-1}}\Big) - \tan^{-1}\Big(\frac{\Omega}{T_2^{-1}}\Big) + \tan^{-1}\Big(\frac{2\Omega}{T_1^{-1}}\Big).\end{aligned} \tag{IV–10}$$

The last step follows with Eqs.(IV-6) and (IV-8). Alternatively, this weak field solution may be obtained directly from the Bloch equations, by substituting $\rho_{22} - \rho_{11} = -1$ in Eq.(II-3b) and successively solving Eqs.(II-3b) and (II-3a) for $\rho_{12}(t)$ and $\rho_{22}(t)$, respectively.

In the case of radiative damping ($T_2 = 2T_1$), the solution simplifies somewhat, because the factor M_{12} from Eq.(IV-6) becomes unity, so that $|M_{12}| = 1$

and $\Phi_{12} = 0$. Thus, the narrowband phase-shift becomes

$$\Phi_{\rm nb}(\Delta) = \Phi_+(\Delta) - \Phi_-(\Delta) = \tan^{-1}\left\{\frac{2\Omega T_2}{1 + T_2^2(\Delta^2 - \Omega^2)}\right\}, \qquad \text{(IV–11)}$$

and the depth-of-modulation of the fluorescence signal becomes

$$M_{\rm nb}(\Delta) = \frac{2\mathcal{L}_+^{1/2}(\Delta)\mathcal{L}_-^{1/2}(\Delta)}{\mathcal{L}_+(\Delta) + \mathcal{L}_-(\Delta)} = \left[1 - \left\{\frac{2\Delta\Omega T_2^2}{1 + T_2^2(\Delta^2 + \Omega^2)}\right\}^2\right]^{1/2}. \qquad \text{(IV–12)}$$

In essence, the results of Eqs.(IV-6)–(IV-12) were first obtained by Feneuille *et al.* [7] (although only for the case of radiative damping), and were obtained independently in this work, namely by calculating the fluorescence response of a two-level atom using the formalism of a time-dependent physical spectrum [11,65], in which the atom is treated as a Lorentzian spectrometer [77].

Figure IV-2 displays the function $\rho_{22}(t;\Delta)$ from Eq.(IV-9) as a function of the detuning Δ, assuming radiative damping. For each of three values ΩT_2, $\rho_{22}(t;\Delta)$ is plotted for five values of the argument of the cosine term in Eq.(IV-9), namely for the values

$$2\Omega t - \Phi_{\rm nb}(\Delta) = k\pi/4; \qquad 0 \le k \le 4. \qquad \text{(IV–13)}$$

Figure IV-2 shows that, for large values of the damping (that is, small values of the product ΩT_2), the fluorescence signal is strongly modulated across the entire detuning range. However, the two frequencies of the fully amplitude modulated (bichromatic) field are essentially unresolved. In the opposite limit, namely that of small damping (large ΩT_2), the fluorescence signal clearly resolves the two frequencies. However, the depth-of-modulation of the signal is smaller than that for large damping. In this respect, Figure IV-2 suggests that there is a reciprocal relation ("uncertainty principle") between the accuracy of simultaneous measurements of spectral and temporal fluctuations in the fluorescence signal [65].

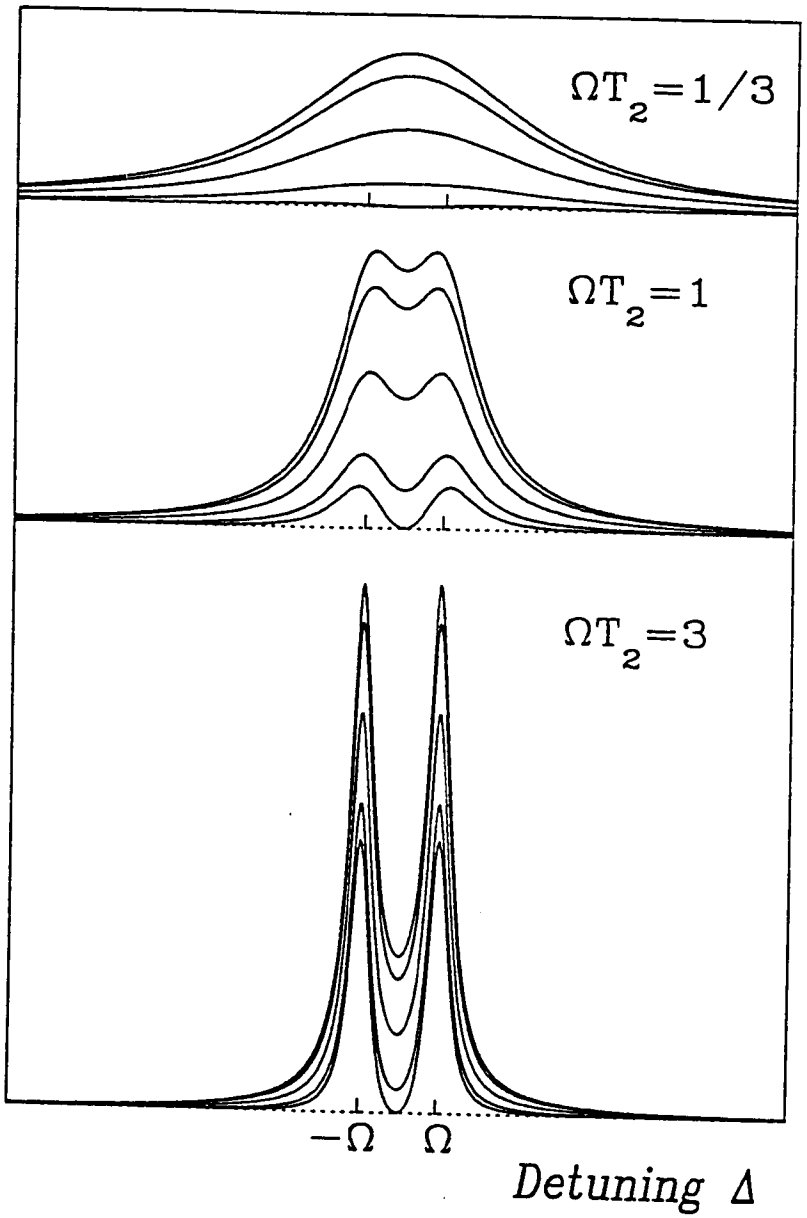


Figure IV–2: *Fluorescence signal as a function of the detuning for several values of the damping.*

The signal, calculated from Eq.(IV-9), is shown for five values of the phase $2\Omega t - \Phi_{nb}$, *as indicated in Eq.(IV-13). The full detuning range is* -10Ω *to* 10Ω.

Figure IV-3 displays the narrowband phase-shifts $\Phi_{nb}(\Delta)$ from Eq.(IV-11) for the same conditions as in Figure IV-2. It is seen that, in each case, the maximum phase-shift occurs for zero detuning. From Eq.(IV-11) it follows that this zero detuning phase-shift is given by

$$\Phi_{nb}(0) = 2\tan^{-1}(\Omega T_2) = 2\tan^{-1}(2\Omega T_1), \qquad \text{(IV-14)}$$

so that, depending on the product ΩT_2, this maximum phase-shift can assume any value between 0 and π. From Eq.(IV-12), the corresponding value of the depth-of-modulation is given by

$$M_{nb}(0) = 1, \qquad \text{(IV-15)}$$

that is, $M_{nb}(0)$ is independent of the product ΩT_2.

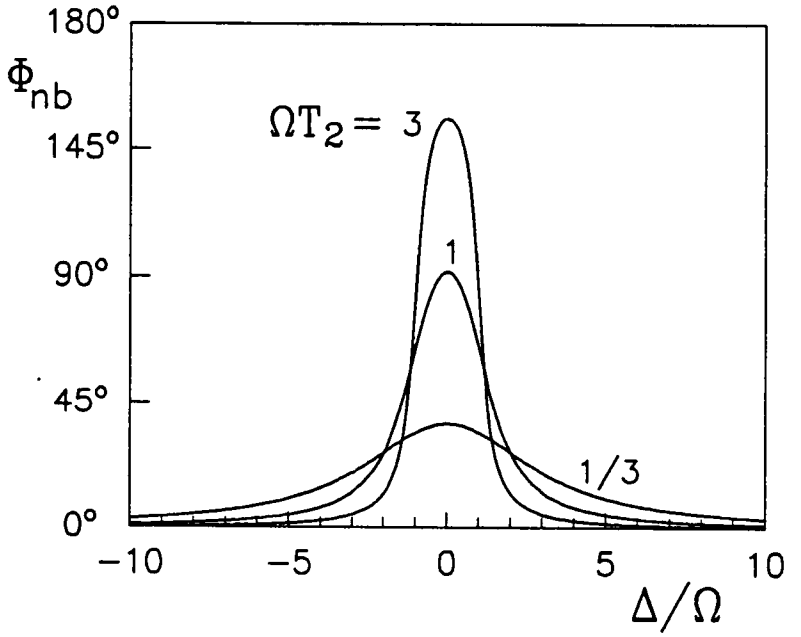


Figure IV–3: *Narrowband phase-shift versus detuning for the same conditions as in Figure IV-2.*

IV–2.2 Broadband solution

Although we are interested primarily in the case of excitation of the atomic system by a narrowband laser, it is instructive to consider also the limit of fully amplitude modulated excitation using a broadband source. This case is treated most conveniently by using the familiar substitution rule (see, for example, Ref.[29])

$$T_2^{-1} \rightarrow T_2^{-1} + \Gamma_s, \tag{IV–16}$$

which indicates that, for a source with a Lorentzian frequency spectrum of width Γ_s, one merely needs to add the source bandwidth to the transverse damping rate of the atomic system. Thus, excitation of the two-level atom by a broadband source can be treated by solving the optical Bloch equations in the limit $T_2^{-1} \rightarrow \infty$ ($T_2 \rightarrow 0$). As shown in Appendix C-2, this reduces the problem of solving three simultaneous differential equations to that of solving a single rate equation, which, for the case of a fully amplitude modulated field, can be solved in terms of modified Bessel functions of integer order. In the weak field limit, the solution for $\rho_{22}(t;\Delta)$ then becomes

$$\rho_{22}(t;\Delta) = R(\Delta)\, T_1 \left\{1 + M_{\rm bb} \cos(2\Omega t - \Phi_{\rm bb})\right\}, \tag{IV–17}$$

where $R(\Delta)$ is the detuning-dependent excitation rate

$$R(\Delta) = \frac{g^2 T_2^{-1}}{\Delta^2 + T_2^{-2}}, \tag{IV–18}$$

and the broadband values of the phase-shift and depth-of-modulation are given by

$$\Phi_{\rm bb} = \tan^{-1}(2\Omega T_1), \tag{IV–19}$$

and

$$M_{\rm bb} = \left\{1 + (2\Omega T_1)^2\right\}^{-1/2}, \tag{IV–20}$$

respectively. These are the familiar values that are used in conventional applications of phase sensitive fluorometry [1,5,6]. Eqs.(IV-17)–(IV-20) can also be obtained directly from Eqs.(IV-7)–(IV-10) by taking the limit $T_2 \to 0$, and replacing the Lorentzian lineshape functions $g^2 \mathcal{L}_{\pm}(\Delta)$ by the broadband excitation rate $R(\Delta)$. Note that the expressions for phase-shift and depth-of-modulation of the fluorescence signal differ significantly from the weak field, narrowband values from Section IV-2.1. For example, the broadband phase-shift Φ_{bb} from Eq.(IV-19) is only half of the narrowband value for zero detuning, given in Eq.(IV-14), and the broadband value for the depth-of-modulation is less than the constant value of unity from Eq.(IV-15) for all values of the product ΩT_1.

IV–2.3 Inhomogeneously broadened solution

Now let us consider the effects of inhomogeneous broadening on the weak field solutions from Sections IV-2.1 and IV-2.2. That is, let us perform the integration from Eq.(IV-5). In so doing, we assume that the inhomogeneous profile $G_{\|}(\Delta)^*$ is much wider than the detuning range in which $\rho_{22}(t;\Delta)$ is significantly different from zero (see Figure IV-2). Thus we compute the ensemble averaged fluorescence signal

$$\overline{\rho_{22}}(t) = \int_{-\infty}^{\infty} \rho_{22}(t;\Delta)\, d\Delta, \qquad \text{(IV–21)}$$

where $\rho_{22}(t;\Delta)$ is given either by Eq.(IV-9) or Eq.(IV-17). In the first case, the result is most easily obtained by contour integration in the complex plane, as shown in Appendix C-3. Thus, Eqs.(IV-17) and (IV-21) yield

$$\overline{\rho_{22}}(t) = \pi g^2 T_1 \left\{1 + M_{ihb} \cos(2\Omega t - \Phi_{ihb})\right\}, \qquad \text{(IV–22)}$$

---

*As noted at the beginning of Section IV-2.1, we drop the primes on Δ, and let it be understood that Δ is actually the detuning in the atom's rest frames.

where the inhomogeneously broadened values for the phase-shift and depth-of-modulation are given by

$$\Phi_{\text{ihb}} = \tan^{-1}(2\Omega T_1), \tag{IV–23}$$

and

$$M_{\text{ihb}} = \left\{1 + (2\Omega T_1)^2\right\}^{-1/2}. \tag{IV–24}$$

Note that these values are independent of the transverse damping rate T_2^{-1}, and that, quite importantly, they are identical to the weak field, broadband results from Eqs.(IV-19) and (IV-20). Thus, for weak fields, a broad source is equivalent to a broad absorber, the latter being defined as an ensemble with a wide inhomogeneous profile. It is a trivial matter to show that substitution of Eq.(IV-17) into Eq.(IV-21) yields, again, the inhomogeneously broadened quantities from Eqs.(IV-22)–(IV-24), since

$$\int_{-\infty}^{\infty} R(\Delta)\, d\Delta = \pi\, g^2, \tag{IV–25}$$

which follows immediately from Eq.(IV-18). Thus, it follows that not only are a broad source and a broad absorber equivalent in the weak field limit, but, in the weak field limit, it does not matter whether a broad ensemble of absorbers is excited by a narrowband or a broadband source. The results from Eqs.(IV-23) and (IV-24) also imply that, in the weak field limit, the familiar expressions for phase-shift and depth-of-modulation of the fluorescence signal may indeed be used in the interpretation of typical LFV data, even when a narrowband laser is used. However, we show in Section IV-3 that this is no longer true in the case of strong excitation.

IV–3 Strong Field Results

For the general case of strong, fully amplitude modulated excitation by a narrowband laser, the upper state population $\rho_{22}(t)$ of the two-level atom is given as a Floquet series [Eq.(III-15)], and the Floquet coefficients are given by continued fractions [Eqs.(III-8)–(III-11)]. Thus, it seems impossible to carry out the integration from Eq.(IV-5) analytically, even for a constant profile $G_{\|}(\Delta)$. Therefore, we have performed the inhomogeneous averaging by numerical integration, that is, by computing the sum

$$\overline{\rho_{22}}(t) = \left(2\Delta_{\max}/N_i\right) \sum_{i=1}^{\infty} \rho_{22}(t;\Delta_i)\, G_{\|}(\Delta_i), \qquad \text{(IV–26a)}$$

where

$$\Delta_i = (i - 1/2)\Delta_{\max}/N_i, \qquad \text{(IV–26b)}$$

and where $\rho_{22}(t;\Delta_i)$ is obtained in terms of its Floquet coefficients, using Eqs.(III-8)–(III-11) and (III-15). The result for $\overline{\rho_{22}}(t)$ is a Floquet series like that of Eq.(III-15), which we write as

$$\overline{\rho_{22}}(t) = \overline{r_0} + \sum_{k=1}^{\infty} \overline{r_{2k}} \cos(2k\Omega t - \overline{\Phi_{2k}}). \qquad \text{(IV–27)}$$

Thus, $\overline{r_0}$, $\overline{r_{2k}}$, and $\overline{\Phi_{2k}}$ denote, respectively, the inhomogeneously broadened values of the DC fluorescence signal, the magnitude of the kth fluorescence harmonic, and the phase-shift with respect to the driving field of the latter. In all calculations, we have used a maximum detuning $\Delta_{\max} = 500\Omega$, and we have chosen $N_i = 10000$ integration elements. Results for a constant profile, namely $G_{\|}(\Delta) = 1/\Omega$ are displayed in Figures IV-4, IV-5, and IV-6 (the scaling by the modulation frequency Ω is to render the coefficients $\overline{r_0}$ and $\overline{r_{2k}}$ dimensionless). Also, results for a Gaussian profile $G_{\|}(\Delta)$ are displayed in Figure IV-7.

Figure IV-4(a) displays the inhomogeneously broadened values for the DC fluorescence $\overline{r_0}$ and the in-phase and quadrature components of the lowest fluorescence harmonic, that is, the quantities $\overline{r_2}\cos\overline{\Phi_2}$ and $\overline{r_2}\sin\overline{\Phi_2}$, respectively, for conditions as given in the figure caption (note that $T_2 = 2T_1$, so that Figure IV-4 corresponds to the case of radiative damping). The results for $\overline{r_0}$ and $\overline{r_2}\cos\overline{\Phi_2}$ should be compared with the quantities $(1-\psi_0)/2$ and $\mathrm{Re}\{-\psi_2\}$ in Figure III-1, respectively. Note that, by the integration over Δ, most of the resonance structure evident in Figure III-1 has disappeared, particularly for the DC fluorescence component. Indeed, for even moderate fields, $\overline{r_0}$ can be approximated reasonably well by replacing the instantaneous intensity $g^2\cos^2\Omega t$ by its temporally averaged value, $g^2/2$, in which case the steady-state solution of the Bloch equations [Eqs.(III-4)] is simply shown to be given by

$$\rho_{22} = \frac{g^2}{2g^2 + \Gamma_v\Gamma_w + \Delta^2(\Gamma_w/\Gamma_u)}. \qquad \text{(IV–28)}$$

Upon setting $\Gamma_u = \Gamma_v = T_2^{-1}$ and $\Gamma_w = T_1^{-1}$, integration of Eq.(IV-28) yields

$$\overline{r_0}' = \int_{-\infty}^{\infty} \rho_{22}(\Delta)\, d\Delta/\Omega = \frac{\pi g^2 T_1/\Omega}{(1+2g^2T_1T_2)^{1/2}}. \qquad \text{(IV–29)}$$

As expected, $\overline{r_0}'$ is a monotonous function of the electric field amplitude. The approximation $\overline{r_0}'$ is shown as the dashed line in Figure IV-4(a).

One immediate implication of the results for the inhomogeneously broadened values $\overline{r_0}$ in Figure IV-4(a) is that, if the time-averaged fluorescence signal is measured, inhomogeneous broadening causes an almost complete "washing out" of the multi-photon resonance structure that is found in the absence of inhomogeneous broadening (see Figure III-1 and the experimental work reported in Ref.[14], where, instead of the terminology multi-photon resonances, the term subharmonic resonances is used). In fact, the washing out of subharmonic resonance

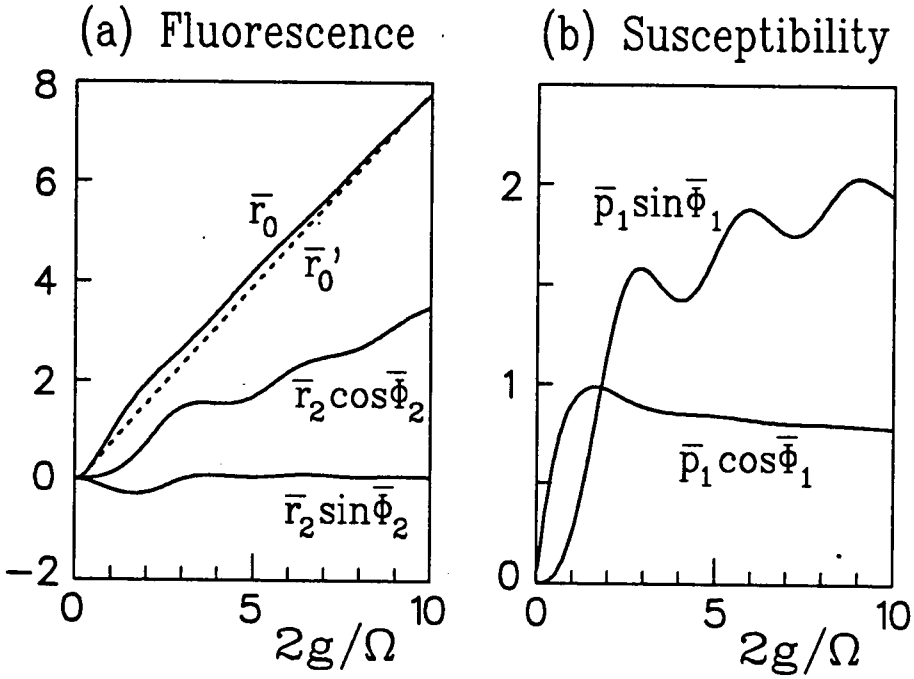


Figure IV–4: *Inhomogeneously broadened values of several fluorescence and susceptibility components.*

Calculations are for $\Omega T_1 = \Omega T_2/2 = 2$ *and a constant, rectangular profile* $G_{\|}(\Delta) = 1/\Omega$, *with* $\Delta_{\max} = 500\Omega$ *and* $N_i = 10000$.

structure due to inhomogeneous broadening has been reported for the related problem of four-wave mixing [78,79]. Thus, it is quite surprising to observe that the modulated fluorescence component $\overline{r_2}\cos\overline{\Phi_2}$ *does* retain some of the multiphoton resonance structure in the limit of substantial inhomogeneous broadening. Similarly, the quadrature component at Ω of the imaginary part of the atomic susceptibility retains significant resonance structure in the limit of large inhomogeneous broadening, as is shown in Figure IV-4(b) [the components $\overline{p_1}\sin\overline{\Phi_1}$ and $\overline{p_1}\cos\overline{\Phi_1}$, which are defined in a way similar to Eq.(IV-27)], are obtained by integrating the imaginary and real parts of the Floquet coefficients ψ_1 from Eq.(III-7),

respectively).

To compare the results from Figure IV-4 to the weak field results calculated in Section IV-2, we have computed the depth-of-modulation $\overline{M_2} = \overline{r_2}/\overline{r_0}$ and the phase-shift $\overline{\Phi_2}$ of the lowest fluorescence harmonic, and have displayed the results in Figure IV-5 as a function of the scaled Rabi frequency. As in Figure IV-4, radiative damping has been assumed, and the integration was performed for a constant profile $G_{\|}(\Delta) = 1/\Omega$. The multi-photon resonance structure, so evident in Figure III-1, is easily discerned in the behavior of $\overline{M_2}$ versus $2g/\Omega$. In fact, the maxima of $\overline{M_2}$ occur at values $2g/\Omega \simeq k\pi$ (k = integer), suggesting that the periodicity of the zero detuning Bessel function solution of Eq.(III-13b) in the limit $2g/\Omega \rightarrow \infty$ is retained in the inhomogeneously broadened quantities. It is easily checked that, for small $2g/\Omega$, the value of $\overline{M_2}$ is correctly given by Eq.(IV-24), which yields ($\Omega T_1 = 2$) $M_{\text{ihb}} = 17^{-1/2} \simeq 0.24$. This value is indicated by the open circle in Figure IV-5(a). Similarly, the weak field value of the phase-shift $\overline{\Phi_2}$ is given correctly by Eq.(IV-23), which yields $\Phi_{\text{ihb}} = \tan^{-1}(4) \simeq 72^0$. This value is indicated by the open circle in Figure IV-5(b). Quite importantly, it should be noted that for values $2g/\Omega$ other than zero, both the depth-of-modulation $\overline{M_2}$ and the phase-shift $\overline{\Phi_2}$ differ significantly from the weak field values. Specifically, we find for the conditions in Figures IV-4 and IV-5 that

$$\overline{M_2} \geq M_{\text{ihb}}; \qquad \text{and} \qquad \overline{\Phi_2} \leq \Phi_{\text{ihb}}, \tag{IV-30}$$

with $\overline{\Phi_2}$ tending toward zero for $2g/\Omega$ much larger than unity. This implies that measurement of the phase-shift of the fluorescence component at the beat frequency of the fully amplitude modulated driving field no longer yields the desired information in a laser fluorescence velocimeter application, if the exciting laser causes significant saturation effects of the two-level system.

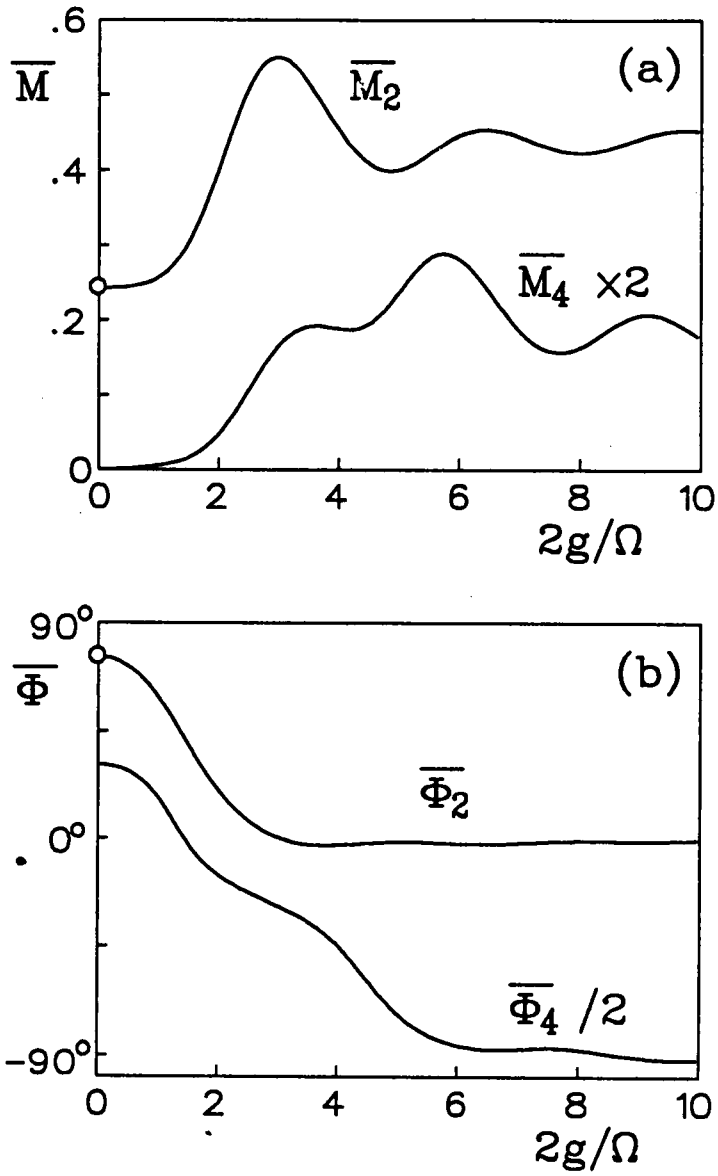


Figure IV–5: *Inhomogeneously broadened values of the depth-of-modulation and phase-shift for several fluorescence harmonics.*

As Figure IV-4, with $\overline{M_2} = \overline{r_2}/\overline{r_0}$ *and* $\overline{M_4} = \overline{r_4}/\overline{r_0}$. *Circles indicate the weak field values from Eqs.(IV-19) [(IV-23)] and (IV-20) [(IV-24)].*

Figure IV-5 displays also the depth-of-modulation $\overline{M_4}$ and the phase-shift $\overline{\Phi_4}$ for the inhomogeneously broadened fluorescence harmonic at twice the beat frequency of the driving field. Of course, for small field amplitudes ($2g/\Omega \ll 1$), the interaction is basically linear, and no additional harmonics are generated. But for large fields, up to 15 percent of the fluorescence intensity is contained in this harmonic, as can be seen from the peak of the curve of $\overline{M_4}$ versus $2g/\Omega$ in Figure IV-5(b). As for the component at 2Ω, the fluorescence component at 4Ω retains significant multi-photon resonance structure, as can be seen from the oscillatory behavior of $\overline{M_4}$, and, to a lesser extent, that of $\overline{\Phi_4}$.

To consider the effect of different ratios of the damping rates T_1^{-1} and T_2^{-1}, we have, again, computed the inhomogeneously broadened values of the depth-of-modulation $\overline{M_2}$ and the phase-shift $\overline{\Phi_2}$ for a constant profile $G_{||}(\Delta) = 1/\Omega$, and have displayed the results in Figure IV-6 for several values of the ratio T_1/T_2. For $T_1/T_2 = 0.5$, the radiative damping case of Figures IV-4 and IV-5 is reproduced. The larger the ratio T_1/T_2, the less the values of $\overline{M_2}$ and $\overline{\Phi_2}$ differ from the values M_{ihb} and Φ_{ihb} (circles in Figure IV-6), even for large values of $2g/\Omega$. This result can be understood by noting that increasing values of T_1/T_2 signify either an increasing collisional deexcitation rate, or, by Eq.(IV-16), an increasing bandwidth of the exciting source. But, in the limit $T_2^{-1} \to \infty$, the broadband excitation rate $R(\Delta)$ from Eq.(IV-8) goes to zero, even for large values of the Rabi frequency g, so that the weak field results from Eq.(IV-19) and (IV-20) hold. Because these results are identical to the inhomogeneously broadened weak field values M_{ihb} and Φ_{ihb}, respectively, the values $\overline{M_2}$ and $\overline{\Phi_2}$ in Figure IV-6 should indeed approach the weak field values for arbitrary values of $2g/\Omega$.

Finally, we investigate the influence of the width of the inhomogeneous profile $G_{||}(\Delta)$ on the inhomogeneously broadened results. Thus, we assume a Gaussian

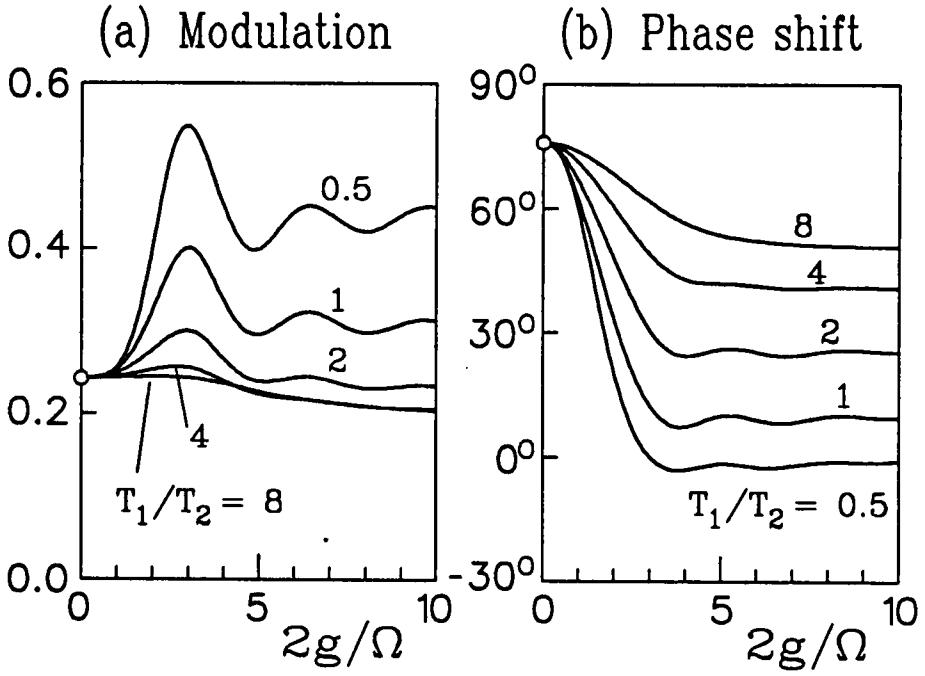


Figure IV–6: *Inhomogeneously broadened values of the depth-of-modulation and phase-shift for several values of the damping ratio.*

As Figures IV-4 and IV-5, for various ratios T_1/T_2, as indicated.

profile centered around $\Delta = 0$:

$$G_{\parallel}(\Delta) = \frac{1}{\Omega} \exp -\left(\frac{\Delta}{\Delta_D}\right)^2. \qquad \text{(IV–31)}$$

In Eq.(IV-31), Δ_D is a measure of the Doppler width of the medium, and, as for the calculations involving a rectangular profile $G_{\parallel}(\Delta)$, the scaling by the modulation frequency Ω is to render the quantities $\overline{r_0}$ and $\overline{r_{2k}}$ from Eq.(IV-27) dimensionless. Calculations were performed for the values $\Delta_D = \Omega$, 3Ω, 10Ω, 30Ω, and 100Ω. The results for the depth-of-modulation $\overline{M_2}$ are displayed in Figure IV-7. As in Figures IV-4, IV-5, and IV-6, the numerical integration from Eqs.(IV-26) was performed using the values $\Delta_{\max} = 500\Omega$ and $N_i = 10000$. Other parameters are

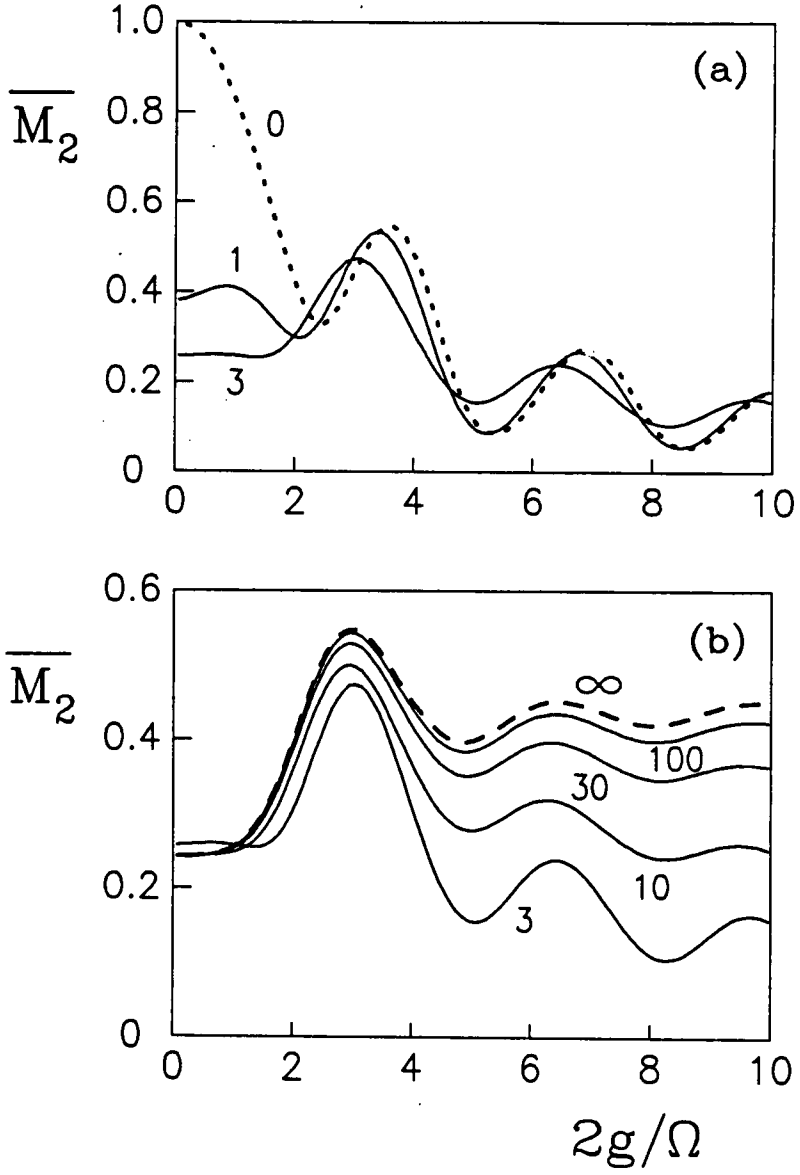


Figure IV–7: *Influence of the Doppler width on the inhomogeneously broadened values of the depth-of-modulation.*

Calculations are for $\Omega T_1 = \Omega T_2/2 = 2$ *and the Gaussian profile from Eq.(IV-31) with* $\Delta_{max} = 500\Omega$ *and* $N_i = 10000$. *Parameters beside the curves denote the scaled values of the Doppler width* Δ_D/Ω.

indicated in the figure caption. Also displayed in Figure IV-7 are the values of $\overline{M_2}$ corresponding to $\Delta_D = 0$ and $\Delta_D = \infty$ (dashed curves), which are obtained in the complete absence of inhomogeneous broadening and for the case of a rectangular inhomogeneous profile (that is, the values from Figures IV-5 and IV-6), respectively. To keep the figure from being too cluttered, curves for $\Delta_D \leq 3\Omega$ [$\Delta_D \geq 3\Omega$] are displayed in Figures IV-7(a) [IV-7(b)], respectively. It is observed that the most characteristic features of the transition from no broadening to maximum broadening actually occur for relatively small values of the Doppler width. Specifically, the unit value of the depth-of-modulation in the weak field limit [cf. Eq.(IV-15)] quickly approaches the limiting value M_{ihb} (or M_{bb}) with increasing Doppler width Δ_D. The results from Figure IV-7 also imply that, if the Doppler width Δ_D greatly exceeds the modulation frequency Ω, the excact shape of the inhomogeneous profile $G_{\|}(\Delta)$ has little effect on the inhomogeneously broadened quantities.

As we have noted, the numerical results from Figures IV-4 through IV-7 have important implications for the interpretation of LFV data. In particular, for strong driving fields, the phase-shift of the fluorescence component at the beat frequency of the driving field becomes essentially zero, independent of the strength of the driving field and the modulation frequency. This would preclude the extraction of the transverse velocity of the fluorescing atoms in the conventional manner (see Ref.[1] and the discussion following Eq.(IV-5) on page 165), thereby defeating the principle of operation of the LFV.

However, the result that significant multi-photon resonance structure remains in the inhomogeneously broadened harmonic components of the fluorescence and susceptibility of the two-level medium is interesting in its own right. For example, in fundamental and applied studies of the field-atom interaction

such as those of Ref.[14], this finding might alleviate the need for meticulously designed atomic beam setups, in which one attempts to eliminate inhomogeneous broadening altogether. Futhermore, we conclude Section IV by noting that there is a remarkable connection between the inhomogeneously broadened resonance behavior of the two-level atom and the Bloch-Siegert resonance curves discussed in Section III-4. In particular, we contend that there is a strong correlation between the resilience of the multi-photon resonance structure of interaction components (that is, the tendency for the oscillatory behavior as a function of the interaction strength $2g/\Omega$ to remain) upon inhomogeneous broadening on the one hand, and the existence of double branches of the corresponding Bloch-Siegert resonance curves on the other hand. Indeed, from this correlation it would be correctly predicted that:

(1) The DC fluorescence component becomes a structureless, monotonically increasing function of the field strength upon inhomogeneous broadening [see Figure IV-4(a)], because it does not possess doubly branched Bloch-Siegert resonance curves [see Figures III-1, III-2, III-3, and Eqs.(III-14), (III-27), and (III-32)];

(2) Fluorescence harmonics become structureless for large $2g/\Omega$ [see Figures IV-4(a), IV-5, IV-6, and IV-7], because the double branches of the corresponding Bloch-Siegert curves converge in this limit [see Figures III-1 and III-4(a), and observe that — for zero detuning — the Bessel zeros $\tilde{x}_{0N}$ and $\tilde{x}_{2k,N}$ converge; see Eq.(III-33) and following];

(3) Harmonics of the susceptibility retain resonance structure even for large $2g/\Omega$ [see Figure IV-4(b)], because the double branches of the corresponding Bloch-Siegert curves become maximally split in this limit [see Figure III-4(b) and observe that — for zero detuning — the Bessel zeros $\tilde{x}_{0N}$ and $\tilde{x}_{2k+1,N}$ become separated by π; see Eq.(III-33) and following];

(4) The onset of inhomogeneously broadened resonance structure as a function of $2g/\Omega$ becomes slower as the order of the interaction increases [compare $\overline{M_2}$ and $\overline{M_4}$ in Figure IV-5(a)], because, in addition to the double branch with quantum number $N = 1$, additional double branches are missing , such as the $N = 3$ double branch for the fluorescence at 4Ω and the susceptibility at 3Ω [see Figure III-4, and the remark under "*Thirdly, ...*" on page 153].

Although the above points *do* constitute a remarkable correlation, the correlation is not easily explained as being a strongly causal one. However, it should be observed that, in Figure III-1, the double branches of the Bloch-Siegert curves of the modulated fluorescence component greatly pronounce their resonance structure over that of the DC component, especially for small detunings. Because, as we have shown in Figure IV-7, the main contribution to the inhomogeneously broadened quantities stems from the region of small detunings, the correlation does indeed become plausible. Because it is not easy to quantify the correlation, it is equally difficult to formally prove or disprove it. However, it should be possible to check whether this correlation holds qualitatively for the interaction of a two-level atom with fields other than a fully amplitude modulated field, for example a field that is not fully amplitude modulated [76].

V DISCUSSION

In Part II, we have investigated in detail the interaction of a fully amplitude modulated, narrowband laser with a two-level atom. Several new and interesting features have come to light. These include a discussion of the resonance behavior of not only the time-averaged fluorescence but that of modulated interaction components also, in terms of Bloch-Siegert resonance curves; the branching of these Bloch-Siegert resonance curves for harmonic components; and the effects of these doubly branched resonances on the inhomogeneously broadened behavior of the two-level medium. Also, several new analytical results have been obtained, namely expressions for the harmonic branches of the Bloch-Siegert curves, and solutions of the optical Bloch equations for zero detuning and unequal longitudinal and transverse damping rates.

As far as the implications for the operation of a laser fluorescence velocimeter are concerned, we have shown that, except for weak excitation, expressions for the depth-of-modulation and phase-shift of the modulated fluorescence signal may differ substantially from the familiar expressions from conventional phase sensitive fluorometry. Unfortunately, the successful operation of a laser fluorescence velocimeter has proven more difficult than anticipated, so that, for now, much of the theory from this work remains hypothetical. However, some of the findings, particularly the resilience of multiple quantum resonance structure upon inhomogeneous broadening, may spurn experimental activities by those workers who are primarily interested in the fundamental aspects of field-matter interaction.

Many extensions of this work are possible. For example, other types of interaction may be investigated by similar techniques, namely excitation of a two-level atom by a narrowband laser that is not fully amplitude modulated, excitation

by a narrowband laser that is frequency (phase) modulated, and excitation by a bichromatic field with unequal intensities in the two modes. As discussed in Section II-3, each of these geometries have mathematically equivalent counterparts in magnetic resonance. Thus, many of the known results from magnetic resonance should be directly applicable to the corresponding optical interactions. Of these we mention in particular the much studied Haroche resonances in a transversely pumped magnetic resonance experiment, which should also be observable in the resonant excitation of an optical two-level system by a phase or frequency modulated source (see Ref. [80] and Appendix D). But just as in the case of the fully amplitude modulated optical interaction and its magnetic counterpart, the other geometries mentioned above have been largely unexplored as far as the resonance behavior of harmonic components of either the fluorescence or susceptibility are concerned. We have found that, in analogy with the FAM case, these systems display also a doubly branched resonance behavior, which, however, is a lot more complicated than for the case of a FAM interaction [76].

Other extensions of this work might include the application of the insights of the Bloch-Siegert resonance structure to the inhomogeneous broadening effects in an equal-intensity, counter-propagating beam geometry [66,67], and the study of atomic systems with more than two levels. For example, one could investigate the dynamics of a pump-probe experiment, in which the FAM-driven two-level system is probed by a weak laser beam which monitors the absorption to a third level, or one might attempt to develop a theory that includes all the magnetic hyperfine levels of, say, the sodium D-lines. Also, some of this work should be of interest to the study of four-wave mixing experiments, which, like the fully amplitude modulated interaction, display subharmonic (or multiple quantum) resonance structure [78,79].

Finally, this work has shown that, despite 25 years of intensive research into the fundamental nature of field-atom interactions, even at the most simplified level of description, namely that of a classical wave of well defined frequency, amplitude, and phase interacting with a two-level quantum system, important discoveries remain to be made: the textbooks do not comprise all of this branch of optical physics yet!

LIST OF REFERENCES

[1] D. Keefer, "Laser fluorescence velocimeter," Appl. Opt. **26**, 91–94 (1987).

[2] F. Durst, A. Melling, and J. H. Whitelaw, *Principles and Practice of Laser-Doppler Anemometry* (Academic, New York, 1981).

[3] D. Keefer, L. M. Davis, C. Parigger, L. M. Smith, private communication.

[4] D. H. Campbell and J. W. L. Lewis, "Detailed temporal behavior of laser-excited sodium tracer in nitrogen and application to nitrogen number density measurements at low densities," Appl. Opt. **20** 4102–4109 (1981).

[5] F. Duschinsky, Z. Phys. **81**, 7 (1933).

[6] E. L. Wehry, ed., *Modern Fluorescence Spectroscopy* (Plenum, New York, 1981).

[7] S. Feneuille, M.-G. Schweighofer, and G. Oliver, "Response of a two-level system to a narrow-band light excitation completely modulated in amplitude," J. Phys. B **9**, 2003–2009 (1976).

[8] L. Armstrong Jr. and S. Feneuille, "Theoretical analysis of the phase shift measurement of lifetimes using monochromatic light," J. Phys. B **8**, 546–551 (1975).

[9] W. A. McLean and S. Swain, "Detuning effects in the phaseshift measurement of lifetimes using monochromatic light," J. Phys. B **9**, 2011–2015 (1976).

[10] R. Saxena and G. S. Agarwal, "AC Stark effect and fluorescence using modulated laser beams; I. Effect of laser fluctuations and arbitrary relaxation parameters," J. Phys. B **12**, 1939–1951 (1979).

[11] W. M. Ruyten, L. M. Davis, C. Parigger, and D. R. Keefer, Atomic response to bichromatic crossed-beam field" in *Advances in Laser Science-III*, A. C. Tam, J. L. Gole, and W. C. Stwalley, eds. (American Institute of Physics, New York, 1988), pp. 155–157.

[12] L. W. Hillman, J. Krasinski, R. W. Boyd, and C. R. Stroud, Jr., "Observation of higher order dynamical states of a homogeneously broadened laser," Phys. Rev. Lett. **52**, 1605–1608 (1984).

[13] L. W. Hillman, J. Krasinski, K. Koch, and C. R. Stroud, Jr., "Dynamics of homogeneously broadened lasers: higher-order bichromatic states of operation," J. Opt. Soc. Am. B **2**, 211–216 (1985).

[14] S. Chakmakjian, K. Koch, and C. R. Stroud, Jr., "Observation of resonances at subharmonics of the Rabi frequency in the saturated absorption of a 100% amplitude-modulated laser beam," J. Opt. Soc. Am. B **5**, 2015–2020 (1988).

[15] K. Koch, B. J. Oliver, S. H. Chakmakjian, and C. R. Stroud, Jr., "Subharmonic instabilities in resonant interactions with bichromatic fields," J. Opt. Soc. Am. B **6**, 58–65 (1989).

[16] P. Thomann, "Optical parametric resonances," J. Phys. B **9**, 2411–2419 (1976).

[17] P. Thomann, "Optical resonances in a strong modulated laser beam," J. Phys. B **13**, 1111–1124 (1980).

[18] B. Blind, P. R. Fontana, and P. Thomann, "Resonance fluorescence spectrum of intense amplitude modulated light," J. Phys. B **13**, 2717–2727 (1980).

[19] J. Margerie and J. Brossel, C. R. Acad. Sci. **241**, 373 (1955); J. M. Winter, C. R. Acad. Sci. **241**, 375 (1955); Ann. Phys. (Paris) **4**, 745 (1959).

[20] F. Bloch and A. Siegert, "Magnetic resonance for nonrotating fields," Phys. Rev. **57**, 522–527 (1940).

[21] W. M. Ruyten, "Subharmonic resonances in terms of multiphoton processes and generalized Bloch-Siegert shifts," J. Opt. Soc. Am. B, to appear October 1989.

[22] W. M. Ruyten, "Multiphoton resonances in the modulated fluorescence from an inhomogeneously broadened medium," Opt. Lett. **14**, 506–508 (1989).

[23] F. Schuda, C. R. Stroud, Jr., and M. Hercher, "Observation of the resonant Stark effect at optical frequencies," J. Phys. B **7**, L198–L202 (1974).

[24] G. C. Bjorklund, "Frequency modulation spectroscopy: a new method for measuring weak absorptions and dispersions," Opt. Lett. **5**, 15–17 (1980).

[25] N. Nayak and G. S. Agarwal, "Absorption and fluorescence in frequency-modulated fields under conditions of strong modulation and saturation," Phys. Rev. A **31**, 3175–3182 (1985).

[26] W. M. Ruyten, "Comment on absorption and fluorescence in strong frequency-modulated and amplitude-modulated fields," Phys. Rev. A **39**, 442–444 (1989).

[27] G. S. Agarwal and N. Nayak, "Saturation of optical susceptibilities in strongly amplitude-modulated fields," J. Phys. B **19**, 3385–3400 (1986).

[28] W. M. Ruyten, "Harmonic behavior of the multiple quantum resonances of a two-level atom driven by a fully amplitude modulated field," Phys. Rev. A **40**, 1447–1455 (1989).

[29] G. S. Agarwal and N. Nayak, "Multiphoton processes in two-level atoms in two intense pump beams," J. Opt. Soc. Am. B **1**, 164–168 (1984).

[30] T. Yabuzaki, N. Tsukada, and T. Ogawa, "Modification of the atomic g-factor by the oscillating rf field," J. Phys. Soc. Jpn. **32**, 1069–1077 (1972).

[31] N. Tsukada, T. Yabuzaki, and T. Ogawa, "Efect of transverse pumping in optical pumping," J. Phys. Soc. Jpn. **33**, 698–707 (1972).

[32] N. Tsukada, T. Koyama, and T. Ogawa, "Observation of new type resonances in double resonance experiment," Phys. Lett. **44A**, 501–502 (1973).

[33] N. Tsukada and T. Ogawa, "Saturation effect in rf spectroscopy for transverse optical pumping," J. Phys. B **6**, 1643–1649 (1973).

[34] N. Tsukada, Y. Murakami, and T. Ogawa, "Saturation effects of transverse resonances in optical pumping experiments," J. Phys. B **6** 2605–2612 (1973).

[35] T. Yabuzaki and T. Ogawa, "Frequency shifts of self-oscillating magnetometer with cesium vapor," J. Appl. Phys **45**, 1342–1355 (1974).

[36] T. Yabuzaki, S. Nakayama, Y. Murakami, and T. Ogawa, "Interaction between a spin-1/2 atom and a strong rf field," Phys. Rev. A **10** 1955–1963 (1974).

[37] N. Tsukada, T. Koyama, and T. Ogawa, "Saturation effects in magnetic resonances for a general magnetic field configuration," J. Phys. B **7**, 799–809 (1974).

[38] T. Yabuzaki, Y. Murakami, and T. Ogawa, "Power shifts of multiphoton transitions in a spin 1/2 system," J. Phys. B **9**, 9–19 (1976).

[39] N. Tsukada, "Saturation effects of a two-level system in two rf fields," J. Phys. Soc. Jpn. **46**, 1280–1287 (1979).

[40] A. M. Bonch-Bruevich, T. A. Vartanyan, and N. A. Chigir, "Subradiative structure in the absorption spectrum of a two-level system in a biharmonic radiation field," Sov. Phys. JETP **50**, 901–906 (1980) [Zh. Eksp. Teor. Fiz. **77**, 1899–1909 (1979)].

[41] G. I. Toptygina and É. E. Fradkin, "Theory of subradiative absorption structure in the interaction between two intense waves in a nonlinear medium," Sov. Phys. JETP **55**, 246–251 (1982) [Zh. Eksp. Teor. Fiz. **82**, 429–440 (1982)].

[42] E. Arimondo and G. Moruzzi, "Bloch-Siegert shift in optically oriènted ^{199}Hg vapour," J. Phys. B **6**, 2382–2389 (1973).

[43] E. Arimondo and R. Corbalan, "multiple quantum transitions in optically oriented ^{87}Rb vapour," J. Phys. B **7**, 2368–2374 (1974).

[44] E. Arimondo and G. Moruzzi, "Radiofrequency multiple-quantum transitions in the presence of an optical pumping cycle," J. Phys. B **9**, 709–721 (1976).

[45] C. Cohen-Tannoudji, "Transverse optical pumping and level crossings in free and 'dressed' atoms," in *Fundamental and Applied Laser Physics*, M. S. Feld, A. Javan, and N. A. Kurnit, eds. (Wiley, New York, 1973), pp. 791–815.

[46] C. Cohen-Tannoudji, J. Dupont-Roc, and C. Fabre, "An experimental check of higher order terms in the radiative shift of a coherence resonance," J. Phys. B **6**, L218–L221 (1973).

[47] R. Loudon, *The Quantum Theory of Light* (Clarendon, Oxford, 1983), 2nd ed., Ch. 2.

[48] L. Allen and J. H. Eberly, *Optical Resonance and Two-Level Atoms* (Wiley, New York, 1975).

[49] Z. Y. Ou and L. Mandel, "Observation of spatial quantum beating with separated photodetectors," Phys. Rev. Lett. **61**, 54–57 (1988).

[50] D. T. Pegg, "Misalignment effects in magnetic resonance," J. Phys. B **6**, 241–253 (1973).

[51] D. T. Pegg, "Semi-classical model of magnetic resonance in intense rf fields," J. Phys. B **6**, 246–253 (1973).

[52] J. H. Shirley, "Solution of the Schrödinger equation with a Hamiltonian periodic in time," Phys. Rev. **138**, B979–B987 (1965).

[53] C. Cohen-Tannoudji, *Cargése Lectures in Physics*, M. Lévy, ed. (Gordon & Breach, New York, 1968), Vol. 2, p. 347.

[54] S. Stenholm, "Saturation effects in rf spectroscopy I. General theory," J. Phys. B **5**, 878–889 (1972).

[55] S. Stenholm, "Saturation effects in rf spectroscopy II. Multiple quantum transitions," J. Phys. B **5**, 890–895 (1972).

[56] S. Stenholm, "Saturation effects in rf spectroscopy III. Mixing of nearly degenerate levels by strong off-resonant fields," J. Phys. B **6**, 1097–1102 (1973).

[57] S. Stenholm and C.-G. Aminoff, "Saturation effects in rf spectroscopy IV. Transverse pumping and Haroche resonances," J. Phys. B **6**, 2390–2408 (1973).

[58] S. Stenholm, "Power series expansion for the rf resonance shift," J. Phys. B **6**, L240–L242 (1973).

[58] S. Stenholm, "Power series expansion for the rf resonance shift," J. Phys. B **6**, L240–L242 (1973).

[59] C. Cohen-Tannoudji, J. Dupont-Roc, and C. Fabre, "A quantum calculation of the higher order terms in the Bloch-Siegert shift," J. Phys. B **6**, L214–L217 (1973).

[60] P. Hannaford, D. T. Pegg, and G. W. Series, "Analytical expressions for the Bloch-Siegert shift," J. Phys. B **6**, L222–L225 (1973).

[61] F. Ahmad and R. K. Bullough, "Analytical expressions for the Bloch-Siegert shift," J. Phys. B **7**, L147–L151 (1974).

[62] F. Ahmad and R. K. Bullough, "Theory of the Bloch-Siegert shift," J. Phys. B **7**, L275–L280 (1974).

[63] S. Swain, "Analytical expressions for the positions of the longitudinal and transverse resonances in radio-frequency spectroscopy," J. phys. B **7**, 2363–2367 (1974).

[64] W. A. McClean and S. Swain, "Crossings and anti-crossings for a spin 1/2 system with arbitrary field orientations, J. Phys. B **9**, 1673–1680 (1976).

[65] L. M. Davis, "Interference between resolvable wavelengths with single-photon-resolved detection," Phys. Rev. Lett. **60**, 1258–1261 (1988).

[66] E. Kyrölä and S. Stenholm, "Velocity tuned resonances as multi-Doppleron processes," Opt. Comm. **22**, 123–126 (1977).

[67] E. Kyrölä and S. Stenholm, "Probe spectroscopy of multi-Doppleron processes," Opt. Comm. **30**, 37–40 (1979).

[68] N. Tsukada and T. Nakayama, "Modulation of optical bistability by an additional laser beam," Phys. Rev. A **25**, 964–977 (1982).

[69] W. M. Ruyten, "Rabi structures in a Doppler broadened gas?" OSA Annual Meeting, 1988 Technical Digest Series, Vol. 11 (Optical Society of America, Washington, DC, 1988), p. 63.

[70] T.-S. Ho and S.-I. Chu, "Semiclassical many-mode Floquet theory: II. Nonlinear photon dynamics of a two-level system in a strong bichromatic field," J. Phys. B **17**, 2101–2128 (1984).

[71] C. S. Chang and P. Stehle, "Quantum-electrodynamical theory of atoms interacting with high-intensity radiation fields," Phys. Rev. A **4**, 641–661 (1971).

[72] D. A. Andrews and G. Newton, Bloch-Siegert shifts in resonances between excited states," J. Phys. B **9**, 1453–1460 (1976).

[74] S. Stenholm and W. E. Lamb, Jr., "Semiclassical theory of a high-intensity laser," Phys. Rev. **181**, 618–635 (1969).

[75] M. Abramowitz and I. A. Stegun, *Handbook of Mathematical Functions* (Dover, New York, 1972), Sec. 9.1.

[76] W. M. Ruyten, "Resonance behavior of a two-level atom driven by amplitude- or frequency-modulated fields," presented at the Sixth Rochester Conference on Coherence and Quantum Optics, Rochester, June 26–28 (1989); proceedings to be published by Plenum, L. Mandel, ed.

[77] J. H. Eberly and K. Wódkiewicz, "The time-dependent physical spectrum of light," J. Opt. Soc. Am. **67**, 1252–1261 (1977).

[78] M. T. Gruneisen, K. R. MacDonald, and R. W. Boyd, "Induced gain and modified absorption of a weak probe beam in a strongly driven sodium vapor," J. Opt. Soc. Am. B **5**, 123–129 (1988).

[79] M. T. Gruneisen, K. R. MacDonald, R. W. Boyd, and D. J. Harter, "Laser beam combining in atomic potassium vapor," OSA Annual Meeting, 1988 Technical Digest Series, Vol. 11 (Optical Society of America, Washington, DC, 1988), p. 123.

[80] W. M. Ruyten, "Optical Haroche and Hanle resonances excited by a resonant phase-modulated field," submitted to Phys. Rev. Lett.

[81] W. H. Press and S. A. Teukolsky, "Evaluating continued fractions and computing exponential integrals," Computers in Physics **2**, Sep/Oct, 88–89 (1988).

[82] P. A. Lakshmi and G. S. Agarwal, "Optical Hanle effect of arbitrary strength and bandwidth," Phys. Rev. A **23**, 2553–2562 (1981).

[83] L.-G. Wang, D. A. Tate, H. Riris, and T. F. Gallagher, "High-sensitivity frequency-modulation spectroscopy with GaAlAs diode laser," J. Opt. Soc. Am. B **6**, 871–876 (1989).

APPENDICES

Appendix A: Zero Detuning Solution

In Appendix A, which is taken from the Appendix of Ref.[21], we solve the Bloch equations from Eqs.(III-1) analytically for the case of zero detuning ($\Delta = 0$). For equal longitudinal and transverse damping rates ($T_1 = T_2$), the Bessel function solution from Eqs.(III-13b) and (III-14) has been known for quite some time (see for example Ref.[27] or any of the references for the equivalent magnetic resonance geometry listed in Table II-1 on page 131). However, for unequal damping rates, the solution has not been calculated before.

For zero detuning, the optical Bloch equations from Eqs.(III-1) can be written in matrix form as ($U = 0$):

$$\frac{d\mathbf{\Psi}}{dt} = \Big[\mathbf{A}_0 + 2g\cos(\Omega t)\mathbf{A}_1\Big]\mathbf{\Psi} - \frac{1}{T_1}\begin{pmatrix}0\\1\end{pmatrix}, \qquad \text{(A-1a)}$$

where $\Psi_1 = V$, $\Psi_2 = W$, and the matrices $\mathbf{A}_0$ and $\mathbf{A}_1$ are given by

$$\mathbf{A}_0 = \begin{pmatrix}-1/T_2 & 0\\ 0 & -1/T_1\end{pmatrix}; \qquad \mathbf{A}_1 = \begin{pmatrix}0 & 1\\ -1 & 0\end{pmatrix}. \qquad \text{(A-1b)}$$

Following Ref.[27] we transform to the new vector $\mathbf{\Phi} \equiv \mathbf{S}^{-1}\mathbf{\Psi}$, where $\mathbf{S}$ is the orthogonal matrix that follows from the diagonalization of $\mathbf{A}_1$. Thus,

$$\mathbf{\Phi} = \mathbf{S}^{-1}\mathbf{\Psi}; \qquad \mathbf{A}_1 = \mathbf{S}\,\mathbf{\Lambda}\,\mathbf{S}^{-1}, \qquad \text{(A-2a)}$$

with

$$\mathbf{\Lambda} = \begin{pmatrix}-i & 0\\ 0 & i\end{pmatrix}; \qquad \mathbf{S}^{-1} = \mathbf{S}^{\mathrm{T}*} = \frac{1}{\sqrt{2}}\begin{pmatrix}1 & i\\ 1 & -i\end{pmatrix}. \qquad \text{(A-2b)}$$

It is easily checked that $\Phi_2 = \Phi_1^*$ so that both V and W can be expressed in terms of $\Phi \equiv \Phi_1$:

$$V(t) = \sqrt{2}\,\mathrm{Re}\{\Phi(t)\}; \qquad W(t) = \sqrt{2}\,\mathrm{Im}\{\Phi(t)\}. \qquad \text{(A-3)}$$

If we define the dimensionless quantities $\tau \equiv t/T_1$, $\omega \equiv \Omega T_1$, $x \equiv 2g/\Omega$, and $\gamma_\pm \equiv \frac{1}{2}(1 \pm T_1/T_2)$, the Bloch equation for $\Phi(\tau)$ becomes

$$\frac{d\Phi}{d\tau} = -\left[\gamma_+ + ix\omega\cos(\omega\tau)\right]\Phi + \gamma_-\Phi^* - i/\sqrt{2}. \qquad \text{(A-4)}$$

To obtain the solution for $T_1 \neq T_2$ (i.e., $\gamma_- \neq 0$) we expand Φ as a perturbation series in γ_-:

$$\Phi(\tau) = \sum_{n=0}^{\infty} \gamma_-^n \Phi^{(n)}(\tau). \qquad \text{(A-5)}$$

The terms $\Phi^{(n)}$ then satisfy the recursion equations

$$\frac{d\Phi^{(n)}}{d\tau} = -\left[\gamma_+ + ix\omega\cos(\omega\tau)\right]\Phi^{(n)} + C^{(n)}, \qquad \text{(A-6a)}$$

with

$$C^{(0)} = -i/\sqrt{2}; \qquad C^{(n)} = \Phi^{(n-1)*}; \quad n \geq 1. \qquad \text{(A-6b)}$$

The homogeneous solution is given by

$$\Phi^{(n)}(\tau) = f(\tau)\, e^{-\gamma_+\tau - ix\sin\omega\tau} = f(\tau) \sum_{l=-\infty}^{\infty} J_l(x) e^{-(\gamma_+ + il\omega)\tau}, \qquad \text{(A-7)}$$

and the general solution becomes:

$$\Phi^{(n)}(\tau) = (-i/\sqrt{2}) \sum_{k=-\infty}^{\infty} e^{ik\omega\tau} \sum_{l=-\infty}^{\infty} \frac{W_l^{(n)}(x) J_{l-k}(x)}{\gamma_+ + il\omega}, \qquad \text{(A-8)}$$

where

$$W_l^{(0)}(x) = J_l(x), \qquad \text{(A-9a)}$$

and

$$W_l^{(n)}(x) = -\sum_{m=-\infty}^{\infty} \frac{\{W_m^{(n-1)}(x)\}^* J_{l+m}(2x)}{\gamma_+ - im\omega}; \qquad n \geq 1. \qquad \text{(A-9b)}$$

In addition to changing summation indices, the Bessel function summation formula

$$\sum_{k=-\infty}^{\infty} J_{l+k}(x) J_{m-k}(x) = J_{l+m}(2x) \qquad \text{(A-10)}$$

has been used in the derivation of Eq.(A-9b). With Eqs.(A-3), (A-5), (A-8) and (A-9) the zero detuning solution is fully determined for arbitrary ratios T_1/T_2.

For equal (but arbitrarily large) damping rates ($T_1 = T_2$) we have $\gamma_- = 0$ and $\gamma_+ = 1$. Thus

$$\phi(\tau) = \phi^{(0)}(\tau) = \sum_{k=-\infty}^{\infty} \varphi_k \, e^{ik\omega\tau}, \tag{A-11a}$$

with

$$\varphi_k = -\frac{i}{\sqrt{2}} \sum_{l=-\infty}^{\infty} \frac{J_l(x)J_{l-k}(x)}{1+il\omega} = -\frac{i}{\sqrt{2}}(-1)^k \sum_{l=-\infty}^{\infty} \frac{J_l(x)J_{k+l}(x)}{1-il\omega}. \tag{A-11b}$$

The last step follows by replacing the summation index l by $(-l)$ and by using the symmetry property $J_{-l}(x) = (-1)^l J_l(x)$. From Eq.(A-11b) it also follows that $\varphi_{-k} = (-1)^{k+1}\varphi_k^*$. With Eqs.(III-3), (III-5), (A-3), and (A-5) it now follows that

$$v_k = (-i)\sqrt{2}\left\{\frac{\varphi_k + \varphi_{-k}^*}{2}\right\} = \begin{cases} \phi_k; & k = \text{odd}; \\ 0; & k = \text{even}, \end{cases} \tag{A-12a}$$

and

$$w_k = (-1)\sqrt{2}\left\{\frac{\varphi_k - \varphi_{-k}^*}{2i}\right\} = \begin{cases} 0; & k = \text{odd}; \\ \phi_k; & k = \text{even}, \end{cases} \tag{A-12b}$$

where ϕ_k is defined as in Eq.(III-13b). With Eqs.(III-7) and (A-12), the zero detuning solution for equal damping rates from Section III-2 is then obtained.

For unequal damping rates ($T_1 \neq T_2$), the solution for $\Phi(\tau)$ from Eqs.(A-8) and (A-9) contains, in general, an infinite number of infinite sums. However, the situation simplifies considerably in the limit of zero damping. Namely, if $T_1 \to \infty$ (i.e., $\omega \to \infty$), only the terms with $l = 0$ in Eq.(A-8) and the terms with $m = 0$ in Eqs.(A-9) contribute, so that

$$W_0^{(n)}(x) = J_0(x)\left[-J_0(2x)/\gamma_+\right]^n. \tag{A-13}$$

Thus the infinite sum from Eq.(A-6) becomes a geometric series, resulting in

$$\Phi(\tau) = \frac{(-i/\sqrt{2})J_0(x)}{\gamma_+ + \gamma_- J_0(2x)} \sum_{k=-\infty}^{\infty} J_{-k}(x) e^{ik\omega\tau}. \qquad \text{(A-14)}$$

In complete analogy with Eqs.(A-11) and (A-12), Eq.(III-27) then follows, with a factor H given by

$$H = \gamma_+ + \gamma_- J_0(2x). \qquad \text{(A-15)}$$

With $T_1/T_2 = \Gamma_v/\Gamma_w$, H may then be written as in Eq.(III-28).

Appendix B: Calculation of Power Series Coefficients of the Generalized Bloch-Siegert Shifts

In Appendix B we present a concise outline of the derivation of the power series expansions of the Bloch-Siegert shifts as given in Eqs.(III-34)–(III-38). For convenience we introduce the variables $x \equiv -(g/\Omega)^2$ and $y \equiv (\Delta_{kN}/\Omega)^2$. Also we rescale the coefficients from Eq.(III-34) according to

$$\alpha_m \equiv -N\, a_{kN}^{(m)}/(-4)^m. \tag{B-1}$$

Substituting Eq.(III-34) into Eq.(III-30) yields a power series expansion for the terms F_n (we reserve the indices N and k for the Nth resonance of the kth harmonic):

$$F_n \equiv \sum_{m=0}^{\infty} F_n^{(m)}\, x^m, \tag{B-2}$$

where

$$F_n^{(0)} = \begin{cases} n - N^2/n; & \text{n=odd,} \\ n; & \text{n=even,} \end{cases} \tag{B-3a}$$

and, for $m > 0$:

$$F_n^{(m)} = \begin{cases} (N/n)\,\alpha_m; & \text{n=odd,} \\ 0; & \text{n=even.} \end{cases} \tag{B-3b}$$

Subsequently we write the continued fraction Y_k from Eq.(III-31) — truncated after n divisions — as a single fraction with numerator A_n. The numerators A_n satisfy the recurrence relation [81]:

$$A_n = F_{k+n+1}\, A_{n-1} + x\, A_{n-2}; \qquad n \geq 0, \tag{B-4a}$$

with

$$A_{-1} = 1; \qquad A_n = 0 \ \text{ for } n < -1. \tag{B-4b}$$

Expanding the A_n's as a power series (dropping the subscripts N and k):

$$A_{N-k+n} \equiv \sum_{m=0}^{\infty} A_n^{(m)}\, x^m \tag{B–5}$$

and substituting Eq.(B-2), this leads to the following recurrence relations, valid for $n \geq k - N$:

$$A_n^{(0)} = F_{N+n+1}^{(0)}\, A_{n-1}^{(0)}, \tag{B–6a}$$

and, for $m > 0$:

$$A_n^{(m)} = A_{n-2}^{(m-1)} + \sum_{l=0}^{m} F_{N+n+1}^{(l)} A_{n-1}^{(m-l)}. \tag{B–6b}$$

To satisfy the condition $Y_k = 0$ from Eq.(III-32) we must require that $A_\infty^{(m)} = 0$ for all $m \geq 0$. This can be accomplished by requiring that

$$\lim_{n\to\infty} \Big\{ A_n^{(m)} = 0; \quad 0 \leq m \leq n+1 \Big\}. \tag{B–7}$$

Because, from Eq.(B-3a), $F_N^{(0)} = 0$, it follows from Eq.(B-6a) that $A_n^{(0)} = 0$ for all $n \geq -1$. From Eq.(B-6b), it then follows that $A_n^{(m)} = 0$ for all $n > m - 1$, *if* one imposes the condition

$$\Big[A_{m-1}^{(m)} = 0 \Big] \Rightarrow \alpha_m; \qquad m = 1, 2, 3, \ldots. \tag{B–8}$$

Thus Eq.(B-7) is satisfied indeed. As is indicated, solving Eq.(B-8) renders successively the desired coefficients α_m.

As an illustration we calculate the first coefficient α_1. By iterating Eq.(B-6b) and using Eqs.(B-3) we obtain

$$A_0^{(1)} = A_{-2}^{(0)} + (N+1)\Big(A_{-3}^{(0)} + \alpha_1 A_{-2}^{(0)} \Big). \tag{B–9}$$

From Eq.(B-6) it can be shown that

$$A_{-p}^{(0)} / A_{-2}^{(0)} = \Theta_{k+p-1}^{N} \Big/ \prod_{q=1}^{p-2} F_{N-q}^{(0)}; \qquad p \geq 2, \tag{B–10}$$

with Θ as defined in Eq.(III-35). Substituting Eq.(B-10) into Eq.(B-9) and requiring that $A_0^{(1)} = 0$ then yields α_1 and, with Eq.(B-1), the first order term of the Bloch-Siegert shift as given in Eq.(III-36).

Higher order terms are obtained in a similar fashion. In order to eliminate terms $A_n^{(m)}$ with $m > 0$, we have used the expressions

$$A_{-3}^{(0)}A_{-2}^{(1)} - A_{-3}^{(1)}A_{-2}^{(0)} = A_{-3}^{(0)}A_{-4}^{(0)} \qquad \text{(B–11)}$$

to obtain α_2 and, in addition to Eq.(B-11), the expression

$$A_{-4}^{(0)}A_{-2}^{(1)} - A_{-4}^{(1)}A_{-2}^{(0)} = A_{-4}^{(0)}\Big[A_{-4}^{(0)} + (N-1)\Big\{F_{N-2}^{(1)}A_{-4}^{(0)} + A_{-5}^{(0)}\Big\}\Big] \qquad \text{(B–12)}$$

to obtain α_3. Eqs.(B-11) and (B-12) can be derived from Eqs.(B-3) and (B-5).

It would seem feasible to write an algorithm based on Eqs.(B-3), (B-6), (B-8), and (B-10) by which arbitrarily high order coefficients α_m can be computed. Although we have given this approach some thought we have been unable to come up with such an algorithm, mainly because of the difficulty of generalizing the implementation of expressions like Eqs.(B-11) and (B-12).

Appendix C: Weak Field Solutions

In Appendix C, we present some of the details of the calculations of the weak field results from Section IV-2. Specifically, Appendices C-1, C-2, and C-3 parallel the Sections IV-2.1, IV-2.2, and IV-2.3.

C-1 Details of narrowband solution

To obtain the weak field solution from Section IV-2.1 from the continued fraction solution in Section III-2, we observe that only the fluorescence components w_0 and w_2 (and w_{-2}) from Eq.(III-5) need to be considered, since, for weak fields, the interaction is linear, so that no additional harmonics are generated. Thus, with Eqs.(II-5c), (III-3), (III-5), (III-7), and (III-12), we obtain [cf. Eq.(III-15)]:

$$\rho_{22}(t) = \frac{1 - w(t)}{2} \simeq (1/2)\Big[1 - \psi_0 - \psi_2 e^{2i\Omega t} - \psi_2^* e^{-2i\Omega t}\Big]. \qquad \text{(C–1)}$$

Furthermore, with Eqs.(III-10) and (III-11), we obtain

$$\psi_0 = \left[1 + (2g/\Gamma_w)\,\mathrm{Im}\{x_1\}\right]^{-1} \simeq 1 - 2gT_1\,\mathrm{Im}\{x_1\}, \qquad \text{(C–2)}$$

and

$$\psi_2 = x_2\, x_1\, \psi_0 \simeq x_2 x_1, \qquad \text{(C–3)}$$

where we have set $\Gamma_w = T_1^{-1}$. Combining Eqs.(C-1)–(C-3) yields

$$\rho_{22}(t) \simeq gT_1\,\mathrm{Im}\{x_1\} + \left[-(1/2)x_2 x_1 e^{2i\Omega t} + \text{c.c.}\right]. \qquad \text{(C–4)}$$

In the weak field limit, it suffices to truncate the continued fractions x_1 and x_2 after one division, so that, from Eq.(III-9):

$$x_i \simeq ig/a_i; \qquad i = 1, 2. \qquad \text{(C–5)}$$

Substituting values for a_1 and a_2 from Eq.(III-8), and setting $\Gamma_u = \Gamma_v = T_2^{-1}$ then yields

$$x_1 \simeq \frac{ig(T_2^{-1} + i\Omega)}{(T_2^{-1} + i\Omega + i\Delta)(T_2^{-1} + i\Omega - i\Delta)}$$
$$= \frac{g/2}{\Delta + \Omega - iT_2^{-1}} - \frac{g/2}{\Delta - \Omega + iT_2^{-1}}, \qquad \text{(C-6)}$$

and

$$x_2 \simeq \frac{ig}{T_1^{-1} + 2i\Omega}. \qquad \text{(C-7)}$$

Thus

$$\text{Im}\{x_1\} = (g/2)\left\{\frac{T_2^{-1}}{(\Delta + \Omega)^2 + T_2^{-2}} + \frac{T_2^{-1}}{(\Delta - \Omega)^2 + T_2^{-2}}\right\}, \qquad \text{(C-8)}$$

and

$$-x_2 x_1 = g^2\left\{\frac{T_2^{-1} + i\Omega}{T_1^{-1} + 2i\Omega}\right\}\left\{\frac{1}{T_2^{-1} + i(\Delta + \Omega)}\right\}\left\{\frac{1}{T_2^{-1} - i(\Delta - \Omega)}\right\}. \qquad \text{(C-9)}$$

Substituting Eqs.(C-8) and (C-9) into Eq.(C-4) then immediately leads to the results in Eqs.(IV-6)–(IV-10).

C-2 Details of broadband solution

In the broadband limit, that is, the limit $T_2^{-1} \to \infty$, Eqs.(III-4) may be reduced to a single rate equation by setting $\dot{u} = \dot{v} = 0$. Solving Eqs.(III-4a) and (III-4b) for u and v successively, and substituting the expression for v into Eq.(III-4c) then yields

$$\dot{w} + \left[T_1^{-1} + 4R\cos^2\Omega t\right] w = T_1^{-1}, \qquad \text{(C-10)}$$

where we have set $\Gamma_u = \Gamma_v = T_2^{-1}$, $\Gamma_w = T_1^{-1}$, and $R = R(\Delta)$ is the detuning dependent excitation rate defined in Eq.(IV-18). The homogeneous solution of

Eq.(C-10) is given by

$$\begin{aligned} w(t) &= f(t)\, e^{-(T_1^{-1}+2R)t-(R/\Omega)\sin 2\Omega t} \\ &= f(t) \sum_{l=-\infty}^{\infty} (-i)^l\, I_l(R/\Omega)\, e^{-(T_1^{-1}+2R)t-2il\Omega t}, \end{aligned} \tag{C-11}$$

where I_l is a modified Bessel function of order l. Substitution of Eq.(C-11) into Eq.(C-10) then gives the general solution

$$w(t) = \sum_{k=-\infty}^{\infty} w_{2k}\, e^{2ik\Omega t}, \tag{C-12}$$

where the Floquet coefficients w_{2k} are given by

$$w_{2k} = i^k \sum_{l=-\infty}^{\infty} \frac{(-1)^l\, I_l(R/\Omega)\, I_{k-l}(R/\Omega)}{1+2RT_1+2il\Omega T_1}. \tag{C-13}$$

Note the strong similarity between Eq.(C-13) and the zero detuning, narrowband solution from Eqs.(III-13b) and (A-8), which, instead of the monotonic, modified Bessel functions I_l contains the oscillatory Bessel functions J_l.

In the weak field limit, the modified Bessel functions can be approximated by

$$I_l(R/\Omega) \simeq (R/2\Omega)^l / l!. \tag{C-14}$$

Retaining only terms of order R^0 and R^1, $\rho_{22}(t)$ can be expanded as in Eq.(C-1), that is,

$$\rho_{22}(t) = \frac{1-w_0}{2} + \left[-(1/2)w_2 e^{2i\Omega t} + \text{c.c.}\right]. \tag{C-15}$$

With Eqs.(C-13) and (C-14), we then find

$$\frac{1-w_0}{2} \simeq \frac{1}{2}\Big(1 - \frac{I_0^2}{1+2RT_1}\Big) \simeq \frac{RT_1}{1+2RT_1} \simeq RT_1, \tag{C-16}$$

and

$$-w_2/2 \simeq (-i/2)\Big(\frac{I_0 I_1}{1+2RT_1} - \frac{I_1 I_0}{1+2RT_1+2i\Omega T_1}\Big) \simeq \frac{RT_1/2}{1+2i\Omega T_1}. \tag{C-17}$$

Substitution of Eqs.(C-16) and (C-17) into Eq.(C-15) then leads immediately to Eqs.(IV-17)–(IV-20) in Section IV-2.2.

C-3 Details of inhomogeneously broadened solution

To perform the integral $\int_{-\infty}^{\infty} \rho_{22}(t;\Delta)d\Delta$ we note that, by Eqs.(C-4), (C-6), and (C-7) the only detuning dependence is contained in the factor x_1. But the corresponding integral of x_1 is performed trivially, by closing the path of integration in one of the half planes, and taking the value of the one and only pole:

$$\int_{-\infty}^{\infty} x_1(\Delta)\, d\Delta = 2\pi i \times (g/2) = \pi g i. \tag{C-18}$$

Substitution of Eqs.(C-18) and (C-7) into Eq.(C-4) then yields

$$\int_{-\infty}^{\infty} \rho_{22}(t;\Delta)\, d\Delta = \pi g^2 T_1 \left\{1 + \frac{(1/2)e^{2i\Omega t}}{1+2i\Omega T_1} + \frac{(1/2)e^{-2i\Omega T_1}}{1-2i\Omega T_1}\right\}, \tag{C-19}$$

which leads immediately to Eqs.(IV-22)–(IV-24) in Section IV-2.3.

Appendix D: Optical Haroche and Hanle Resonances Excited by a Resonant Phase-Modulated Field

The material in Appendix D is essentially that of Ref. [80]. To adapt the manuscript to this dissertation, the original references are replaced with those on page 188. Also, some reference to the material in Sections I through V is made:

From their inception, optical resonance experiments have followed in the steps of their magnetic predecessors. For example, Rabi oscillations, free induction decay, and spin echoes were first studied in magnetic doublets. And, of course, the very formulation of semiclassical Bloch equations occured in this branch of physics. Recently, we have discussed some analogies between optical and magnetic interactions involving modulated fields [26]. In particular, we have shown that the concepts of multiple quantum resonances and their associated Bloch-Siegert shifts apply to the interaction of a fully amplitude modulated field with a two-level atom [21,22,28]. Here we point out that two other well known effects from the magnetic resonance literature should be realizable in an optical resonance experiment, namely those of Haroche and Hanle resonances (See the references in Table II-1(c) on page 131; also, for a discussion of the optical Hanle effect in a different context see Ref. [82]).

Consider, first, the Bloch equations for the magnetization $\mathbf{M}$ of a spin-1/2 system subjected to a magnetic field $\mathbf{H}$ and a circularly polarized light beam, propagating along the $\hat{3}$-axis (Figure D-1), with associated optical pumping rate Λ_{mag} (see Eq.(II-22) on page 128):

$$d\mathbf{M}/dt = -\mathbf{\Gamma M} + \gamma \mathbf{M} \times \mathbf{H} + \Lambda_{\mathrm{mag}} \hat{\mathbf{e}}_3. \qquad \text{(D-1)}$$

Here, $\mathbf{\Gamma}$ is a diagonal damping matrix, and γ is the gyromagnetic ratio of the

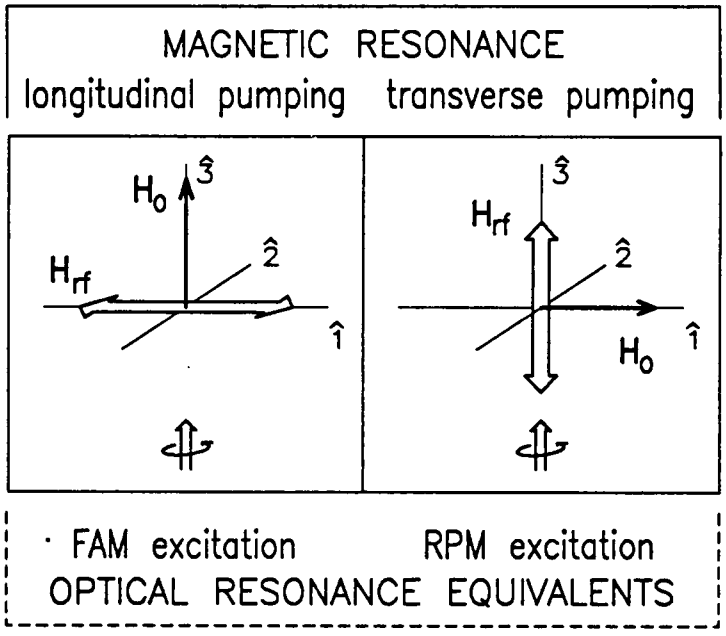


Figure D–1: *Magnetic resonance geometries, whose optical counterparts are as indicated.*

(FAM = fully amplitude modulated; RPM = resonant phase modulated).

magnetic doublet. Of the many possible magnetic field configurations, the longitudinal and transverse geometries have received the most attention. In both, an oscillating radiofrequency (rf) field $\mathbf{H}_{rf}$ is applied perpendicular to a static Zeeman field $\mathbf{H}_0$, which is either longitudinal or transverse to the optical pumping beam (Figure D-1). Thus, the magnetic "torque" $\mathbf{R}_{mag} \equiv -\gamma\mathbf{H}$ is given by

$$\mathbf{R}^{\parallel}_{mag} = (\omega_{rf} \cos \Omega t,\, 0,\, \omega_0), \tag{D–2}$$

or

$$\mathbf{R}^{\perp}_{mag} = (\omega_0,\, 0,\, \omega_{rf} \cos \Omega t), \tag{D–3}$$

respectively, where Ω is the frequency of the rf field, and ω_0 and ω_{rf} are the Rabi

frequencies associated with $\mathbf{H}_0$ and $\mathbf{H}_{\rm rf}$. The two geometries are characterized by odd and even resonances, respectively. That is, for weak rf fields, resonances occur when ω_0 is an odd (even) multiple of Ω, and the corresponding transitions can be attributed to the absorption of an odd (even) number of real (virtual) rf photons [53,21]. As the rf amplitude increases, the resonances shift and eventually disappear. These shifts are known as Bloch-Siegert shifts and have been calculated by many authors (see Section II-4.2 on page 133). For example, to lowest order, the shifts of the resonances in the time-averaged fluorescence or absorption signals are given by

$$\omega_0 = N\Omega\left[1 - a_N(\omega_{\rm rf}/4\Omega)^2\right], \qquad \text{(D–4)}$$

where $a_1 = 1$ for the single quantum resonance, and $a_N = 4/(N^2 - 1)$ for photon numbers $N > 1$ [54–57]. Apart from their parities, odd and even resonances differ in another important regard, namely their power broadening: Whereas the widths of the odd-N resonances vary as the Nth power of the rf amplitude $\omega_{\rm rf}$, the even-N resonances are unbroadened to lowest order in the rf amplitudes, and their associated Bloch-Siegert shifts can be measured for even weak rf fields [31–34,45,53]. The latter are the so-called Haroche resonances. In the transverse pumping geometry, there is also a resonance at $\omega_0 = 0$. This is the zero-field crossing resonance or Hanle resonance, and has been interpreted as giving rise to the dressing of the atomic Landé factor by the rf field, according to $g_{\rm rf} = g_0 J_0(\omega_{\rm rf}/\Omega)$, where J_0 is the zeroth-order Bessel function [53].

Consider now an optical resonance experiment on a two-level atom. The optical Bloch equations can be written as in Eqs.(D-1), by introducing the Bloch vector $\mathbf{\Phi}$, whose components, respectively, are the real and imaginary parts of the atomic polarization and the population inversion (see Eq.(II-12) on page 125):

$$d\mathbf{\Phi}/dt = -\mathbf{\Gamma}\mathbf{\Phi} + \mathbf{R}_{\rm opt} \times \mathbf{\Phi} + \Lambda_{\rm opt}\hat{\mathbf{e}}_3. \qquad \text{(D–5)}$$

Here, $\Lambda_{\rm opt}$ is the scaled equilibrium inversion and, again, $\mathbf{\Gamma}$ is a diagonal damping matrix. The optical "torque" $\mathbf{R}_{\rm opt}$ depends on the driving field and the frame in which Eq.(D-5) is expressed. For example, for a constant, monochromatic field $E^{\rm C}(t) = 2\mathcal{E}\cos\omega t$, and a frame that rotates at the two-level transition frequency ω_{12}, $\mathbf{R}_{\rm opt}$ is given, exactly, by

$$\mathbf{R}^{\rm C}_{\rm opt} = (-2\kappa\mathcal{E}\cos\omega t,\, 0,\, \omega_{12}), \tag{D–6}$$

where κ is the dipole coupling constant. Eqs.(D-2) and (D-6) are fully equivalent. Indeed, by substituting the appropriate variables, this equivalence leads, with $N = 1$ in Eq.(D-4), to the conventional optical Bloch-Siegert shift, namely $\Delta = \omega_{12} - \omega = -(\kappa\mathcal{E})^2/4\omega$. As we have shown another equivalent interaction is that of a two-level atom driven by a fully amplitude modulated (FAM) field [21,22,28]: $E^{\rm FAM}(t) = 2\mathcal{E}\cos\Omega t\cos\omega t$. Indeed, in a frame rotating at the detuning $\Delta = \omega_{12} - \omega$, the torque $\mathbf{R}_{\rm opt}$ for this interaction is given by

$$\tilde{\mathbf{R}}^{\rm FAM}_{\rm opt} = (-\kappa\mathcal{E}\cos\Omega t,\, 0,\, \Delta), \tag{D–7}$$

where Ω is the modulation frequency, and where the tilde indicates that the rotating wave approximation (RWA) has been made. The multiple quantum resonances associated with this FAM interaction have been observed experimentally by Chakmakjian *et al.*, namely in the time-averaged fluorescence from a beam of sodium atoms [14]. Because these authors studied the resonances for small detunings ($|\Delta| \leq \Omega$) and relatively large fields ($\kappa\mathcal{E} \geq \Omega$), they used the term "subharmonic resonances" rather than "multiple quantum resonances:" For zero detuning and zero damping, the time-averaged fluorescence signal has maxima for modulation frequencies Ω that are subharmonics of the Rabi frequency $\kappa\mathcal{E}$, namely, for $\Omega = \kappa\mathcal{E}/x_{0n}$, where the x_{0n}'s are the zeros of the J_0-Bessel function.

Figure D-2 shows that multiple quantum resonances and subharmonic resonances are the limiting behaviors of the same resonance structures, and, in both magnetic and optical resonance, the shifts of the resonances from the weak-field values have been termed generalized Bloch-Siegert shifts.

Experimental verification of the conventional optical Bloch-Siegert shift, namely that associated with Eq.(D-6), is improbable because for the super-intense fields necessary to produce a Rabi frequency $\kappa\mathcal{E}$ on the order of the optical frequency ω, the two-level approximation is no longer valid [48]. Similarly, for the FAM interaction studied by Chakmakjian *et al.*, measurement of the weak-field Bloch-Siegert shifts is complicated by the power broadening of the odd-N resonances. Nevertheless, we contend that measurement of the weak-field Bloch-Siegert shifts from Eq.(D-4) should be possible in an optical resonance experiment, namely one in which the FAM field is replaced by a resonant phase-modulated (RPM) field of the form

$$E^{\mathrm{RPM}}(t) = 2\mathcal{E}\cos(\omega_{12}t - M\sin\Omega t), \tag{D–8}$$

where, again, $\dot{\Omega}$ is the modulation frequency, and M is the modulation index. In a frame rotating at the instantaneous frequency of the RPM field, the optical torque associated with Eq.(D-8) becomes

$$\tilde{\mathbf{R}}_{\mathrm{opt}}^{\mathrm{RPM}} = (-\kappa\mathcal{E},\, 0,\, M\Omega\cos\Omega t), \tag{D–9}$$

where, as for the FAM case, the RWA has been made, and the detuning Δ has been set to zero. Comparison of Eq.(D-9) with Eq.(D-3) shows that this RPM interaction is the optical equivalent of a transversely pumped magnetic resonance experiment. Therefore it should display the narrow, even-N, Haroche resonances, as well as the zero-field Hanle resonances.

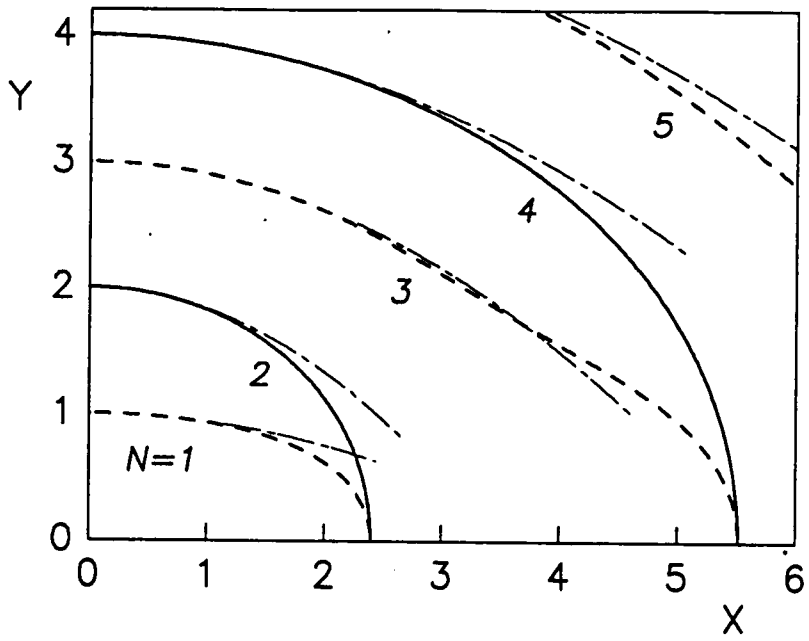


Figure D–2: *Generalized Bloch-Siegert resonance curves for both odd and even resonances, obtained in the limit of vanishing damping.*

Odd-N and even-N resonances are represented by dashed and solid curves, respectively. As shown in Ref. [63], these curves satisfy the condition $\tilde{\chi}_1 = 0$, *where* $\tilde{\chi}_1$ *follows by backward recursion of* $\tilde{\chi}_k = k - p_{kN}Y^2/k - X^2/4\tilde{\chi}_{k+1}$, *with* $p_{kN} = 1$ (0) *for* $k + N =$ *even (odd). The lowest-order shifts from Eq.(D-4) are indicated by the thin lines. The coordinates* X *and* Y *are defined below. The limiting behaviors are given by* $Y = N$ *for* $X = 0$ *and by* $J_0(X) = 0$ *for* $Y = 0$.

	odd-N			*even-N*	
$\mathbf{R}$	$\mathbf{R}^{\parallel}_{\mathrm{mag}}$	$\mathbf{R}^{\mathrm{C}}_{\mathrm{opt}}$	$\tilde{\mathbf{R}}^{\mathrm{FAM}}_{\mathrm{opt}}$	$\mathbf{R}^{\perp}_{\mathrm{mag}}$	$\tilde{\mathbf{R}}^{\mathrm{RPM}}_{\mathrm{opt}}$
X	$\omega_{\mathrm{rf}}/\Omega$	$2\kappa\mathcal{E}/\omega$	$\kappa\mathcal{E}/\Omega$	$\omega_{\mathrm{rf}}/\Omega$	M
Y	ω_0/Ω	ω_{12}/ω	Δ/Ω	ω_0/Ω	$\kappa\mathcal{E}/\Omega$

Both the Haroche and Hanle resonances can be computed by substituting Eq.(D-9) into Eq.(D-5), and solving the RPM interaction as a Floquet series whose coefficients are given by scalar continued fractions [57]: If we introduce the polarization and population decay rates $\Gamma_1 = \Gamma_2 = T_2^{-1}$ and $\Gamma_3 = -\Lambda_{\rm opt} = T_1^{-1}$, and define the dimensionless intentity $I = (\kappa\mathcal{E})^2 T_1 T_2$, the dimensionless modulation rate $\mathcal{M} = (M\Omega T_2/2)^2$, and the factors $b_k^{(j)} = 1 + ik\Omega T_j$ $(j = 1, 2)$ and θ_k such that $\theta_k = 1$ $(\theta_k = 0)$ for $k =$ even $(k =$ odd$)$, these continued fractions S_k are obtained, for $k \geq 1$, by backward recursion of

$$S_k = \mathcal{M}/\left(S_{k+1} + b_k^{(2)} + \theta_k I / b_k^{(1)}\right). \tag{D-10}$$

Thus, the time-averaged upper state population $\rho_{22}^{(0)}$ is given by

$$\rho_{22}^{(0)} = \tfrac{1}{2} I/\left(1 + I + 2\mathrm{Re}\{S_1\}\right). \tag{D-11}$$

For zero modulation, $S_1 = 0$, and $\rho_{22}^{(0)}$ follows a simple saturation curve as a function of the intensity I. However, as the modulation index M increases, two new effects become manifest, as is illustrated in Figure D-3: These are the Haroche and Hanle resonances.

As in magnetic resonance, the Hanle effect determines the behavior of $\rho_{22}^{(0)}$ for small fields. Indeed, in Figure D-3, the behavior of the curves at the origin depends greatly on the modulation index M. It may be shown that, for weak fields and small damping, $\rho_{22}^{(0)}$ can be approximated by

$$\rho_{22}^{(0)} \simeq \tfrac{1}{2} I J_0^2(M) = \tfrac{1}{2} (\kappa\mathcal{E})^2 T_1 T_2 J_0^2(M). \tag{D-12}$$

Thus, the slow rise of the curve with $M = 2.4$ in Figure D-3 is explained by the vanishing of the J_0-Bessel function. The appearance of the factor $J_0(M)$ in Eq.(D-12) is analogous to the dressing of the atomic Landé factor by a similar factor in a transversely pumped magnetic resonance experiment [53].

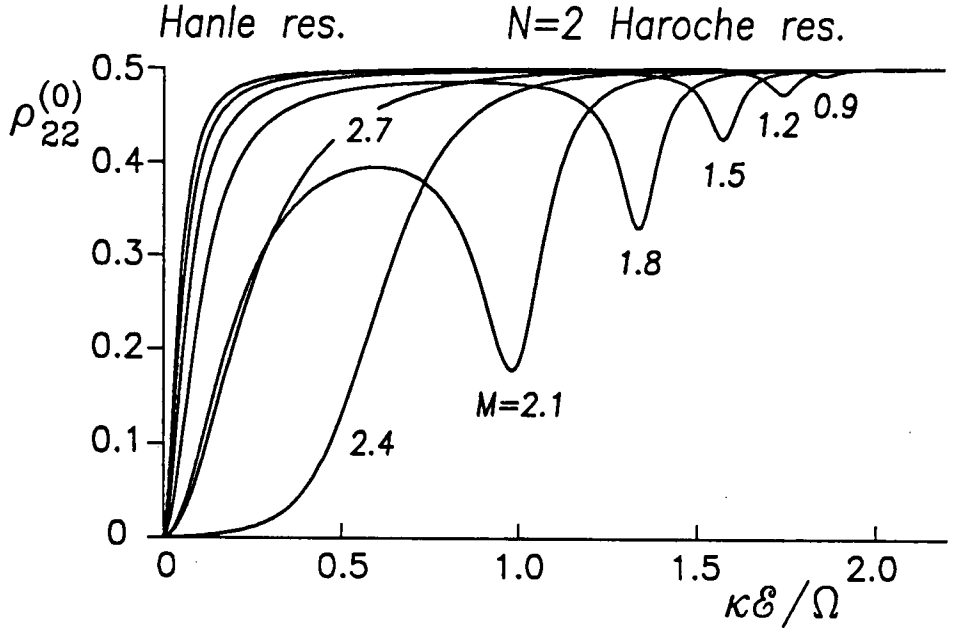


Figure D–3: *Time-averaged upper state population as a function of the scaled electric field.*

Curves are shown for various values of the modulation index M ($\Omega T_1 = \Omega T_2/2 = 20$). The optical Hanle and Haroche resonances occur for $\kappa\mathcal{E} \simeq 0$ and $\kappa\mathcal{E} \lesssim 2\Omega$, respectively.

Similarly, in Figure D-3, the Haroche resonances manifest themselves as dips in the saturated values of $\rho_{22}^{(0)}$ near $\kappa\mathcal{E} = N\Omega$, with $N = 2, 4, 6, \ldots$. For weak modulation, the positions of the resonances are given by the expressions for the weak-field Bloch-Siegert shifts from Eq.(D-4). For example, the $N = 2$ resonance is located at $\kappa\mathcal{E}/\Omega \simeq 2 - M^2/6$. In general, the resonances shift along the solid curves in Figure D-2. Thus, the $N = 2$ resonance disappears for $M \simeq 2.4$, as it merges with the Hanle resonance.

Because it is difficult to achieve modulation indices in excess of unity in practice, it should be easier to detect Haroche resonances in the modulated components of the fluorescence signal. These components can also be obtained from

the continued fraction solution. For example, in terms of the quantities from Eqs.(D-10) and (D-11), the complex amplitude of the component of $\rho_{22}(t)$ that is modulated at 2Ω is given by

$$\rho_{22}^{(2)} = -\rho_{22}^{(0)}\left(S_1 S_2 / M b_2^{(1)}\right). \tag{D-13}$$

Figure D-4 shows that the $N = 2$ Haroche resonance shows up as a pronounced resonance feature in the modulated signal, even for small values of M. For small M, small damping, and $\kappa\mathcal{E} \simeq 2\Omega$, Eq.(D-13) may be approximated by

$$\rho_{22}^{(2)} \simeq \frac{iM^2/32T_1}{\kappa\mathcal{E} - 2\Omega + \frac{1}{6}M^2\Omega + i\Gamma}, \tag{D-14}$$

where $2\Gamma = T_1^{-1} + T_2^{-1}$. Thus, for small M, the position of the $N = 2$ resonance is the same as that of the corresponding dip in the time-averaged component $\rho_{22}^{(0)}$. From Eq.(D-14) it follows also that both the shift and the strength of the resonance are proportional to M^2, and that the width of the resonance is determined solely by the damping rates, as is indicated in Figure D-4. Thus, the Haroche resonances are indeed unbroadened to lowest order in the modulation index and field strength, so that the prospect for experimentally measuring the associated Bloch-Siegert shift seems quite good. Not only would such a measurement provide the first observation of an optical Bloch-Siegert shift, but the narrow resonance structure of the Haroche resonances might be exploited in spectroscopic applications, perhaps foremost in those involving semiconductor lasers, where large amplitude- and phase-modulation have already been achieved [83]. In any event, the manifestation of Haroche and Hanle resonances in the interaction of a phase-modulated field on resonance with a two-level quantum system are noteworthy new features in the rather new fields of phase- and frequency-modulation spectroscopy.

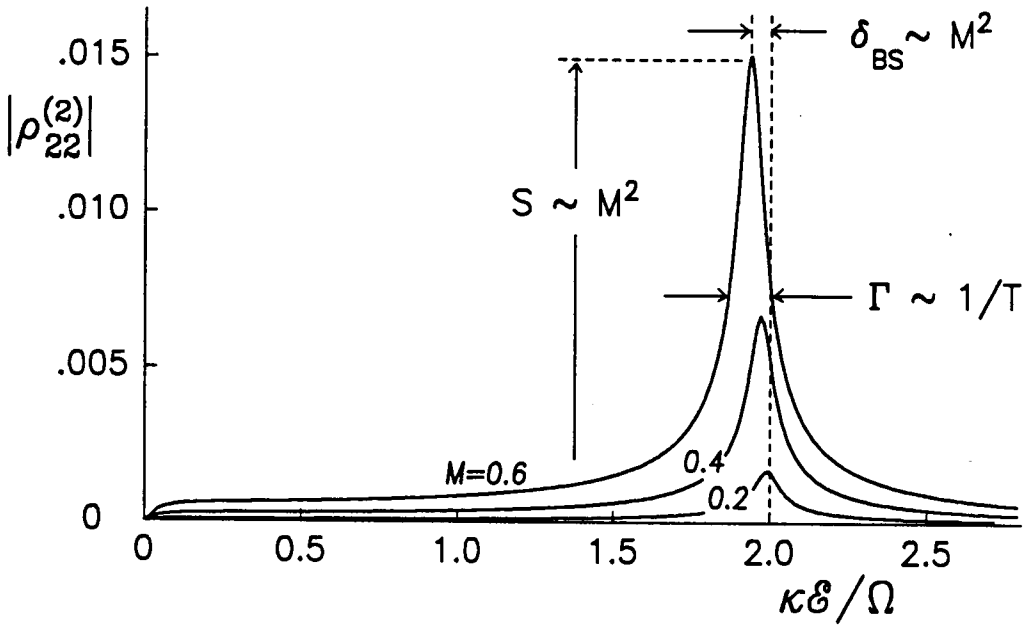


Figure D–4: *As Figure D-3 for the magnitude of the upper state population modulated at twice the modulation frequency.*

This component at 2Ω displays clearly the $N = 2$ Haroche resonance.

Appendix E: List of Abbreviations and Symbols

In Part II, the following abbreviations are used:

AM, FM	Amplitude Modulated, Frequency Modulated.
DC	(Direct Current): time-averaged.
FAM	Fully Amplitude Modulated.
LDV, LFV	Laser Doppler Velocimeter, Laser Fluorescence Velocimeter.
rf	radio frequency.
RWA	Rotating Wave Approximation.
VDCF	Vanishing Damping Continued Fraction.

Below follows also a list of symbols found in Sections I through V. Symbols that occur only in the Appendices are not included. In case of slight variations in notation only the primary definition is mentioned. The alphabetical order of the list is: small Roman, capital Roman, small Greek, capital Greek.

a_0	Bohr radius $\simeq 0.529\mathring{A}$.
a_k	Coefficients of FAM solution defined in Eq.(III-8).
$a_{kN}^{(m)}$	Bloch-Siegert shift coefficients from Eq.(III-34).
b	Rabi frequency associated with the oscillating magnetic field in a longitudinally pumped geometry [Eq.(II-32)].
e	Electron charge.
f_k, g_k	VDCF coefficients defined in Eqs.(III-19) and (III-21).
g	Rabi frequency associated with FAM field from Eq.(III-2).
g_0	Gyromagnetic ratio of magnetic multiplet.
$\hbar$	Plank's constant divided by 2π.
i, k, l, m	Summation indices or other indices.
k	Order of harmonic component.

$\mathbf{k}$, $\mathbf{k}_1$, $\mathbf{k}_2$, k	Wave vectors and magnitude thereof.
n	Order of Bloch-Siegert shift expansion in Eq.(III-34).
n_a	Number of absorbed photons in multi-photon transition.
p_{12}	Electric dipole moment of two-level transition.
p_k	Product of continued fractions $x_k^{[0]}$ defined in Eq.(III-24).
$\overline{r_{2k}}$, $\overline{r_0}'$	Exact and approximate Floquet coefficients of $\overline{\rho_{22}}(t)$.
t	Time coordinate.
$u(t)$, $v(t)$, $w(t)$	Real and imaginary parts of the atomic susceptibility, and inversion of the two-level system, respectively [Eq.(III-3)].
u_k, v_k, w_k	Floquet expansion coefficients for $u(t)$, $v(t)$, and $w(t)$.
$\mathbf{v}$, $v_\parallel$, $v_\perp$	Atomic velocity vector and components thereof.
x_k, $x_k^{[0]}$, $x_k^{[1]}$	Continued fractions of FAM solution from Eq.(III-9) and Taylor coefficients thereof [Eq.(III-17)].
x_{kl}, $\tilde{x}_{kN}$	Zeros of integer order Bessel functions [Eq.(III-33)].
$z(t)$, z_k, z_k^{VDCF}	Generic notation for the variables $u(t)$, $v(t)$, $w(t)$, the coefficients u_k, v_k, and z_k, and their VDCF limit.
$\mathbf{C}$	Inhomogeneous term in optical Bloch equations [Eq.(II-12)].
$E(t)$	Electric field of exciting radiation.
$\mathcal{E}$, $\mathcal{E}_a$, $\mathcal{E}_b$, $\mathcal{E}_i(t)$	Electric field amplitudes.
F_k	Rescaled terms f_k from Eq.(III-30).
$G_\parallel(\Delta)$	Inhomogeneous profile associated with the parallel velocity distribution in a LFV geometry.
H	Correction factor for unequal damping rates [Eq.(III-28)].
H_{int}	Interaction Hamiltonian from Eq.(II-4).
$\mathbf{H}(t)$, H_x, H_y, H_z	Magnetic field vector and components thereof.
H_0, H_{rf}, H_{ri}	Magnitudes of static, oscillating, and rotating fields $\mathbf{H}(t)$.
$J_l(x)$	Integer order Bessel function of order l.

$\mathcal{L}_{\pm}(\Delta)$	Lorentzian line profiles defined in Eq.(IV-17).
M	Modulation index of AM or FM electric field.
$\mathbf{M}$, $\mathbf{M}_0$	Magnetization vector and equilibrium value thereof.
M_{12}	Complex depth-of-modulation defined in Eq.(IV-6).
M_{nb}, M_{bb}, M_{ihb}	Depths-of-modulation of fluorescence harmonics.
$\overline{M_{2k}}$	Depth-of-modulation defined as $\overline{r_{2k}}/\overline{r_0}$.
N	Quantum number of multiple quantum resonance.
N_i	Number of integration elements in Eqs.(IV-26).
$R(\Delta)$	Broadband excitation rate from Eq.(IV-18).
$\mathbf{R}$	Interaction "torque" vector in optical Bloch equations.
T_1, T_2	Longitudinal and transverse relaxation times.
T_P	Characteristic pumping time associated with $\mathbf{M}_0$.
$U(t)$, $V(t)$, $W(t)$	Real and imaginary parts of the atomic susceptibility, and inversion of the two-level system, respectively [Eq.(II-5)].
W_{eq}	Equilibrium value of atomic inversion $W(t)$.
Y_k	VDCF continued fraction defined in Eq.(III-31).
β	Bohr magneton.
γ_u, γ_v	Damping ratios Γ_u/Γ_w and Γ_v/Γ_w.
$\delta_{k,0}$	Kronecker delta.
θ	Angle between laser beams in LFV geometry or angle between static and oscillating magnetic fields.
κ	Dipole coupling constant defined in Eq.(II-7).
ρ_{11}, ρ_{12}, ρ_{21}, ρ_{22}	Two-level system density matrix elements; the upper state population ρ_{22} is associated with the fluorescence signal.
$\tilde{\rho}_{12}$	Rotating frame value of ρ_{12}.
$\rho_{11}^{(0)}$, $\rho_{22}^{(0)}$	Equilibrium values of ρ_{11}, ρ_{22}.
$\overline{\rho_{22}}$	Ensemble averaged value of ρ_{22}.

$\varphi_i(t)$, $\varphi_l(t)$	Phase factors of electric field components.
ϕ_k, ϕ_k^0	Zero detuning values of ψ_k from Eqs.(III-13)–(III-14).
ψ_k	Combined Floquet coefficients from Eq.(III-7).
ω	Frequency of rf magnetic field [Eq.(II-32)].
ω_0	Rabi frequency associated with the static magnetic field in a longitudinally pumped geometry [Eq.(II-32)].
ω, ω_i, ω_l, $\omega_\pm$	Frequency components of electric field $E(t)$.
ω_l, ω_l'	Carrier frequencies of FAM field in laboratory frame and atom's rest frames.
ω_{12}	Two-level atom transition frequency (optical interaction).
Γ_u, Γ_v, Γ_w	Damping rates associated with $U(t)$, $V(t)$, $W(t)$.
Γ_s	Bandwidth of optical source.
Δ, Δ_{opt}, Δ'	Detunings of the carrier frequency of FAM field in laboratory frame and atom's rest frames (primed).
Δ, Δ_{mag}	Zeeman splitting between atomic doublets.
Δ_{max}, Δ_D	Rectangular and Doppler widths of $G_{\parallel}(\Delta)$.
Δ_i	Detuning value in the summation from Eqs.(IV-26).
$\Delta_{kN}^{(n)}$	Detuning value of multiple quantum resonance [Eq.(III-34)].
Θ_k^N	Truncation parameter defined in Eq.(III-35).
$\mathbf{\Lambda}$	Diagonal damping matrix in Bloch equations.
$\mathbf{\Phi}$	Bloch vector defined in Eq.(II-11).
Φ_{12}	Phase factor associated with the quantity M_{12} [Eq.(IV-6)].
Φ_{nb}, Φ_{bb}, Φ_{ihb}	Phase-shifts of fluorescence harmonics.
$\overline{\Phi_{2k}}$	Inhomogeneously broadened phase-shifts from Eq.(IV-27).
Ω, Ω'	Modulation frequencies of FAM field in laboratory frame and atom's rest frames.
$\Omega_i^{(\pm)}(t)$	Generic Rabi frequencies defined in Eq.(II-17b).

VITA

Wilhelmus (Wim) M. J. Ruyten was born on August 4, 1959 in Swalmen, the Netherlands. Upon graduation from the "Bisschoppelijk College" (high school) in nearby Roermond in 1977 he attended the Eindhoven University of Technology in Eindhoven, the Netherlands. After a three month stint at Philips' Research Laboratories in Eindhoven and a nine month exchange visit to Purdue University, West Lafayette, Indiana, he graduated "met lof" (with honor) as "Ingenieur in de Technische Natuurkunde" (Master of Science in Physics) from EUT on July 4, 1984.

After marrying the former M. Belle Pribble from Cynthiana, Kentucky, and relocating in the United States, he attended the University of Tennessee Space Institute in Tullahoma, Tennessee, where he worked in the Center for Laser Applications as a research assistant and as a predoctoral fellow. Here this dissertation research was carried out, culminating in the Ph.D. degree in Physics on August 11, 1989.

Mr. Ruyten is a member of Phi Kappa Phi and the American Institute of Physics, through the Optical Society of America, and received the All-American Scholar Collegiate Award in 1989.